Vibrational Investigation of Aromatics and their weakly bonded Clusters by Dispersed Fluorescence Spectroscopy and Franck-Condon Analysis

Inaugural-Dissertation

zur Erlangung des Doktorgrades
der Mathematisch-Naturwissenschaftlichen Fakultät
der Heinrich-Heine-Universität Düsseldorf

vorgelegt von

Frieder Ortwin Benjamin Stuhlmann
aus Herdecke

Düsseldorf, Januar 2014

aus dem Institut für Physikalische Chemie I
der Heinrich Heine-Universität Düsseldorf

Gedruckt mit der Genehmigung der
Mathematisch-Naturwissenschaftlichen Fakultät der
Heinrich-Heine-Universität Düsseldorf

Referent:	Prof. Dr. Karl Kleinermanns
Koreferent:	Prof. Dr. Michael Schmitt

Tag der mündlichen Prüfung: 23.01.2014

“I would like -if I may- to take you on a strange journey.”

the Criminologist, the Rocky Horror Picture Show

Contents

Symbols and Abbreviations

	Physical Constants from Reference [1]
h	Planck Constant $h = 6.62606957 \cdot 10^{-34}$ Js
$\hbar$	Planck Constant $\hbar = h/2\pi = 1.05457173 \cdot 10^{-34}$ Js
e_0	Elementary Charge $e_0 = 1.60217657 \cdot 10^{-19}$ C
k_B	Boltzmann Constant $k_B = 1.38064881 \cdot 10^{-23}$ J/K
R_0	Universal Gas Constant $R_0 = 8.31446217$ $\mathrm{JK^{-1}mol^{-1}}$
m_{el}	Mass of the Electron $m_{\mathrm{el}} = 9.10938291 \cdot 10^{-31}$ kg
ε_0	Vacuum Permittivity $\varepsilon_0 = 8.85418782 \cdot 10^{-12}$ $\mathrm{C^2J^{-1}m^{-1}}$
a_0	Bohr Radius $a_0 = 4\pi\varepsilon_0\hbar^2/e_0^2 m_{\mathrm{el}} = 5.29177211 \cdot 10^{-11}$ m
E_h	Hartree Energy $E_h = 2hcR_\infty = 4.35974434 \cdot 10^{-18}$ J
R_∞	Rydberg-Constant $R_\infty = m_{\mathrm{el}} e_0^4/8h^3 c\varepsilon_0^2 = 1.09737316 \cdot 10^5$ $\mathrm{cm^{-1}}$

	Methods and Equipment
LIF	Laser Induced Fluorescence
HRLIF	High Resolution Laser Induced Fluorescence
DF	Dispersed Fluorescence
HF	Hartree-Fock Theory
R2PI	Resonant two Photon Ionisation Spectroscopy
REMPI	Resonance-Enhanced Multi-Photon Ionisation Spectroscopy
NMR	Nuclear Magnetic Resonance Spectroscopy
TOF	Time of Flight (Mass Spectrometry/Spectroscopy)
PMT	Photomultiplier Tube
ICCD	Intensified Charge-Coupled Device
YAG	Yttrium Aluminium Garnet (Nd:$Y_3Al_5O_{12}$)
BBO	Beta Barium Borate ($\beta-BaB_2O_4$)
KDP	Potassium Dihydrogen Phosphate (KH_2PO_4)
SHG	Second Harmonic Generation
THG	Third Harmonic Generation
MCP	Micro-Channel Plate

OPO	Optical Parametric Oscillator
OPA	Optical Parametric Amplifier
KTP	Potassium Titanyl Phosphate ($KTiOPO_4$)
B_mA_n	Benzene-Acetylene Cluster
Ph_mA_n	Phenol-Acetylene Cluster
5CI	5-Cyanoindole
BI	Benzimidazole
THC	Tetrahydrocarbazole
AM1	Austin Model 1[2]
DFT	Density Functional Theory
DFT-D/b97d	Density Functional Theory with Dispersion-Correction[3]
MRCI	Multi-Reference Configuration Interaction (as in e.g. DFT/MRCI)[4]
MP2	Møller-Plesset Perturbation Theory
CCSD	Coupled-Clusters Singles and Doubles
CC2	A variant of CCSD[5]
RI-	Resolution of the Identity (as in e.g. RI-MP2 or RI-CC2)
SCS-	Spin-Component Scaling[6] (as in e.g. SCS-MP2 or SCS-CC2)
-SAPT	Symmetry-Adapted Perturbation Theory (as in e.g. DFT-SAPT)
TZVP/TZVPP	Triple Zeta Valence plus Polarisation Basis Set[7]
cc-pVTZ	Correlation Consistent Polarised Valence Triple Zeta Basis Set
aug	Augmented (e.g. aug cc-pVTZ for SCS-MP2 Calculations)
aVDZ	Augmented (for SCS-MP2) Valence Double Zeta Basis Set
FC	Franck-Condon
HT	Herzberg-Teller

Operators, Matrices and Similar

$\hat{\mu}_{\text{el}}$	Electronic Transition Dipole Moment Operator
S	Duschinsky Matrix
$\vec{d}$	Displacement Vector
$\hat{H}$	Hamiltonian
∇	Nabla Operator
∇^2	Laplacian Operator
$\hat{F}$	Fock Operator
$\hat{J}$	Coulomb Operator
$\hat{K}$	Exchange Operator (from Hartree-Fock Theory)
$\hat{U}$	Fluctuation Operator in the CC2 Method
H_ν	Hermite Polynomial

$\mathbf{T}$	Hougen-Watson Axis Switching Matrix
$\mathbf{B}$	Block Matrix of the Form $diag\left(\mathbf{T}R_{3i-2}, \mathbf{T}R_{3_i-1}, \mathbf{T}R_{3i}\right)$
$\mathbf{L}$	Transformation Matrix Containing the Eigenvectors of the Duschinsky-Matrix
$\mathbf{C}$	Displacement Matrix
λ_ω	Matrix in the Form $\lambda_\omega = diag\left(\sqrt{\omega_1}, \sqrt{\omega_2}, \ldots, \sqrt{\omega_{N_{\mathrm{vib}}}}\right)$
$\mathbf{J}$	Transformation Matrix $\mathbf{J} = \lambda_{\omega''}\mathbf{S}\lambda_{\omega'}^{-1}$
$\vec{\delta}$	Vector $\vec{\delta} = \frac{\lambda_{\omega'}\vec{d}}{\sqrt{\hbar}}$
$\mathbf{Q}$	Transformation Matrix $\mathbf{Q} = \left(1 + \mathbf{J}^T\mathbf{J}\right)^{-1}$
$\mathbf{P}$	Transformation Matrix $\mathbf{P} = \mathbf{JQJ}^T$
$\mathbf{R}$	Transformation Matrix $\mathbf{R} = \mathbf{QJ}^T$

Variables and Parameters

ν	Frequency in Hz
E, ϵ	Energy (of an Ensemble, Electronic State, Orbital, . . .)
$\tilde{\nu}$	Frequency in cm^{-1}
λ	Wavelength in nm
τ	Lifetime
k	Rate Constant
Γ	Reducible or Irreducible Representation (Symmetry)
R, r	Cartesian Coordinate/Distance of Nuclei (R) or Electrons (r)
q	Mass-weighted Cartesian Coordinate
Q	Normal Coordinate
N	Number of a Quality denoted by the Subscript
FC	Franck-Condon Factor
I	Intensity
P	Transition Probability
M	Transition Dipole Moment
T	Absolute Temperature in K
V	Volume in m^3
Kn	Knudsen Number
H	Enthalpy
U	Internal Energy
p	Pressure
m	Mass in kg
m_{mol}	Molecular Mass in g/mol
v, u	Velocity
M	Mach Number

c_s	Local Speed of Sound
ϵ	Collision Constant
j_0	Coefficient $j_0 = e_0^2/4\pi\varepsilon_0 = 2,30707735 \cdot 10^{-28}$ Jm
T	Kinetic Energy
V	Potential Energy
Z	Nuclear Charge
n	Density
$t_{\nu'}^{\nu''}$	Excitation Amplitude t =(Overlap Integral $\langle \nu' \mid \nu'' \rangle$)
λ	Eigenvalue of a Matrix
ω	Circular Frequency $\omega = 2\pi\nu$ in inverse Seconds
$t_{\dots}$	Delay Time
el	Electronic (as Subscript)
vib	Vibratory (as Subscript)
rot	Rotationally (as Subscript)
$''$	Ground State (as Superscript)
$'$	Excited State or occupied Spin-Orbital (as Superscript)
mol	Molecular Property (as Subscript)
$\Vert$	Parallel to a given Reference
$\perp$	Perpendicular to a given Reference
Ψ	Total Wavefunction
ψ	Partial Wavefunction (denoted by Subscript)
$\vec{\nu}$	Vibrational State Wavefunction expressed as Quantum String
ϕ	Spin-Orbital
φ	Basis Function
L	Angular Momentum Quantum Number
M	Magnetic Momentum Quantum Number
S	Electron Spin Momentum Quantum Number
J	Total Angular Momentum Quantum Number $J = L + S$
q	Ring Quantum Number (analogous to L)
Q	Total Ring Quantum Number (analogous to J)
ν_i	Vibrational Quantum Number

Miscellaneous Abbreviations

S	Singlet State
T	Triplet State
$^1\mathrm{L}_a/^1\mathrm{L}_b$	Low-lying Excited Singlet States in the Nomenclature of Platt[8]

Fl	Fluorescence
Ph	Phosphorescence
VR	Vibrational Relaxation
IC	Internal Conversion
ISC	Intersystem Crossing
IVR	Internal Vibrational Redistribution
Ex	Excitation (as Subscript)
Em	Emission (as Subscript)
IR	Infrared
UV	Ultraviolet

1. Introduction

The structure of a molecule is determined by its nuclear and electronic framework. Different techniques exist to investigate this framework by the interaction of the molecular system with electromagnetic fields. Some examples are diffraction of x-rays, nuclear magnetic resonance with a high-frequency field or absorption and emission of photons which change the rotational (microwave), vibrational (infrared) or electronic (ultraviolet) state of the molecule depending on the photon energy.[9, 10]

While many of those methods in a multitude of technical realisations (depending on the nature of the sample and the exact kind of problem) are used routinely to investigate the properties of the electronic *ground* state of a molecule or aggregate, the investigation of the molecular structure in *excited* (singlet) states however, is more challenging.

The field of electronic spectroscopy is concerned with this research, since the electronic geometry is a direct indicator for the nuclear geometry. *Fluorescence spectroscopy in supersonic jets* allows for the investigation of both electronic ground state and the "bright" excited electronic states that are accessible by absorption and from which luminescence can be observed.

In this work, the structures of aromatics and their aggregates in the electronic ground state and the first excited electronic singlet state are investigated.

The clusters of these aromatics are bonded by weak π–π or H–π interactions, which are also an important force e.g. in biochemical processes.[11–14] One aim of this work is to gain a better understanding of these interactions.

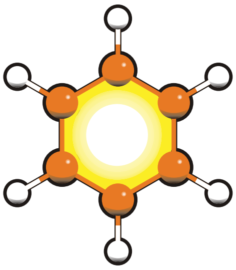

Figure 1.1: Benzene

Chapters 5 and 6 describe the structures of small aggregates of benzene (Figure 1.1) and phenol (Figure 1.2) with acetylene (Figure 1.3). One reliable method to identify organic compounds is *infrared spectroscopy*. Earlier works concentrated on the characteristic C–C stretch vibration of the acetylene moiety at around 3200 cm^{-1}[15] and the O–H stretch vibration at around 3500 cm^{-1}.[16] The frequencies of these vibrations shift depending on the *binding motif* (further to the red as more electron density is drawn from the vibrating bond, thus decreasing the bond order and the force constant) and this shift can be verified by high-level *ab initio* calculations that are in turn used to assign the cluster structure.

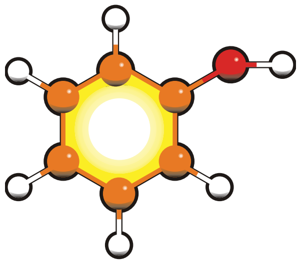

Figure 1.2: Phenol

This spectral region is reached by e.g. difference frequency mixing techniques, and the near infrared to middle infrared spectrum can be probed directly e.g. by spectral holeburning techniques. A much more significant feature of each organic compound however is found in the *fingerprint region* from 500 to 1500 cm^{-1} as the frequencies of the skeleton vibrations are found in this spectral range.[9] Additionally, the inter-molecular vibrations of clusters show frequencies in the far infrared between 10 and 200 cm^{-1}, or in other words the low *terahertz* region.

Absorption spectroscopy in this spectral region is very costly, as bright and narrowband light sources and detectors for THz radiation are scarce and expensive.[17, 18] As of today, only expensive quantum cascade lasers[19] or free electron lasers such as FELIX[20] are suitable for this spectral region.

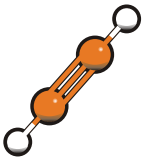

Figure 1.3: Acetylene

The method used in this work - *dispersed fluorescence* - circumvents this need for far infrared radiation. The light source here is a frequency doubled dye laser operating in the UV spectral region ($\sim 33000-38000$ cm^{-1} depending on the dye employed in the respective project). Vibrational states of the first electronic excited singlet state are excited. When the measurement takes place in a supersonic jet, the only pathway to relax to the electronic ground state is *fluorescence*. Infrared spectra in the region below 3000 cm^{-1} are then obtained indirectly by subtracting the energy that is dissipated by fluorescence from the energy with which the molecule was excited.

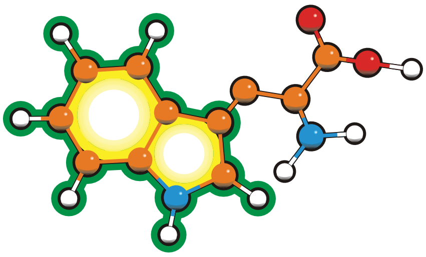

Figure 1.4: Tryptophane with highlighted indole-chromophore

Other interesting aromatics which were investigated are the derivatives of indole, the chromophore of the aromatic amino acid tryptophane. Figure 1.4 shows the structure of tryptophane with its chromophore highlighted in green. When the fluorescence spectra of proteins are measured, the observed fluorescence is mostly that of the indole side chains.

Indole and its derivatives have *two near-degenerate electronic states* accessible to laser spectroscopy, called ^1L_a and ^1L_b in the nomenclature of Platt.[8]

While the $^1\mathrm{L}_b$ state is stabilised in non-polar surroundings and shows a structured emission spectrum, the more polar $^1\mathrm{L}_a$ state is stabilized in polar media and generally shows an unstructured spectrum. The energetic order of the states can switch according to the polarity of the solvent. The energetic order of $^1\mathrm{L}_a$ and $^1\mathrm{L}_b$ and the resulting fluorescence spectrum is therefore a valuable marker of the *chemical surrounding* of the probed tryptophane-moiety.

The $^1\mathrm{L}_a$-$^1\mathrm{L}_b$-gap can also be influenced by introducing functional groups into the chromophore in addition to solvent effects. Determining and understanding the effects of different manipulations of the chromophore on its electronic structure can help in the analysis of biomolecules and is the second aim of this work.

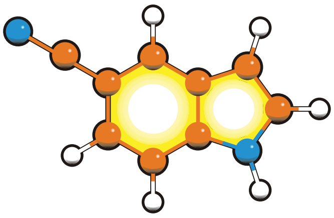

Figure 1.5: 5-Cyanoindole

5-Cyanoindole has an electron withdrawing cyano-group in the 5-position that stabilises the $^1\mathrm{L}_a$ sufficiently enough, so that this state becomes the emitting state. The spectra of 5-cyanoindole and its determined geometry change upon electronic excitation are presented in Chapter 7.

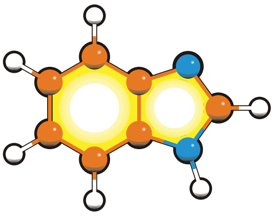

Figure 1.6: Benzimidazole

The other derivative investigated in this work is benzimidazole. As seen in Figure 1.6, the carbon in 3-position is replaced by a nitrogen atom in this structure. Benzimidazole provides an interesting case as the exact nature of the fluorescent state is still unknown. *Ab initio* studies of the absorption and emission spectra of benzimidazole on a very high level of theory show a disagreement with laser induced fluorescence measurements and the energetic order of the excited states depends strongly on the method used.[21–23]

The $^1\mathrm{L}_a$ and $^1\mathrm{L}_b$ state are very close in this molecule (they show a gap of around 1000 cm^{-1} in the isolated molecule) and probably mix to an extent that makes it impossible to unambiguously label them in the nomenclature of Platt.

The *geometry change* of both heteroaromatic compounds upon electronic excitation has been researched by a combination of dispersed fluorescence and *Franck-Condon analyses*. If the probed transitions are allowed by the Franck-Condon principle,[24–26] the absorption and fluorescence intensity pattern is determined by geometry changes upon electronic excitation. In the Franck-Condon analysis described in Chapter 3.5, this geometry change is derived from the intensity distribution in fluorescence spectra.

For this, the program FCFIT that was written in our workgroup[27, 28] is used.

The starting geometries of both electronic states are calculated with high-level *ab* *initio* methods implemented in the TURBOMOLE program package.[29] The methods used are chosen depending on the system that is investigated and are described in Chapter 3.1.

The geometry of the excited state is then distorted along certain normal coordinates and the emission spectra are simulated. The geometry change that leads to a reproduction of the measured spectra is found if they are well reproduced by the Franck-Condon simulation.

The quality of the geometry fit is enhanced by the addition of the rotational constant changes of the investigated molecule and a number of its isotopomers determined by high resolution laser induced fluorescence.[30]

Herzberg-Teller coupling explains the intensity of transitions through the perturbation of the emitting state by a near-lying singlet state. According to the Franck-Condon principle, those transitions would be forbidden. The program FCFIT allows for the Herzberg-Teller correction of simulated vibronic spectra.

Both 5-cyanoindole and benzimidazole show *Herzberg-Teller* activity[31] after an energy threshold that is reached by the UV laser (around 1000 cm^{-1} above the electronic origin) and the spectra of benzene are based completely on this vibronic coupling.

The Herzberg-Teller correction shows a significant improvement of the simulated spectra and fitted geometry change of 5-cyanoindole while the wealth of Franck-Condon intensities and rotational constant changes measured for benzimidazole allows to present in this work a complete fit of its geometry change even without Herzberg-Teller correction.

Part I

Theoretical Background

2. Measurement Principles

This chapter provides a short summary over the complex field of electronic spectroscopy in a scope suited for the comprehension of the publications in part II of this work. For a more detailed insight into the background to photophysics and laser spectroscopy, the books of Klán and Wirz[32] and Demtröder[10, 33] are recommended to the reader.

2.1 Photophysical Pathways

In this work the interaction between light and matter has been harnessed to determine the properties -such as electronic and nuclear structure- of different molecules. If certain requirements are met, a molecule can absorb a photon and store its energy in several degrees of freedom. One of those requirements is that the energy $h\nu$ of the absorbed photon correlates with the energy gap ΔE between two energetic states of the molecule:

$$E' - E'' = h\nu \tag{2.1}$$

Properties of the ground state are indicated by double prime ($''$) and properties of the excited state are indicated by single prime ($'$) in this nomenclature.

In the ultraviolet and visible range of the electromagnetic spectrum, the absorbed energy is large enough to promote an electron from one occupied molecular orbital to a higher lying unoccupied orbital. In most cases, this electronic transition leads also to a vibrational and rotational excitation. If that is the case, the transition is described as *vibronic* or *rovibronic*. The energy of such a transition in inverse centimetres (cm^{-1}) is described by Equation 2.2:

$$\tilde{\nu} = \tilde{\nu}_{\text{el}} + \tilde{\nu}_{\text{vib}} + \tilde{\nu}_{\text{rot}} \tag{2.2}$$

with the electronic wavenumber $\tilde{\nu}_{\text{el}}$, the vibrational wavenumber $\tilde{\nu}_{\text{vib}}$ and the rotational wavenumber $\tilde{\nu}_{\text{rot}}$. Their energies differ by several orders of magnitude: some 10^4 cm^{-1} (UV-visible range) for $\tilde{\nu}_{\text{el}}$, $10^2 - 10^3$ cm^{-1} (infrared region) for $\tilde{\nu}_{\text{vib}}$ (in some cases even as low as some 10 cm^{-1}, in the THz-region) and below that $\tilde{\nu}_{\text{rot}}$.

Two other requirements are the compliance of this transition with electronic and symmetry *selection rules.* Table 2.1 sums up the electronic selection rules, which are related to the change of quantum numbers (L, M, S, J) describing the electronic states.

Table 2.1: Electronic selection rules for electric dipole transitions

category	rule	applicability
angular momentum	$\Delta L = \pm 1$	multi-electron atoms with l-s coupling*
magnetic momentum	$\Delta M = 0$	absorption of linear polarised light
	$\Delta M = \pm 1$	absorption of circular polarised light
electron spin momentum	$\Delta S = 0$	exceptions lead to ISC (see text)
total angular momentum	$\Delta J = 0, \pm 1$	with $J = L + S$. But $J = 0 \nrightarrow J = 0$

*as opposed to jj-coupling (e.g. in heavy atoms)

The symmetry selection rule (which becomes important in Section 2.3.2) states that a symmetry allowed transition must be allowed regardless of the symmetry operations applied to it. Thus, the matrix product of the characters of all representations Γ involved in the transition (electronic states, vibrations, electronic transition dipole moment operator, etc.) has to include the totally symmetric representation Γ_1 of the point group to which the molecule belongs. This is expressed in Equation 2.3 for an electronic excitation and in Equation 2.4 for a vibronic excitation:

$$\Gamma_{\psi'_{\mathrm{el}}} \times \Gamma_{\hat{\mu}_{\mathrm{el}}} \times \Gamma_{\psi''_{\mathrm{el}}} \supset \Gamma_1 \tag{2.3}$$

$$\Gamma_{\psi'_{\mathrm{el}}} \times \Gamma_{\psi'_{\mathrm{vib}}} \times \Gamma_{\hat{\mu}_{\mathrm{el}}} \times \Gamma_{\psi''_{\mathrm{el}}} \times \Gamma_{\psi''_{\mathrm{vib}}} \supset \Gamma_1 \tag{2.4}$$

In vibrational spectroscopy those selection rules can be summarised to: *Vibrational transitions are infrared active if the dipole moment of the probed molecule is changing while the molecule is vibrationally excited and Raman active if its polarizability is changing.* A more detailed introduction into molecular symmetry and its implications for spectroscopy is given in the books of Bishop [34], Engelke [35] and Janiak [36].

The transition between the vibrationless electronic ground state and the vibrational ground state of the first excited state of the same multiplicity is called the *electronic origin* of a vibronic spectrum, since the features from the vibronic adiabatic transitions are based on that $\nu'_0 \leftarrow \nu''_0$-transition. If the electronic origin has no intensity due to violated selection rules (see Section 2.3.2), the energetically lowest allowed vibronic transition from the electronic ground state is called the *false origin*, since the other features in the spectrum are based on that transition.

Since the energy of the absorbed photon is now stored in some excited state of the molecule for a finite amount of time τ, several pathways open up to dispose of this energy and return to the electronic ground state. Those are either photochemical reactions, or photophysical redistribution of the excess energy.

One handy way to visualise photophysical pathways is the *Jablonski diagram*, a term scheme first proposed by Aleksander Jabłónski[37]. Figure 2.1 shows such a diagram. In this very simplified form, only two singlet states and one triplet state are shown to explain the basic energetic pathways in a molecule after excitation by a photon with the energy $h\nu_{\mathrm{Ex}}$ (illustrated by the blue wave) to some vibrational state $\nu_{i>0}$ in the first electronic excited state S_1.

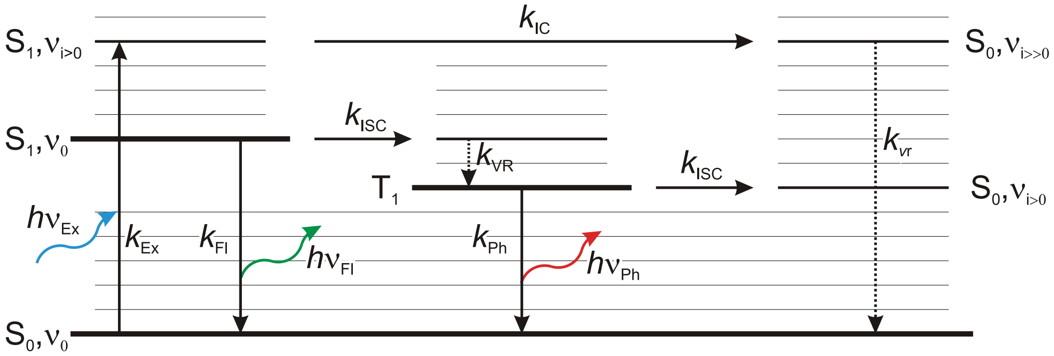

Figure 2.1: Jablonski diagram with the fundamental energetic pathways after excitation to $S_1\nu_{i>0}$. S = singlet state, T = triplet state, ν = vibrational state, k = rate constant, $h\nu$ = photon energy, Fl = fluorescence, Ph = phosphorescence, VR = vibrational relaxation, IC = internal conversion, ISC = inter system crossing. Transitions are indicated by straight arrows, wavy arrows indicate photons, decreasing in energy from blue to red.

The electronic ground state in most organic molecules is a singlet state S_0 in which all electrons are paired according to Hund's rules and the resulting total electron spin is zero.[38] Since the selection rule for the electron spin momentum states that $\Delta S = 0$, only transitions to higher singlet states are possible.

A non-radiative pathway to dispense of the energy is *vibrational relaxation* VR. The energy that is stored in some vibrational degree of freedom is distributed over a whole ensemble of molecules by collisions. The energy can also be distributed to rotational degrees of freedom by *Coriolis coupling*, when the combination of the displacement vectors from degenerate vibrations leads to displacement vectors that describe a rotation of the whole molecule. In large molecules of low symmetry, this degeneration can happen by chance because of the high density of vibrational states. In the condensed phase, where many collision partners are present, vibrational relaxation prohibits the observation of fluorescence from vibrational excited states. This is commonly known as *Kasha's rule*. If the molecule is excited in a surrounding, where nearly no collisions take place (e.g.

in a molecular beam, after adiabatic cooling equalised the velocity distribution of all particles), vibrational relaxation is not possible and the fluorescence occurs from the vibrational excited state.

Vibrational relaxation leads to the vibrational ground state of the underlying electronic state. If that is an excited electronic state, the residual energy has to be dissipated through other channels.

Three different horizontal channels are available through vibrational coupling. Those are isoenergetic but can open new relaxation pathways that were inaccessible from the starting state.

If the excited state (e.g. $S_1\nu_{i>0}$) is isoenergetic with some high lying vibrational state of a lower lying electronic state with the same multiplicity (e.g. $S_0\nu_{i\gg 0}$), *internal conversion* IC to that vibrational state can take place. This can lead back from high electronic singlet states to the electronic ground state through conical intersections.

Internal conversion, coupled with fast vibrational relaxation and heat dissipation, is a major photo protection mechanism in the DNA[39]. In most molecules it is only fast for transitions from higher electronically excited states to the lowest excited state and leads to Kasha's rule: *The emitting electronic level of a given multiplicity is the lowest excited level of that multiplicity*[40]. He estimated a rate k_{IC} to the S_1 at the order of 10^{13} $s^{-1}$for common systems.

Such a vibrational coupling can also occur between states of different multiplicity. In that case, *intersystem crossing* ISC takes place. Since the spin of one electron is reversed, the transition is forbidden and this process is rather slow in most molecules (compared to other channels) with a k_{ISC} below 10^7 s^{-1}. It is preferentially found in molecules with heavy or paramagnetic atoms where strong spin-orbit coupling is found. After ISC (and possibly vibrational relaxation to the $T_1\nu_0$), the energy can be redistributed to another electronic singlet state either isoenergetic by a second step of ISC or under emission of a photon by phosphorescence. Triplet molecules are also accessible for chemical reactions with e.g. triplet-oxygen or other radicals.

Another kind of vibrational coupling –which is not shown in Figure 2.1– is *intramolecular vibrational redistribution* IVR. If the density of vibrational states is high enough, overtones or combinations of low frequency vibrations can be isoenergetic with higher frequency vibrations. In that case, the energy can be redistributed to those vibrational modes like in IC or ISC. The difference to those channels is, that all vibrational levels involved in IVR correspond to the same electronic level. The time constant of IVR at a given excitation energy is proportional to the size of the excited molecule, since the number of vibrational normal modes is $3N_{\mathrm{nuc}}-6$ for non-linear molecules. For molecules above the size of benzene, k_{IVR} can become larger then 10^{12} s^{-1}. For benzene at a vibrational

S_0 energy of 5186 cm^{-1}, $k_{\mathrm{IVR}} = 1.3 \cdot 10^{11}$ s^{-1} is found[41].

The energy that is stored in the molecule after excitation or non radiative transitions can be lost by the emission of a photon with the energy $h\nu \leq h\nu_{\mathrm{Ex}}$. This pathway is called luminescence. Depending on the electronic state in which the energy is stored, either fluorescence or phosphorescence takes place. The energy of that photon depends on the energy gap between the excited and ground state.

If the luminescence occurs between states of the same multiplicity (like $S_0 \leftarrow S_1$ or $T_1 \leftarrow T_2$), it is called *fluorescence*. The fluorescence photon in Figure 2.1 is illustrated by a green wave, since some of the energy $h\nu_{\mathrm{Ex}}$ has already been lost through other channels. This red shift between absorption and emission is also known as the *Stokes shift*[42]. The energy $h\nu_{\mathrm{Fl}}$ of the fluorescence photon is smaller and its wavelength red shifted. This fluorescence can either occur spontaneous or induced by another photon.

If the luminescence takes place from any state of a different multiplicity than the electronic ground state, it is called *phosphorescence*. In Figure 2.1 this is indicated by a red wave, since the energy gap between T_1 and S_0 is even smaller than between S_1 and S_0 in this example and the wavelength of the resulting photon is shifted further to the red. Since the spin of the excited electron has to be reversed, the lifetime of the triplet state is usually very long (up to the magnitude of hours) and phosphorescence is rather slow compared to e.g. fluorescence.

Table 2.2 sums up the orders of magnitude of the time constants given in ref. [32], page 28. Those time constants are inverse to the lifetime τ of the involved energetic levels in seconds.

Table 2.2: Orders of magnitude of time constants from Figure 2.1

Process	notation	scale in s^{-1}
Absorption	k_{Ex}	10^{15}
Internal conversion	k_{IC}	$10^{6} - 10^{12}$
Inter system crossing (S→T)	k_{ISC}	$10^{6} - 10^{12}$
Inter system crossing (T→S)	k_{ISC}	$\leq 10^{9}$
Vibrational relaxation	k_{VR}	$10^{12} - 10^{13}$
Intramolecular vibrational redistribution	k_{IVR}	10^{12}
Fluorescence	k_{Fl}	$10^{7} - 10^{9}$
Phosphorescence	k_{Ph}	$\leq 10^{6}$

2.2 Laser Spectroscopy

2.2.1 Laser Induced Fluorescence

To record a *laser induced fluorescence* (LIF) spectrum, the frequency of a probe laser is scanned. If the laser is resonant with a vibronic transition of the probe molecule, fluorescence can be observed.

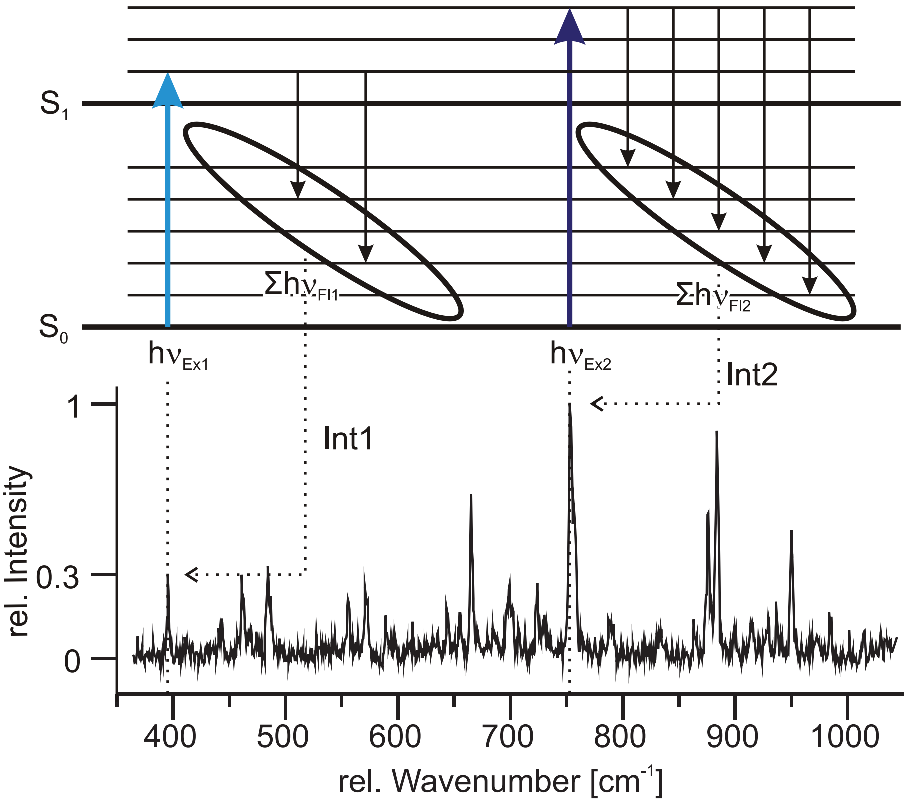

Figure 2.2: Jablonski diagram and example of a LIF spectrum. The plotted vibrational lines do not represent the actual vibronic levels that correspond to the measured bands. $h\nu$/straight arrows: photon energy, dotted lines/arrows: qualitative analogy to the measured category, Ex: excitation, Fl: fluorescence, Int: signal intensity.

Figure 2.2 shows an example of a laser induced fluorescence spectrum of 5-Cyanoindole (compare Figures 7.2 and 7.5 in Chapter 7) along with a Jablonski scheme to exemplify two of the observed bands. The straight arrows indicate energy gaps, that correlate to the energy $h\nu$ of absorbed ($S_1 \leftarrow S_0$) or emitted ($S_0 \leftarrow S_1$) photons. In a LIF-spectrum, the detected intensity is plotted against the excitation wavenumber. A band is observed when the excitation energy is resonant with a vibronic transition and fluorescence is allowed from this excited state. This is indicated by the dotted lines that connect arrows in the term scheme with features in the spectrum. In this example, $\tilde{\nu}_{h\nu_{\mathrm{Ex1}}} \approx 400\ \mathrm{cm}^{-1}$

and $\tilde{\nu}_{h\nu_{\mathrm{Ex2}}} \approx 750\ \mathrm{cm}^{-1}$ are observed. Since no wavelength selective elements are used, the experimental intensity (relative to that of the $\nu'_0 \leftarrow \nu''_0$ transition) of a given band is proportional to the integral over all fluorescence photons that are emitted from the corresponding excited state. This is indicated by the dotted arrows to the intensity scale.

This picture is very sketchy, so the energetic levels that are plotted in the Jablonski scheme do not represent the actual levels that are involved in the observed transitions. A more accurate depiction would show ν'_9 as excited state of Ex1 and ν'_{20} for Ex2 respectively. Also, since only an arbitrary few emitting transitions are indicated, the fluorescence intensity in this figure is described by a sum instead of an integral.

In this method, the vibrational levels of the excited electronic state are probed. The vibrational levels of the electronic ground state are indistinguishable.

2.2.2 Dispersed Fluorescence

To investigate the vibrational levels of the electronic ground state, the probe laser is fixed on one of the transitions that are known from the LIF spectrum and the fluorescence light is dispersed on a holographic grating and the intensity relative to that of the strongest transition is plotted against the fluorescence wavenumber relative to that of the scattered excitation light.

This method is known as *dispersed fluorescence* (DF). Figure 2.3 shows an example of a dispersed fluorescence spectrum (one detail of the DF spectrum of the electronic origin of 5-Cyanoindole, compare Figure 7.3 in Chapter 7) along with a Jablonski scheme to explain the observed bands. As with Figure 2.2, straight arrows indicate energy gaps resonant with photon energies $h\nu$ and dotted lines indicate the corresponding bands. The energies $h\nu_{\mathrm{Fl}_{0-n}}$ are detected and the excitation energy is subtracted.

The resulting relative wavenumbers correspond directly to the far infrared frequencies of the vibrational modes in the electronic ground state, indicated by coloured arrows. In this example, one potential fluorescence transition is forbidden and a gap in the dispersed fluorescence spectrum results, where the anticipated band has zero intensity.

The difference to the intensity pattern observed in direct measurement of infrared absorption bands (e.g. with Fourier transform IR spectroscopy or direct absorption by free electron lasers) is, that the transitions probed in dispersed fluorescence spectroscopy gain intensity from Franck-Condon integrals between vibrational wavefunctions of different electronic states (and infrared frequencies are determined indirectly) and not from pure vibrational excitation. Thus, in some cases, ground state vibrations that are visible in absorption spectra can be undetectable in dispersed fluorescence and vice versa as different selection rules apply. Information from dispersed fluorescence and direct IR absorption

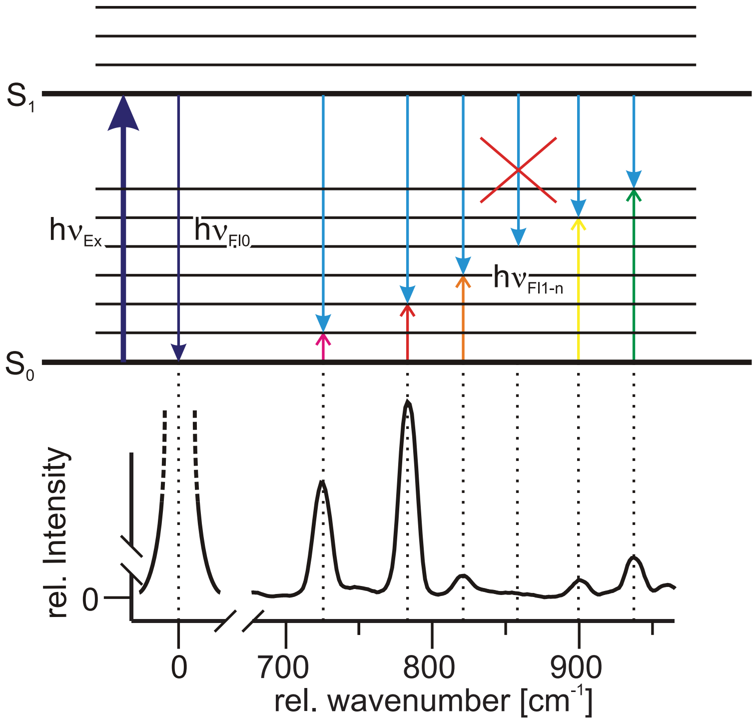

Figure 2.3: Jablonski diagram and example of a DF spectrum. The plotted vibrational lines do not represent the actual vibronic levels that correspond to the measured bands. $h\nu$/straight blue/light blue arrows: photon energy, other straight arrows: derived far-IR energy gaps, dotted lines/arrows: qualitative analogy to the measured category, Ex: excitation, Fl: fluorescence

are therefore in many cases complementary.

2.3 Line Intensities and Linewidths

As already indicated in Figures 2.2 and 2.3, not every transition that fits Equation 2.1 leads to a sharp feature in the experimental spectrum. The observed bands differ in intensity and show a certain width around a base frequency ν_0 that is the consequence of a combination of different effects. Those are discussed in Detail in Reference [10] on pages 41-64 and should only be skimmed here as the experimental setup described in Chapter 4 is optimised for the research presented in this work.

2.3.1 Spectral Line Profiles

The spectral linewidth of the probe laser is accountable to some extent, as all transitions that fall into the linewidth of the excitation laser are excited. Detectors and dispersive elements also have a limited resolution and are chosen fitting to the experiment. For example: By using a laser with a very narrow linewidth (like in *high resolution laser* *induced fluorescence* spectroscopy), the underlying rotational structure of the vibronic bands would become visible.

Other effects are *Doppler broadening* due to the velocity distribution of the probed molecules in several directions and *impact broadening* due to collisions of probed molecules with each other or with inert molecules that lead to energy redistribution after the laser excitation. Those two effects are drastic in condensed phase and minimised in molecular beams.

Doppler Broadening

As Doppler broadening depends on the Maxwell-Boltzmann velocity distribution in the thermally equilibrated gas described by Equation 2.5 with particle mass m and velocity v, the resulting line shape is a *Gauss profile* as described by Equation 2.6.

$$f(v)dv = \sqrt{\frac{m}{2\pi k_B T}} \cdot e^{\frac{mv^2}{2K_B T}} dv \tag{2.5}$$

$$G_\nu = \frac{2}{\delta\nu}\sqrt{\frac{ln(2)}{\pi}} \cdot e^{-4ln(2)\left(\frac{\nu-\nu_0}{\delta\nu}\right)^2} \tag{2.6}$$

This velocity distribution is picked up again in Section 2.5 as it becomes important in the discussion of the supersonic free jet. The value that is interesting for the analysis of broadening effects is the *full width at half maximum* (FWHM), δv. For the Gauss profile resulting from Doppler broadening it is defined in Equation 2.7 with molar mass m_{mol}, speed of light c and universal gas constant R_0.[10]

$$\delta\nu = \frac{2\nu_0}{c}\sqrt{\frac{2R_0 T ln(2)}{m_{\mathrm{mol}}}} = 7.16 \cdot 10^{-7}\nu_0\sqrt{\frac{T}{m_{\mathrm{mol}}}} \tag{2.7}$$

Natural Linewidth

A broadening effect intrinsic to the probed molecule is the *natural linewidth*: Following Heisenbergs uncertainty principle, the energy of an electronic state with the lifetime τ is only definable to an extent given in Equation 2.8:

$$\Delta E' = \frac{\hbar}{\tau'} \tag{2.8}$$

This leads to an uncertainty of frequency for the transition to this state from the electronic ground state or vice versa.

$$\delta\nu = \frac{\Delta E'}{h} = \frac{1}{2\pi\tau'} = \frac{\gamma}{2\pi} \tag{2.9}$$

The resulting Profile is a *Lorentzian profile* given in Equation 2.10 with a damping constant $\gamma \ll \nu_0$ and the FWHM defined in Equation 2.9.

$$L(v) = \frac{\gamma}{4\pi^2 \left(\nu - \nu_0\right)^2 + \left(\frac{\gamma}{2}\right)^2} \tag{2.10}$$

From the combination of Doppler broadening and natural linewidth follows a Voigt profile that is described by Equation 2.11.[10]

$$V(\nu) = \int_{-\infty}^{\infty} G\left(\nu'\right) \cdot L\left(\nu - \nu'\right) d\nu' \tag{2.11}$$

If a transition between two excited states is probed, the uncertainty of the energy of both states contributes to the broadening. The width of a spectral line is thus an indicator for the lifetime of the excited state, if the other broadening effects are known.

Time of Flight in Supersonic Jets

Further broadening effects are *saturation broadening* at a very high excitation laser power and *time of flight* broadening in supersonic jets. This time of flight broadening replaces the natural linewidth if the duration of stay of the sample molecules is shorter than their excited state lifetime. The resulting line profile is another Gauss profile with the FWHM $\delta\nu$ given in Equation 2.12 since the intensity in the laser profile is generally described by a Gauss profile. Considering the fact, that the molecule passes several curved wavefronts leads to the FWHM given in Equation 2.13 with particle velocity perpendicular to the laser beam $v_\perp$, laser wavelength λ, laser beam diameter d and radius of curvature R.[10]

$$\delta\nu = \left(\frac{4v_\perp}{d}\right)\sqrt{2ln(2)} \approx \frac{4.7v_\perp}{d} \tag{2.12}$$

$$\delta\nu = \frac{4v_\perp}{d}\sqrt{2ln(2)}\sqrt{1 + \left(\frac{\pi d^3}{R\lambda}\right)^2} \tag{2.13}$$

2.3.2 The Franck-Condon Principle

Following the Born-Oppenheimer approximation[43], the total wavefunction of a molecule can be separated into a *nuclear* and an *electronic* wavefunction:

$$\Psi = \psi_{\text{el}}(r) \cdot \psi_{\text{nuc}}(R) \tag{2.14}$$

As the masses of the nuclei are very large compared to that of an electron, nuclear motions are several orders of magnitude slower than those of the much lighter electrons.

This leads to the Franck-Condon principle[24–26]: *Electronic transitions happen without any change in the nuclear geometry and starting from their equilibrium geometry.* This is indicated by vertical arrows in Figure 2.4.

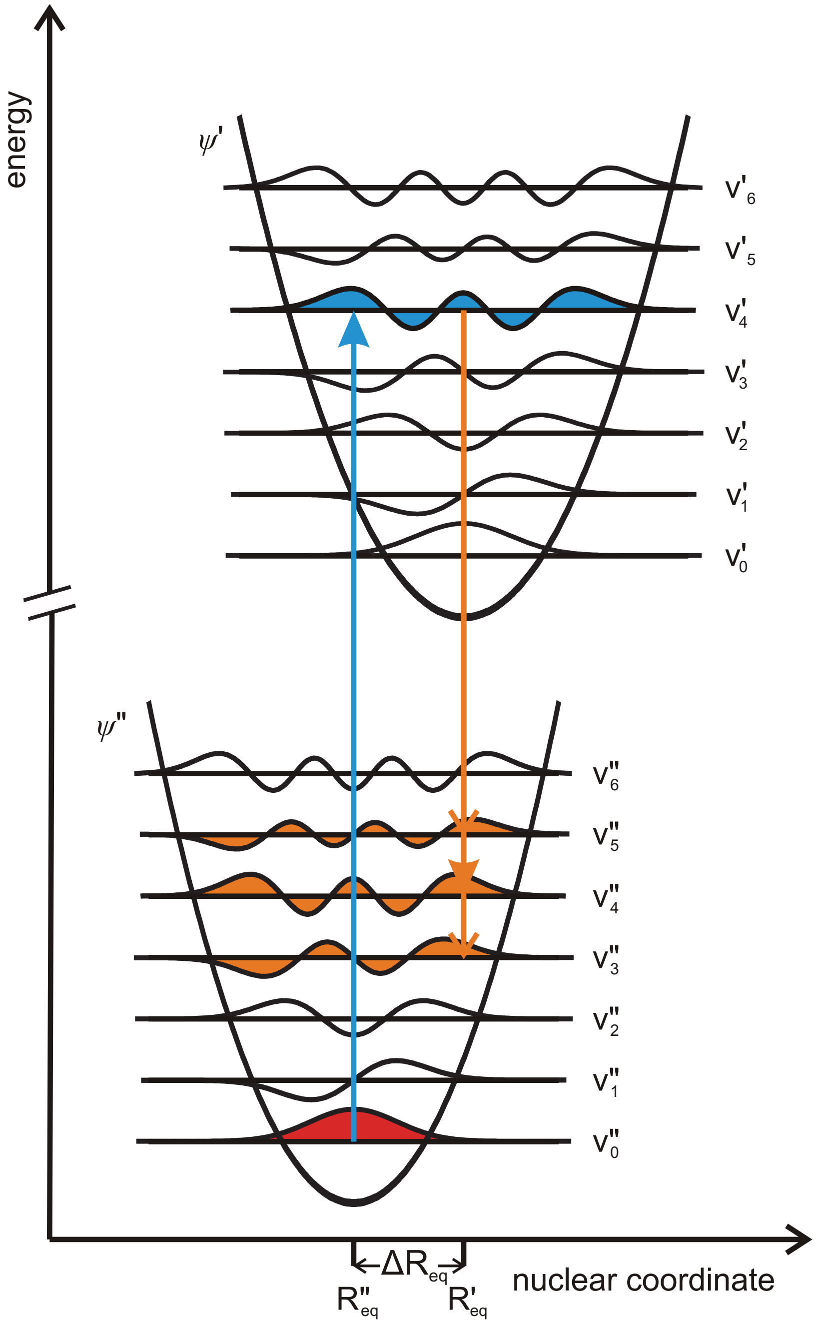

Figure 2.4: Energy level diagram illustrating some transitions between two electronic states E″ and E′. The blue arrow illustrates the vibronic excitation from ν_0'' to ν_4'. The orange arrows illustrate vibronic transitions from the excited state ν_4' to different vibrational states ν'' in the electronic ground state: The thick arrow indicates the transition to the vibrational state ν_4'', which shows a good overlap of the vibrational wavefunctions *at that nuclear coordinate*, the thin arrows indicate a less good overlap.

If normal coordinates Q are used instead of Cartesian coordinates R, ψ_{nuc} from Equation 2.14 becomes the N_{vib}-dimensional *vibrational wavefunction* $\psi_{\mathrm{vib}}(Q)$, where N_{vib} is the number of normal modes ν of the molecule. The displacement of the equilibrium geometry is then described by Equation 2.16 instead of the one-dimensional shift ΔR_0.

This two dimensional depiction of a multi dimensional problem is of course extremely simplified. The arrows in Figure 2.4 can only depict overlap *products* of the wavefunctions involved at discrete nuclear coordinates, while the transition probability for each transition depends on the overlap *integral* over all nuclear coordinates. It is defined as

$$\int \left[\psi'_{\mathrm{vib}}\left(Q'\right)\right]^{*} \psi''_{\mathrm{vib}}\left(Q''\right)\ dQ' = \left\langle \nu'_1 \dots \nu'_{N_{\mathrm{vib}}} \,\middle|\, \nu''_1 \dots \nu''_{N_{\mathrm{vib}}} \right\rangle \tag{2.15}$$

which depends anti proportionally on the shift ΔR_{eq} of the two potential energy curves.

It is very convenient to express ψ_{vib} as a vector $\vec{\nu}$ which contains the elements ν_i with $i = 1, \dots, N_{\mathrm{vib}}$ and the values of ν_i representing the number of quanta in the ith normal mode. Such a vector is generally called *quantum string* and this notation becomes very useful in later chapters. The wavefunction of the excited state is the *bra* $\langle \nu' |$ and the wavefunction of the ground state is the *ket* $| \nu'' \rangle$ in this notation regardless of the direction of the transition.[1] The ket is always complex conjugate by definition of the Dirac bra-ket[44], but since the harmonic oscillator wavefunctions and all operators used in the following equations are real, their complex conjugate is the original function and thus they commute.

The normal coordinates in both electronic states are linked by a linear orthogonal transformation[45] first described by Duschinsky in Reference [46]:

$$Q' = \mathbf{S}Q'' + \vec{d} \tag{2.16}$$

As mentioned above, Q'' and Q' are the N_{vib}-dimensional normal coordinates which describe the normal modes in the electronic ground and excited states respectively. $\mathbf{S}$ is a $N_{\mathrm{vib}} \times N_{\mathrm{vib}}$ rotation matrix called the *Duschinsky matrix* and $\vec{d}$ is a N_{vib}-dimensional displacement vector. This transformation is explained in detail in Chapter 3.2.2.

The intensity of this transition is the square of the absolute value of its transition probability:

$$I = \mid P \mid^2; \qquad P = M_{\mathrm{vib}} + M_{\mathrm{el}} \tag{2.17}$$

Its *vibronic transition dipole moment* M_{vib} is defined as

$$M_{\mathrm{vib}} = \langle \psi'_{\mathrm{vib}} \,|\, \hat{\mu}_{\mathrm{el}}(Q) \,|\, \psi''_{\mathrm{vib}} \rangle \tag{2.18}$$

---

[1] In some publications, initial and final state are noted as $|m, v\rangle$ and $|n, w\rangle$, where ψ_{el} are noted as m and n and ψ_{vib} are noted as v and w.

with the *electronic transition dipole moment operator* $\hat{\mu}_{\text{el}}(Q)$

$$\hat{\mu}_{\text{el}}(Q) = \langle \psi'_{\text{el}} \,|\, \mu_r \,|\, \psi''_{\text{el}} \rangle \,; \qquad \mu_r = \sum_g e_0 \vec{r}_g \tag{2.19}$$

with the elementary electric charge e_0 and the position vector $\vec{r}_g$ of the gth electron.

The electronic transition dipole moment operator $\hat{\mu}_{\text{el}}$ can be approximated by expanding it in a Taylor series about the equilibrium position at Q_0. If the series is truncated after the first term, $\hat{\mu}_{\text{el}}$ becomes a constant factor.

M_{el} can be defined analogous if the electronic wavefunctions are replaced by the vibrational wavefunctions and the electronic transition dipole moment operator is replaced by a nuclear transition dipole moment operator μ_R which contains the position vectors and charges of the nuclei.

Inserting Equation 2.19 into Equation 2.18, then inserting both the resulting term for M_{vib} and the analogue for M_{el} into Equation 2.17 followed by separation of the resulting equation for P into nuclear and electronic terms leads to[2]

$$P = \langle \psi'_{\text{vib}} \,|\, \psi''_{\text{vib}} \rangle \cdot \langle \psi'_{\text{el}} \,|\, \mu_r \,|\, \psi''_{\text{el}} \rangle + \langle \psi'_{\text{el}} \,|\, \psi''_{\text{el}} \rangle \cdot \langle \psi'_{\text{vib}} \,|\, \mu_R \,|\, \psi''_{\text{vib}} \rangle \tag{2.20}$$

The integral $\langle \psi'_{\text{vib}} | \psi''_{\text{vib}} \rangle$ is the overlap integral mentioned above and defined in Equation 2.15, also called the *Franck-Condon Integral.* The square of its absolute value is called the *Franck-Condon factor*, the calculation of which is described in Chapter 3.2.

The integral $\langle \psi'_{\text{el}} | \hat{\mu}_{\text{el}} | \psi''_{\text{el}} \rangle$ is the *orbital selection rule* for the underlying electronic transition.

Since the electronic wavefunctions of both states are orthogonal to each other by definition, the integral $\langle \psi'_{\text{el}} | \psi''_{\text{el}} \rangle$ vanishes and the second term of Equation 2.20 becomes zero.

2.3.3 Herzberg-Teller Coupling

In some cases, transitions that appear forbidden by the Franck-Condon principle (P in Equation 2.20 equals zero) are observed in experimental spectra. A physical explanation for this is given by Herzberg and Teller in Reference [31]. As mentioned above, $\hat{\mu}_{\text{el}}$ defined in Equation 2.19 can be expanded in a Taylor series about Q_0 that is truncated after the first term. This approximation is sufficient for transitions that can be explained by the Franck-Condon principle alone.

To describe the transition dipole moment M_{vib} in the Franck-Condon-Herzberg-Teller

---

[2] Keep in mind for future reference, that ψ_{vib} and $\vec{\text{v}}$ are synonymous and the nomenclature is switched based on whether the electronic wavefunctions appear or not.

approximation, the Taylor series is truncated after the second term and the resulting $\hat{\mu}_{\text{el}}$ is inserted into Equation 2.18. This leads to Equation 2.21 for the transition dipole moment depending on the normal coordinates Q_i for all N_{vib} normal modes ν_i[47].

$$M_{\text{vib}} = \hat{\mu}_{\text{el}}(Q_0)\, \langle \vec{\nu}' \,|\, \vec{\nu}'' \rangle + \sum_i \left(\frac{\delta \hat{\mu}_{\text{el}}}{\delta Q_i} \right)_{Q_0} \langle \vec{\nu}' \,|\, Q_i \,|\, \vec{\nu}'' \rangle \tag{2.21}$$

For symmetry forbidden transitions, the first term (the orbital selection rule) becomes zero, but if vibronic coupling is possible, the transition can gain intensity due to the second term. In that case the excited vibration distorts the molecule in such a way, that during its oscillation the excited state resembles that of a higher lying electronic state which is accessible by a symmetry allowed transition.

This is known as *intensity stealing* or *intensity borrowing*.

One example is the *false origin* of benzene, which was probed for the spectra discussed in Chapter 5.

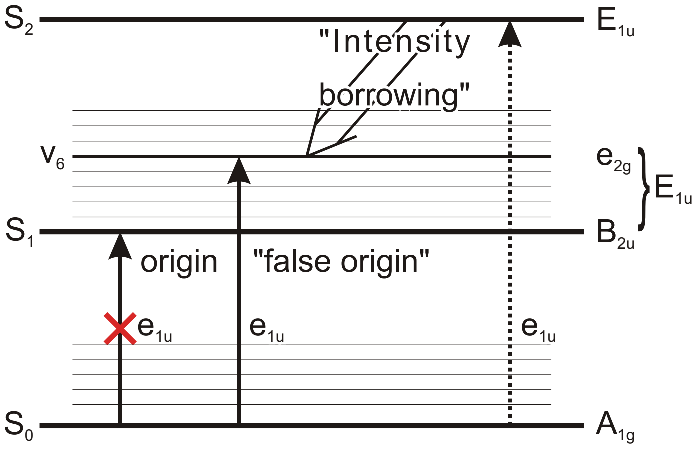

Figure 2.5: Term scheme illustrating intensity borrowing to the false origin of benzene. On the right side, the symmetries of the involved states are given. The $B_{2u} \leftarrow A_{1g}$-transition is symmetry forbidden (see Equation 2.22), while the $E_{1u} \leftarrow A_{1g}$-transition is allowed. Due to the combination of any e_{2g}-vibration with the B_{2u} electronic state, the symmetry of that vibronic state resembles E_{1u} and the vibronic transition gains ("borrows") intensity from the allowed $E_{1u} \leftarrow A_{1g}$-transition.

Benzene has D_{6h} symmetry. The totally symmetric representation for this point group is A_{1g}. The first electronic excited state has B_{2u} and the electronic transition dipole moment operator e_{1u} symmetry[48]. Equation 2.3 is not satisfied for the electronic origin of benzene since

$$\begin{aligned} \Gamma_{\mathrm{S_1}} \times \Gamma_{\hat{\mu}_{\mathrm{el}}} \times \Gamma_{\mathrm{S_0}} &= \Gamma_{\mathrm{origin}} \\ \Gamma_{\mathrm{B_{2u}}} \times \Gamma_{\mathrm{e_{1u}}} \times \Gamma_{\mathrm{A_{1g}}} &= \Gamma_{\mathrm{E_{2g}}} \\ \Rightarrow \Gamma_{\mathrm{origin}} &\not\supset \Gamma_{\mathrm{A_{1g}}} \end{aligned} \tag{2.22}$$

Electronic transitions to a higher electronic state $\mathrm{E_{1u}} \leftarrow \mathrm{A_{1g}}$ are symmetry allowed:

$$\begin{gathered} \Gamma_{\mathrm{E_{1u}}} \times \Gamma_{\mathrm{e_{1u}}} \times \Gamma_{\mathrm{A_{1g}}} \supset \Gamma_{\mathrm{A_{1g}}} \\ \text{or} \\ \langle \mathrm{E_{1u}} \,|\, \mathrm{e_{1u}} \,|\, \mathrm{A_{1g}} \rangle \neq 0 \end{gathered} \tag{2.23}$$

Figure 2.5 shows a term scheme to illustrate vibrational coupling in benzene. The involved states are labelled in the usual nomenclature on the left hand side and denoted by their symmetry on the right hand side. The left arrow indicates the symmetry forbidden electronic origin transition described by Equation 2.22, the right arrow indicates the allowed $\mathrm{S_2} \leftarrow \mathrm{S_0}$-transition described by Equation 2.23. During the oscillation of any vibrational $\mathrm{S_1}$ mode with $\mathrm{e_{2g}}$ symmetry, the $\mathrm{S_1}$ geometry is distorted:

$$\Gamma_{\mathrm{e_{2g}}} \times \Gamma_{\mathrm{B_{2u}}} = \Gamma_{\mathrm{E_{1u}}} \tag{2.24}$$

This leads to the allowed vibronic transition indicated by the middle arrow, that "borrows" its intensity from the $\mathrm{E_{1u}} \leftarrow \mathrm{A_{1g}}$-transition:

$$\begin{aligned} \Gamma_{\mathrm{S_1}} \times \Gamma_{\nu_6} \times \Gamma_{\hat{\mu}_{\mathrm{el}}} \times \Gamma_{\mathrm{S_0}} &= \Gamma_{\text{false origin}} \\ \Gamma_{\mathrm{B_{2u}}} \times \Gamma_{\mathrm{e_{2g}}} \times \Gamma_{\mathrm{e_{1u}}} \times \Gamma_{\mathrm{A_{1g}}} &= \Gamma_{\mathrm{A_{1g}}} + \Gamma_{\mathrm{A_{2g}}} + \Gamma_{\mathrm{E_{2g}}} \\ \Rightarrow \Gamma_{\text{false origin}} &\supset \Gamma_{\mathrm{A_{1g}}} \end{aligned} \tag{2.25}$$

The fluorescence spectrum of benzene consists of the vibronic transitions that are based on this false origin $\mathrm{S_1}\nu_6 \leftarrow \mathrm{S_0}\nu_0$, which is shifted to the blue with respect to the $\mathrm{S_1}\nu_0 \leftarrow \mathrm{S_0}\nu_0$-transition:

$$\begin{aligned} \tilde{\nu}_{\text{false origin}} &= \tilde{\nu}_{\text{origin}} + \tilde{\nu}_6 \\ &= 38005\mathrm{cm}^{-1} + 601\mathrm{cm}^{-1} = 38606\mathrm{cm}^{-1} \end{aligned} \tag{2.26}$$

2.3.4 Hot Bands, Combination Bands and Overtones

Not all features in an absorption or emission spectrum can be assigned to normal modes of the probed molecule. Some of those features belong to background noise and unintentionally excited trace molecules or clusters in the illuminated region. Other types of features are *hot bands*, *combination bands* and *overtones*.

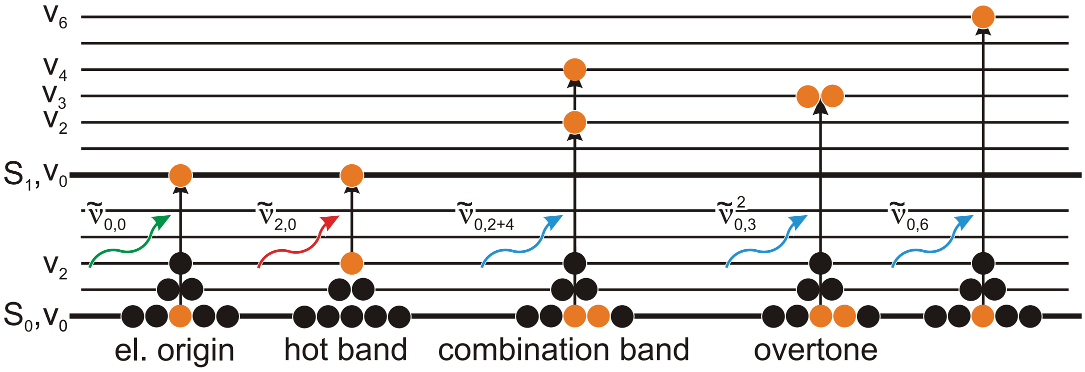

Figure 2.6: Term scheme to visualise different types of vibronic excitations. Wavy arrows indicate photons, descending in energy from blue to red. Straight arrows indicate transitions. Only relevant vibrational states are labelled and the indices $''$ and $'$ have been omitted for better readability. Quanta in the initial distribution are indicated by black dots, redistributed quanta are highlighted in orange

These three types of bands are shown schematically in Figure 2.6: Quanta in the different normal modes ν_i are indicated by dots. Black dots indicate the initial distribution in the electronic ground state that is described by the Boltzmann factor given in Equation 2.27. Orange dots indicate the redistribution to S_1 vibrational modes after excitation with photons that are indicated by wavy lines.

The first case starting from the left is the electronic origin $\nu'_0 \leftarrow \nu''_0$, induced by a photon with the energy $\tilde{\nu}_{0,0}$. The rightmost case is the vibronic excitation $\nu'_6 \leftarrow \nu''_0$, induced by a photon with the energy $\tilde{\nu}_{0,6}$ for comparison with the special cases. If those examples are expressed in bra-ket notation they read $\left\langle \vec{0}' \middle| \vec{0}'' \right\rangle$ and $\langle 000001|0\rangle$ and their transition probabilities are the square of the absolute value of those integrals.

The second case is the hot band $\nu'_0 \leftarrow \nu''_2$ or $\langle 0|01\rangle$. A hot band is the feature that is observed when vibrational states of the electronic ground state are populated thermally prior to the excitation[49]:

$$\nu''_i = \frac{\nu''_0 \cdot g_i \cdot e^{-\frac{h\nu_i}{k_B T}}}{\sum_j g_j \cdot e^{-\frac{h\nu_j}{k_B T}}} \tag{2.27}$$

With the population of the ith ground state mode ν''_i (e.g. $\nu_2 = 1$ means that the second mode is excited with one quantum), the population of the vibrational ground state ν_0'', the degeneracies g of every vibrational energy level, the frequencies ν of each vibration in Hz and the temperature T in Kelvin. The sum over j runs over all ground state vibrations, their combinations and their overtones.

Hot bands appear on the red side of the respective $S_1\nu_i \leftarrow S_0\nu_0$-transitions, since the energy needed for this excitation is reduced by the amount of energy stored in the ground state mode:

$$\tilde{\nu}_{2,0} = \tilde{\nu}_0 - \tilde{\nu}_{\nu_2''} \tag{2.28}$$

The next case is the combination band $\nu_2' + \nu_4' \leftarrow \nu_0''$ or $\langle 0101|0\rangle$. One photon with the energy $\tilde{\nu}_{0,2+4}$ distributes two quanta between ν_2' and ν_4'. The energy of this photon exceeds the origin excitation energy by an amount given in Equation 2.29

$$\tilde{\nu}_{0,2+4} = \tilde{\nu}_0 + \tilde{\nu}_{\nu_2'} + \tilde{\nu}_{\nu_4'} \tag{2.29}$$

assuming harmonicity. $\tilde{\nu}_{0,2+4} = \tilde{\nu}_{0,6}$ in that case and both assignments to a given band are reasonable without further data. The energy gaps between the vibrational levels in an anharmonic potential decrease with increasing energy, so that combination bands calculated in an anharmonic approximation show a frequency distinct from the harmonic combination of the respective normal modes.

Figure 2.7 shows an example of combination bands in the dispersed fluorescence spectrum of the phenol-acetylene dimer investigated in Chapter 6. The assignment was verified in this case by the comparison with monomer spectra which show no bands in that spectral region.

Second from the right in Figure 2.6 is shown the excitation to the first overtone of ν_3' (or in other words $\nu_3' = 2$ after the redistribution) by a photon with the energy $\tilde{\nu}_{0,3^2}$. In bra-ket notation the transition is written as $\langle 002|0\rangle$. Assuming harmonicity, the frequency of the overtones of a normal mode are multiples of the respective normal mode frequency and the energy needed for this transition is described by Equation 2.30:

$$\begin{gathered} \tilde{\nu}_{0,3^2} = \tilde{\nu}_0 + 2 \cdot \tilde{\nu}_3 \\ \text{and} \\ \tilde{\nu}_{0,3^2} = \tilde{\nu}_{0,2+4} = \tilde{\nu}_{0,6} \end{gathered} \tag{2.30}$$

One example for a typical progression of overtones $\nu_i'' = 1, 2, 3, \cdots \leftarrow \nu_i' = 1$ of the excited band in emission spectra is shown in Figure 2.8. It shows the dispersed fluorescence spectrum obtained after the excitation of Q_{24}' of benzimidazole at $\tilde{\nu}_{\text{origin}} + 731$ cm^{-1}. In this variation of Figure 8.5 in Chapter 8, only the Q_{24} progression is labelled. Their experimentally determined frequencies are very close to the harmonically estimated values:

1550.1 cm^{-1} vs. $2 \cdot 772.6$ cm^{-1} = 1545.2 cm^{-1} and 2327.4 cm^{-1} vs. $3 \cdot 772.6$ cm^{-1} = $2317,8$ cm^{-1}.

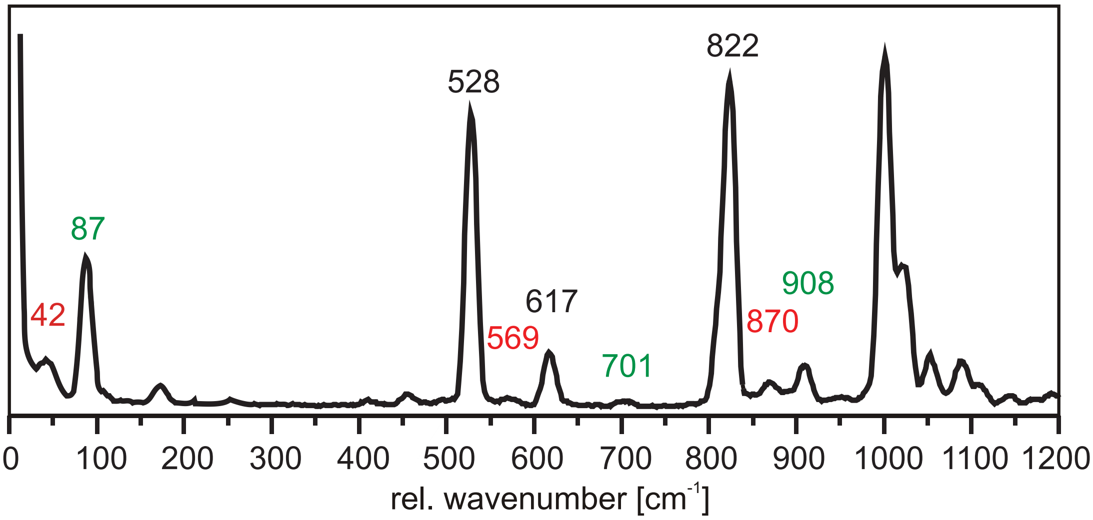

Figure 2.7: Dispersed fluorescence spectrum of the electronic origin of phenol in the phenol-acetylene cluster. Only selected features are assigned in a colour coded way: The red and green labelled features below 200 cm^{-1} belong to intermolecular cluster vibrations. The black labelled features belong to normal modes of phenol, while the red and green labelled features above 500 cm^{-1} are combination bands, where both kinds of modes (black+red or black+green) are excited.

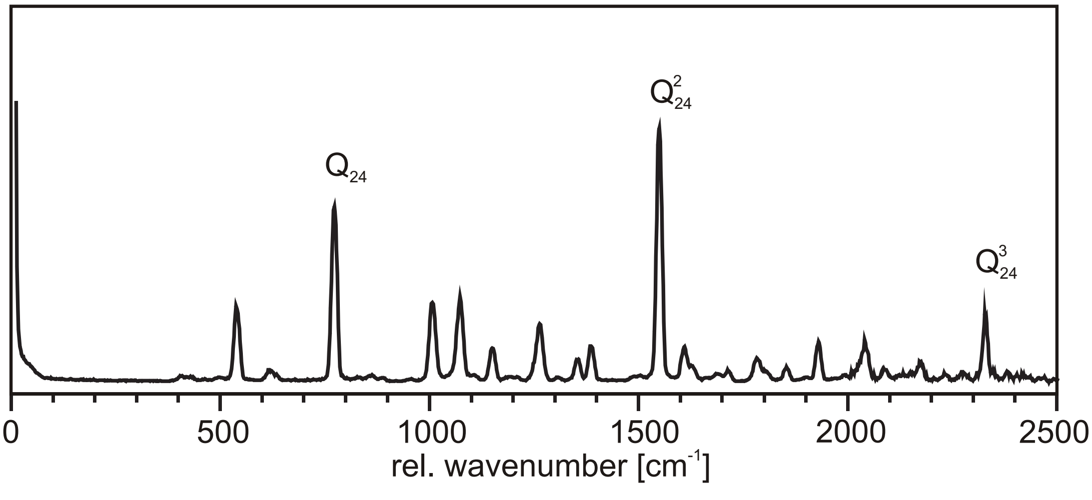

Figure 2.8: Dispersed fluorescence spectrum of the Q'_{24} band of benzimidazole, after excitation trough $\tilde{\nu}_{\text{origin}}$+731 cm^{-1} only the Q_{24} progression is labelled in this figure.

2.4 The Platt Nomenclature

The introduction already mentioned the $^1\mathrm{L}_a$ and $^1\mathrm{L}_b$ state of indole derivatives. This nomenclature that was introduced for cata-condensed hydrocarbons by Platt[8] and adapted for indole derivatives by Weber[50] is very important in later discussions.

These states are the lowest excited singlet states of the systems described by this nomenclature. It should be explained first in its original context:

Cata-condensed hydrocarbons are aromatic systems described by the formula $\mathrm{C}_{4n+2}H_{2n+4}$ and each carbon belongs to one or two rings. Platt describes the π-orbitals of these system as being *like that of the orbitals of a free electron travelling in a one-dimensional loop of constant potential around the perimeter*[8] and the energy of the electron with the equation from the *particle in a one-dimensional box*:

$$E_\pi = \frac{q^2h^2}{2m_{\mathrm{el}}x^2} \tag{2.31}$$

In Equation 2.31, x is the "length" of the conjugated π-electron system and q is the ring quantum number. It becomes apparent from this equation, that the energy levels are quadratically spaced and - as the particle may travel clockwise or counter-clockwise around x - doubly degenerate, except for the lowest orbital with $q = 0$.

Figure 2.9 shows a scheme of the energy levels of the π-electrons denoted by their quantum number q and the index assigned to these shells by Platt. As each of the $4n+2$ carbon atoms contributes one electron to the conjugated system, the highest occupied shell is that with the quantum number n Platt assigns the index f to this highest occupied shell and numbers the unoccupied shells ascending beginning with h.

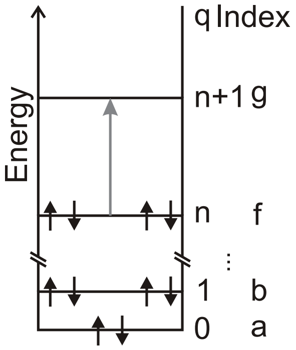

Figure 2.9: Energetic states of the π-electrons in a cata-condensed aromatic, labelled by their ring quantum number q and their index in the Platt nomenclature. The electronic transition from the highest occupied orbital to the lowest unoccupied orbital is indicated by the grey arrow

The ring quantum number q is comparable to the angular momentum l and can be expressed as a vector perpendicular to the plane of the molecule. Nevertheless, the values of q can be treated as scalars since they are restricted to one dimension. With this, a *total ring quantum number* Q is defined analogous to the *total angular momentum.* The states are then denominated according to their value of the total ring quantum number: $Q = 1, 2, 3, \ldots, 2n, 2n+1, 2n+2 \Rightarrow A, B, C, \ldots, K, L, M$.

Excited states are described as linear combinations. The grey arrow in Figure 2.9 indicates the excitation of one electron from the $f(q = n)$ to the $g(q = n + 1)$ shell, this leads to $Q = n \pm (n + 1)$ and the result is two doubly degenerate $B(Q = 1)$ and $L(Q = 2n + 1)$ states. Both sets are present as singlet and as triplet state.

This degeneracy is lifted for molecules which show a lower symmetry than benzene. According to the third of Hund's rules, the state with the highest total Q (that is analogue to L as stated above) is the energetically lower state.[38] The L states are thus always below the B states. Their resulting sublevels are denoted a and b, depending on the orientation of the nodal planes of the molecular orbital as shown in Figure 2.10.

The nodal planes are indicated by blue dashed lines in this figure and the electron density distribution is indicated by yellow shading.[3] The ^1L_a state is shown in Figure 2.10(a) and is characterised by an electron density that is mostly localised at the *atoms*. The ^1L_b state is shown in Figure 2.10(b) and the electron density is localised in the *bonds* in this state.

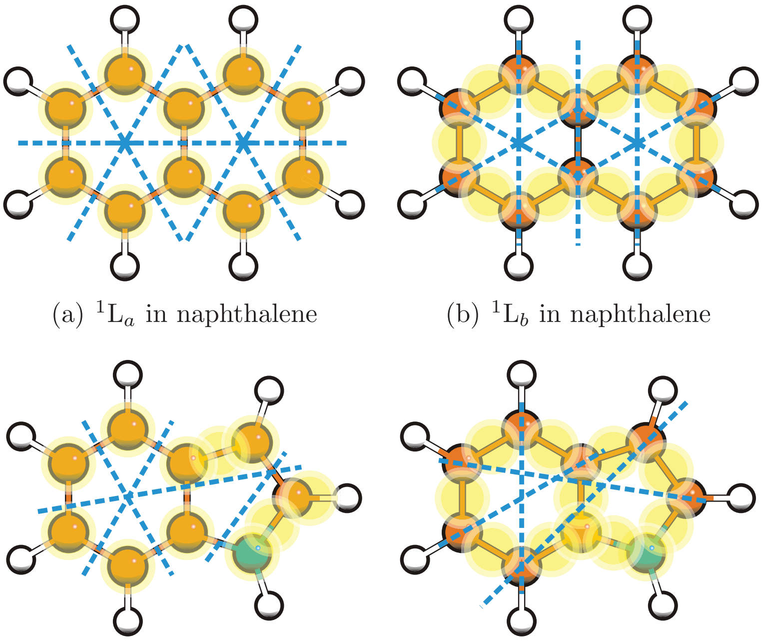
(a) ^1L_a in naphthalene (b) ^1L_b in naphthalene

(c) ^1L_a in indole (d) ^1L_b in indole

Figure 2.10: Nodal planes (blue dashed line) in the ^1L_a and ^1L_b states of naphthalene (a,b) and indole (c,d). The electron density distribution is implied for illustration purposes.

This nomenclature can be adapted to indole and its derivatives. In indole, two CH groups are replaced by one NH group compared to naphthalene. Since the nitrogen contributes two π-electrons, it is isoelectronic with naphthalene in this regard (10 π-electrons).

Figures 2.10(c,d) show the ^1L_a and ^1L_b state of indole.[51] Only the largest electron

---

[3] This shading is only for illustration purposes and does not represent an actual orbital scheme

density elements from Reference [51] are shown in this figure and distinctions between sign and extent have been omitted for this illustration.

2.5 Spectroscopy in Supersonic Jets

All spectra in this work are measured after co-expansion of the sample with a carrier gas through a pulsed nozzle into a *supersonic free jet*.

If an ideal gas is kept at a stagnation pressure p_0 and a temperature T, the *mean free path* λ_0 of the molecules with diameter d_{mol} in that reservoir is given by Equation 2.32:

$$\lambda_0 = \frac{k_B T}{\sqrt{2}\pi d_{\text{mol}}^2 p_0} \tag{2.32}$$

If all other conditions are kept constant it scales anti proportionally with increasing stagnation pressure p_0. For helium ($d_{\text{mol}} = 28$ pm) at $p_0 = 300$ kPa and $T \approx 290$ K it can be estimated to $\lambda_0 \approx 60$ nm.

The expansion through a nozzle with diameter d can be described by the *Knudsen number Kn* given in Equation 2.33 and distinguished into two cases[52]:

$$Kn_0 = \frac{\lambda_0}{d} \tag{2.33}$$

$Kn > 1$: The mean free path is large against the nozzle diameter. Collisions are negligible during the expansion and the resulting *continuous free jet* is suited for sub-Doppler spectroscopy which allows e.g. the resolution of the rotational structure of fluorescence bands.

$Kn < 1$: The mean free path is small against the nozzle diameter. The resulting jet is described by fluid mechanics and a high number of collisions occurs during the expansion, leading to *adiabatic cooling* of the expanded gas.

2.5.1 Adiabatic Cooling

As the term “adiabatic cooling” already suggests, no exchange of energy between the expanded gas and its surrounding takes place during the supersonic expansion. Its enthalpy $H = U + pV$ remains constant but, as the particles gain a large momentum towards the region of lower pressure, the internal energy U must be reduced in compliance with the energy conservation rule as it is converted into translational energy.

The enthalpy of one mole gas with the molar mass m_{mol} is described by Equation 2.34[10]

$$U_0 + p_0V_0 + \frac{1}{2}m_{\mathrm{mol}}u_0^2 = U + pV + \frac{1}{2}m_{\mathrm{mol}}u^2 \tag{2.34}$$

with the performed work pV and the flow momentum $\frac{1}{2}m_{\mathrm{mol}}u^2$.

The gas volume V_0 in the reservoir is thermally equilibrated if the emanating gas volume is small against the reservoir volume. The flow velocity $u_0 = 0$ in that case. Under the consideration that the ambient pressure p in the vacuum chamber is very low against the stagnation pressure p_0 ($p \approx 10^{-4} \cdot p_0$) it can be declared that $p = 0$ and Equation 2.34 is simplified to Equation 2.35:

$$\begin{gathered} U_0 + p_0V_0 = U + \frac{1}{2}m_{\mathrm{mol}}u^2 \\ \Rightarrow \\ U = U_0 + p_0V_0 - \frac{1}{2}m_{\mathrm{mol}}u^2 \end{gathered} \tag{2.35}$$

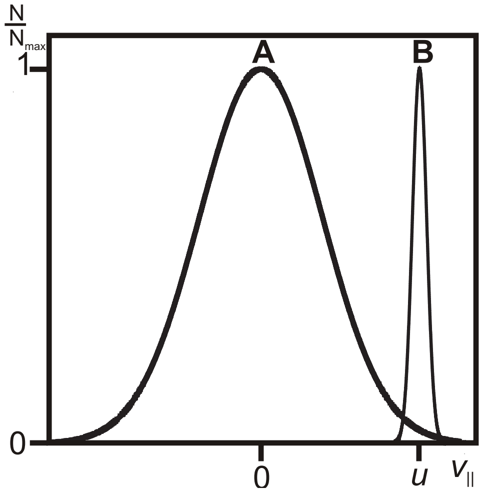

Figure 2.11: Normalised distribution $\frac{N}{N_{\mathrm{max}}}$ of the velocity in flow direction $v_{\|}$ of the particles in the reservoir (case A) and in the free jet (case B). A: Maxwell distribution (see Equation 2.36) about 0, B: Narrow distribution about flow velocity u (see Equation 2.37).

For an ideal gas with atomic mass m in kg the velocity distribution in flow direction $\frac{N}{N_0}\left(v_{\|}\right)$ in the reservoir is described by the one-dimensional Maxwell distribution given in Equation 2.36 and shown in Figure 2.11 case A. The high number of collisions during the first few millimetres in the jet leads to momentum equilibration between its particles, that means a "translational temperature" $T_{\|} \sim 10$ K and a narrow velocity distribution about u:

$$\frac{N}{N_0}\left(v_{\|}\right) = e^{-\frac{mv_{\|}^2}{2k_BT_0}} \tag{2.36}$$

$$\frac{N}{N_0}\left(v_{\|}\right) = e^{-\frac{m\left(v_{\|}-vu\right)^2}{2k_BT_{\|}}} \tag{2.37}$$

Not only the translational momenta are equilibrated trough collisions, the energy stored in rotational and vibrational degrees of freedom is also equalised through the whole ensemble of molecules in the jet and converted into translational energy by a large margin. Since the sample consists of polyatomic molecules with $3N_{\mathrm{nuc}}$ degrees of freedom and is heated to at least its melting point this rotational and vibrational energy has to be redistributed very efficiently for the spectroscopic methods described above. For this, only a very small fraction of sample molecules is co-expanded in a jet mainly consisting of noble gas atoms (the *carrier gas*). This allows for a very efficient adiabatic cooling down to the zero point vibrational energy of the sample since noble gases are atomic gases without any rotational or vibrational degrees of freedom.

The temperature of the sample molecules in the jet can be separated into four constituents: The translational temperature in flow direction $T_{\|}$ and perpendicular to it $T_{\perp}$, the rotational temperature T_{rot} and the vibrational temperature T_{vib}. Since the cross-section for the momentum transfer to translation from rotation or vibration is smaller than for the translation, a thermal disequilibrium results.

The rotational temperature of a sample molecule is reduced significantly after 100 collisions with carrier gas atoms[52]. The reduced occupation of higher rotational states J is described by Equation 2.38:

$$\frac{N}{N_0}(J) = (2J+1)e^{-\frac{E_{\text{rot}}}{k_B T_{\text{rot}}}} \tag{2.38}$$

The conversion from vibrational energy into translational energy is even less efficient as the cross-section is even smaller then for rotation. Approximately 10^4 collisions are needed to condense the population to the vibrational zero point energy. The small fraction of vibratory hot molecules leads to the emergence of vibrational “hot bands” as described in Section 2.3.4.

In the volume that is probed by the excitation laser, most molecules moving with velocity components perpendicular to the flow direction are removed from the jet. In more elaborate *molecular beam* experiments this is refined by one or more *skimmers* -pinholes that cut out the central part of the jet profile. The final composition of temperatures in a molecular beam experiment with typical values for T is as follows:

$$T_{\perp} \sim 0 < T_{\|} \sim 1 \text{ K} < T_{\text{rot}} \sim 1-5 \text{ K} < T_{\text{vib}} \sim 10-20 \text{ K}$$

2.5.2 Anatomy of the Supersonic Free Jet

Figure 2.12 shows the gas flow in the immediate vicinity of the nozzle during the adiabatic expansion. It can be classified into three regions that are characterised by their *Mach number M*:

$$M = \frac{v}{c_s} \tag{2.39}$$

For atomic gases, the Mach number at a distance x downstream from the nozzle with diameter d can be calculated from Equation 2.40 that was found empirically by Ashkenas and Sherman[53]. The highest possible Mach number M_{max} was found empirically by Anderson and Fenn[54] and is given in Equation 2.41 with mean free path λ_0 and effective collision constant ϵ. For example: $M_{\mathrm{max}} = 133(p_0 d)^{0.4}$ for Argon.

$$M = 3.26\left(\frac{x}{d} - 0.075\right)^{0.67} - 0.61\left(\frac{x}{d} + 0.075\right)^{-0.67} \tag{2.40}$$

$$M_{\mathrm{max}} = 2.05\epsilon^{-\frac{1-\gamma}{\gamma}}\left(\frac{\lambda_0}{d}\right)^{-\frac{1-\gamma}{\gamma}} \tag{2.41}$$

A high Mach number means, that the particles in the jet are moving with a high velocity v compared to the speed of sound c in their surrounding .

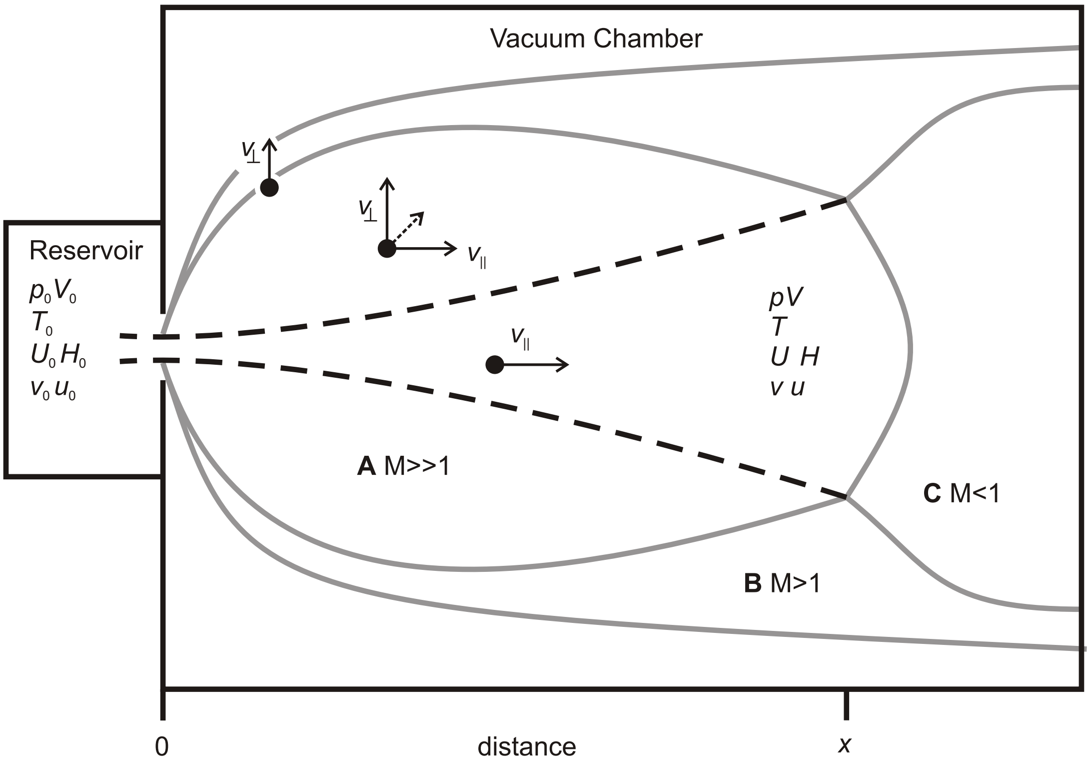

Figure 2.12: The gas flow structure in the adiabatic expansion can be classified into three regions depending on the local Mach number: A with $M \gg 1$: zone of silence, B with $M > 1$: barrel shock, C, with $M < 1$: Mach disc

This is the case for the *zone of silence*, also known as *Mach bottle*. In this region, marked as case A in Figure 2.12, the particle velocities are very high. It is the region in the jet where the adiabatic cooling described above happens and thus it is the only interesting region for spectroscopy.

Case B shows the region where the particle density decreases rapidly since it consists mainly of molecules with velocity components perpendicular to the flow direction of the jet. If the local pressure falls below the residual pressure of the surrounding vacuum, the resulting *over-expansion* leads to the formation of a shock front due to re compression. This is called *barrel shock* and is removed by the skimmer in experiments with molecular beams.

Another shock front that propagates with the jet is the *Mach disk*, marked as case C in Figure 2.12. Here, the particle velocities fall below the speed of sound in the carrier gas. The location x of the Mach disk relative to the nozzle can be calculated with Equation 2.42[52]:

$$\frac{x}{d} = \sqrt{0.67 \cdot \frac{p_0}{p}} \tag{2.42}$$

it depends on the nozzle diameter d, the stagnation pressure p_0 and the residual pressure p in the vacuum chamber.

In the experiments described in this work, $p = 3$ bar is used, the residual pressure is $p_0 \sim 10^{-7} - 10^{-6}$ bar and the nozzle diameter is $d = 0.3 - 1$ mm depending on the experiment (mostly 0.5 mm). This leads to a Mach disc that is $x \approx 425$ mm away from the nozzle at worst conditions. As the measurements are carried out in the region between 3 mm and 10 mm downstream from the nozzle, the Mach disc has no impact on the beam quality.

As mentioned above, spectroscopy is carried out in the zone of silence in a jet mainly consisting of the noble gas Helium. $M \approx 9$ in the experiments in this work. For an ideal gas at a temperature T, the local speed of sound can be calculated by Equation 2.43 with the molar mass m_{mol} and the heat capacities C_p and C_V.

$$c_s = \sqrt{\frac{\gamma R_0 T}{m_{\text{mol}}}} \qquad \text{with} \qquad \gamma = \frac{C_p}{C_V} \tag{2.43}$$

As atomic gases have no rotational and vibrational degrees of freedom, their heat capacities are independent of the temperature and given in Equations 2.44 and 2.45.

$$C_V = \left(\frac{\partial U}{\partial T}\right)_V = \frac{3}{2} R_0 \tag{2.44}$$

$$C_p = C_V + R_0 = \frac{5}{2} R_0 \tag{2.45}$$

Including Equations 2.44 and 2.45 in Equation 2.43 leads to Equation 2.46 for the speed of sound in the carrier gas:

$$c_s = \sqrt{\frac{5}{3} \frac{R_0 T}{m_{\text{mol}}}} \tag{2.46}$$

2.5.3 Maximum Particle Velocity

The maximum particle velocity v_{max} can be estimated with Equation 2.47, as the energy conservation rule requires that the sum of potential and kinetic energy remains constant during the expansion.

$$H + \frac{1}{2} \cdot v_{\text{max}}^2 = H_0 \tag{2.47}$$

Enthalpy H of the carrier gas can be expressed with its heat capacity C_p:

$$H = C_p T \tag{2.48}$$

Inserting Equation 2.48 into Equation 2.47 leads to Equation 2.49:

$$C_p T + \frac{1}{2} v_{\text{max}}^2 = C_p \cdot T_0 \tag{2.49}$$

Since the heat capacity C_p was defined in Equation 2.45 in $\frac{\text{J}}{\text{mol}\cdot\text{K}}$ it has to be divided by the molar mass m_{mol} in order to yield the velocity in $\frac{m}{s}$ Rearranging Equation 2.49 and expressing the heat capacity in this way leads to Equation 2.50 for the maximum velocity.

$$v_{\text{max}} = \sqrt{2 \cdot \frac{C_p}{m_{\text{mol}}} \cdot (T_0 - T_i)} \tag{2.50}$$

The properties discussed in this chapter are listed for the noble gases in Table 2.3. Only helium and argon or the mixture of them are suitable as carrier gases in the experiments presented in this work. All values were calculated with $T_0 = 293$ K and $T = 20$ K.

Table 2.3: Comparison of noble gases at $T_0 = 293$ K and $T = 20$ K

Gas	Molar mass m_{mol} [g·mol^{-1}]	Speed of sound c m·s^{-1}	Heat capacity $C_p m^{-1}$ J·kg^{-1}·K^{-1}	Maximum velocity v_{max} m·s^{-1}
Helium	4.00	263.23	5196.25	1684
Neon	20.18	117.19	1029.98	750
Argon	39.95	83.29	520.28	533
Xenon	131.29	45.94	158.33	294

3. Calculations and Fit

Some concepts of quantum mechanics, like selection rules, overlap integrals, the Born-Oppenheimer, Franck-Condon and Herzberg-Teller approximations and the harmonic oscillator were already introduced in Chapter 2.3. This chapter introduces the *ab initio* methods and the mathematical basis of the Franck-Condon fit used in this work.

The electronic structures of the investigated molecules were optimised using *density functional theory* (DFT), *second order Møller-Plesset perturbation theory* (MP2) or *coupled-cluster theory* (CC2). The DFT-calculations were enhanced by using *dispersion correction* (-D) or *multireference configuration interaction* (-MRCI) depending on the project. *Resolution of the identity* approximation (RI-) and *spin-component scaling* (SCS-) were taken into account for the MP2 or CC2-calculations. All those methods are described in the sections below and in detail in the references given in this chapter.

These optimised structures of the electronic ground or excited state were used as a basis to numerically calculate vibrational frequencies and generate the input files for the Franck-Condon fit. In this fit, vibronic spectra are simulated by Franck-Condon factors calculated from the electronic structures of the electronic ground and first excited state and the geometry of the excited electronic state is distorted from the *ab initio* geometry until the experimental spectra are well reproduced by the simulation.

Ab initio geometry optimisations and frequency calculations were performed with the programs TURBOMOLE[55] versions 5.10 (Chapters 5 and 6) and 6.3[29] (Chapters 7 and 8), the subsequent geometry fit was performed using the program FCFIT[27, 28] that was developed in our work group and is described in Section 3.2. Starting geometries for the *ab initio* geometry optimisations of the aromatic-acetylene clusters were generated with the "random structure generator"[56] also developed in our work group and described in Section 3.4, utilising the semi-empirical program MOPAC[57] for a first binding energy estimation.

3.1 Quantum Chemical Calculations

The quantum physical characterisation of a molecule is based on the time-independent Schrödinger equation:

$$\hat{H}\Psi_n(\vec{r},\vec{R}) = E_n\Psi_n(\vec{r},\vec{R}) \tag{3.1}$$

$\Psi_n(r,R)$ is the total wavefunction of the state n mentioned in Chapter 2.3.2, dependent on the nuclear coordinates $\vec{R}$ and the electronic coordinates $\vec{r}$. $\hat{H}$ is the *Hamilton operator* (or short "Hamiltonian") that acts on Ψ and is defined according to the individual problem and the method used. Generally speaking it contains the total energy of the system at hand. E_n is the eigenvalue of Ψ_n and describes the energy of that state denoted with its main quantum number n.

$$\hat{H} = T + V \tag{3.2}$$

The Hamiltonian for the one-dimensional oscillator which leads to the solutions for ψ_{vib} presented in Equation 3.54 is defined in Equation 3.3 with displacement x, moving mass m and force constant k.

$$\hat{H} = -\frac{\hbar^2}{2m}\frac{d^2}{dx^2} + \frac{1}{2}kx^2 \tag{3.3}$$

As mentioned in Chapter 2.3.2, the Born-Oppenheimer approximation leads to a separation of Ψ into nuclear and electronic wavefunctions. The electronic Hamiltonian is given in Equation 3.4 with $j_0 = \frac{e_0^2}{4\pi\varepsilon_0}$,[1] the electron mass m_{el}, the nuclear charge Z_l and the electron coordinates r.[44] The nuclear coordinates become a constant parameter as all calculations are done in the framework of the Born-Oppenheimer approximation.

$$\hat{H} = -\frac{\hbar}{2m_{\text{el}}}\sum_i^{N_{\text{el}}}\nabla_i^2 - j_0\sum_i^{N_{\text{el}}}\sum_l^{N_{\text{nuc}}}\frac{Z_l}{r_{li}} + \frac{1}{2}j_0\sum_{i\neq j}^{N_{\text{el}}}\frac{1}{r_{ij}} \tag{3.4}$$

The electronic configuration of a state is described by a Slater determinant[58] given in Equation 3.5 with spinorbitals $\phi(\vec{r})$ for each single electron. This representation accounts to the Pauli principle that states that the wavefunction for two identical fermions is antisymmetric with respect to exchange of those particles, since the value of this determinant is zero if it contains at least two identical columns (electrons of the same spin that occupy the same orbital).

---

[1] In computational chemistry it is customary to define $j_0 = 1$ and $\frac{\hbar}{2m_{\text{el}}} = 1$. In this unit system, distances are expressed as multiples of the Bohr radius a_0 and energies are expressed as multiples of the Hartree energy E_h (or short Bohr and Hartree).

$$\psi_{\mathrm{el}}(\vec{r}) = det(\phi_1\phi_2\ldots\phi_N) = \frac{1}{\sqrt{N!}} det \begin{pmatrix} \phi_1(\vec{r}_1) & \phi_2(\vec{r}_1) & \ldots & \phi_N(\vec{r}_1) \\ \phi_1(\vec{r}_2) & \phi_2(\vec{r}_2) & \ldots & \phi_N(\vec{r}_2) \\ \vdots & \vdots & \ddots & \vdots \\ \phi_1(\vec{r}_N) & \phi_2(\vec{r}_N) & \ldots & \phi_N(\vec{r}_N) \end{pmatrix} \tag{3.5}$$

Figuratively speaking, the rows represent all available spinorbitals and the columns represent the occupation of those orbitals (one electron per row if the determinant describes a valid state of the described system).

3.1.1 The Hartree-Fock Method

The Hartree-Fock approach is the fundamental way of finding the most reasonable electronic structure of a given state. The elements of the Slater determinant are varied following the Rayleigh-Ritz principle until the lowest value is achieved. The energy obtained by a variational method can be regarded as upper bonds to the exact energy of the described state.

In the Hartree-Fock approximation, each electron is considered to be moving in the electrostatic field of the nuclei and an *average* field of the other electrons. This average description of the electron correlation is more refined in *post-HF methods* described in later sections.

The Hartree-Fock equation is a non-linear eigenvalue problem of the form

$$\hat{F}\left|\psi_m\right\rangle = E_m\left|\psi_m\right\rangle \tag{3.6}$$

m denotes the number of the molecular orbital $\psi = det(\phi_1\phi_2\ldots\phi_N)$ here. All wavefunctions in this chapter until Section 3.1.8 describe electrons, so the additional subscript $_{\mathrm{el}}$ is omitted. The Fock-operator $\hat{F}$ has the general form

$$\hat{F} = \hat{H}_1 + \sum_i^{N_{\mathrm{el}}} \left\langle \psi_i \middle| \hat{H}_2 \middle| \psi_i \right\rangle - \left|\psi_i\right\rangle \left\langle\psi_i\right| \hat{H}_2 \tag{3.7}$$

$$\hat{H}_1 = -\frac{\Delta r}{2} - \sum_k^{N_{\mathrm{nuc}}} \frac{Z_k}{|r - R_k|} \qquad \hat{H}_2 = \frac{1}{|r_1 - r_2|} \tag{3.8}$$

$\hat{H}_1$ describes the one-particle part of the Hamiltonian and $\hat{H}_2$ describes the two-particle part. The sum in Equation 3.7 runs over the occupied (lowest eigenvalue) orbitals of all i electrons and the sum in Equation 3.8 runs over the all k nuclei. Z_k is the charge of each nucleus, $r - R_k$ is the distance of the electron to the kth nucleus and $r_1 - r_2$ is the distance between two electrons.

For closed shell systems (no unpaired electrons), the Fock-Operator is defined in terms of the one-electron Hamiltonian $\hat{H}_{1\mathrm{el}}$, Coulomb operator $\hat{J}_m$ and exchange operator $\hat{K}_m$. All operators are defined in Equations 3.9 to 3.11. The sum in Equation 3.9 runs over all *occupied* molecular orbitals m'.

$$\hat{F} = \hat{H}_{1\mathrm{el}} + \sum_{m'} \left[2\hat{J}_{m'}(1) - K_{m'}(1) \right] \tag{3.9}$$

$$\hat{J}_m(1)\psi_m(1) = j_0 \int \psi^*_{m'}(2) \frac{1}{r_{12}} \psi_m(1)\psi_{m'}(2) d\tau_2 \tag{3.10}$$

$$\hat{K}_m(1)\psi_m(1) = j_0 \int \psi^*_{m'}(2) \frac{1}{r_{12}} \psi_{m'}(1)\psi_m(2) d\tau_2 \tag{3.11}$$

As the name suggests, the Coulomb operator describes the Coulomb repulsion between electrons. The exchange operator represents the modification of this energy due to spin correlation effects. As in Equation 3.4, $j_0 = \frac{e_0^2}{4\pi\varepsilon}$ or $j_0 = 1$ depending on the unit system used.

The Hartree-Fock equation can be expressed in matrix notation with the orbitals $|\psi_m\rangle$ represented by linear combinations of basis functions $|\varphi_i\rangle$:

$$|\psi_m\rangle = \sum_i^n c_{im} |\varphi_i\rangle \tag{3.12}$$

Equation 3.7 is the expressed with the Fock matrix $\mathbf{F}$ and overlap matrix S:

$$\mathbf{F}c_m = E_m S c_m \tag{3.13}$$

$$F_{ji} = \left\langle \varphi_j \middle| \hat{F} \middle| \varphi_i \right\rangle \qquad\qquad S_{ji} = \langle \varphi_j \,|\, \varphi_i \rangle \tag{3.14}$$

$$\tag{3.15}$$

The Hartree-Fock method is the basis for most *ab initio* and semi-empirical methods. Each method has its own strengths and weaknesses and is chosen depending on the problem that should be described by the calculation.

3.1.2 Basis Sets

The basis functions φ_i are collected in basis sets that are optimised for certain calculations. This method to describe molecular orbitals as linear combinations of atomic orbitals is known as the *linear combination of atomic orbitals* (LCAO) ansatz. These basis functions are typically Gaussian-type atomic orbitals and follow from analytical solutions of the wavefunction of the hydrogen atom.

Gaussian functions obey the radial-angular decomposition with respect to spherical coordinates r, Θ, θ. Each orbital is described by a radial part R_l and a spherical harmonic Y_{lm} that defines the nodes (zero for s, one for p,...) of the orbital.

$$\varphi(r) = R_l(r) Y_{lm}(\Theta, \theta) \tag{3.16}$$

To optimise the Gaussian function for the description of the electronic wavefunction, Gaussian basis sets are contracted. The radial part is the expressed as a sum of normalised exponential functions with normalisation constant $A(l, \alpha_p)$ and contraction coefficient c_p for the primitive with exponent α_p:

$$R_l(r) = r^l \sum_{p=1}^{P} c_p A(l, \alpha_p) e^{-\alpha_p r^2} \tag{3.17}$$

A minimum basis set is one in which a single basis function is used for each orbital of each atom in a Hartree-Fock calculation on the free atom, e.g. 2s and 3p basis functions for any atom in the second period. The basis sets used for the calculations presented in this work (e.g. the *triple zeta valence plus polarisation* basis set TZVPP[7] or cc-pVTZ[59]) are extended by polarisation functions. These polarisation functions can distort the atomic orbitals in a way that allows for a more accurate description of the molecular orbitals that are made up of them. An example is shown in Figure 3.1.

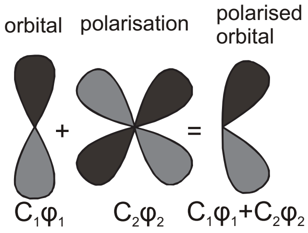

Figure 3.1: The combination of a p-orbital with a d-polarisation function leads to a better approximation of the form of a binding p-orbital.

Another common addition to basis sets are diffuse functions. These very shallow Gaussian basis functions are suitable to describe the “tail” portion of atomic orbitals at large distances from the nucleus and are important for the calculation of e.g. anions.

The “cc-p” in the basis set name abbreviations stands for *correlation-consistent polarised* and “V” indicates that only valence orbitals are described in these basis sets. The correlation-corrected basis sets include successively larger shells of polarization (correlating) functions (d, f, g,...)

Since the valence orbitals are important for molecular bonding, they are commonly represented by multiple basis functions. The spatial extent of the electron density can then be adjusted appropriately to the particular molecular environment. The term *triple* *zeta* (TZ) in the basis set names refers to the number of functions used for each valence orbital as zeta ζ was used to represent the exponent of a Slater type orbital before the emergence of Gaussian type orbitals.[60]

For example: The hydrogen atom is represented by 14 basis functions in the cc-pVTZ basis set.

3.1.3 Semi-Empirical Methods

The cheapest quantum chemical calculations in terms of calculation time are semi-empirical methods. These methods are based on the Hartree-Fock ansatz, but are simplified by many approximations and parameters from empirical data in contrast to ab initio calculations which calculate these parameters from physical constants.

Within the framework of Hartree-Fock calculations, some pieces of information (such as two-electron integrals) are approximated or completely omitted. In order to correct for this loss, semi-empirical methods are parametrized: Their results are fitted by a set of parameters to produce results that best agree with experimental data or high-level ab initio results.

One example is the method *Austin Model 1* (AM1).[2] It is a generalization of the modified neglect of differential diatomic overlap approximation.[61]

A minimal basis set is used to describe the valence electrons that move in the field of a fixed core of nucleus and inner shell orbitals in this approximation. The total energy E_{mol} of the molecule is the sum of the electronic energy E_{el} and the repulsions E_{AB} between the cores of bonded atoms A and B.[61]

$$E_{\text{mol}} = E_{\text{el}} + \sum_{A<B}\sum E_{AB} \tag{3.18}$$

A and B are the numbers of the cores that are direct neighbours. This repulsion is calculated in the AM1-method by the modified core repulsion formula:[2]

$$E_{AB} = Z_A Z_B \gamma_{ss} \left[1 + F(A) + F(B)\right] \tag{3.19}$$

with

$$F(A) = exp\left(-\alpha_A R_{AB}\right) + \sum_i K_{A_i} exp\left[L_{A_i}\left(R_{AB} - M_{A_i}\right)^2\right] \tag{3.20}$$

$$F(B) = exp\left(-\alpha_B R_{AB}\right) + \sum_j K_{B_j} exp\left[L_{B_j}\left(R_{AB} - M_{B_j}\right)^2\right] \tag{3.21}$$

All parameters in these equations are found semi-empirically as described above. R_{AB}

denotes the distance between both cores, i and j run over all cores, M gives the multipole moment of each core. γ_{ss} is an empiric interaction term, L is a constant factor that determines the width of each Gaussian and K is another parameter that is optimised to fit the calculated result (e.g. for the total energy) for a model system to the empiric value.

This method was parametrised on a number of hydrocarbons for the use on organic molecules and their clusters. 13-16 empirical parameters are given for each atom and most of them have have been found using a brute force approach.

3.1.4 Density Functional Theory

In density functional theory, finding the solutions of the Slater determinant is avoided by using the Hohenberg-Kohn theorem, that *each potential* $V_{\mathit{eff}}\left(\vec{r}\right)$ *in the non-degenerate ground state of a N-electron system is described by only one electron density distribution* $n\left(\vec{r}\right)$.[62]

The electron density is determined and all further properties of the electronic ground state are then described by *functionals* of this *electron density.*

To calculate the electron density, N_{el} one-electron wavefunctions ψ_j, the *Kohn-Sham functions* are formulated for each electron. $n\left(\vec{r}\right)$ is then the sum of the square of the absolute value of these wavefunctions over all electrons:

$$\left(-\frac{1}{2}\nabla^2 + V_{\mathrm{eff}}\left(\vec{r}\right) - E_j\right)\psi_j\left(\vec{r}\right) = 0 \tag{3.22}$$

$$n\left(\vec{r}\right) = \sum_{j=1}^{N_{\mathrm{el}}} \left|\psi_j\left(\vec{r}\right)\right|^2 \tag{3.23}$$

The effective potential $V_{\mathrm{eff}}\left(\vec{r}\right)$ from the Kohn-Sham Equation 3.22 depends itself on the density as shown in Equation 3.24. Because of this, the solutions are found iteratively.

$$V_{\mathrm{eff}}\left(\vec{r}\right) = V\left(\vec{r}\right) + \int \frac{n\left(\vec{r}\,'\right)}{\left|\vec{r}-\vec{r}\,'\right|} d^3\vec{r}\,' + V_{\mathrm{XC}}\left(\vec{r}\right) \tag{3.24}$$

$V\left(\vec{r}\right)$ is an external potential describing the attractive force between electrons and nuclei. The second term of Equation 3.24, also called the *Hartree term* describes the electron-electron interaction while $V_{\mathrm{XC}}\left(\vec{r}\right)$ is the exchange correlation potential for the multi-electron system.

This exchange correlation potential can be calculated by different methods. The basis for the methods used for the calculations presented in this work are based on the *generalised gradient approximation* (GGA). In this approach, not only the density $n\left(\vec{r}\right)$ is considered, but also its gradient with respect to space. In hybrid methods like B3LYP, the GGA approach is combined with variational methods analogous to Hartree-Fock. This hybrid approach leads to much more precise results for molecules than the pure GGA approximation at reasonable computation times.

Dispersion Interactions - DFT-D

A general drawback of the DFT method is, that long range interactions responsible for van der Waals and dispersive forces are not accounted for.[63–65] This drawback is insignificant if small molecules are calculated, but the structure of clusters like those discussed in Chapters 5 and 6 and folded proteins is determined by those forces.

One method that is optimised to describe those weak interactions is the B97-D functional proposed by Grimme *et al.*.[3] The energy $E_{\text{DFT-D}}$ is expressed as the sum of Kohn-Sham energy $E_{\text{KS-DFT}}$ determined e.g. by a GGA approach and an empirical dispersion correction E_{disp}:

$$E_{\text{DFT-D}} = E_{\text{KS-DFT}} + E_{\text{disp}} \tag{3.25}$$

$$E_{\text{disp}} = -s_6 \sum_{i=1}^{N_{\text{nuc}}-1} \sum_{j=i+1}^{N_{\text{nuc}}} \frac{C_6^{ij}}{R_{ij}^6} f_{\text{dmp}}\left(R_{ij}\right) \tag{3.26}$$

C_6^{ij} denotes the dispersion coefficient for atom pair ij, s_6 is a global scaling factor depending on the DFT method used and R_{ij} is the inter atomic distance. f_{dmp} is a damping function given in Equation 3.27 with the van der Waals radius R_r to avoid near-singularities for small distances.

$$f_{\text{dmp}}\left(R_{ij}\right) = \frac{1}{1 + e^{-d\left(\frac{R_{ij}}{R_r - 1}\right)}} \tag{3.27}$$

Since some of the parameters from Equation 3.26 have to be found empirical, this method is a combination of ab initio and semi-empirical calculations.

Multi-Reference Configuration Interaction - DFT/MRCI

Only occupied orbitals are described with Hartree-Fock theory. Because of this, only the electronic ground state is described reasonably well with a single Slater determinant. To describe excitations, the unoccupied *virtual* orbitals must be taken into account.

For this, the wavefunction of the electronic state is expressed as a linear combination of all possible Slater determinants (reference configurations) arising from a complete set of spinorbitals. If the electronic ground state is expressed in this way, its energy can be calculated with much more precision. This method is known as *configuration interaction.*

The difference between the best Hartree-Fock energy (wich is always below the exact energy because of the variational method used) and the exact energy of a system is called the *correlation energy.* Of course, the precision and computation time rises with the number of reference states and a trade off between precision and cost has to be found.

One implementation of configuration interaction in the DFT framework is the DFT/MRCI approach of Grimme *et al.*.[4] In this approach, the CI-matrix elements to correct the DFT-energy are constructed empirically. For this, an active space consisting of a number of highest occupied orbitals and lowest unoccupied orbitals from the Kohn-Sham determinant is constructed and all single and double excitations are taken into account. The reference states are either chosen manually or automatically and describe the dominant configurations that the described state is made up of. From this, the final wavefunctions for the different electronic states are calculated.

The Hamiltonians that are used to construct the CI-matrix (one for diagonal elements and one for off-diagonal elements) include empiric correction factors. It is thus a semi-empirical expansion of the DFT theory.

3.1.5 Variationality vs. Size-Consistency

If the solution of the Slater determinant is found variationally as in the methods described above, the resulting energy is the upper limit of the exact energy. This leads to the assumption, that a lower energy is automatically a better result. The disadvantage of these methods however, is their lack of *size-consistency.*

A method is size consistent if the energy of a many-electron system is proportional to the number of electrons N_{el} in the limit $N_{\mathrm{el}} \rightarrow \infty$.[44] For example: In a size-consistent method, the total energy of a molecule AB computed at a infinite nuclear distance $R_{\mathrm{AB}} = \infty$ has the same value as the sum of the energies of A and B separately computed with the same method.

The magnitude of the size-consistency error increases with the size of the molecule. The following methods lead to size-consistent results but are not variational, so the lowest energy is not automatically the best result.

3.1.6 Møller-Plesset Perturbation Theory

One alternative to variation theory used in Hartree-Fock and DFT approaches is perturbation theory. Time-independent perturbation theory is based on the fact that the exact Hamiltonian $\hat{H}$ can be separated into a simple model Hamiltonian $\hat{H}^{(0)}$ and a contribution $\hat{H}^{(1)}$ that is also time-independent:

$$\hat{H} = \hat{H}^{(0)} + \hat{H}^{(1)} \tag{3.28}$$

$\hat{H}^{(1)}$ is the *perturbation.* If perturbation theory is used to find the energy of the electronic ground state of a molecule, $\hat{H}^{(0)}$ is the zero-order Hamiltonian from the Fock operators of the Hartree-Fock *self consistent field* method as described by Equation 3.29. This application of perturbation theory was first introduced by Møller and Plesset.[66]

$$\hat{H}^{(0)} = \hat{H}_{\mathrm{HF}} = \sum_{i}^{N_{\mathrm{el}}} \hat{F}_i \tag{3.29}$$

The first-order perturbation is given by Equation 3.30 that becomes Equation 3.31 with the definitions from Equations 3.9 to 3.11, since the exact Hamiltonian $\hat{H}$ is the electronic Hamiltonian.

$$\hat{H}^{(1)} = \hat{H} - \hat{H}_{\mathrm{HF}} \tag{3.30}$$

$$\hat{H}^{(1)} = j_0 \sum_{j} \frac{1}{r_{ij}} - \sum_{m'} \left[2\hat{J}_m(i) - \hat{K}_m(i) \right] \tag{3.31}$$

The sum over j in Equation 3.31 omits electron i and as in Equation 3.9, the sum over m' is over all occupied spinorbitals

The energy $E^{(2)}$ in second-order Møller-Plesset perturbation theory (MP2) is given by Equation 3.32 where ψ_J is an eigenfunction of the $\hat{H}_{\mathrm{HF}}$ corresponding to eigenvalue $E_J^{(0)}$ and describes a multiply excited determinant.[44]

$$E^{(2)} = \sum_{J \neq 0} \frac{\left\langle \psi_J \,\middle|\, H^{(1)} \,\middle|\, \psi_0 \right\rangle \left\langle \psi_0 \,\middle|\, H^{(1)} \,\middle|\, \psi_J \right\rangle}{E_0^{(0)} - E_J^{(0)}} \tag{3.32}$$

The MP2 energy E_{MP2} is then a sum of four-center-two-electron integrals. As above, the superscript $'$ indicates occupied orbitals while numbers m, n without superscript indicate unoccupied orbitals and ϵ is the orbital energy.

$$E_{\mathrm{MP2}} = \frac{1}{4} \sum_{m',n',m,n} \left[t_{m'n'}^{mn} \left\langle m'n' \,\middle|\, mn \right\rangle \right] \tag{3.33}$$

with amplitudes

$$t_{m'n'}^{mn} = \frac{\left\langle m'n' \,\middle|\, mn \right\rangle}{\epsilon_{m'} + \epsilon_{n'} - \epsilon_m - \epsilon_n} \tag{3.34}$$

The calculation cost of Møller-Plesset calculations can be cut drastically (by a factor of 5-10 depending on the program and basis set) with very small errors[67] by using the *resolution of the identity* (RI) approximation. In this approximation, the calculation and transformation of four-center-two-electron integrals that is needed for MP2 as shown in Equation 3.33 is replaced by that of three-center integrals using symmetry arguments. This is accomplished by using auxiliary functions given in auxiliary basis sets optimised for this approximation. The implementation of RI-MP2 in TURBOMOLE was done by Weigend *et al.*.[68]

Another improvement of MP2 is *spin-component scaling.*[6] The correlation energy is partitioned into parallel and antiparallel spin components in this approach that are scaled separately. This leads to a better accuracy for the calculated energy as deficiencies of the used basis sets are negated by the individual scaling.

The MP2 energy is separated into a contribution from electrons of parallel spin $E_{\updownarrow\updownarrow}$ and antiparallel spin $E_{\uparrow\downarrow}$ (the orbitals from Equation 3.33 are of course spin orbitals in this context) and is corrected by introducing the respective scaling factors $s_{\updownarrow\updownarrow}$ and $s_{\uparrow\downarrow}$:[6]

$$E_{SCS-MP2} = E_{\updownarrow\updownarrow} + E_{\uparrow\downarrow} \tag{3.35}$$

$$E_{\updownarrow\updownarrow} = \frac{1}{2} \sum_{m'_{\uparrow},n'_{\uparrow}} e_{m'_{\uparrow}n'_{\uparrow}} + \frac{1}{2} \sum_{m'_{\downarrow},n'_{\downarrow}} e_{m'_{\downarrow}n'_{\downarrow}} \tag{3.36}$$

$$E_{\uparrow\downarrow} = \sum_{m'_{\uparrow},n'_{\downarrow}} e_{m'_{\uparrow}n'_{\downarrow}} \tag{3.37}$$

with the pair energies

$$e_{m'_{\uparrow}n'_{\uparrow}} = \sum_{m_{\uparrow},n_{\uparrow}} \left(t^{m_{\uparrow}n_{\uparrow}}_{m'_{\uparrow}n'\uparrow} - t^{n_{\uparrow}m_{\uparrow}}_{m'_{\uparrow}n'\uparrow} \right) \left\langle m'_{\uparrow}m_{\uparrow} \,\middle|\, n'_{\uparrow}n_{\uparrow} \right\rangle \tag{3.38}$$

$$e_{m'_{\downarrow}n'_{\downarrow}} = \sum_{m_{\downarrow},n_{\downarrow}} \left(t^{m_{\downarrow}n_{\downarrow}}_{m'_{\downarrow}n'\downarrow} - t^{n_{\downarrow}m_{\downarrow}}_{m'_{\downarrow}n'\downarrow} \right) \left\langle m'_{\downarrow}m_{\downarrow} \,\middle|\, n'_{\downarrow}n_{\downarrow} \right\rangle \tag{3.39}$$

$$e_{m'_{\uparrow}n'_{\downarrow}} = \sum_{m_{\uparrow},n_{\downarrow}} t^{m_{\uparrow}n_{\downarrow}}_{m'_{\uparrow}n'_{\downarrow}} \left\langle m'_{\uparrow}m_{\uparrow} \,\middle|\, n'_{\downarrow}n_{\downarrow} \right\rangle \tag{3.40}$$

The amplitudes t in these equations are defined analogous to Equation 3.34.

3.1.7 The Coupled-Cluster Approach

Another method that is size-consistent but not variational is the *coupled-cluster* (CC) method.

In the coupled-cluster approach, the exact electronic wavefunction ψ is linked to the

Hartree-Fock wavefunction ψ_0 by a *cluster operator* C, like the exact Hamiltonian and the Hartree-Fock Hamiltonian are linked in perturbation theory:[44]

$$\psi = e^C \cdot \psi_0 \tag{3.41}$$

with the exponential operator e^C expanded in a series:

$$e^C = 1 + C + \frac{1}{2!}C^2 + \frac{1}{3!}C^3 + \dots \tag{3.42}$$

This method was first introduced by Coester and Kümmel for studying nuclear physics phenomena.[69, 70]

In quantum chemistry, the effect of the cluster operator C describes the sum of effects of a one-electron excitation operator C_1, two-electron excitation operator C_2 and so on:

$$C = C_1 + C_2 + \dots + C_{N_{\mathrm{el}}} \tag{3.43}$$

with orbitals and excitation amplitudes defined in the same way as above and

$$C_1\psi_0 = \sum_{m',m} t^m_{m'}\psi^m_{m'} \quad C_2\psi_0 = \sum_{m',n',m,n} t^{mn}_{m'n'}\psi^{mn}_{m'n'} \quad \dots \tag{3.44}$$

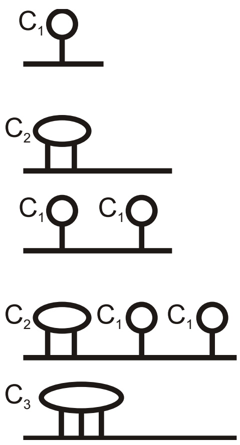

Figure 3.2: Graphical representation of connected and disconnected clusters.

The explicit form of operator C is not important since its effect is expressed by the values of the single-, double-,…-excitation amplitudes t.

The effect of e^C on ψ_0 yields not only the terms $C_1\psi_0, C_2\psi, \dots$ but also mixed terms $C_1C_1\psi_0, C_1C_2\psi_0 \dots$. As C_1 describes a single excitation, a second application of C_1 should lead to a double excitation as described by C_2. The difference is, that in the first case a product of two single excitation amplitudes results while in the latter case one double excitation amplitude appears. This difference is expressed by describing the results as *disconnected* or *connected* double-excitation. They are represented in Figure 3.2 up to the triple-excitation.

The coupled-cluster equations are commonly truncated to reduce computation time. In *coupled-clusters singles and doubles* (CCSD), C is approximated by $C = C_1 + C_2$.

Related to CCSD is the CC2 approach[5] that was used for the coupled-cluster calculations presented in this work.

In CCSD, the energy is calculated with the Hamilton operator $\hat{H}_{\text{ex}}$ constructed with the single- and double-excitation terms defined above:

$$E_{\text{CCSD}} = \left\langle \psi_0 \middle| \hat{H}_{\text{ex}} \middle| \psi_0 \right\rangle \tag{3.45}$$

This Hamiltonian is split into a Fock operator $\hat{F}$ and a *fluctuation operator* $\hat{U}$ that describes the difference between the electron-electron repulsion and the Fock potential:

$$\hat{H}_{\text{ex}(t)} = \hat{F} + \hat{U} \tag{3.46}$$

$\hat{U}$ contains single-excitations in zero order and double-excitations in first order. In CC3 the triple-excitations are included in second order. CC2 combines advantages of MP2 and CCSD and the results are thus more precise than that of MP2 calculations at less computational cost than that of CCSD calculations.[5]

Like Møller-Plesset theory it can be combined with resolution of the identity[71] or spin-component scaling[72] and it can be used both to calculate the electronic ground state[73] and excited electronic states.[74]

3.1.8 Calculation of Vibrational Frequencies

Calculation of the second derivatives of the total energy with respect to the nuclear coordinates leads to the *molecular Hessian*. These derivatives can either be calculated analytically or numerically depending on the program and the planned accuracy or computation time. The Hessians used for the calculations in this work were calculated numerically with the NumForce script of the Turbomole program suite.

To calculate vibrational frequencies and displacements, the Hessian is mass-weighted[2] and diagonalised, yielding the *eigenvalues* λ_i which are the *force constants* of the molecular vibrations and the *eigenvectors* which are the corresponding *normal coordinates*.[75] This diagonalisation ist explained in Section 3.2.2.

For this, the introduction of *mass-weighted coordinates* q and *normal coordinates* Q which were mentioned in Section 2.3.2 is important. The mass-weighted coordinate q_i for each nucleus i is defined with its mass m_i and the Cartesian displacement coordinate x_i as

$$q_i = \sqrt{m_i} x_i. \tag{3.47}$$

---

[2] The mass-weighted Hessian is sometimes referred to simply as Hessian depending on the definition of the nuclear coordinates in the respective context.

To simplify the equations needed for the normal mode analysis, the displacement of the nuclei are expressed with normal coordinates. As the vibration of two nuclei in a polyatomic molecule is distributed between all bonds since the centre of mass must be conserved, the normal coordinates are expressed as linear combinations of the mass-weighted coordinates in the form that in Equation 3.48 is fulfilled, following from their definition as eigenvectors of the mass-weighted force constant matrix. This definition through the potential energy V negates the need for the Cartesian coordinates of each nucleus.

$$V = \frac{1}{2}\sum_i \lambda_i Q_i \tag{3.48}$$

With normal coordinates, the Hamiltonian for the molecule vibrations is given in Equation 3.49. The resulting Schrödinger equation is given in Equation 3.50.

$$\hat{H}_{\mathrm{vib}} = \sum_i \hat{H}_i \qquad \hat{H}_i = -\frac{1}{2}\hbar^2 \frac{\partial^2}{\partial Q_i^2} + \frac{1}{2}\lambda_i Q_i^2 \tag{3.49}$$

$$-\frac{1}{2}\hbar^2 \frac{\partial^2 \psi_{\mathrm{vib}}\left(Q_i\right)}{\partial Q_i^2} + \frac{1}{2}\lambda_i Q_i^2 \psi_{\mathrm{vib}}\left(Q_i\right) = E\psi_{\mathrm{vib}}\left(Q_i\right) \tag{3.50}$$

The form of ψ_{vib} in the harmonic oscillator approximation is explained further in Section 3.2 (Equation 3.54). The energy levels of the ith normal mode with the vibrational quantum number $\mathrm{v}_i = 0, 1, 2, \ldots$ and the force constant λ_i:

$$E_i = \left(\mathrm{v}_i + \frac{1}{2}\right)\hbar\sqrt{\lambda_i} \tag{3.51}$$

The fundamental frequencies $\tilde{\nu}$ in cm^{-1} are calculated from the Hessian in Cartesian coordinates with the left Equation 3.52 with the reduced mass μ or from the Hessian in internal coordinates (see Section 3.2.2) with the right Equation 3.52.[75] The exact pathway from the geometry optimisation to the vibrational frequencies depends on the chosen software and it is important to bear in mind which coordinate system is used.

$$\tilde{\nu}_i = \frac{1}{2\pi}\sqrt{\frac{\lambda_i}{\mu}} \qquad \tilde{\nu}_i = \sqrt{\frac{\lambda_i}{4\pi^2 c^2}} \tag{3.52}$$

3.2 Franck-Condon Factors

As described in Section 2.3.2, the intensity of vibronic transitions can be calculated with the help of the Franck-Condon principle.

Disregarding Herzberg-Teller effects, the intensity of a transition between electronic states depends on the overlap integral between the vibrational wavefunctions $\psi'_{\mathrm{vib}}(Q')$ of the initial state and $\psi''_{\mathrm{vib}}(Q'')$ of the final state defined in Equation 2.15. The square of its absolute value is called the *Franck-Condon factor* and is defined as

$$FC = \left|\langle \psi'_{\mathrm{vib}}(Q') \,|\, \psi''_{\mathrm{vib}}(Q'') \rangle\right|^2 \tag{3.53}$$

3.2.1 One-dimensional Franck-Condon Factors

In the harmonic oscillator approximation (see Figure 2.4 on Page 17), the solutions of these wavefunctions for each vibrational state ν are given in Equation 3.54:[44]

$$\psi_\nu(Q) = N_\nu H_\nu(Q) e^{-\frac{1}{2}Q^2} \tag{3.54}$$

Its eigenstates are described by *Hermitian polynomials* $H_n(x)$ that are calculated recursively from a starting point $H_0(Q) = 1$:

$$H_\nu(Q) = (-1)^\nu \cdot e^{Q^2} \frac{d^\nu}{dQ^\nu} \left(e^{-Q^2}\right) \tag{3.55}$$

and normalised by the scale factor

$$N_\nu = \frac{1}{\sqrt{2^\nu \nu!} \cdot \sqrt{\pi}} \tag{3.56}$$

Inserting Equation 3.54 into Equation 2.15 or the integral from Equation 3.53 leads to Equation 3.57 for the overlap integral:

$$\langle \nu' \,|\, \nu'' \rangle = N_{\nu'} N_{\nu''} \int H_{\nu'}(Q') e^{-\frac{1}{2}(Q')^2} H_{\nu''}(Q'') e^{-\frac{1}{2}(Q'')^2} dQ'\, dQ'' \tag{3.57}$$

With $H_{0''}(Q'') = 1$ and the displacement of the equilibrium normal coordinates $Q'' = Q' - k$ Equation 3.57 becomes Equation 3.58 for the fundamental progression $\langle \nu' \,|\, 0'' \rangle$ from the vibrational and electronic ground state to all accessible vibrational states in the electronic excited state. The emission from the vibrational ground state in the excited electronic state to the vibrationally excited electronic ground state can be expressed analogue.

$$\langle \nu' \,|\, 0'' \rangle = N_{\nu'} N_{\nu''} \int e^{-\frac{1}{2}(Q'-k)^2} H_{\nu'}\left(Q'\right) e^{-\frac{1}{2}(Q')^2} dQ' \tag{3.58}$$

The first step to simplify this equation is to express the Hermitian polynomials for the harmonic oscillator by its generating function given in Equation 3.59:

$$e^{kQ-\frac{1}{2}k^2} = e^{-\frac{1}{2}k^2} \sum_n \frac{1}{n!} H_n(Q) \left(\frac{k}{2}\right)^n \tag{3.59}$$

This leads to Equation 3.60:

$$\langle \nu' \,|\, 0'' \rangle = N_0 N_{\nu'} \int e^{-\frac{1}{2}(Q')^2} e^{-\frac{1}{4}k^2} \sum_n \frac{1}{n!} H_n\left(Q'\right) \left(\frac{k}{2}\right)^n H_{\nu'}\left(Q'\right) e^{-\frac{1}{2}(Q')^2} dQ' \tag{3.60}$$

All terms of the sum with $n \neq \nu'$ vanish since the Hermitian polynomials are orthogonal to each other:

$$\langle \nu' \,|\, 0'' \rangle \, e = N_0 N_{\nu'} \frac{1}{\nu'!} \left(\frac{k}{2}\right)^{\nu'} e^{-\frac{1}{4}k^2} \int e^{-(Q')^2} \left[H_{\nu'}\left(Q'\right)\right]^2 dQ' \tag{3.61}$$

The remaining integral is defined as

$$N_{\nu'}^2 \int e^{-(Q')^2} \left[H_{\nu'}\left(Q'\right)\right]^2 dQ' = 1 \tag{3.62}$$

and this leads to the final Equation 3.63 for the Franck-Condon integral $\langle \nu' \,|\, 0'' \rangle$:.

$$\langle \nu' \,|\, 0'' \rangle = \frac{N_0}{N_{\nu'}} \frac{1}{\nu'!} \left(\frac{k}{2}\right)^{\nu'} e^{-\frac{1}{4}k^2} \tag{3.63}$$

and with Equation 3.56:

$$\langle \nu' \,|\, 0'' \rangle = \frac{1}{\sqrt{2^{\nu'} \nu'!}} \frac{1}{\nu'!} \left(\frac{k}{2}\right)^{\nu'} e^{-\frac{1}{4}k^2} \tag{3.64}$$

Each Franck-Condon integral $\langle \nu' \,|\, \nu'' \rangle$ for a one-dimensional harmonic oscillator can be derived from Equation 3.65 and the Hermite polynomials are not required for the calculation.[76, 77]

$$\langle \nu' \,|\, \nu'' \rangle = \frac{1}{\langle 0' \,|\, 0'' \rangle} \sum_{n=0}^{min(\nu',\nu'')} \frac{1}{n!} \sqrt{\frac{\nu'! \nu''!}{(\nu'-n)!\,(\nu''-n)!}} \langle \nu'-n \,|\, 0'' \rangle \langle 0' \,|\, \nu''-n \rangle \tag{3.65}$$

The sum $\sum_{n=0}^{min(\nu',\nu'')}$ runs over the vibrational state quantum numbers with the upper limit $min\left(\nu', \nu''\right)$ being the lesser of the two values. If n could become larger than that, the values of some terms in this equation could become negative and that would be absurd in this model.

3.2.2 Multi-dimensional Franck-Condon Factors

As already mentioned in Section 2.3.2, the normal coordinates Q of initial and final state in N_{vib}-dimensional systems are linked by the linear orthogonal transformation[45] given in Equation 3.66.

$$Q'' = \mathbf{S}Q' + \vec{d} \tag{3.66}$$

The Duschinsky Transformation

The rotation matrix $\mathbf{S}$ (or *Duschinsky Matrix*) and the displacement vector $\vec{d}$ can be calculated from the *force constant matrices* of both electronic states and the nuclear masses according to Equation 3.67 for $\mathbf{S}$ and 3.68 for $\vec{d}$:[78]

$$\mathbf{S} = (\mathbf{L}'')^T\mathbf{L}' \tag{3.67}$$

$$\vec{d} = (\mathbf{L}'')^T\mathbf{M}^{-1}\left(\vec{R}''_{\text{eq}} - \vec{R}'_{\text{eq}}\right) \tag{3.68}$$

$\mathbf{L}$ is a matrix containing the eigenvectors of the force constant matrix as rows, $\mathbf{M}$ is a diagonal matrix containing the square roots of the atomic masses in the form $M^{-1}_{i,i} = \frac{1}{\sqrt{m_i}}$, $\vec{R}_{\text{eq}}$ is the equilibrium geometry analogous to Figure 2.4 for the one-dimensional case.

For multi-dimensional systems, the orientation of the molecular axis in each electronic state is given by the *Eckart conditions*[79, 80] with the mass m_i and the equilibrium position $\vec{R}_{\text{eq},i}$ of the ith nucleus in the described state:

$$\sum_{i=1}^{N_{\text{nuc}}} m_i\vec{R}_{\text{eq},i} = \vec{0} \tag{3.69}$$

The Eckart conditions allow the separation of the external (rotation and translation) motions from the internal (vibration) motions and minimise the coupling between these two. The origin $\vec{0}$ of the internal coordinate system in each electronic state is conserved regardless of the nuclear motion, because it is always positioned at the center of mass:

$$\sum_{i=1}^{N_{\text{nuc}}} m_i\vec{R}_{\text{eq},i} \times \vec{R}_i = \vec{0} \tag{3.70}$$

Hougen-Watson Axis Reorientation

Equations 3.69 and 3.70 hold true for each electronic state. This leads to an effect called *axis-switching*:[81] the necessary reorientation of the internal coordinate system upon electronic excitation, which is achieved by the *Hougen-Watson matrix* described in Equation 3.73. Considering axis-switching in Equations 3.67 and 3.68 leads to the corrected Equations 3.71 and 3.72:[75]

$$\mathbf{S} = (\mathbf{L}'')^T \mathbf{B}^{-1} \mathbf{L}' \tag{3.71}$$

$$\vec{d} = (\mathbf{L}'')^T \mathbf{M}^{-1} \left(\mathbf{B}^{-1} \vec{R}''_{\text{eq}} - \vec{R}'_{\text{eq}} \right) \tag{3.72}$$

The matrix **B** is a $N_{\text{nuc}} \times N_{\text{nuc}}$ diagonal block matrix. Each block is build up of the 3×3 Hougen-Watson axis-switching matrix **T** and the vectors describing the equilibrium geometry of one electronic state. The axis switching matrix in zero order is determined from Equation 3.73 following from the Eckart conditions:

$$\sum_{i=1}^{N_{\text{nuc}}} m_i \begin{pmatrix} R''_{eq,3i-2} \\ R''_{eq,3i-1} \\ R''_{eq,3i} \end{pmatrix} \times \left(\mathbf{T}_0^{-1} \begin{pmatrix} R''_{eq,3i-2} \\ R''_{eq,3i-1} \\ R''_{eq,3i} \end{pmatrix} \right) = 0 \tag{3.73}$$

The movement of the nuclei during the vibration period is neglected if the axis switching matrix is calculated in zero order. Sando and Spears[82] showed that this approximation is sufficient because the neglected non-linear effects are insignificant.

The Hougen-Watson matrix **T** is determined stepwise from Equation 3.73. In the first step, a 3×3 matrix **C** is defined for every displacement of any one nucleus upon the transition:

$$\mathbf{C}_{\alpha\beta} = \sum_{i=1}^{N_{\text{nuc}}} m_i \left[\left(\vec{R}''_{\text{eq},i} \right)_{\alpha} \left(\vec{R}'_{\text{eq},i} \right)_{\beta} \right] \tag{3.74}$$

Indices α and β in Equation 3.74 are variables for the Cartesian coordinates x, y, z of the nucleus. Every $\mathbf{C}_{zz}$ for a planar molecule becomes zero because the nuclei are only displaced along the x and y axes.

Diagonalising the product $\mathbf{C}^T\mathbf{C}$ leads to another two matrices in the second step: $\mathbf{\Omega}$ which contains the resulting eigenvectors as columns and the diagonal matrix ρ which contains the corresponding eigenvalues. With these matrices Equation 3.75 is obtained for $\mathbf{T}_0$:

$$\mathbf{T}_0 = \mathbf{\Omega} \mathbf{\Lambda} \rho^{\frac{1}{2}} \mathbf{\Omega}^T \mathbf{C}^{-1} \tag{3.75}$$

The matrix $\mathbf{\Lambda}$ in this equation is another 3×3 diagonal matrix with any combination of $+1$ and -1 as diagonal elements. This leads to eight possible solutions for $\mathbf{T}$.

Since $\mathbf{T}$ is a rotation matrix, only solutions which result in a positive determinant are reasonable. The final step is finding the right solution by constructing $\mathbf{B}_0$ and using it on $\vec{R}_{\text{eq}}$. The right solution is the Hougen-Watson matrix that leads to the smallest displacement.

Doktorovs Recursion Formula

The Franck-Condon integral for any transition in a one-dimensional harmonic oscillator can be calculated from $\left\langle \vec{0}' \middle| \vec{0}'' \right\rangle$ using Equation 3.65. A similar *recursion formula* was derived for the multi-dimensional harmonic oscillator under consideration of the Duschinsky effect by Doktorov, Malkin and Man'ko[47, 83]. Contrary to the approximation of Duschinsky, the multi-dimensional problem is not expressed as a combination of many one-dimensional harmonic oscillator wavefunctions, but as one multi-dimensional wavefunction for each state in the work of Doktorov *et al.*. This leads to overlap integrals and thus intensities that are better suited to describe the experimentally observed values for large systems.

As for the one-dimensional harmonic oscillator, the starting point is the Franck-Condon integral of the electronic origin:

$$\left\langle \vec{0}' \middle| \vec{0}'' \right\rangle = 2^{\frac{N_{\text{vib}}}{2}} \left[\prod_{j=1}^{N_{\text{vib}}} \sqrt{\frac{2\omega_j''}{\omega_j'}} \right] det(\mathbf{Q})^{\frac{1}{2}} e^{-\frac{1}{2}\vec{\delta}(1-\mathbf{P})\vec{\delta}} \tag{3.76}$$

Matrices $\mathbf{J}$,$\mathbf{Q}$,$\mathbf{P}$ and $\mathbf{R}$ and the vector $\vec{\delta}$ describe the Duschinsky transformation in multi-dimensional space and are defined by the circular frequencies of all vibrations and matrix $\mathbf{S}$ and displacement vector $\vec{d}$ from Equation 3.66:

$$\omega = 2\pi\nu \tag{3.77}$$

$$\lambda_\omega = diag\left(\sqrt{\omega_1}, \sqrt{\omega_2}, \ldots, \sqrt{\omega_{N_{\text{vib}}}}\right) \tag{3.78}$$

$$\mathbf{J} = \lambda_{\omega''} \mathbf{S} \lambda_{\omega'}^{-1} \tag{3.79}$$

$$\vec{\delta} = \frac{\lambda_{\omega'} \vec{d}}{\sqrt{\hbar}} \tag{3.80}$$

$$\mathbf{Q} = \left(1 + \mathbf{J}^T \mathbf{J}\right)^{-1} \tag{3.81}$$

$$\mathbf{P} = \mathbf{J}\mathbf{Q}\mathbf{J}^T \tag{3.82}$$

$$\mathbf{R} = \mathbf{Q}\mathbf{J}^T \tag{3.83}$$

To calculate the overlap integral $\langle \vec{\nu}' \,|\, \vec{\nu}'' \rangle$ it is expressed by its generating function $\langle \vec{\gamma} \,|\, \vec{\alpha} \rangle$.[83] The *coherent state*[84] $|\vec{\alpha}\rangle$ is the initial state and $|\vec{\gamma}\rangle$ is the final state here and since its elements γ_i and α_i are *complex numbers*, they are not interchangeable in this integral! Those coherent states describe wave packets which move without spreading along the classical trajectories in the phase space of the system.[83] The complex numbers γ_i and α_i give the classical coordinates of the initial point of the trajectory in N_{vib} dimensional space. They are defined as the eigenstates of all annihilation operators $a_i\,|\alpha\rangle = \alpha_i\,|\alpha\rangle$ from the N_{vib}-dimensional harmonic oscillator.[44]

The explicit expression for the coherent state $|\vec{\alpha}\rangle$ is given in Equation 3.84 and the overlap integral $\langle \vec{\gamma} \,|\, \vec{\alpha} \rangle$ is given in Equation 3.85 with circular frequency ω_i and normal coordinate Q_i of each normal mode in the initial state.

$$|\vec{\alpha}\rangle = (\pi\hbar)^{-\frac{N}{4}} \left(\prod_{i=1}^{N_{\text{vib}}} \sqrt{\omega_i}\right) exp\left[\sum_{i=1}^{N_{\text{vib}}}\left(-\frac{1}{2}\frac{\omega_i}{\hbar}Q_i^2 + \sqrt{\frac{2\omega_i}{\hbar}}\alpha_i Q_i - \frac{1}{2}\alpha_i^2 - \frac{1}{2}\left|\alpha_i\right|^2\right)\right] \tag{3.84}$$

$$\begin{aligned}\langle \vec{\gamma} \,|\, \vec{\alpha} \rangle = &\left\langle \vec{0}' \,\middle|\, \vec{0}'' \right\rangle exp\left[-\frac{1}{2}\left(|\vec{\alpha}|^2 + |\vec{\gamma}|^2\right)\right] \\ &\cdot exp\Bigg[-\frac{1}{2}\left(\vec{\alpha}\vec{\gamma}^*\right)\begin{pmatrix} 1-2\mathbf{Q} & -2\mathbf{R} \\ -2\mathbf{R}^T & 1-2\mathbf{P}\end{pmatrix}\begin{pmatrix}\vec{\alpha} \\ \vec{\gamma}^*\end{pmatrix} \\ &+ \sqrt{2}\left(\vec{\alpha}\vec{\gamma}^*\right)\begin{pmatrix} -\mathbf{R} & 0 \\ 0 & 1-\mathbf{P}\end{pmatrix}\begin{pmatrix}\vec{\delta} \\ \vec{\delta}\end{pmatrix}\Bigg]\end{aligned} \tag{3.85}$$

The most general expression for any overlap integral $\langle \vec{\nu}' \,|\, \vec{\nu}'' \rangle$ that follows from expansion of Equation 3.85 into a power series is given in Equation 3.86 with the Hermite polynomials $H_{\vec{\nu}}(\sigma, \tau)$ of $2N_{\text{vib}}$ variables.

$$\langle \vec{\nu}' \,|\, \vec{\nu}'' \rangle = \left\langle \vec{0}' \,\middle|\, \vec{0}'' \right\rangle \left[\prod_{j=1}^{N_{\text{vib}}} \frac{1}{\sqrt{\nu_j'!\nu_j''!}}\right] H_{\nu'\nu''}\left(\sigma, \tau\right) \tag{3.86}$$

The multi-variable Hermite polynomials $H_{\nu'\nu''}(\sigma, \tau)$ describing the displacement of initial and final state are defined as a sum of single-variable polynomials $H_\nu(\sigma)$ in Equation 3.87.[85] The single-variable Hermite polynomials are described for the one-dimensional harmonic oscillator in Equations 3.55 and 3.59.

$$H_\nu(\sigma, \tau) = \sum_{i=0}^{\left[\frac{\nu}{2}\right]} \frac{(-1)^i \nu! H_{\nu-2i}(\sigma)\sigma^{2i}\tau\nu - 2i}{i!(\nu - 2i)!} \tag{3.87}$$

The N_{vib}-dimensional arguments σ and τ are written in Equation 3.88 with the matrices and vectors defined in Equations 3.77-3.83.

$$\begin{pmatrix} \sigma \\ \tau \end{pmatrix} = \sqrt{2} \begin{pmatrix} 1 - 2\mathbf{Q} & -2\mathbf{R} \\ -2\mathbf{R}^T & 1 - 2\mathbf{P} \end{pmatrix}^{-1} \begin{pmatrix} -\mathbf{R} & 0 \\ 0 & 1 - \mathbf{P} \end{pmatrix} \begin{pmatrix} \vec{\delta} \\ \vec{\delta} \end{pmatrix} \tag{3.88}$$

For the transitions from or to the vibrational ground state of one electronic state Equation 3.86 is simplified to Equation 3.89 and 3.90 with the classical Hermite polynomial describing the final or initial vibrational state:

$$\left\langle \vec{\nu}' \middle| \vec{0}'' \right\rangle = \left\langle \vec{0}' \middle| \vec{0}'' \right\rangle \left[\prod_{k=1}^{N_{\mathrm{vib}}} \sqrt{\nu_k'!} \right] H_{\nu'}(\tau) \qquad \tau = \sqrt{2} \left(1 - 2\mathbf{P}\right)^{-1} \left(1 - \mathbf{P}\right) \vec{\delta} \tag{3.89}$$

$$\left\langle \vec{0}' \middle| \vec{\nu}'' \right\rangle = \left\langle \vec{0}' \middle| \vec{0}'' \right\rangle \left[\prod_{i=1}^{N_{\mathrm{vib}}} \sqrt{\nu_i''!} \right] H_{\nu''}(\sigma) \qquad \sigma = -\sqrt{2} \left(1 - 2\mathbf{Q}\right)^{-1} \mathbf{R} \vec{\delta} \tag{3.90}$$

Recurrence relations for the overlap integrals 3.86 follow immediately from the generating function 3.85. By differentiating Equation 3.86 with respect to α_i and collecting terms with equal powers of α_i and γ_i^*, Doktorov *et al.* obtained the recursion formula 3.91 that is used to calculate the overlap integrals for emission transitions. All indices i, j, k, l in Equations 3.91-3.96 describe the mode number:

$$\begin{aligned} &\left\langle \vec{\nu}' \,\middle|\, \nu_1'', \ldots, \nu_i'' + 1, \ldots, \nu_{N_{\mathrm{vib}}}'' \right\rangle = \\ &\quad 2 \sum_{k=1}^{N_{\mathrm{vib}}} \mathbf{R}_{ik} \sqrt{\frac{\nu_k'}{\nu_i'' + 1}} \left\langle \nu_1', \ldots, \nu_k' - 1, \ldots, \nu_{N_{\mathrm{vib}}}' \,\middle|\, \nu_1'', \ldots, \nu_i'', \ldots, \nu_{N_{\mathrm{vib}}}'' \right\rangle \\ &\qquad + \sum_{j=1}^{N_{\mathrm{vib}}} \left(2\mathbf{Q} - 1\right)_{ij} \sqrt{\frac{\nu_j''}{\nu_i'' + 1}} \left\langle \vec{\nu}' \,\middle|\, \nu_1'', \ldots, \nu_j'' - 1, \ldots, \nu_{N_{\mathrm{vib}}}'' \right\rangle \\ &\qquad\qquad - \left(\mathbf{R}\vec{\delta}\right)_i \sqrt{\frac{2}{\nu_i'' + 1}} \left\langle \vec{\nu}' \,\middle|\, \nu_1'', \ldots, \nu_i'', \ldots, \nu_{N_{\mathrm{vib}}}'' \right\rangle \end{aligned} \tag{3.91}$$

Similarly, differentiation with respect to γ_k^* gives the recursion formula for absorption:

$$
\begin{aligned}
&\left\langle \nu'_1, \ldots, \nu'_k + 1, \ldots, \nu'_{N_\mathrm{vib}} \,\middle|\, \vec{\nu}'' \right\rangle = \\
&\quad 2\sum_{i=1}^{N_\mathrm{vib}} \mathbf{R}_{ki} \sqrt{\frac{\nu''_i}{\nu'_k + 1}} \left\langle \nu'_1, \ldots, \nu'_k + 1, \ldots, \nu'_{N_\mathrm{vib}} \,\middle|\, \nu''_1, \ldots, \nu''_i - 1, \ldots, \nu''_{N_\mathrm{vib}} \right\rangle \\
&\qquad + \sum_{l=1}^{N_\mathrm{vib}} (2\mathbf{P} - 1)_{kl} \sqrt{\frac{\nu'_l}{\nu'_k + 1}} \left\langle \nu'_1, \ldots, \nu'_l - 1, \ldots, \nu'_{N_\mathrm{vib}} \,\middle|\, \vec{\nu}'' \right\rangle \\
&\qquad + \left[(1 - \mathbf{P})\,\vec{\delta}\right]_k \sqrt{\frac{2}{\nu'_k + 1}} \left\langle \nu'_1, \ldots, \nu'_k, \ldots, \nu'_{N_\mathrm{vib}} \,\middle|\, \vec{\nu}'' \right\rangle
\end{aligned}
\tag{3.92}
$$

3.3 Herzberg-Teller Terms

A practical way to calculate the value of the sum $\sum_i \left(\frac{\delta \hat{\mu}_\mathrm{el}}{\delta Q_i}\right)_{Q_0} \langle \vec{\nu}' \,|\, Q_i \,|\, \vec{\nu}'' \rangle$ in Equation 2.21 is to calculate the partial derivatives of the transition dipole moment with respect to the normal modes.[86] In this work (see Chapter 7) they are determined numerically from DFT/MRCI calculations (see Section 3.1.4) of the excited state using symmetric finite differences as described by Equation 3.93. Herzberg-Teller coupling has a stronger influence on absorption spectra than on emission spectra because the perturbing state is energetically closer to the excited electronic state than to the electronic ground state. This means, that the direction of the transition becomes important in contrast to the formula of the Franck-Condon approximation.

$$
\left(\frac{\delta \hat{\mu}_\mathrm{el}}{\delta Q_i}\right)_{Q_0} = \frac{\hat{\mu}_\mathrm{el}\left(Q_0 + \Delta Q_i\right) - \hat{\mu}_\mathrm{el}\left(Q_0 - \Delta Q_i\right)}{2\Delta Q_i} \tag{3.93}
$$

The integrals $\langle \vec{\nu}'' \,|\, Q_i \,|\, \vec{\nu}' \rangle$ can be calculated from the FC integrals in the following way:

$$
\begin{aligned}
\langle \vec{\nu}'' \,|\, Q_i \,|\, \vec{\nu}' \rangle = \sqrt{\frac{\hbar}{4\pi\nu}} \Big[&\sqrt{\nu'_i} \left\langle \vec{\nu}'' \,\middle|\, \nu'_1, \ldots, \left(\nu'_i - 1\right), \ldots, \nu'_{N_\mathrm{vib}} \right\rangle \\
&+ \sqrt{\nu'_i + 1} \left\langle \vec{\nu}'' \,\middle|\, \nu'_1, \ldots, \left(\nu'_i + 1\right), \ldots, \nu'_{N_\mathrm{vib}} \right\rangle \Big]
\end{aligned}
\tag{3.94}
$$

3.4 The Random Structure Generator

As mentioned above, the starting structures for the clusters discussed in Chapters 5 and 6 were created with the *random structure generator* written by Thomas Häber.[56] The monomer structures are optimised beforehand (e.g. with DFT-D or RI-MP2) and the imported into the random structure generator. The combinations for the different clusters and the bindings which allow flexible torsions are selected in a drag and drop interface. The first selected monomer is the central moiety of the cluster, while all other monomers are positioned around it randomly inside a pre-defined solvation box. Solvent radii and binding energy thresholds are chosen based on data of similar systems and given in the input.

The structures obtained by randomising the positions of all monomers relative to the central one and rotating by random degrees around flexible torsions are then optimised by the semi-empirical method AM1[2] utilising the MOPAC[57] program package.

Figure 3.3 on page 56 shows a flowchart diagram of this process. After selecting all monomers, the starting conformation is randomised. If the loop is finished, a random cluster is generated by successively adding monomers, randomising the position and orientation of each monomer and checking if the distance of any two atoms is below their van der Waals radii.

The structure is then optimised using MOPAC. If the optimised cluster is no duplicate of an already optimised cluster, its energy and Z-matrix (zmat) are written into the output. Otherwise it is discarded. The maximum number of generated clusters is specified in the input or the cycle is intercepted manually.

During this structure generation, the position and orientation of the monomers are varied by applying 3D-transformation matrices to the x-, y- and z-coordinates of each atom. The optimised clusters are given with their semi-empirical binding energy in the user interface and reasonable clusters are then selected and their Cartesian coordinate matrices are exported for further optimisation on a higher level of theory.

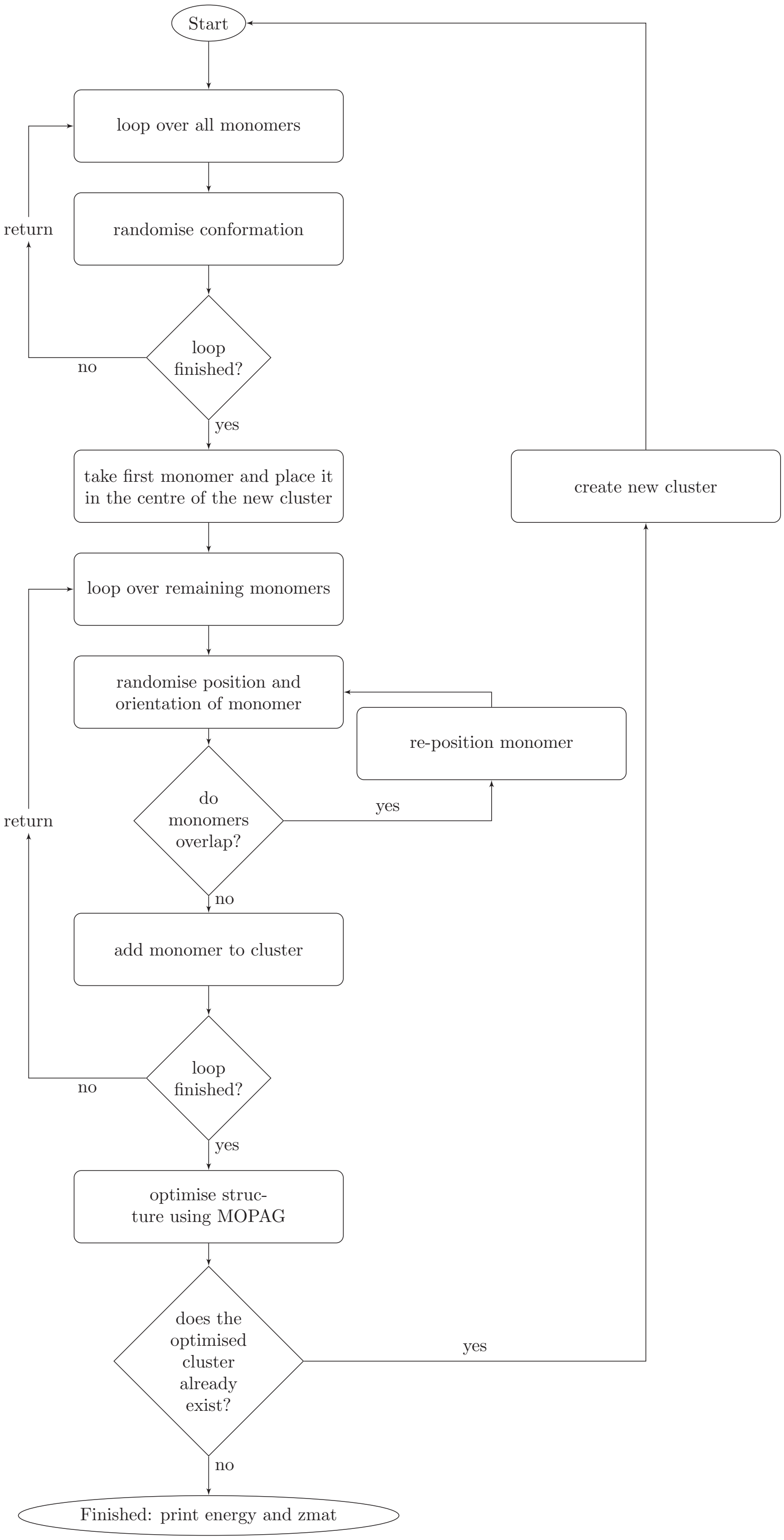

Figure 3.3: Flowchart diagram of the basic steps in generating the random cluster structures.

3.5 The Program FCfit

Based on the recurrence relations described by Doktorov*et al.*[47, 83], the program FCfit[87] was developed to simulate absorption and emission spectra from calculated Franck-Condon factors. The first version of FCfit was written by Stephan Schumm and developed further by Petra Imhof and Daniel Krügler.[27, 28, 88][3]

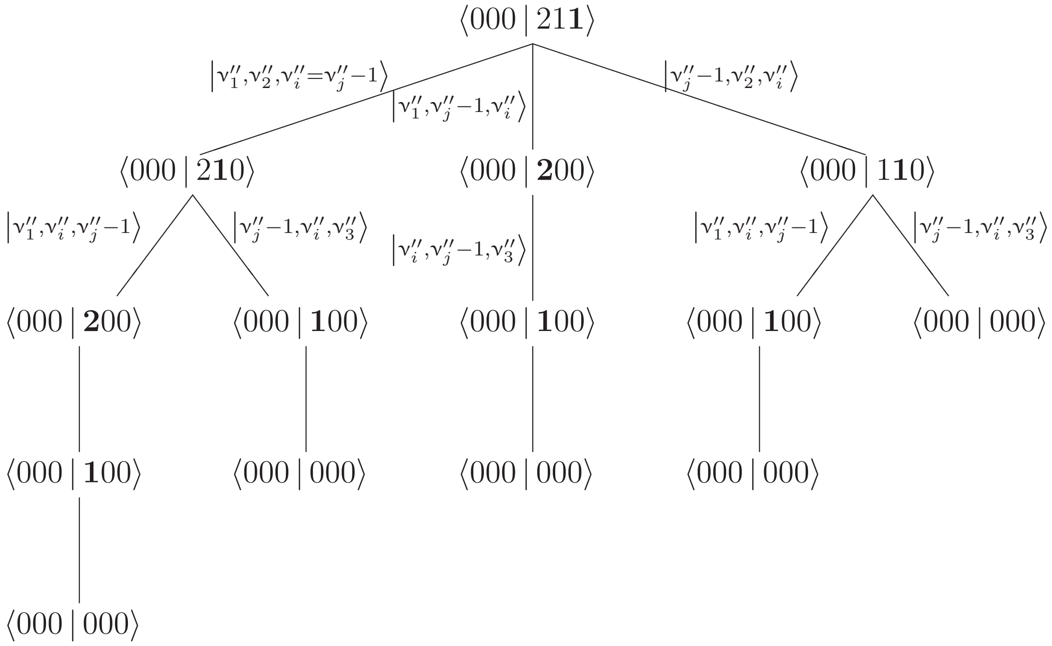

Figure 3.4: Recurrence tree for the overlap integral $\langle 000\,|\,211\rangle$. Recurrence relations are applied to the bold quantum number. The lines indicating the first two steps are labelled with the ket of the integral from the second term of Equation 3.91. For example: As the sum runs over all non-zero quantum numbers, the three integrals $\langle 000\,|\,210\rangle$,$\langle 000\,|\,200\rangle$ and $\langle 000\,|\,110\rangle$ are needed for the calculation of $\langle 000\,|\,211\rangle$ depending on the value of j.

Figure 3.4 shows the recurrence tree for the calculation of the overlap integral $\langle 000\,|\,211\rangle$ of a molecule with three vibrational states of freedom. Equation 3.91 is used for this recursion and is in each step applied to the bold quantum number. As the vibrational quantum numbers are zero for all vibrations in the excited electronic state and different from zero for all vibrations in the electronic ground state in this example, the first term vanishes and the sum of the second term runs over three integrals. For the next step, only two non-zero quantum numbers remain in the ket for the left and right branch and only one for the middle branch.

For the emission $\left\langle \vec{0}' \,\middle|\, 1''_k \right\rangle$ from the vibrational ground state of the excited electronic

---

[3] There are several typos concerning the subscripts and superscripts in the recurrence relations given in those original publications resulting from erroneous transcription from reference [47] to our notation. The revised equations are given in Equation 3.91 and 3.92 of this work.

state to any one vibrational state of the electronic ground state, where all quantum numbers $\nu'_k, \nu''_i, \nu''_j = 0$ and only $\nu''_i + 1 = 1$, the terms of the sums in Equation 3.91 vanish and the integral can be calculated from $\mathbf{R}\ \vec{\delta}$ and $\left\langle \vec{0}' \middle| \vec{0}'' \right\rangle$ with Equation 3.95. The values of $\mathbf{P}$, $\mathbf{J}$, $\mathbf{R}$ and $\vec{\delta}$ are calculated from the mass-weighted Hessian matrix and the equilibrium geometries from *ab initio* calculations as described in Section 3.2.2.

$$\left\langle \vec{0}' \middle| 0''_1, \ldots, 1''_k, \ldots, 0''_{N_{\mathrm{vib}}} \right\rangle = \sqrt{2}\,(1 - \mathbf{P})\,\vec{\delta}\mathbf{J}_k \left\langle \vec{0}' \middle| \vec{0}'' \right\rangle \tag{3.95}$$

Similarly, for the absorption $\left\langle 1'_k \middle| \vec{0}'' \right\rangle$, all quantum numbers $\nu''_i, \nu'_l, \nu'_k = 0$ and $\nu'_k{+}1 = 1$. The terms of the sums vanish and the overlap integral is calculated from $\mathbf{P}$, $\vec{\delta}$ and $\left\langle \vec{0}' \middle| \vec{0}'' \right\rangle$:

$$\left\langle 0'_1, \ldots, 1'_i, 0'_{N_{\mathrm{vib}}} \middle| \vec{0}'' \right\rangle = -\sqrt{2}\left(\mathbf{R}\vec{\delta}\right)_i \left\langle \vec{0}' \middle| \vec{0}'' \right\rangle \tag{3.96}$$

All branches lead to the origin after a different number of recursion steps. That integral is calculated by Equation 3.76.

As this example and Table 3.1 show, many integrals are calculated multiple times in this approach, as all branches have to be processed. More than half of the calculations can be omitted, if the integrals are calculated, stored and accessed in an intelligent way.

Table 3.1: Summary of the calculations needed for the recurrence tree of the integral $\langle 000 \,|\, 211 \rangle$ depicted in Figure 3.4.

Number of Recursion steps	4
Total number of calculated integrals	14
Number of times $\langle 000 \,\vert\, 200 \rangle$ is calculated	2
Number of times $\langle 000 \,\vert\, 100 \rangle$ is calculated	4
Number of times $\langle 000 \,\vert\, 000 \rangle$ is calculated	5
Number of redundant calculations	8

The number of calculated integrals is first reduced to a reasonable number by two limits that are given in the input for the fit:

Only final states up to a limited harmonic energy are reasonable: Lines that exceed the range of the experimental spectrum (up to 2000 cm^{-1} for LIF and 3000-4000 cm^{-1} for DF depending on the laser performance and fluorescence quantum yield of the probed system) or have zero intensity are superfluous for the evaluation of the simulation.

The second limit is the number of quanta that a mode is excited by in the final state: It is subdivided into the maximum total quanta in the final state and the maximum quanta in each vibration of this state. For example: Combinations of 4 quanta and more, or the fourth and higher overtone are very unlikely to be observed.

In this work, the limits were set to 3000 cm^{-1} total harmonic energy, 3 maximum total quanta and 3 maximum quanta in a single vibration. It is generally not recommendable to set these limits above 4000 cm^{-1} and 4 quanta since higher limits lead to a significantly longer computation time without improving the the calculated result.

As mentioned above, the integrals have to be calculated and stored in ascending order from $\left\langle \vec{0}' \middle| \vec{0}'' \right\rangle$ (electronic origin, Equation 3.76), $\left\langle \vec{0}' \middle| 0_1, 0_2, \ldots \nu''_i + 1, \ldots, 0_{N_\mathrm{vib}} \right\rangle$ and $\left\langle 0_1, \ldots, 0_2, \ldots, \nu'_k + 1, \ldots, 0_{N_\mathrm{vib}} \middle| \vec{0}'' \right\rangle$ (only one non-zero quantum number, Equations 3.95 and 3.96), $\left\langle \vec{\nu}' \middle| 0_1, 0_2, \ldots \nu''_i, \ldots, \nu''_j + 1, \ldots, 0_{N_\mathrm{vib}} \right\rangle$ and $\left\langle 0_1, \ldots, 0_2, \ldots, \nu'_k, \ldots, \nu'_j + 1, \ldots, 0_{N_\mathrm{vib}} \middle| \vec{\nu}'' \right\rangle$ (one more quant in any quantum number, Equations 3.91 and 3.92) up to the target integral to ensure that all integrals needed for the next recursion step are already calculated. Two possible realisations of this are binary trees as described and used for example by Gruner *et al.*[89] and hash tables.

In the program FCFIT, nested hash tables are used. A detailed discussion of is done by Schumm in reference [88] and the implementation is described in references [27] and [28] and it should only be described on a superficial level here.

The quantum strings describing bra and ket of the integral are converted into polyadic numbers and used as keys to the values of those hash tables as indicated in Figure 3.5. The parent hash table links the bra-keys to the associated subspectra. These subspectra are hash tables which link the ket-keys to the values of the Franck-Condon factors of the bra-ket.

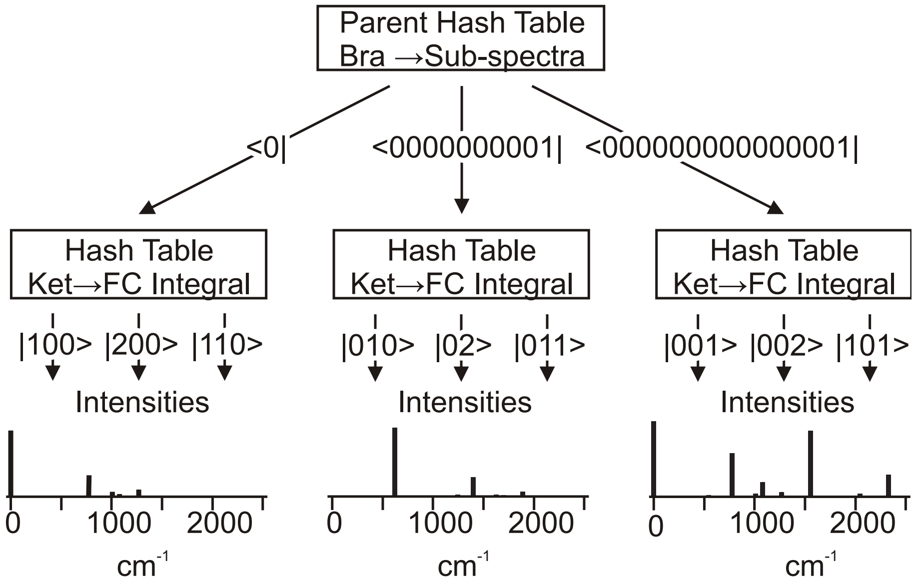

Figure 3.5: Storage of and access to FC-Integrals during the recursion: A parent hash-table connects each bra to the accessible subspectra. Each bra-vector points to another hash-table that connects each ket to the value of an overlap integral. The combination of one bra with all accessible kets leads to a simulated spectrum containing the intensities $|\langle \vec{\nu}' \,|\, \vec{\nu}'' \rangle|^2$.

From these Franck-Condon factors, the relative line intensities are calculated according to Equation 3.97 with the Franck-Condon factor FC_{ref} of the reference transition and a frequency dependence factor V depending on the type of experiment that should be reproduced by the simulated spectrum.[4] In the current version of our program, all FC-integrals contributing to the intensity pattern in one spectrum share one bra. This means, that spectra containing hot bands are not well reproduced as those start from a different initial state. An expansion of the program to simulate hot spectra is currently under development by Alexander Wohlert. It is based on the approach of Berger *et al.*[90] and uses the FCFIT routines for the calculation of the intensity pattern from each bra that are afterwards weighted and summed up to a hot spectrum.

$$I_{\mathrm{rel.}}\left(\mathbf{v}'' \leftarrow \mathbf{v}'\right) = V \cdot \frac{\langle \mathbf{v}' \,|\, \mathbf{v}'' \rangle^2}{FC_{\mathrm{ref}}} \tag{3.97}$$

FC_{ref} is the square of the overlap integral of the reference transition. In emission spectra, the strongest transition apart from $\left\langle \vec{0}' \,\middle|\, \vec{0}'' \right\rangle$ is used as reference, since the intensity of the origin in experimental spectra is biased by stray light from the excitation laser. V depends on the experiment that is described by the simulation.[91] $V = 1$ if no frequency correction is used, V_{Abs} is used for absorption spectra and V_{Em} for emission spectra. For the simulation of emission spectra, V_{Em}^3 is used for photon counting detectors (like the ICCD chip or PMT) and V_{Em}^4 is used for energy detecting experiments. The factors used in FCFIT are given in Equations 3.98 and 3.99:

$$V_{\mathrm{Abs}} = \frac{\tilde{\nu}_{\mathrm{base}} + \tilde{\nu}'_i}{\tilde{\nu}_{\mathrm{base}} + \tilde{\nu}'_{\mathrm{ref}}} \tag{3.98}$$

$$V_{\mathrm{Em}} = \frac{\tilde{\nu}_{\mathrm{base}} - \tilde{\nu}''_i}{\tilde{\nu}_{\mathrm{base}} - \tilde{\nu}''_{\mathrm{ref}}} \tag{3.99}$$

The wavenumbers used in these equations are visualised in Figure 3.6: $\tilde{\nu}_{\mathrm{base}}$ is the energy of the basic vibronic transition of the subspectrum. In absorption spectra (excluding hot bands) it is the energy of the electronic origin and in emission spectra it is the excitation energy leading to the initial state. $\tilde{\nu}_i$ is the harmonic energy of the vibration i that is excited in the final state. The resulting sum or difference is the total energy of that transition. This arbitrary example shows the integral $\langle 010 \,|\, 001 \rangle$ both in the absorption and in the emission spectrum.

---

[4] Keep in mind that in the literature concerning Franck-Condon factors the integrals are written so, that the excited state is always the bra and the ground state is always the ket regardless of the direction of the transition, but in the description of the program FCFIT "bra" denotes the initial state und "ket" denotes the final state since it was written with emission spectra in mind.

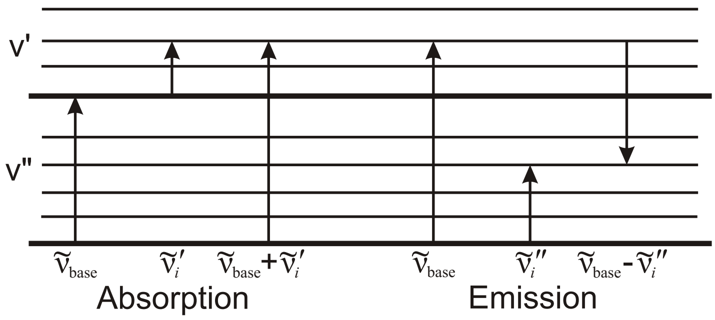

Figure 3.6: Term scheme to visualise the transitions used for the $\tilde{\nu}$ dependency correction for one line $\langle 01\,|\,001\rangle$ in an absorption (Equation 3.98) and an emission (Equation 3.91) spectrum.

Recalling Equation 2.20, the transition probability and thus the intensity depends on both the FC integral and the orbital selection rule but, as the orbital selection rule is concerned only with the underlying electronic transition and its value is the same for all vibrations based on that transition, the FC-factor is sufficient for the calculation of the relative intensities.

The simulated intensities are compared to experimental values and the geometry of one chosen state is then distorted along selected normal modes until the deviation χ^2 between experimental and simulated intensities is minimised. The intensities can be weighted to compensate for unassertive assignment of observed lines or line intensities that are poorly described by the harmonic model. The assignment of the spectral lines - and in some cases even that of the initial state - is refined after each fit (in some cases starting from a simulation or pure rotational constants fit) until a satisfactory agreement between simulated and experimental data is reached. As the list of assigned transitions grows, the number of normal modes that are used in the fit can be expanded. It has been proven to improve the fit if the list of changed normal modes is expanded successively by 2-4 modes after each fit and if unassigned transitions are provided explicitly with 0 intensity in the input files.

The harmonic approximation leads to some restrictions for the geometry fit. The first restriction is that contraction and elongation along one normal coordinate (the sign of ΔR in Figure 2.4) leads to the same result if only relative intensities are used to calculate the deviation between simulation and experiment. This drawback is compensated if the information about the molecular geometry is enhanced by the changes of the rotational constants upon excitation via rotationally resolved spectroscopy. For example: The simultaneous fit of five emission spectra with 20-40 assigned lines in each spectrum and the change of the rotational constants of four different isotopomers allowed for a complete and unambiguous fit of the planar excited state geometry of benzimidazole that is presented in Chapter 8

The overall deviation that is minimised during the fit is described by Equation 3.100:

$$\chi^2_{\text{total}} = \sum_{n=1}^{N_{\text{Int}}} W_n \left(I_{\exp,n} - I_{\text{sim},n}\right)^2 + \sum_{m=1}^{N_{\Delta Rot}} W_m \left(\Delta Rot_{\exp,m} - \Delta Rot_{\text{sim},m}\right)^2 \tag{3.100}$$

The second restriction follows from the shape of the harmonic potential. Since the potential energy gradient along the normal coordinate during each vibration is approximated by a parable, inversion vibrations are not well described by that model. Since the potential energy has a local maximum instead of the total minimum at the supposed equilibrium position, the model used in the fit cannot describe the emission spectrum from a state that is described by such a double minimum potential. This disadvantage is important to consider if such vibrations are excited in the investigated molecule and as it can lead to a failed fit - if ignored - or serve to reassure the assignment of the investigated absorption band. Fermi resonances are also not well described by the model.

Two local and two additional global minimisers are implemented for the fit. All results presented in this work were obtained by using the NL2SOL[92, 93] minimiser -which is a modified Levenberg-Marquardt[94, 95] algorithm. The other local minimiser is the non-gradient optimizer PRAXIS[96, 97]. Suitable starting values can be found by using the global minimizers PGA[98] which uses genetic algorithms or the simulated annealing algorithm SIMANN[99].

All options (like file names, changed normal modes, starting values, fit solver, etc.) for the fit are collected in a control file. A graphic user interface to generate this control file is under development. The experimental intensities along with their assignments are given in separate files with the extension .exp. Spectra to additional Bras that are not used in the fit can be simulated with the fitted geometry. This option has been used e.g. for the emission spectra from states that are poorly described by the harmonic approximation or for absorption spectra to exclude doubtful data from the fit. The *ab initio*-outputs are converted by separate tools like “TurboMol2ZmtHss”, which converts the TURBOMOLE Hessian output into the format which is needed as input for the FCFIT program.

4. Experimental Setup

The experimental setup has been changed in some details over the course of this work, but the general composition that is shown in Figure 4.1 still holds true. It allows both for the measurement of laser induced fluorescence and dispersed fluorescence that were described in Section 2.2. A movable mirror allows to switch between both detectors.

In this setup, the light from a *Nd:YAG laser* is frequency converted (green line) and shaped by a telescope from a beam with a round profile of approximately 8 mm diameter to a beam with a rectangular profile of approximately 5 mm height and 30 mm width. With this shaped beam, a *dye laser* (a modified Lambda Physics FL-3002) is pumped and the radiation of this dye laser (yellow line) is then frequency doubled and used as the probe beam for the laser spectroscopy (dark blue line).

It is coupled into a vacuum chamber via two deflecting prisms and crosses perpendicularly with a supersonic free jet. The vacuum chamber is evacuated by an *oil diffusion pump* that is supported by a *rotary pump* to reach a residual pressure at the magnitude of $10^{-4} - 10^{-5}$ mbar. The residual pressure during the measurement is typically at around $8 \cdot 10^{-4}$ mbar.

The *fluorescence* light (light blue line) from the irradiated sample volume is collected perpendicularly to laser and particle beam by a biconvex lens with 50 mm focal length and a large angle of aperture that is situated 50 mm from the crossing point. It is then focused on the entry slit of a 1 m *Czerny-Turner monochromator* (Jobin-Yvon THR 1000) by a plano-convex lens with 500 mm focal length.

In the monochromator, the fluorescence light is either reflected on the grating in zero order and imaged on a *photomultiplier tube* (PMT) for LIF or dispersed on the grating in first or second order and imaged on either the *intensified charge-coupled device* (ICCD) chip for DF. The movable mirror situated directly before the detectors serves to switch between detectors while the movable mirror situated after the grating is adjusted to position the the focal plane of the reflected light on the chosen detector. The entry slit is opened completely for LIF or opened to 30 μm for DF.

Both detectors are cooled by Peltier elements to reduce noise from dark current. The

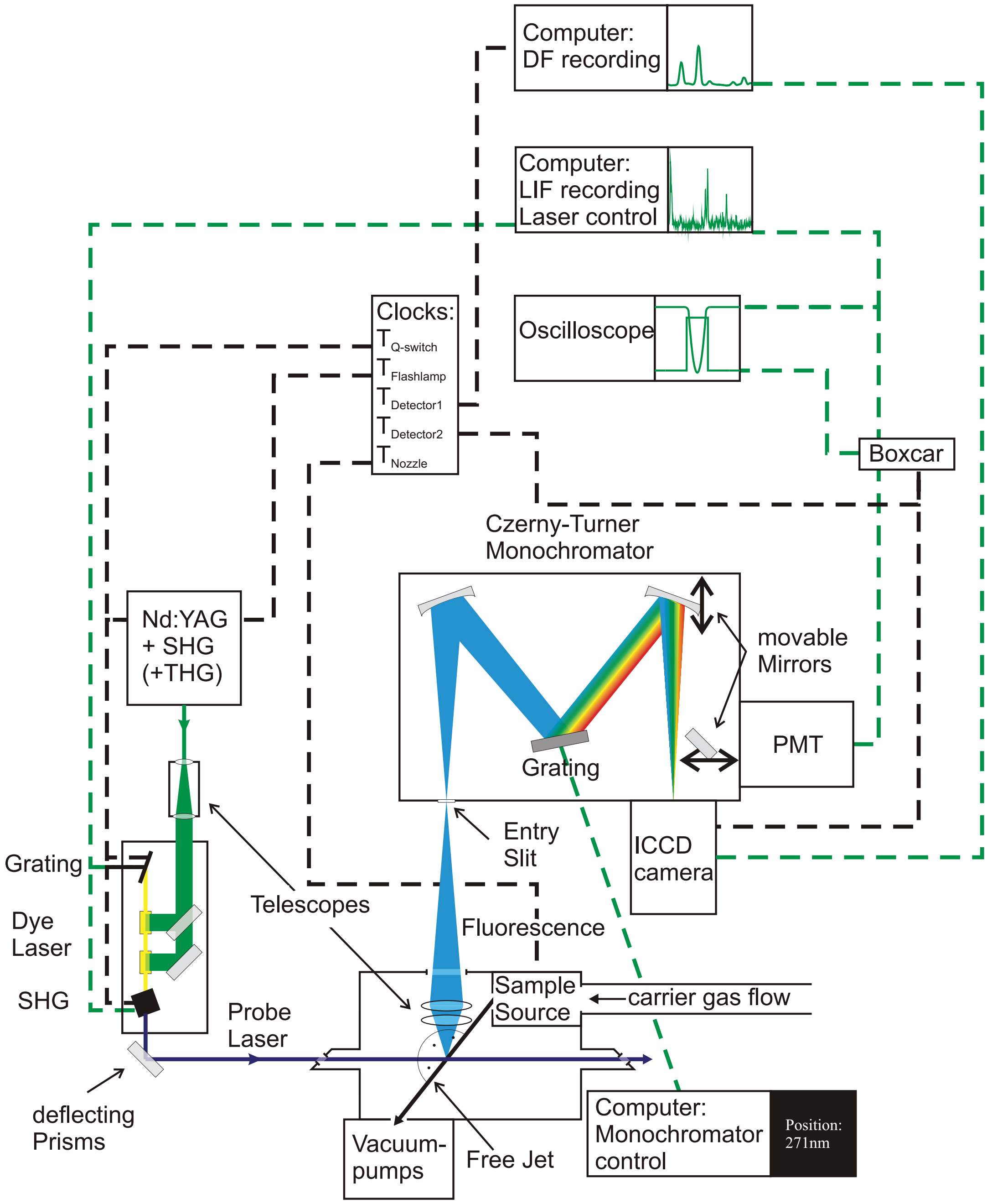

Figure 4.1: Schematic depiction of the experimental setup. Coloured straight lines indicate light beams: Green: pump laser (532 or 355 nm), yellow: fundamental of the dye laser (∼ 520 – 640 nm), dark blue: second harmonic of the dye laser (∼ 260 – 320 nm), light blue: collected fluorescence light, rainbow: dispersed fluorescence light. The black straight line indicates the free jet. Dashed black lines indicate TTL signal paths from the clocks and green dashed lines indicate data paths between the computers and stepping motors or detectors.

Table 4.1: Specifications of both used pump lasers

Property	INDI-40	SpitLight 600	Unit
Max. Pulse Energy			
1064 nm	450	750	mJ
532 nm	200	400	mJ
355 nm	100	200	mJ
Output Characteristics			
Pulse With	5-8	7	ns
Divergence	0.5	< 0.5	mrad
Beam Diameter	< 10	6.5	mm
Timing Jitter*	± 0.5	$< \pm 1$	ns
Energy Stability	± 2	$< \pm 1$	%

* if triggered internally. The jitter depends only on the clocks if triggered externally

heat of the oil diffusion pump and the PMT cooling elements is dissipated by tap water, while the camera cooling is supported by a closed cycle of distilled water with Sodium azide since the narrow channels on the cooling elements are susceptible to clogging e.g. by limescale or algae.

The signal detection and procession is described in Section 4.4.

The motors in the dye laser and monochromator are controlled by computers. Signal paths are indicated by black dashed lines in Figure 4.1.

4.1 The Laser Systems

The probe beam is generated by a combination of two lasers as indicated in Figure 4.1. The Nd:YAG laser is a four state laser with a neodymium-doped yttrium aluminium garnet (Nd:$Y_3Al_5O_{12}$) as laser medium. The transition used leads to emission with a wavelength of 1064 nm and that light is frequency doubled by a BBO crystal to yield 532 nm. For the measurements of the benzene-acetylene clusters and some measurements of benzimidazole it is further converted in a second crystal to 355 nm since the emission of the dye laser is shifted at least 10 nm red from the *pump wavelength*. Two different Nd:YAG lasers were used during the the course of this work and their specifications are listed in Table 4.1. The Innolas SpitLight 600 reaches a much higher pulse power than the Quanta-Ray INDI-40, especially at 355 nm. But for experiments where only the 532 nm emission is needed, the INDI is perfectly suited as pump laser. The pulse energy is tuned to 100-140 mJ for optimal performance of the dye laser.

This emission is used to pump a dye laser. As the name suggests, the laser medium is a fluorescent dye with a high quantum yield. The broad emission spectrum of such a dye allows to vary the laser emission over a wealth of wavelengths. This laser can be described as four state laser in principle, but the fluorescence emission is broadened by collisions with solvent molecules (see Chapter 2.3). The peak and spectral area of the fluorescence can be shifted by the polarity of the solvent and this was used extensively to optimise the scan range of the laser for the spectra presented in this work.

In the experiments presented in this work, a modified Lambda Physics FL-3002 was used. In this model, the laser output from the resonator is amplified two times by being led through the excited dye solution in two cuvettes as indicated in Figure 4.1. The final UV output power is between $0.1 - 2$ mJ depending on the dye condition and the pump power. In most experiments, the UV power is tuned to ~ 0.5 mJ at ~ 120 mJ pump power.

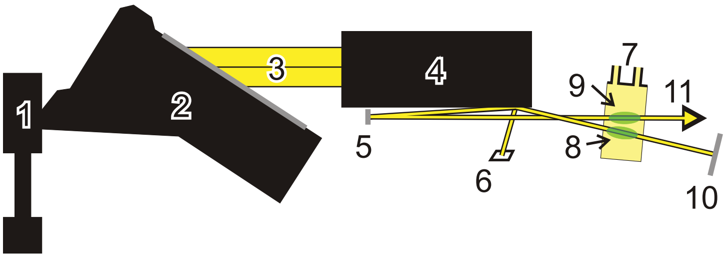

Figure 4.2: Schematic setup of the dye laser resonator:[100] 1: Sine drive, 2: Grating and tilt able holder, 3: expanded laser beam, 4: 66x prism expander, 5: feedback mirror, 6: monitor reflex, 7: dye cuvette, 8: pumped volume (oscillator), 9: pumped volume (pre-amp), 10: cavity end mirror, 11: fundamental laser.

Figure 4.2 shows the *Littrow resonator* of this dye laser. A *holographic grating* (2) in the resonator is used to select the wavelength that is amplified by the laser process. It is tilted by a sine drive (1) consisting of a stepping motor and an elevating screw. The Dye that circulates through the cuvette (7) is pumped by the Nd:YAG at two different regions. The emission from the lower region (8) -the *oscillator output*- passes the cavity between mirrors 5 and 10 and amplified by inducing emission in the upper pumped region (9) -the *pre-amp*. To illuminate a large region on the grating, the oscillator output is expanded by a *prism beam expander* (4). A small fraction of the emission reflected from the grating is deflected to a small target (6). This spot is called the “monitor reflex” and used to distinguish between *laser* and *amplified spontaneous emission* during the adjustment.

The stepping motors for grating and SGH and their controlling electronic were exchanged by Sirah Laser- und Plasmatechnik and the laser is controlled by their software in the present setup, all other components are original Lambda Physics parts. The specifications of this laser are given in Table 4.2. The beam characteristics are taken from the original manual[100] while the mechanical properties are specified by the technicians at

Table 4.2: Specifications of the modified Fl-3002 dye laser by Lambda Physics and Sirah.

Property	Value
Mechanical properties	
Resonator type	Littrow
Littrow grooves	600 Lines/mm
Littrow order	3-8
Maximum steps (grating)	534000
Sine drive screw pitch	0.55 mm/turn
Maximum steps (SHG)	305000
Beam properties	
Bandwidth	$\sim 0.2\ \mathrm{cm}^{-1}$
Frequency stability	$< 0.05\ \mathrm{cm}^{-1}/\mathrm{K}$
Wavelength reproducibility	$\pm 6.3 \cdot 10^{-4}$ nm
Wavelength accuracy	0.1 nm
Divergence	0.5 mrad
Beam diameter	2.5 mm

Sirah[101] for the refurbished resonator.

A KDP crystal is used for the second harmonic generation and the UV light is then separated from the fundamental emission by a *prism separator*.

4.2 The Sample Source

The principle of spectroscopy in supersonic jets is explained in Chapter 2.5. For the generation of the jet the *thermal source* shown in Figure 4.3 is used if the sample is solid at room temperature. For the benzene-acetylene clusters discussed in Chapter 5, a gas mixture was prepared by filling an evacuated 10 l gas cylinder with benzene, acetylene and helium at defined partial pressures and only the *pulsed valve* was used from the shown source. For the phenol-acetylene clusters discussed in Chapter 6, a mixture of acetylene and helium was used as carrier gas and phenol is kept in the reservoir. Additionally, a second reservoir that is equipped with cooling elements is located upstream of the sample reservoir. It is used e.g. to enrich the carrier gas with water for the investigation of water clusters.

The sample reservoir and valve mount are equipped with *heating resistors*. The polymer parts (gaskets, poppet, non-stick coating of the movable parts) can be heated to around 473 K and the valve is heated 20 K above the reservoir temperature to prevent depositions in the valve. The reservoir temperature is set to the melting point of the sample in the first test runs and then optimised for the best signal to noise-ratio. A

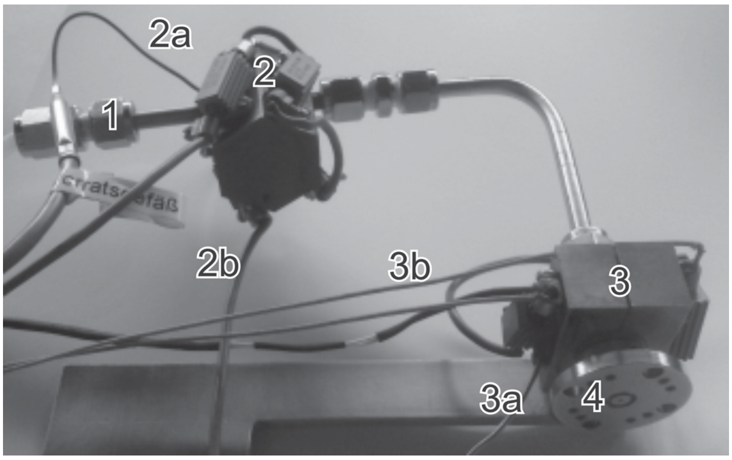

Figure 4.3: Sample source for the supersonic jet. 1: Swagelok®-adapter for the carrier gas feed, 2: heatable reservoir, 2a: temperature detector, 2b: power cable, 3: heatable pulsed valve, 3a: temperature probe, 3b: power cable, 4: valve cap with shaped nozzle.

temperature as low a possible is preferred to suppress the emergence of hot bands and to extend the measurement period after which the sample has to be refilled.

The pulsed valve is a general valve type 9. Valve caps with different nozzle diameters and shapes are used depending on the project. For most spectra presented in this work, a cap with a conical nozzle of 0.5 mm diameter was used.

4.3 Temporal Management

Most components of the experimental setup are synchronised by clocks as indicated by black dashed lines in Figure 4.1. For most experiments, self-made clocks from our technician Klaus Kelbert were used. Those were replaced by a Stanford clock (DG645) during the research on benzimidazole. The timings that have been proven to yield the best results are given in Table 4.3. Those values give the delay time from a t_0 for each pulse cycle to the trigger pulses for the different electronics. The experiment is pulsed with 10 Hz.

The trigger for the pulsed valve is adjusted for different gas mixtures or to excited different regions in the jet. That optimisation is on the scale of ±0.8 ms. All other values have been optimised for the *optical path length* from the pump laser to the detectors. The trigger pulse for the Q-switch is looped through to the dye laser control as trigger to move the motors for grating and SHG crystal during scans. The “detectors” trigger pulse is used as master trigger for the camera control, acquisition software and boxcar integrator and processed further by those electronics. The form of the trigger pulses depends on the triggered electronics and can be varied very flexibly with the Stanford clock. In current setup, all components are TTL compatible and each one is triggered on the rising edge.

Table 4.3: Timings for the trigger pulses.

Trigger	Delay in ms	Voltage in V	Duration in μs
Flash lamp INDI*	2.7880	7	2
Q-switch INDI*	3.0200	5	20
Pulsed valve	1.2372	5	350
Detectors	2.9921	5	10

*the SpitLight input necessitated 12 V pulses with the same delay and duration.

Because of that, the trigger duration is not very critical above a minimum of some μs.

4.4 Data Acquisition and Processing

As shown in Figure 4.1, two different detectors are used in this setup. The *photomultiplier tube* (PMT) is used for LIF spectra and the gated *intensified charge-coupled device* (ICCD) camera is used for DF. Both detectors can be used for both methods (and in fact, the PMT has been used for DF measurements during down times of the camera), but for technical reasons they are best suited for these allocated roles.

4.4.1 Photomultiplier Tube

A photomultiplier tube is an vacuum tube outfitted with a number of *dynodes* between a *photocathode* and the corresponding anode. Every incident photon that strikes the photocathode leads to emission of an electron that is accelerated towards the first dynode and multiplied by secondary emission. Each dynode has a voltage that is $\sim$ 100 V more positive than that of the photocathode. The observed signal is the current between photocathode and anode that depends on the number of incident photons.

The photomultiplier tube used in this experiment is a Thorn EMI 97890A, cooled by Peltier elements and tap water to reduce the dark current. Its signal is integrated by a gated *boxcar integrator* (Stanford research SR 250) over a gate of around 50 ns depending on the temporal stability of the signal. This gate is optimised before every LIF measurement and adjusted to be as narrow as possible to enhance the signal to noise ratio.

If it is used for DF measurements, the exit slit of the monochromator is closed accordingly to the entry slit and the grating is turned slowly to scan over the whole emission range. For LIF measurements both slits are completely open to maximise the incident light intensity.

4.4.2 Intensified Charge-coupled Device

The main focus of attention of this work is dispersed fluorescence and the use of a *gated ICCD camera* as detector is very practical for this method. The monochromator used in this setup is a Jobin-Yvon THR 1000 that is controlled by a self-made control box and DOS program. Its grating is blazed with 2400 grooves/mm and a lattice parameter of 400 nm. No exit slit is used in front of the camera. Thus, the emission that is dispersed on the grating is reflected on the camera aperture and resolved spatially. This enables the measurement of a spectrum over around 400-600 nm in first grating order or half of that in second grating order (at a higher spectral resolution) on a *shot to shot* basis.

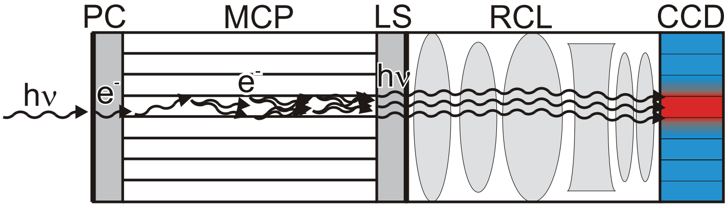

Figure 4.4: Schematic cross-section through an ICCD camera.[102] The incident photon $h\nu$ is intensified by a combination of components and detected space-resolved on the CCD-chip. PC: photo cathode, MCP: multichannel plate, LS: luminescent screen, RCL: relay coupling lenses, CCD: charge-coupled device. Blue rectangles indicate pixels that are not illuminated, the red rectangle indicates the illuminated pixel. The model used in our setup utilises an optical fibre strand instead of the lens array.

Figure 4.4 shows the setup of such a camera. Incident photons strike the photocathode (PC) which produces a primary electron that is multiplied. Unlike the PMT described above, the multiplication happens in a *micro-channel plate* (MCP). The electrons are accelerated in a strong electric field towards a luminescent screen (LS) and forced to hit the walls by the channel geometry. On each collision, secondary electrons are emitted by the channel material until the cascade of electrons reaches the luminescent screen at the end of the channel. The luminescence from this screen is guided by a lens array (RCL) or an optical fibre strand to the charge-coupled device. Each pixel of this CCD is a photo active transistor accumulating a charge proportional to the number of incident photons. A control circuit then causes each capacitor to transfer its content to its neighbour until the charge amplifier is reached. The charge is then converted into voltage that is amplified and processed by the analog/digital converter and the software. The illumination time is 20 seconds for each image.

A typical image is shown with the corresponding DF spectrum in Figure 4.5. In this experiment, a LaVision Flamestar camera is used. The CCD chip is of the type TH7863 with 576×384 pixels, each pixel is 23×23 μm in size. The image region spans 288×384

pixel, as the other half are the *memory zone* needed for the operation principle of the camera.

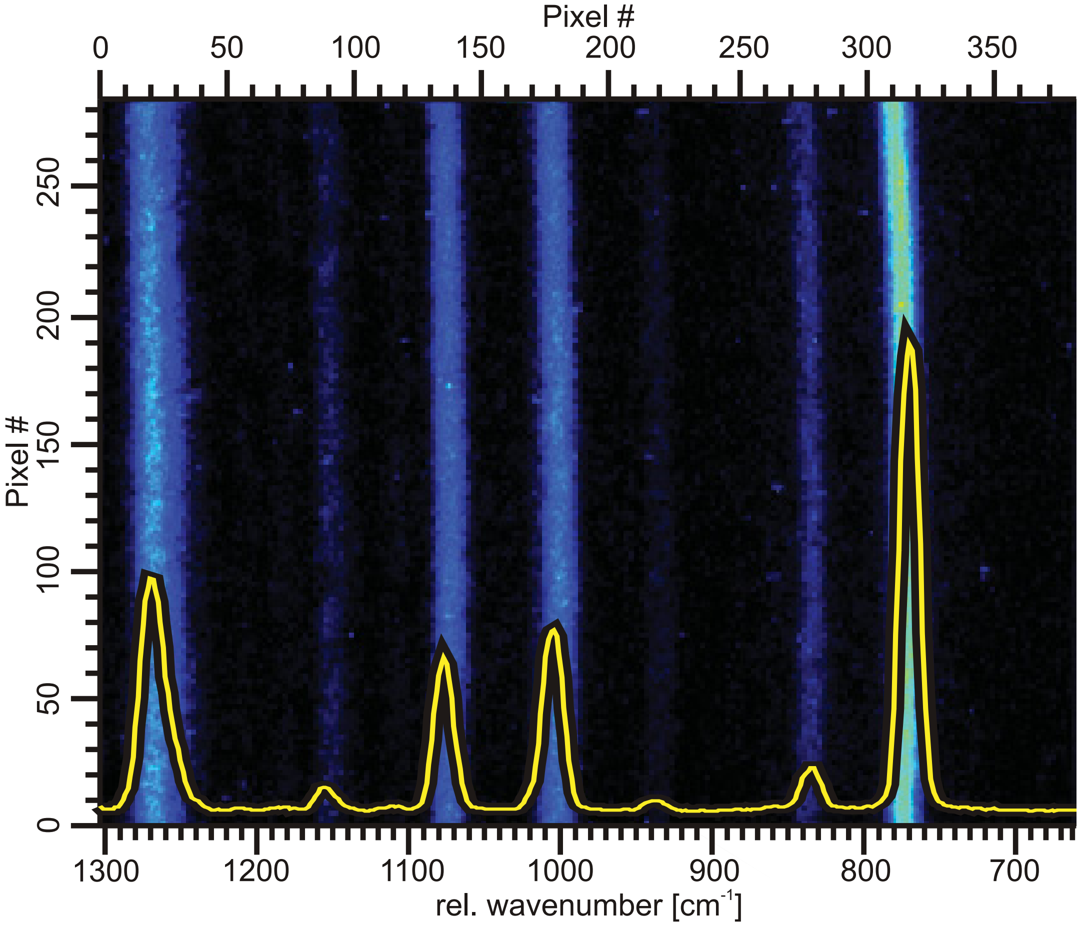

Figure 4.5: Average over 50 camera images at a single monochromator position and corresponding DF spectrum. The intensities of the DF bands are integrals over the vertical pixel "brightness" in the vertical region from 40-240 pixel at that horizontal pixel position. The excited transition is the benzimidazole electronic origin at 36021 cm^{-1} and the monochromator position is 287 nm

The charge induced in each pixel, or "brightness" of this pixel is colour coded depending on the chosen resolution. In the shown image, the intensity increases from black (zero), over different shades of blue into red (maximum) and white (overexposed). The sensitivity of the CCD chip decreases from left to right, but this effect is only visible in the baseline of the spectrum at very low light intensities. Each *vertical line* in this image corresponds to a band in the emission spectrum, while scattered illuminated pixels correspond to stray light from other sources.

This is very convenient, as real features of the spectrum can be distinguished from artefacts by the inspection of the camera images, even at very low line intensities. 50 images are processed for each *subspectrum*[1] either by summing the illumination intensities

---

[1] the term subspectrum has another meaning in this context than in the discussion of the FCfit.

up, averaging or calculating the root mean square.

The lines are bend vertically and the horizontal intensity reflects the spatial adjustment of the excitation laser. Because of this, only the vertical region of 40-240 pixels is used for the translation of the image into a spectrum. The intensity at each point in the spectrum is the integral over the intensity of these 200 pixels at each horizontal pixel position.

To translate the *horizontal pixel position* into a *spectral position*, the CCD chip is calibrated at each monochromator position. For this, the stray light from the carrier gas beam (argon is better suited for this than helium) or a needle on the valve cap is used, depending on the laser intensity. The dye laser is tuned to a certain wavelength and the horizontal pixel position of the stray light is then used as *calibration point*. At each monochromator position, the calibration points are then fitted by a polynomial and this polynomial is in turn used to calculate the wavenumber corresponding to every horizontal pixel position.

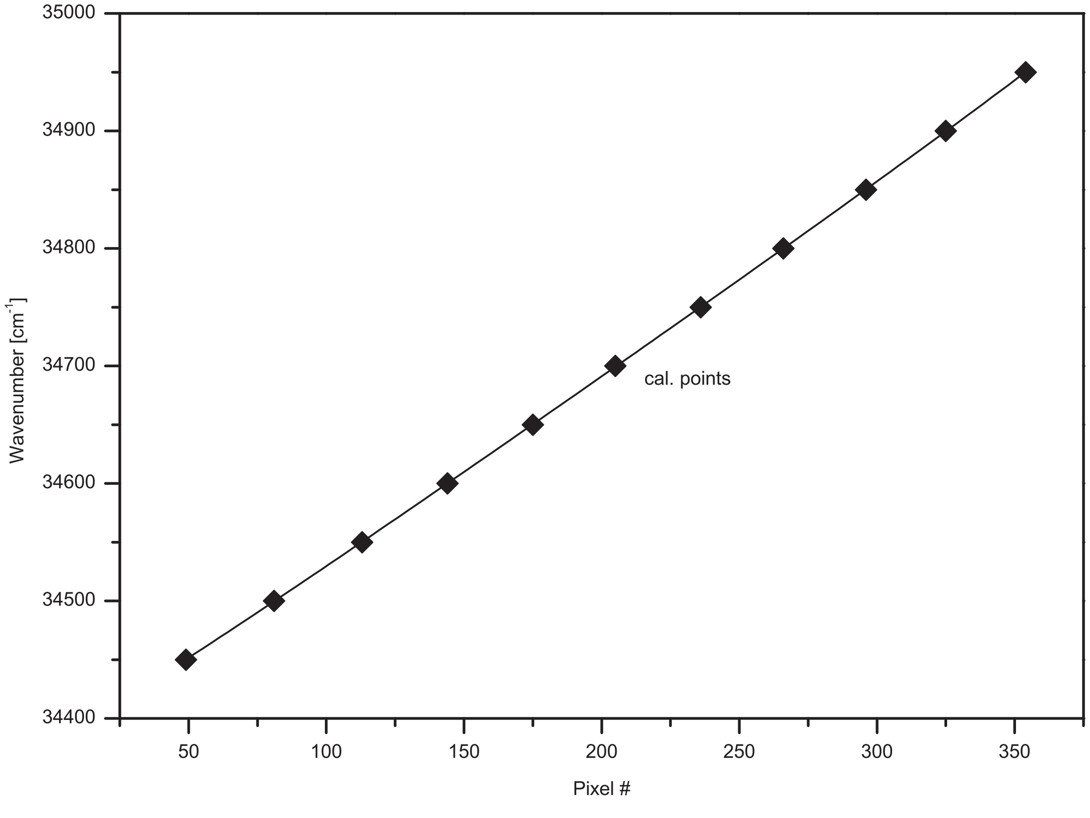

Figure 4.6: Calibration points and fit for the calibration of the grating at 290 nm

Figure 4.6 shows such a wavenumber calibration for the monochromator position 290 nm. The calibration points are taken at an interval of 50 cm^{-1}. The used dye was Pyrromethene 597. The final fit function in that particular calibration is given in Equation 4.1:

Here is means the part of a DF spectrum that fits on one camera image.

$$\tilde{\nu}_{\text{fit}} = 34377.49 + 1.43 \cdot x + 1.2 \cdot 10^{-3} \cdot x^2 - 3.5 \cdot 10^{-6} \cdot x^3 + 4.5 \cdot 10^{-9} \cdot x^4 \tag{4.1}$$

with the fitted wavenumber $\tilde{\nu}_{\text{fit}}$ and the horizontal pixel position x at the calibration laser frequency $\tilde{\nu}_{\text{cal}}$. The correlation factor R^2 is 0.99999 and the sum of least squares χ^2 1.08. The very small coefficients for terms higher than linear may lead to the assumption, that a linear calibration function is sufficient. But this leads to a significant error that is visible when the spectra taken at different monochromator positions are overlapped.

The *diffraction angle* θ_m -and thus the horizontal position on the chip- of light with the wavelength λ depends on the grating angle θ_i -corresponding to the monochromator position- following Equation 4.2 with lattice parameter d and grating order n.[10]

$$\theta_m = arcsin\left(\frac{n\lambda}{d} - sin\left(\theta_i\right)\right) \tag{4.2}$$

This sine-relation (or its reciprocal, since the calibration points are taken in cm^{-1} for the fit) is approximated well enough by a polynomial of fourth order in the spatial region reflected by a camera image. A linear fit leads to considerable deviations between subspectra taken at different monochromator position.

After the translation of pixel scale to an absolute wavenumber scale it is converted into relative wavenumbers. If the excitation frequency is visible in the image, the wavenumber of its intensity maximum is subtracted from all other frequencies. If not, the subspectrum is overlapped with a subspectrum that is already given in relative wavenumbers and the scale is modified in such a way, that overlapping features have the same wavenumber in the new subspectrum as in the already finalised part.

After compiling the complete spectrum from all of these subspectra, the intensities of all subspectra are normalised in such a way that the strongest transition of the complete spectrum apart from the transition with $\sum_i \delta\nu_i = 0$ (which is biased by stray light from the excitation laser) has the intensity 1 and the baseline is at intensity 0. Especially at very low fluorescence intensities, the sensitivity gradient of the CCD chip becomes visible and the baseline has to be corrected accordingly.

Part II

Publications

5. Towards a Spectroscopical and Theoretical Identification of the Isolated Building-Blocks of the Benzene-Acetylene Cocrystal

Markus Böning[1], Benjamin Stuhlmann[1], Gernot Engler[1], Matthias Busker[1], Thomas Häber[1,2], Adem Tekin[3], Georg Jansen*[4], and Karl Kleinermanns*[1]

ChemPhysChem **2013**, *14(4)*, 837-46, doi: 10.1002/cphc.201200701

5.1 Abstract

Isomer- and mass-selective UV and IR-UV double resonance spectra of the BA_3, B_2A, and B_2A_2 clusters of benzene (B) and acetylene (A) are presented. Cluster structures are assigned by comparison with the UV and IR spectra of benzene, the benzene dimer, as well as the BA, BA_2, and B_2A clusters. The intermolecular vibrations of BA are identified by dispersed fluorescence spectroscopy. Assignment of the cluster structures is supported by quantum chemical calculations of IR spectra with spin-component scaled second-order Møller-Plesset (SCS-MP2) theory. Initial propositions for various structures of the BA_3

---

[1] Institut für Physikalische Chemie
Heinrich-Heine Universität Düsseldorf
Universitätsstr. 1, 40225 Düsseldorf (Germany)
E-mail: kleinermanns@uni-duesseldorf.de

[2] Current address: Karlsruher Institut für Technologie (KIT)
Engler-Bunte-Institut, Bereich Verbrennungstechnik
Engler-Bunte-Ring 1, 76131 Karlsruhe (Germany)

[3] Informatics Institute
Istanbul Technical University
34469 Maslak, Istanbul (Turkey)

[4] Fakultät für Chemie
Universität Duisburg-Essen
Universitätsstr. 5, 45117 Essen (Germany)
E-mail: georg.jansen@uni-due.de

and B_2A_2 aggregates are generated with model potentials based on density functional theory combined with the symmetry-adapted perturbation theory (DFT-SAPT) approach. Shape and relative cluster stabilities are then confirmed with SCS-MP2. T-shaped geometries are the dominant structural motifs. Higher energy isomers are also observed. The detected cluster structures are correlated with possible cluster formation pathways and their role as crystallization seeds is discussed.

5.2 Introduction

Cocrystals with defined molecular composition can be synthesized by co-condensation of gaseous compounds in fixed molar ratios followed by multiple heating/cooling cycles, as long as the cocrystal is more stable than the crystals of the pure components. The basic structural motifs of the unit cell in principle are comparable to nanocrystals (clusters) synthesized in gas jets by adiabatic cooling. However, cooperative effects may lead to crystal structures which do not necessarily represent the most stable cluster isomer in the gas phase. But since supersonic jet cooling is a nonequilibrium process, higher-energy cluster isomers are often formed along with the most stable forms. That opens the possibility to directly study isolated unit cell structures of crystals or their building blocks in the form of clusters. Isomer- and mass-selective high-resolution spectroscopy can be used to determine the electronic and structural properties of the clusters, which can be used to identify the sequence of cluster formation steps and to relate it to the crystallization process.

Cocrystals of benzene (B) and acetylene (A) with defined molecular composition have been synthesized by cocondensation of gaseous compounds in fixed molar ratios and characterized by X-ray structure analysis.[103] The structure of the 1:1 benzene-acetylene cocrystal has a basic packing motif of first neighbours consisting of T-shaped BA arrangements, stabilized by $CH\cdots\pi$ interactions between the acidic CH group of acetylene and the π system of the benzene ring. The relatively strong $CH\cdots\pi$ interaction of typically $\leq 2.5\ \mathrm{kcal}\cdot\mathrm{mol}^{-1}$ energy[104] has found broad interest due to its importance in the stabilization of supramolecular aggregates, crystal packing, molecular recognition and folding of proteins.[14, 105, 106] The benzene-acetylene dimer (BA) is a typical case of such a stronger $CH\cdots\pi$ interaction. Clusters with 2 benzene moieties such as B_2A are able to form $\pi\cdots\pi$ bonds between the two benzene moieties which, might compete with the benzene-acetylene $CH\cdots\pi$ interaction.

Benzene-acetylene aggregates have already been studied by several groups. IR spectra of the acetylenic C-H stretching vibration have been observed in bulk solution,[107] Ar matrices,[108] and supersonic jets.[109] NMR measurements show a characteristic high field chemical shift of the acetylenic proton which points to a close CH$\cdots\pi$ contact.[110] Resonant two photon ionization (R2PI)[111–113] and laser-induced fluorescence (LIF) spectroscopy[109] revealed UV absorptions at +137 cm^{-1} (BA), +127 cm^{-1} (BA$_2$, isomer 1), +123 cm^{-1} (BA$_2$, isomer 2) and +116 cm^{-1} (BA$_3$) relative to the 6^1_0 band of benzene at 38606 cm^{-1},[114, 115] but only velocity map imaging allowed for an unambiguous assignment of the cluster size.[111]

High level *ab initio* calculations predict a T-shaped structure of BA. The acetylene is situated on the C_6 symmetry axis of the benzene ring and forms a CH$\cdots\pi$ bond with the aromatic π-system.[116–120] IR-UV double resonance studies confirm the T-shaped structure of BA and a ring structure for isomer 2 of BA$_2$. The acetylenic CH stretch vibration is red-shifted by -22 cm^{-1} (BA) and $-27/-30$ cm^{-1} (BA$_2$, isomer 2) relative to the ν_3 mode of bare acetylene.[109] A comparative study of several aromatics with acetylene showed a positive correlation of the IR red shifts with the π-electron density but only a weak negative correlation with the polarizability of the aromatic ring, which indicates that the 1:1 cluster is primarily stabilized by a CH$\cdots\pi$ (hydrogen) bond rather than by van der Waals interaction.[109] Herein, we present the intermolecular vibrations of BA in the far-IR spectral range obtained by high-resolution dispersed fluorescence (DF) spectroscopy. The intermolecular vibrations are sensitive probes of the cluster interaction potential.

Previously we reported isomer selected IR/UV double resonance spectra of both isomers of BA$_2$ as well as of BA$_3$ and B$_2$A.[15] Isomer 1 of BA$_2$ has a double T-shaped structure, which is also found in the benzene-acetylene 1:1 cocrystal[103] along the c-axis and might be the seed nucleus in the crystallization process of the cocrystal. The structure of BA$_3$ derives from both isomers of BA$_2$ by adding a third acetylene unit, which points to a stepwise aggregation in which acetylene molecules are successively added to previously formed BA$_n$ clusters. Isomer 1 of BA$_2$ with its double T-shaped structure grows to the BA$_3$ structure by addition of a third acetylene molecule sideways to one acetylene unit and the benzene ring. The structure of BA$_3$ is also formed by adding an acetylene perpendicular to the free side of the benzene ring of Isomer 2 of BA$_2$. Herein, we present high-resolution IR spectra of a further isomer of BA$_3$, which also derives from the double T-shaped BA$_2$ structure by addition of a third acetylene unit perpendicular to one of the other acetylenes (T-shaped acetylene motifs). Finally, B$_2$A is a combination of the most stable T-shaped B$_2$[121–126] and BA[109, 116–119] aggregates. Overall, T-shaped structures dominate the observed benzene-acetylene clusters in supersonic jets.[15, 109]

To follow the pathway of crystallization from the simplest seed up to the packing motif of a crystal and to learn more about the interplay between CH$\cdots\pi$ bonds and $\pi\cdots\pi$ interactions, we decided to investigate benzene-acetylene clusters containing two benzene moieties. We present a detailed vibrational analysis of the different benzene-acetylene clusters and report the R2PI and IR-UV double resonance spectra of B_2A_2. The vibrational spectra will be compared to quantum chemical calculations for structural assignments. We then relate the cluster structures to its smaller precursors and derive possible pathways for their formation in supersonic jets.

5.3 Experimental Section

5.3.1 IR-UV Double Resonance Spectroscopy

The basic principles of our IR-UV experimental setup were described in detail elsewhere.[127–129] A gas mixture of 0.8% benzene (Acros Organics, $> 99\%$), 1.0% acetylene (Air Liquide, 2.6) and 98.2% helium (Air Liquide, 5.0) was expanded through the 300 µm orifice of a pulsed valve (Series 9, General Valve) at a stagnation pressure of 3 bar. The molecules were cooled down to a few Kelvin in the adiabatic expansion where they formed clusters. For comparison, gas mixtures of 0.8% benzene and various acetylene contents (0.2, 2.5 and 5.0%) in helium were also used.

The skimmed molecular beam (skimmer diameter 1 mm) crossed the UV excitation laser (LAS, frequency doubled, 10 µJ/pulse) and the ionization laser (FL 2002, Lambda Physics, frequency doubled, > 500 µJ/pulse) at right angle inside the ion extraction region of a linear time-of-flight (TOF) mass spectrometer in Wiley-McLaren configuration. The UV excitation and ionization lasers are spatially and temporarily overlapped. Resonant two photon ionization (R2PI) spectra were recorded by scanning the frequency of the excitation laser between 38500 and 38800 cm^{-1}, while the ionization laser was kept at a wavelength of 274 nm (≈ 36500 cm^{-1}) and at 280 nm (≈ 35700 cm^{-1}) for comparison. The two-colour scheme minimized excess energy in the ions and reduced the amount of fragmentation after ionization.

For the IR-UV double resonance experiments, a pulsed IR laser beam (burn laser) was aligned collinear to the UV excitation beam (probe laser) and fired 150 ns before the latter. The IR laser frequency was scanned over the vibrational transitions and removed vibrational ground-state population if resonant, while the UV excitation laser was kept at a frequency resonant with a vibronic transition of a single cluster isomer. By monitoring the ion mass signal as a function of IR frequency, cluster mass and isomer selective infrared spectra, detected as ion dips, were obtained. IR laser light was generated by a two-stage setup,[130] which produced IR radiation between 2800 and 4000 cm^{-1} (10 Hz, > 4 mJ/pulse). An injection seeded Nd-YAG laser (Spectra Physics Pro 230, linewidth $< 3.10 - 3$ cm^{-1}) was used to pump a two stage IR laser system consisting of an optical parametric oscillator (OPO) and an optical parametric amplifier (OPA). The resonator of the OPO stage was in grazing-incidence-grating configuration. While light of the zero order of diffraction was coupled out, the first order of diffraction was retroreflected by a tunable mirror to the rotatable KTP crystal.[130] This configuration enabled the reduction of the IR linewidth to 0.05 cm^{-1} compared to 4 cm^{-1} of the former OPO stage setup without grating used for the measurements in Ref.[15].

5.3.2 Dispersed Fluorescence

The experimental setup for DF spectroscopy is described in detail in refs.[131, 132]. A gas mixture of benzene (1.0%) and acetylene (2.5%) in helium was expanded through a pulsed nozzle with a 500μm orifice. The output of a Nd:YAG laser (Innolas SpitLight 600)-pumped dye laser (Lambda Physics, FL3002) was frequency doubled and crossed perpendicularly with the molecular beam.

The fluorescence light was collected perpendicularly to laser and jet and was imaged on the 30μm entrance slit of a 1 m monochromator (Jobin Yvon, grating with 2400 grooves $\cdot$ mm^{-1} blazed at 400 nm for first and second order). The DF was recorded by an intensified CCD camera (Flamestar II, La Vision). A DF spectrum was obtained by summing the signal of 200 laser pulses and by subtracting the background that emerged from scattered light. A new background was taken after 25 of these single spectra. The final DF spectra were averages over 100-200 of these single spectra to obtain a better signal-to-noise ratio. This scheme allowed for simultaneous imaging of a DF spectrum over about 600 cm^{-1}.

5.4 Calculations

The systematic generation of the structures of weakly bound aggregates between molecules quickly becomes a very demanding task with increasing number of monomers. In the case at hand, in which we are mainly interested in aggregates composed of four monomers, there are already more than a dozen intermolecular degrees of freedom. Furthermore, for the computation of the vibrational spectra of the various aggregate structures the intramolecular degrees of freedom need to be geometry optimized as well. We thus used a two-step procedure consisting of: 1) generating aggregate structures from model potentials that were derived from quantum chemical calculations of intermolecular potential energy surfaces for rigid monomers; and 2) using these structures as starting points in subsequent full geometry optimizations by quantum chemical methods, followed by the calculation of the vibrational spectra at the same level of theory.

5.4.1 Generation of Cluster Structures

To calculate potential energy surfaces for the interaction of an acetylene molecule with a benzene molecule and between two benzene molecules, the DFT-SAPT method[133–136] was used, that is, a combination of a description of the electronic structure of the monomers through density functional theory (DFT) with subsequent computation of intermolecular interaction energies by symmetry-adapted perturbation theory (SAPT).[137, 138] For various characteristic structures of the acetylene dimer and benzene dimer[136] and the acetylene-benzene complex,[120] DFT-SAPT has been shown previously to yield interaction energies in excellent agreement with the "'gold standard"' quantum chemical method for intermolecular interactions, that is, single and double excitation coupled cluster theory including perturbative triple excitations (CCSD(T)). DFT-SAPT has already been used as a basis for the development of analytical model potentials for interacting molecules,[139, 140] as is also the case for the SAPT(DFT) approach,[141–143] developed in parallel to DFT-SAPT and differing from it chiefly in technical details. In particular, we mention the SAPT(DFT)-based model potentials for the benzene dimer.[144, 145]

An analytical model potential for the acetylene dimer has recently been derived from complete basis set (cbs) limit DFT-SAPT interaction energies for 829 dimer geometries with small to mid-range intermolecular distances, complemented by 10192 large-distance geometries which were treated in the multipole approximation.[140] In this model a potential five sites are employed to represent each acetylene molecule, that is, the two carbon atoms, fixed at a distance of 1.2028 Å, the hydrogen atoms, fixed at a C–H distance of 1.0618 Å, and the C–C bond midpoint. The interactions between the sites at the two acetylene molecules were described through a modified Born-Mayer (exp-6) potential,[146] which includes a damping of the dispersion contribution at short interatomic distances and a damped Coulomb interaction between the partial charges located at the sites. The same strategy was applied to generate cbs limit DFT-SAPT-based analytical model potentials for acetylene-benzene and the benzene dimer.[147] Herein, the benzene molecule is represented through a total of 26 sites: all atomic positions, characterized by a C–C distance of 1.3915 Åand a C–H distance of 1.0800 Å, and sites describing the π clouds, which were placed 0.47 Åabove and below the carbon atoms[148] and above and below the molecular center. Note that the model potentials of refs.[144, 145] exclusively use in-plane sites for the benzene molecule. Details of the fit of the parameters occurring in the modified Born-Mayer potentials for acetylene-benzene and benzene-benzene will be given elsewhere.

Using the original DFT-SAPT model potential of ref. [140] for the acetylene dimer and the analogous dimer potentials for acetylene-benzene and benzene-benzene,[147] random structures of the BA_3 and B_2A_2 aggregates were generated and subsequently geometry optimized through a simulated annealing (SA).[149] In the SA implementation, the Metropolis criterion[150] is used for the approval of a movement on the potential energy surface and the cluster is annealed by taking half of the temperature of the previous step. In this way seven minima on the 15-dimensional rigid-body potential energy surface BA_3 were found, while nine minima on the 16-dimensional surface for B_2A_2 were obtained (see below).

5.4.2 Computation of Vibrational Spectra

The aggregate structures obtained above were then fully geometry optimized with spin-component-scaled second-order Møller-Plesset perturbation theory (SCS-MP2).[6] SCS-MP2 is known to yield interaction energies in good agreement with CCSD(T) for systems dominated by $\pi \cdots \pi$[151, 152] and $CH \cdots \pi$[120] interactions. All SCS-MP2 calculations were carried out in the resolution-of-the-identity (RI) approximation, by correlating valence electrons only and using the aug-cc-pVDZ orbital basis set[59, 153, 154] along with the corresponding MP2 auxiliary basis set.[67] Tightened electronic and geometrical parameter convergence thresholds were employed before the numerical determination of force constants from central differences with analytical gradients, as implemented in the TURBOMOLEV6.0 quantum chemistry program package.[55, 73, 155, 156] All of the optimized structures could thus be confirmed as minima on the full-dimensional potential energy surfaces, with the exception of the two highest-energy structures of B_2A_2 , each one of which showed one imaginary frequency with a magnitude smaller than 7 cm^{-1}. The corresponding vibrational modes concern a parallel displacement between two adjacent benzene rings (structure H, see below) and a relative rotation between two distant benzene rings (structure J), that is, movements for which a very shallow potential energy curve is expected. We thus presume that it is safe to use the acetylene ν_3 modes for these structures in our assignment of the experimental spectra.

Nearly all of the SCS-MP2-optimized aggregate structures could hardly be distinguished from the corresponding structures obtained from the DFT-SAPT model potential. The exception is the lowest-energy structure of BA_3 , which is termed structure A in the following. It displays C_S symmetry at the SCS-MP2 level whereas with the model potential it is C_1 symmetrical. The geometries are nevertheless closely related: in both cases an acetylene unit pointing with its axis to the center of the benzene molecule is flanked by two acetylene molecules which point to the former's center. Although with the model potential the energy of formation, E_{model}, of the structure A of BA_3 from its monomers is found to be $-35.48\ \mathrm{kJ \cdot mol^{-1}}$, the counterpoise-corrected[157] interaction energy, E_{int}, at the SCS-MP2/aug-cc-pVDZ level is calculated to be $-27.46\ \mathrm{kJ \cdot mol^{-1}}$ only. Most of the deviation presumably has to be attributed to the basis set incompleteness error in our SCS-MP2 calculations, another part to methodological differences between SCS-MP2 and DFT-SAPT, and a remaining part to three- and four-body contributions that were not taken into account in the DFT-SAPT model potential. In the SCS-MP2 geometry optimizations the internal degrees of freedom of each molecule were allowed to relax upon formation of the aggregate, in contrast to the model potential structure optimizations. The relaxation of the monomers is accompanied by a repulsive relaxation energy, which is overcompensated by a growth of the magnitude of the attractive interaction energy. The sum of both contributions, often denoted as stabilization energy, E_{stab}, thus corresponds to the electronic contribution to the energy of formation of the aggregate. It amounts to $-27.27\ \mathrm{kJ \cdot mol^{-1}}$ for structure A of BA_3 . Finally, the vibrational contribution, E_{vib}, due to the change of the zero-point energy (ZPE) upon cluster formation has to be taken into account. For structure A of BA_3, E_{vib} is calculated to be $+10.73\mathrm{kJ \cdot mol^{-1}}$ in the harmonic approximation on the SCS-MP2/aug-cc-pVDZ level of theory.

Table 5.1 collects the differences of ΔE_{int} , ΔE_{stab} , and ΔE_{vib} of the interaction, stabilization, and ZPE energies of the remaining structures from the values for structure A given above. It also displays the model potential energies with respect to that of structure A. Note that the ordering of the structures according to E_{stab} of SCS-MP2 and the DFT-SAPT model potential energies E_{model} is virtually the same, apart from an interchange of structures C and D. One should also be aware that the harmonic approximation is often strongly violated for the intermolecular vibration modes, so that any modification of the energetic ordering upon inclusion of E_{vib} should be considered with caution. Finally, note that structures with an energy difference of a few fractions of a $\mathrm{kJ \cdot mol^{-1}}$, such as A, B, C, and possibly D, should perhaps best be considered as isoenergetic.

Table 5.1: Model potential energies, E_{model}, along with SCS-MP2 interaction, E_{int}, stabilization, E_{stab}, and zero-point vibrational energy differences, E_{vib}, for various structures of BA_3 with respect to the corresponding values for structure A $(-35.48, -27.46, -27.27, \text{and} + 10.73\ \mathrm{kJ \cdot mol^{-1}}, \text{respectively})$.

Structure	ΔE_{model}	ΔE_{int}	ΔE_{stab}	ΔE_{vib}
A	0.00	0.00	0.00	0.00
B	0.06	0.05	0.09	0.32
C	0.82	0.09	0.13	-0.12
D	0.59	0.35	0.31	1.14
E	1.71	1.46	1.51	-0.24
F	2.51	3.24	3.50	-0.37
G	6.62	6.30	6.15	1.90

Table 5.2 shows the corresponding results for the various structures of B_2A_2. Here the energetic ordering according to E_{stab} differs more strongly from that of E_{model}. Yet, it should be noted that the DFT-SAPT and the SCS-MP2 relative energies never deviate by more than 1.3 $\mathrm{kJ \cdot mol^{-1}}$, and that differences in the energetic ordering occur only within the group of structures C-F representing an energy interval of about 1.5 $\mathrm{kJ \cdot mol^{-1}}$ (SCS-MP2) or 1.1 $\mathrm{kJ \cdot mol^{-1}}$ (DFT-SAPT model).

Table 5.2: Model potential energies, E_{model}, along with SCS-MP2 interaction, E_{int}, stabilization, E_{stab}, and zero-point vibrational energy differences, E_{vib}, for various structures of B_2A_2 with respect to the corresponding values for structure A $(-42.66, -34.03, -33.80, \text{and} + 11.80\mathrm{kJ \cdot mol^{-1}}, \text{respectively})$.

Structure	ΔE_{model}	ΔE_{int}	ΔE_{stab}	ΔE_{vib}
A	0.00	0.00	0.00	0.00
B	1.99	1.86	1.89	-0.84
C	2.66	2.02	2.03	-0.75
D	2.25	2.59	2.65	-0.23
E	3.17	2.80	2.75	0.27
F	3.35	2.93	2.86	0.71
G	2.31	3.32	3.56	0.58
H	7.57	7.32	7.17	-1.04
J	8.59	9.19	9.03	3.04

For comparison with the experimental spectra, the most important results of the SCS-MP2 calculations are the IR frequencies and intensities which stem from the antisymmetric CH stretch mode ν_3 of the acetylene molecules. Due to the approximations entering the quantum chemical calculations and the harmonic approximation, the calculated frequencies differ considerably from experiment: for the BA dimer in its T-shaped minimum configuration we obtained ν_3 of acetylene as $3415.74\mathrm{cm^{-1}}$ with SCS-MP2/aug-cc-pVDZ whereas the experimental value is $3266.7\mathrm{cm^{-1}}$.[109] The calculated ν_3 frequencies presented in the following section were thus multiplied with the resulting scaling factor of 0.95637.

5.5 Results

5.5.1 R2PI Spectra

UV spectra of benzene-acetylene clusters with one benzene molecule (BA_n) have been reported previously[109, 111–113] and assigned to different cluster sizes by velocity map imaging spectroscopy.[111] To facilitate an easier comparison with the B_2A_n spectra and to illustrate similarities, we present herein a comprehensive summary of the UV spectra of all benzene-acetylene clusters measured so far. Figure 5.1 shows the two-colour resonance-enhanced R2PI spectra of BA_n ($n = 1, 2, 3$) and B_2A_n clusters ($n = 1, 2$) in the region of the 6^1_0 band of benzene, together with the benzene monomer (B)[114, 115] and benzene dimer (B_2).[121, 123, 125] Arrows indicate relative frequency shifts. Cluster size assignments are given by labels.

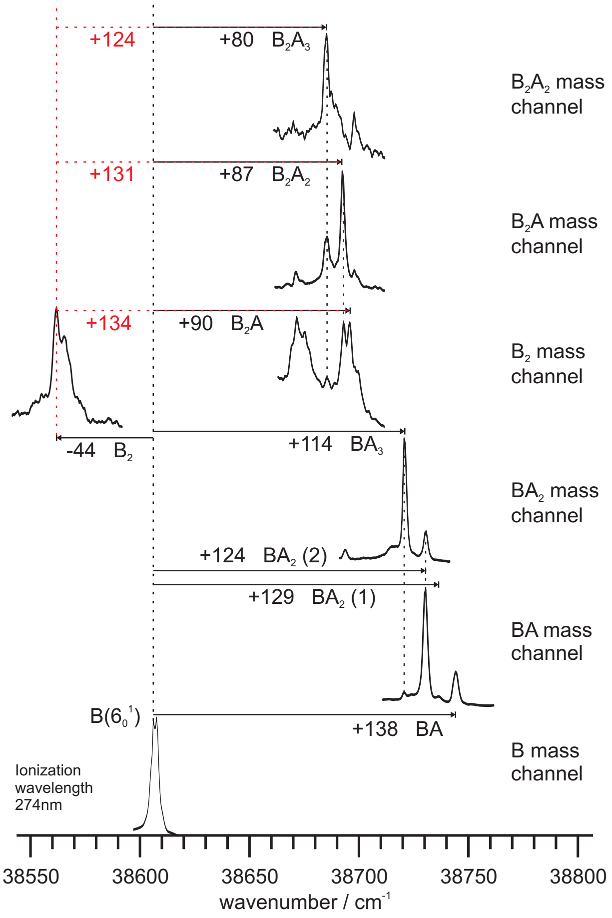

Figure 5.1: Two-colour R2PI spectra of benzene (B)-acetylene (A) clusters (BA_n and B_2A_n) in the region of the 6^1_0 band of benzene at 38606 cm^{-1}.[114, 115] Also shown is the R2PI spectrum of the benzene dimer (B_2)[121, 123, 125] and the relative shifts of the cluster absorptions with respect to the B or B_2 bands. (Ionization at 274 nm.)

Benzene-acetylene clusters B_mA_n undergo extensive fragmentation after ionization by losing at least one acetylene molecule, so that the cluster spectra can be obtained with higher quality on the $B_mA_n - 1$ mass channels, even under the gentle conditions of our two-colour experiment (ionization at 274 and 280 nm). The relative shifts of the BA_n cluster bands are in agreement with the literature[109, 111–113] to within 1 cm^{-1}. The simplest benzene-acetylene cluster, BA, has a T-shaped structure.[109, 116–120] Its UV absorption is blue-shifted by 138 cm^{-1} relative to the 6^1_0 band of the benzene monomer. Apparently the cluster stability is reduced in the electronically excited state due to a lower π-electron density in the benzene ring upon $\pi\pi*$ excitation, as in other π-hydrogen-bonded clusters.[158, 159] Successively adding more acetylene molecules leads to a small red shift of the vibronic transitions (see Figure 5.1).

The benzene dimer has a T-shaped structure too and shows an absorption 44 cm^{-1} to the red of the benzene monomer origin,[121, 123, 125] which is split due to a coupling to a vibrational mode.[125] The excitation is mainly localized in the ”‘stem”’ benzene moiety, while the ”‘top”’ moiety shows long vibrational progressions with maximum absorptions less than 10% of the ”‘stem”’.[121, 122, 124, 126] In other words, the π-system of the absorbing chromophore is not part of a $CH \cdots \pi$ interaction as it is in BA. This also explains the different frequency shifts (red versus blue) of B_2 and BA versus B.

The UV absorption of B_2A is blue-shifted by 134 cm^{-1} relative to B_2 . Following the above argument we can immediately conclude that 1) the acetylene molecule forms a $CH \cdots \pi$ bond with the absorbing chromophore in B_2A and 2) the structure of B_2A probably derives directly from B_2 by adding acetylene in a T-shaped arrangement, because the magnitude of the blue shift is almost the same as that between B and BA. This is supported by IR-UV double resonance spectra in comparison to *ab initio* calculations (see below and ref.[15]).

Finally, B_2A_2 is red-shifted by only 3 cm^{-1} relative to B_2A and both transitions overlap. Therefore both isomers are to a different extent excited by the UV laser. Due to extensive fragmentation of B_2A_2 its UV resonance at B_2 +131 cm^{-1} is clearly detectable on the B_2A and B_2 mass channels. Thus, IR-UV spectra on both UV resonances represent a superposition of both clusters. The separation of the isomer-specific B_2A and B_2A_2 IR-UV spectra and the structural assignment of the B_2A_2 cluster will be discussed in Section 5.5.2.

Like the BA_n clusters, B_2A_n clusters also show a red shift of the UV resonance with increasing number of acetylene molecules.

The relatively strong band at the B_2 +110 cm^{-1} spectral portion on the B_2And B_2A mass channels (see Figure 5.1) leads to the assumption of a second B_2A or more likely a further B_2A_2 isomer. But IR-UV spectra showed a variety of weak bands on a broad background, which prevents a precise assignment.

5.5.2 IR-UV Spectra

Before discussing the IR-UV double resonance spectrum of B_2A_2 and the new isomer of BA_3, we will summarize the most important structural motifs of our previous measurements, which is necessary for a better understanding of the structural assignment of the larger clusters. Figure 5.2 shows the IR-UV double resonance spectra of both isomers of BA2 and that of B_2A in the region of the ν_3 band of acetylene (asymmetric CH stretch vibration).[15] The clusters were excited at their respective UV transitions (Figure 5.1) and ionized at 274 nm. Also shown are the cluster structures. Vibrations are assigned by the line colours. Structural and vibrational assignments are based on comparison with

MP2/TZVP and MP2/TZVPP calculations.[15] Not shown here are the spectrum and structure of the T-shaped BA cluster, which absorbs at 3266.7 cm^{-1}.[109]

All cluster structures found so far in supersonic jets are also the most stable isomers at the MP2/TZVPP level of theory. In the case of BA_2 two isomers were identified. Isomer 2 is energetically more stable than isomer 1 by 0.71 $\mathrm{kJ \cdot mol^{-1}}$ at this level of theory, which is reflected by the different UV intensities (Figure 5.1).

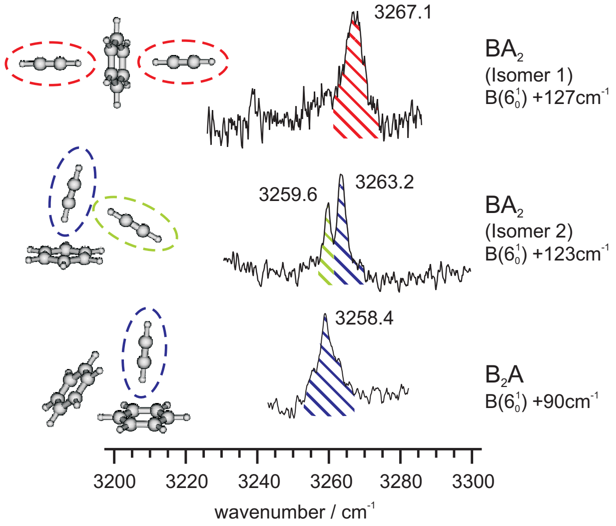

Figure 5.2: IR-UV double resonance spectra of both isomers of BA_2 and of $\mathrm{B}_2\mathrm{A}$. The clusters were excited at their respective UV transitions (see Figure 5.1) and ionized at 274 nm. Shown to the left are the corresponding cluster structures. Vibrations are assigned by the line colours. The structural and vibrational assignments are based on comparison with MP2/TZVPP calculations.[15] The two lower IR-UV double resonance spectra were remeasured with the high resolution of our new IR OPO laser system. For earlier measurements of these isomers see ref. [15].

The acetylene molecules can be divided into three groups according to their local environment, which shows up in their vibrational frequencies. Isomer 1 of BA_2 has a double T-shaped structure with one acetylene on either side of the benzene ring. Due to its high symmetry only one linear combination of the ν_3 vibrations of both acetylene molecules has nonzero intensity. Its absorption maximum is almost identical to that of BA, since the T-shaped local environment of the acetylene molecules is the same in both clusters. Isomer 2 of BA_2 has a ringlike structure and shows two absorptions red-shifted relative to the ν_3 vibration of BA. The vibration corresponding to the higher absorption frequency at 3263.2 cm^{-1} is almost exclusively localized on the acetylene molecule that forms the $\mathrm{CH} \cdots \pi$ bond with the benzene ring. The second acetylene molecule, which forms a CH hydrogen bond with the C≡C triple bond of the first acetylene and "'docks"' sideways between two CH bonds of the benzene ring, absorbs at 3259.6 cm^{-1}.

$\mathrm{B}_2\mathrm{A}$ shows a single absorption at 3259.4 cm^{-1}. From the R2PI spectra we concluded that acetylene forms a $\mathrm{CH} \cdots \pi$ bond with the absorbing chromophore, that is, with the "'stem"' of the T-shaped arrangement of the two benzene molecules. This is reflected by the most stable cluster isomer depicted in Figure 5.2.[15] Interestingly, the acetylene molecule in $\mathrm{B}_2\mathrm{A}$ is in a similar arrangement to the first acetylene molecule in BA_2 (isomer 2), but now the second acetylene molecule is replaced by another benzene ring. Apparently the interaction with the "'top"' benzene molecule in $\mathrm{B}_2\mathrm{A}$ leads to a slightly stronger red shift than the interaction with the second acetylene molecule in BA_2. In summary, both the formation of a CH $\cdots \pi$ bond and the interaction with the C≡C triple bond lead to a red shift of the asymmetric C–H stretching vibration.

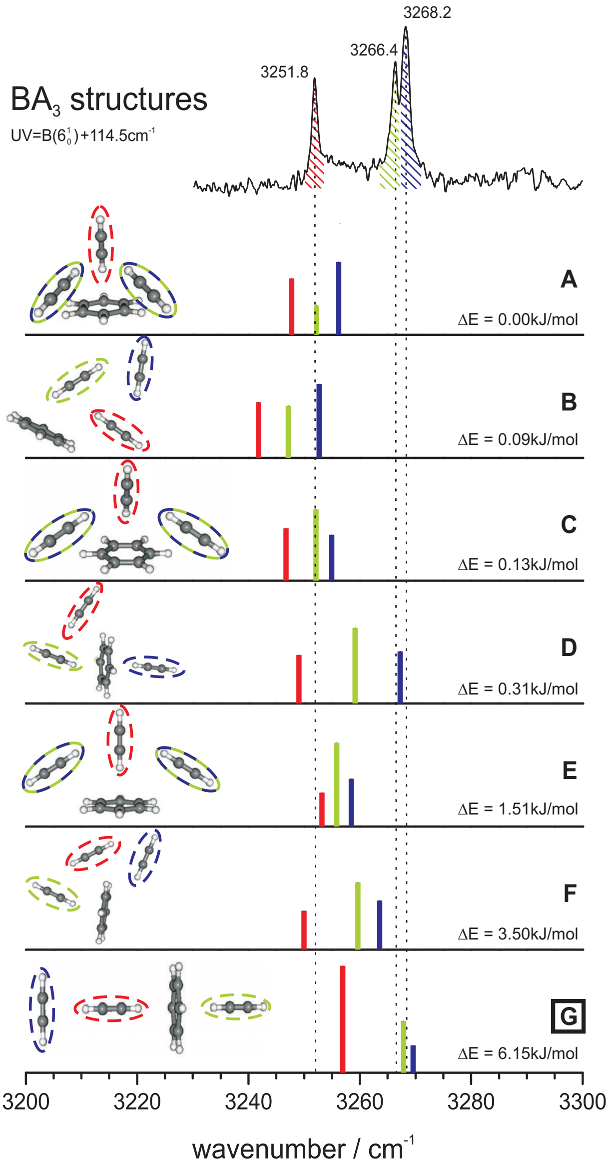

Figure 5.3: IR-UV double resonance spectrum of BA_3 obtained with the UV excitation laser tuned to $6^1_0 + 114.5$ cm^{-1}. Also shown are the calculated and scaled stick spectra of selected isomers ($\Delta E < 7$ kJ $\cdot$ mol^{-1}) at the SCS-MP2/aVDZ level of theory. Structures are depicted and arranged in order of their relative cluster stabilization energies. Vibrations are assigned by the line colours. The degenerate vibrations of the symmetric structures A, C, and E are indicated by bicoloured lines. The most likely structure G that we assign to the spectrum is labelled with a square.

Figure 5.3 shows the IR-UV spectrum of isomer 2 of BA_3, which we observed at a UV frequency of B(6^1_0) + 114.5 cm^{-1} with our high-resolution IR-OPO laser system. The UV resonance of isomer 1 of BA_3 (ref. [15] and Figure 5.9) is close to that of isomer 2 (B(6^1_0) + 116 cm^{-1}) and the intensity of its IR spectrum depends sensitively on the expansion conditions and acetylene content. We cannot exclude, however, that the spectrum of isomer 1 of BA_3 in ref. [15] has contributions from fragmentation of larger cluster ions, which also show IR absorptions near ≈ 3260 cm^{-1}. The spectrum in Figure 5.3 was taken under conditions at which the broad band at ≈ 3260 cm^{-1} of isomer 1 was minimized by reducing the acetylene content to 1.0%. Higher concentrations (2.5 and

5.0%) lead to an increasing intensity of the broad band at ≈ 3260 cm^{-1}, whereas lower concentrations (0.2%) lead to an unaccaptable degradation of the signal-to-noise ratio. Three IR bands are observed, one at 3251.8 cm^{-1} and the others closely spaced at 3266.4 and 3268.2 cm^{-1}. Figure 5.3 also shows the IR stick spectra of the most stable isomers of BA_3 calculated in the harmonic approximation at the SCS-MP2/aVDZ level of theory.

Structures A, C, and E differ by the angle formed between the "‘side-on"’ acetylenes (A: 60°, C: 120°, E: 180°). Due to the high symmetry of the isomeric structures, the vibrational modes are no longer isolated (located) on either one of the "‘side-on"’ acetylenes, as indicated by different line colours in Figure 5.3. Rather, the two higher frequencies are assigned to symmetric and antisymmetric linear combinations of the ν_3 vibrations of both "‘side-on"’ acetylenes. Isomers A, C, and E are ruled out because they show almost equally spaced bands and their calculated vibrational frequencies are red-shifted by about 10 cm^{-1} relative to the experimental frequencies. Isomer B shows a similar band pattern and red shift to isomers A, C, and E and is ruled out, too.

Structure D has been previously assigned to isomer 1 of BA_3 (see Figure 3 in ref. [15]), but it does not reflect the experimental frequencies observed here for isomer 2. Among the remaining isomers F and G, only the calculated IR spectrum of the higher-energy isomer G agrees reasonably well with the measured spectrum of isomer 2. Although the relative intensities of the three bands are different, possibly as a consequence of the harmonic approximation used in the calculations, the theoretical band distances of 11.0 and 1.7 cm^{-1} fairly well reproduce the experimental values of 14.6 and 1.8 cm^{-1}, respectively. A similar band pattern is predicted at the RIMP2/TZVPP level of theory in ref. [15]. Isomer G has a considerably higher energy than the most stable structure A. The energy difference is 6.15 $\text{kJ} \cdot \text{mol}^{-1}$ at the SCS-MP2/aVDZ level and even 9.50 $\text{kJ} \cdot \text{mol}^{-1}$ at the RIMP2/TZVPP level. However, one has to be careful upon comparing cluster dissociation energies $E(\text{BA}_3) - -E(\text{B}) - -3E(\text{A})$ directly with experimental formation probabilities. BA_3 clusters are most likely formed by adding one acetylene monomer to an already existing BA_2 cluster, rather than by simultaneously adding three acetylene molecules and one benzene molecule (see Section 5.6). For a kinetic pathway of successive addition of a monomer to a cluster with one benzene or one acetylene less, the energy change can be very different from the dissociation energies. Isomer G can be formed easily by adding one acetylene to isomer 1 of BA_2 (see Figure 5.9).

Figure 5.4a shows the normalized IR-UV spectra with the UV laser tuned to $6^1_0 + 90$ cm^{-1} (preferentially B_2A resonance, red line) and $6^1_0 + 87$ cm^{-1} (preferentially B_2A_2 resonance, blue line) on the B_2 mass channel. Since the UV resonances of B_2A and B_2A_2 are shifted by only 3 cm^{-1}, both isomers are excited to some extent at the two UV

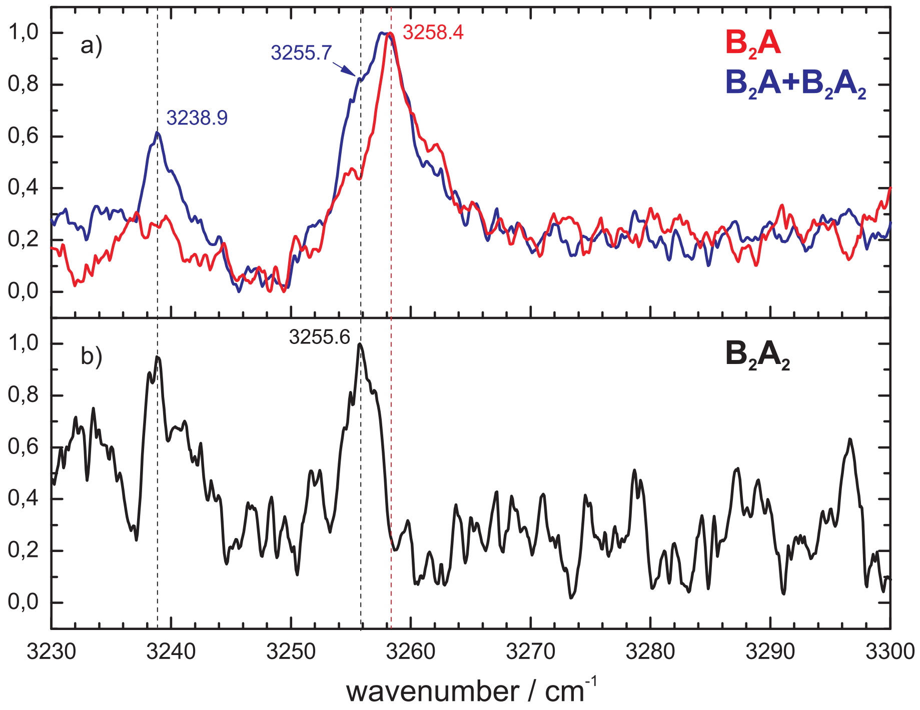

Figure 5.4: a) Normalized IR-UV ion dip spectra on the B_2 mass channel. UV excitation preferentially at the B_2A resonance ($6^1_0 + 90$ cm^{-1}, red line) and at the B_2A_2 resonance ($6^1_0 + 87$ cm^{-1}, blue line). b) B_2A_2-specific spectrum, obtained as a normalized difference spectrum (blue curve minus red curve).

frequencies. The red curve with its peak at 3258.4 cm^{-1} represents an ion dip spectrum of the almost pure B_2A isomer (see Figure 5.2). The weak band at $\approx$ 3239 cm^{-1} and a shoulder at $\approx$ 3255 cm^{-1} arise from the B_2A_2 isomer. The blue curve depicts a superposition of the isomer-specific bands of B_2A and B_2A_2. A spectrum of pure B_2A_2 (Figure 5.4b) with peaks at 3238.9 and 3255.6 cm^{-1} is obtained by subtracting the red curve from the blue curve. Both IR spectra show a broad, $\approx$ 15 cm^{-1} wide background absorption around 3260 cm^{-1}. This broad band probably arises from extensive fragmentation of higher clusters. Similar broad absorptions are observed in the IR-UV spectra on higher mass channels.

The most outstanding feature is the ν_3 frequency at $\approx$ 3239 cm^{-1}, which is the lowest acetylene stretch frequency measured by us up to now for benzene-acetylene clusters ($HC \equiv CH$ monomer$\nu_3$at3287 cm^{-1}). Our calculations at the SCS-MP2/aVDZ level show that structures with multiple $CH(A) \cdots C \equiv C(A)$, $CH(A) \equiv \pi(B)$, and $CH(B) \cdots C \equiv C(A)$ interactions show such a low ν_3 frequency for the ”‘entangled”’ acetylene.

A structural assignment of B_2A_2 is depicted in Figure 5.5. The pattern of the experimental B_2A_2 spectrum is compared with the calculated spectra of the nine most stable isomers at the SCS-MP2/aVDZ level of theory. Structures are arranged by relative cluster stabilization energies ΔE(for energies $< 9\mathrm{kJ} \cdot \mathrm{mol}^{-1}$). Structures E, F, H, and J can be

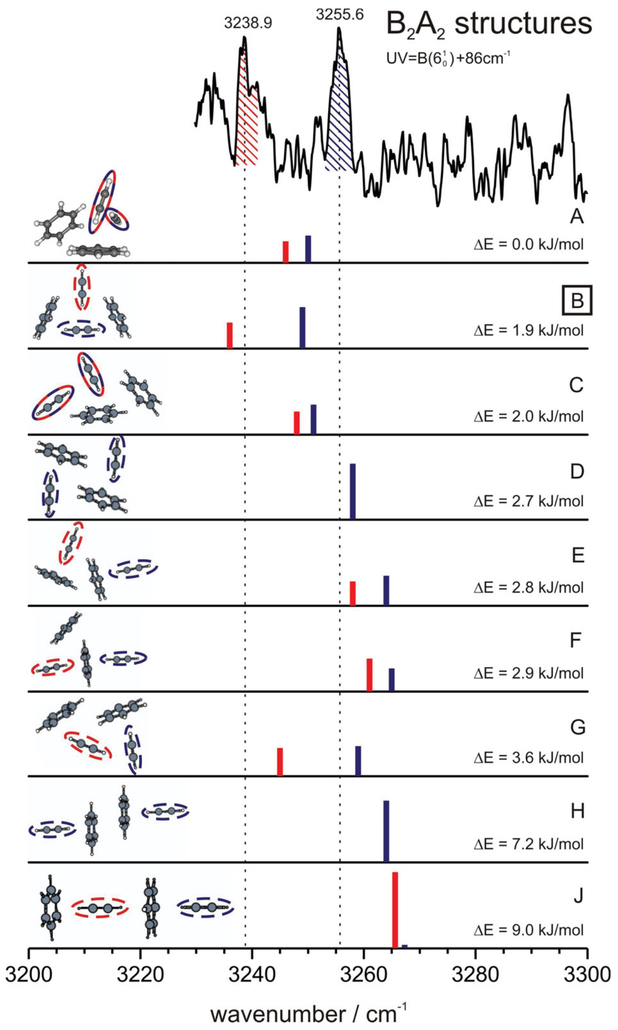

Figure 5.5: IR-UV double resonance spectrum of B_2A_2 obtained with the UV excitation laser tuned to $6^1_0 + 87$ cm^{-1}. Also shown are the calculated and scaled stick spectra of selected isomers ($\Delta E < 9$ kJ·mol^{-1}) at the SCS-MP2/aVDZ level of theory. Relative cluster stabilization energies ΔE(in kJ·mol^{-1}) are referred to the most stable structure. The most likely structure B is labelled with a square. Vibrations are assigned by the line colours. The bicoloured lines indicate degenerate vibrations.

ruled out as candidates for explaining the experimental spectrum due to their blue shift of more than 20 cm^{-1} relative to the experimental frequencies. Isomers D and H are highly symmetric, so they show only one IR-active vibration. Hence they can be ruled out, too. The most stable structure A and structure C differ only in the position of the sideways-attached benzene. The angle between the T-shaped acetylenes and the benzene ring is ≈ 120° for structure A and 180° for structure C. Both isomers are ruled out because their IR band pattern does not agree with the experimental frequencies. The calculated spectra of the structures B and G are in good agreement with the measured vibrational frequencies. In particular, the characteristic band at ≈ 3239 cm^{-1} is represented well by the calculated spectrum of structure B. Hence we assign it to be the most likely structure of the observed B_2A_2 spectrum. Furthermore, isomer B of B_2A_2 can easily be formed by adding either an acetylene or a benzene moiety to its precursors B_2A or isomer 2 of BA_2 . However, a precursor with two nearly parallel displaced benzene moieties as in structure G was not yet observed by us. Thus structure G can only arise from isomer 2 of BA_2. A possible cluster formation pathway is illustrated in Figure 5.9.

5.5.3 Dispersed Fluorescence Spectra

Figure 5.6 shows the LIF spectrum of BA at $B(6-0^1)+138$ cm^{-1} and of BA$_2$ at $B(6^1_0)+124$ cm^{-1}. The LIF frequencies are in good agreement with the R2PI frequencies displayed in Figure 5.1.

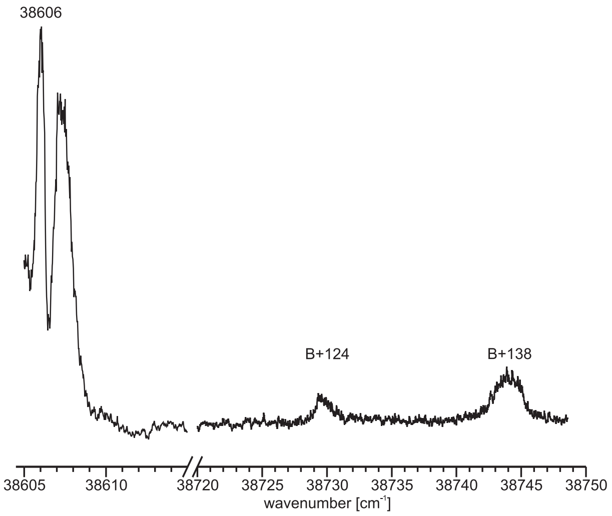

Figure 5.6: LIF spectrum of a gas mixture of benzene (1.0%) and acetylene (2.5%) in helium. The bands at 38730 and 38744 cm^{-1} are assigned to BA$_2$ and BA, respectively.

Figure 5.7 shows the DF spectra of the false origin (6^1_0) of the benzene moiety in BA$_1$ taken at $B(6^1_0)+138$ cm^{-1} and in the monomer. In Figure 5.7a, three bands at 62.4, 94, and 131.7 cm^{-1} are clearly discernible in the region of the low-frequency intermolecular vibrations below 200 cm^{-1}. Two of these intermolecular vibrations are observed as combination bands of the intermolecular benzene vibrations $(979+67, 979+138, 1210+69$ cm$^{-1})$. Figure 5.7b shows that those bands are not visible in the monomer spectra. Also, the observed monomer vibrations are red-shifted in the cluster.

Figure 5.8 displays the intermolecular vibrations of BA calculated at the SCS-MP2/aVDZ level of theory. Three translational and two rotational degrees of freedom disappear when B and A form a BA cluster. The corresponding motions can be recognized again as three hindered translations and two hindered rotations. Due to the C_{6v} symmetry of BA the two hindered rotations are degenerate, and this is also the case for the hindered X- and Y-translation modes. Hence we expect three vibrational bands in the far-IR region of BA. All three should be symmetry allowed because we excite the "‘false origin"’ $B(6^1_0)$ (weakly disturbed in the acetylene clusters) so that the vibronic

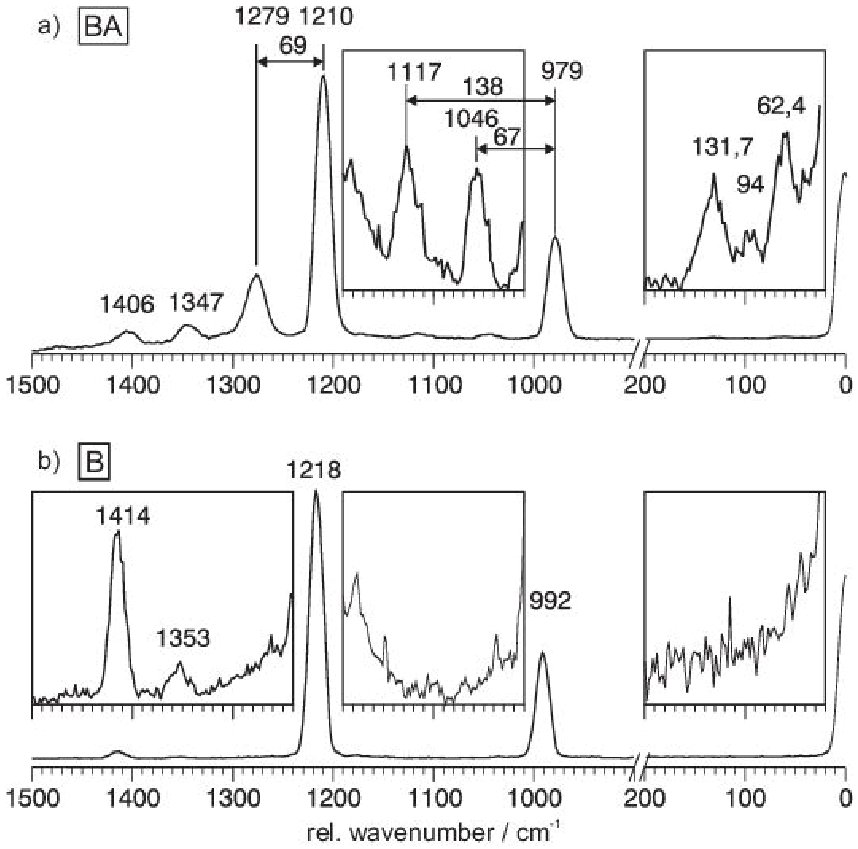

Figure 5.7: DF spectra after excitation through a) 38744 cm^{-1} (BA) and b) 38606 cm^{-1} (benzene monomer). The additional features in (a) compared to (b) are assigned to intermolecular vibrations and to combination bands between benzene and intermolecular vibrations. The insets in the region $20 - 200$ cm^{-1} are enhanced by 100; the insets in the regions 1010-1190 and $124 - 1500$ cm^{-1} are enhanced by 25.

transition moment including the symmetries of the intermolecular vibrations transforms totally symmetric in C_{6v}. Hence we assign the band at 62.4 cm^{-1} to the (twofold degenerate) hindered rotation of acetylene, the band at 94 cm^{-1} to the (degenerate) hindered translation of acetylene in the x and y directions, and the band at 131.7 cm^{-1} to the hindered translation of acetylene in the z direction, perpendicular to the benzene ring. The agreement of the calculated harmonic intermolecular vibrational frequencies with the (probably anharmonic) measured frequencies is not very good, as expected, but allows for an assignment based on the ordering of the frequencies.

5.6 Discussion and Conclusions

Based on the observed structures we can now try to unravel the possible cluster formation pathways (Figure 5.9). Starting from the simplest benzene-acetylene cluster, BA,

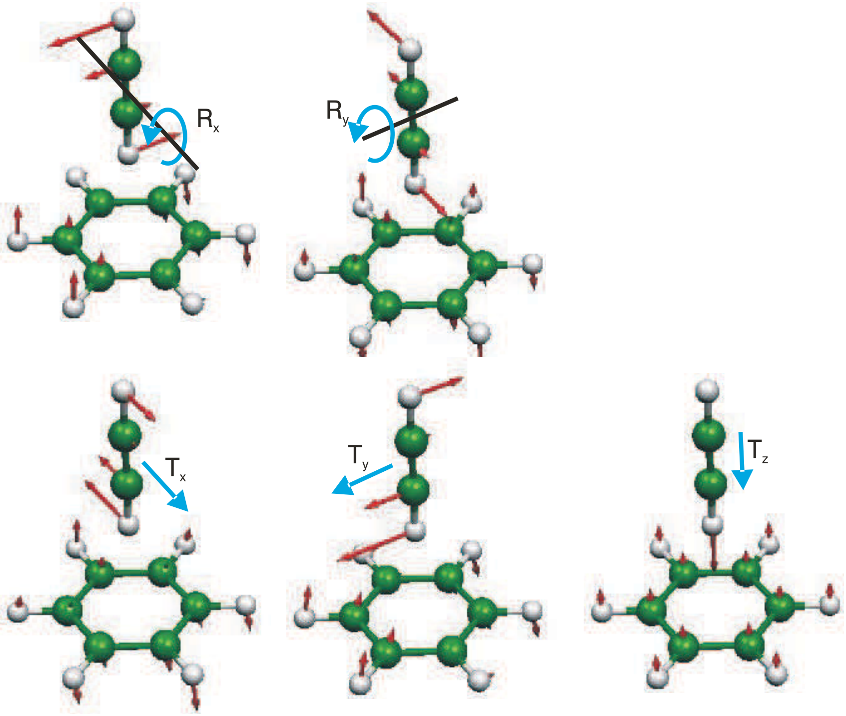

Figure 5.8: Intermolecular vibrations of BA_1, calculated at the SCS-MP2/aVDZ level of theory. Vectors created with Molekel 4.3.[160, 161] The intermolecular vibrations arise from hindered rotations and translations along the three spatial axes x, y, z. The calculated frequencies for R_x and R_y (degenerate), T_x and T_y (degenerate), and T_z are $41.7, 90.6$ and 95.6 cm^{-1}, respectively, at the SCS-MP2/aVDZ level of theory. It is shown that the hindered rotations and translations are mixing to some extent at this level of theory.

both isomers of BA_2 are formed by adding another acetylene molecule. The ringlike isomer 2 is the most stable structure and is formed with larger abundance than isomer 1. This is confirmed by its more intense UV absorption, if we assume similar UV transition probabilities for both isomers. As mentioned earlier, cluster formation in supersonic jets is not just controlled by thermodynamics, but to a large extent by kinetics so that the cluster abundances are influenced by the formation probabilities as well. Both isomers of BA_2 are precursors of the BA_3 isomer 1 by adding another acetylene molecule either to acetylene or to benzene in a T-shaped arrangement. Isomer 2 of BA_3 arises from the addition of acetylene perpendicular to one of the T-shaped acetylene molecules of isomer 1 of BA_2. Our results support a stepwise aggregation mechanism in which acetylene is attached to preformed BA_n clusters, rather than by first forming acetylene clusters (such as the T-shaped A_2 dimer or cyclic A_3 trimer) and attaching them to a benzene ring.

We can derive a similar scheme for the B_2A_n clusters, but now each cluster in principle has two precursors. B_2A might be formed from B_2 by adding acetylene perpendicular to the ”‘stem”’ benzene of the dimer. But also the addition of benzene sideways to the

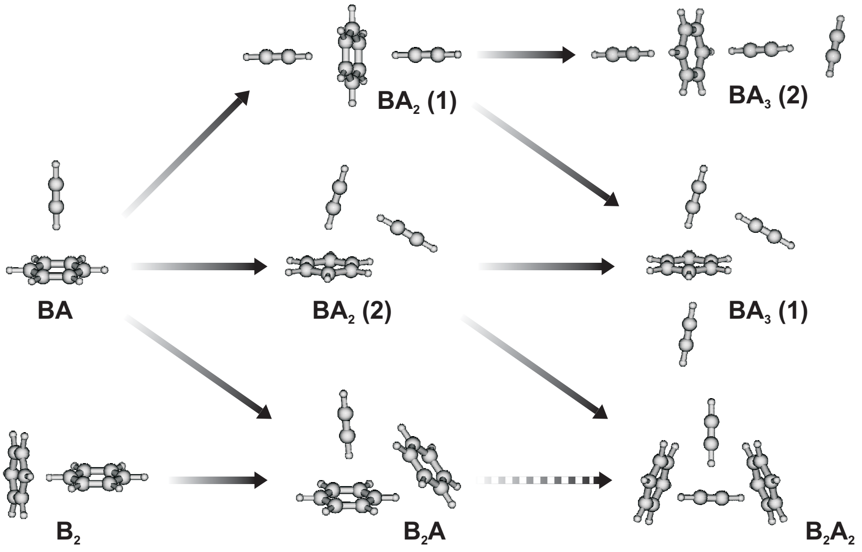

Figure 5.9: Representation of the benzene-acetylene cluster formation pathways based on the structures observed in supersonic jets (this work and ref. [15])

T-shaped BA might lead to B_2A. In the same way, B_2A_2 can be formed from isomer 2 of BA_2 by adding another benzene on top of the acetylene and parallel to the benzene. Although it is not the most obvious formation pathway, B_2A_2 might also arise from B_2A by diffusion of one acetylene molecule between the two benzene moieties and simultaneously moving the benzene to an H-shaped arrangement. We would like to mention in this context that the stacked and parallel displaced two BA_2 (1) moieties depicted as the B_2A_4 part of the unit cell of the benzene-acetylene cocrystal[103] has no direct precursor in Figure 5.9, but requires a rearrangement of the molecules in order to be formed out of the observed structures. If further acetylene molecules saturate the benzene T-shaped docking possibilities, an opening of the distorted B_2 T shape of B_2A to a parallel displaced arrangement of the two benzene rings seems possible in B_2A_4. Future experimental and theoretical investigations are necessary to search for other isomers, to obtain a more precise description of the energetics, and to explore possible pathways that would lead to structural motifs of the cocrystal.

5.7 Acknowledgements

This work was supported by the Deutsche Forschungsgemeinschaft (FOR 618-TP D and FOR 618-TP E).

5.8 Contributions

Title: Towards a Spectroscopical and Theoretical Identification of the Isolated Building-Blocks of the Benzene-Acetylene Cocrystal.

Authors: Markus Böning, Benjamin Stuhlmann, Gernot Engler, Matthias Busker, Thomas Häber, Adem Tekin, Georg Jansen and Karl Kleinermanns.

submitted to: ChemPhysChem (Impact Factor: 3.412)

This paper concludes a major part of the sub-projects D (quantum chemical calculations of molecular aggregates) and E (stepwise aggregation of small molecules) of the research group 618 of the Deutsche Forschungsgemeinschaft. The oldest results in this paper were accumulated by Matthias Busker and Thomas Häber and they are mostly an extended analysis of the data (R2PI and IR-UV spectra of different Benzene-Acetylene clusters) given in ref. [15].

New R2PI and IR-UV double resonance spectra with an improved experimental setup and on larger clusters were conducted by Markus Böning and Gernot Engler, who also did a lot of work on the technical side of the double resonance experiment.

Georg Jansen and Adem Tekin supplied the SCS-MP2 and DFT-SAPT calculations, which were used to interpret the old and new spectral data of different Benzene-Acetylene clusters.

My part was mostly the measurement and interpretation of LIF and DF spectra and the adaption of the DF experiment (e.g. the installation of a new laser system) for this task.

Disclaimer: Since the paper was originally published in greyscale, the colour-code of the vibrations in Figures 5.2,5.3 and 5.5 is replaced by line styles in that version. Degenerate vibrations are marked with dot-and-dashed lines instead of bicoloured lines. For the same reason, the colour coding in Figure 5.4 was changed as follows: red was changed to grey and blue was changed to fat black.

6. Isomer-Selective Vibrational Spectroscopy of Jet-Cooled Phenol-Acetylene Aggregates

Markus Böning[1], Benjamin Stuhlmann[1], Gernot Engler[1], and Karl Kleinermanns*[1]

J. Phys. Chem. A **2013**, *117(15)*, 3214-3220, doi: 10.1021/jp3125796

6.1 Abstract

The structures of the phenol (Ph)–acetylene (A) clusters $PhA_{1,2,3}$ and Ph_2A_1 are assigned on the basis of isomer and mass specific IR-UV double resonance spectroscopy and compared to the structure of the PhA cocrystal. The structures of the $PhA_{1,2,3}$ clusters are dominated by phenol–acetylene π-hydrogen bonds whereas Ph_2A_1 binds via $OH \cdots OH \cdots C \equiv C$ interaction with dominating Ph–Ph hydrogen bond like in the phenol dimer and acetylene attached to the free OH group of the proton acceptor phenol. The macroscopic crystal is a clathrate of phenol with acetylene with hydrogen bridges only between the phenol molecules and not between phenol and acetylene.[162] A possible aggregation pathway is proposed in which larger phenol clusters like Ph_6 are cyclic with no free OH available anymore to which acetylene could attach as proton acceptor.

6.2 Introduction

Aromatic–acetylene clusters have attained interest as model systems to study competition between hydrogen bonding and dispersion interaction and for structural comparison with their macroscopic cocrystals. Thereby small clusters composed of a few monomer moieties

---

[1] Institut für Physikalische Chemie
Heinrich-Heine Universität Düsseldorf
Universitätsstr. 1, 40225 Düsseldorf (Germany)
E-mail: kleinermanns@uni-duesseldorf.de

often show compact structures with a maximum number of the strongest H-bond, dipole, and dispersion interactions whereas crystals usually show more open structures influenced by the larger number of neighbours and long-range cooperative effects. Sometimes the components form clathrates or do not cocrystallize at all.

The structures of the nanocrystals obtained by adiabatic cooling in gas jets can be compared most readily to structures obtained from quantum chemical calculations; however, they do not necessarily represent global minimum energy arrangements, because jet cooling is a nonequilibrium process and cluster formation therefore is often dominated by kinetics. Phenol and acetylene assemble due to noncovalent intermolecular interactions.[16]

The most prominent one is the σ-hydrogen bond between a lone pair of electrons of an electronegative atom (proton acceptor) and a proton donor.[119, 163, 164]

It exhibits a binding energy of $5 - 15\ \mathrm{kJ \cdot mol^{-1}}$.[16, 165] If the π-system of an unsaturated compound is the proton acceptor, a *uppi*-hydrogen bond with a binding energy below $5\ \mathrm{kJ \cdot mol^{-1}}$[16, 165] is formed.

It is well-known that such noncovalent interactions play an important role in crystal packing[103, 166] and many biochemical processes, like protein folding and receptor binding.[11–14]

Previous studies revealed that $\mathrm{CH} \cdots \pi$ bonds are the dominant interactions in clusters of benzene and acetylene.[15, 167] Fujii et al.[16] reported an $\mathrm{OH} \cdots \pi$ bond for the 1:1 phenol–acetylene cluster instead of a $\mathrm{CH} \cdots \pi$ interaction. By using resonant two-photon ionization (R2PI) spectroscopy, we observed the strongest UV absorption band of $\mathrm{PhA_1}$ at $-246\ \mathrm{cm^{-1}}$[16] relative to the $S_1 \leftarrow S_0$ transition of the phenol monomer at $36348.7\ \mathrm{cm^{-1}}$.[30, 168] The structural assignment is supported by further quantum chemical calculations at the MP2/6-31++G(d,p) level of theory performed by Pejov et al.[169] Here we show that $\mathrm{PhA_2}$ and $\mathrm{PhA_3}$ clusters form $\mathrm{CH} \cdots \pi$ bonds in addition to the dominant $\mathrm{OH} \cdots \pi$ bond and that $\mathrm{Ph_2A}$ exhibits phenolic $\mathrm{OH} \cdots \mathrm{O}$ interaction similar to that of the phenol dimer with acetylene attached to the free OH of $\mathrm{Ph_2}$. X-ray analysis shows that the macroscopic cocrystal of phenol forms clathrates with inclusion of non hydrogen-bonded acetylene.[162, 170]

Up to now only the structure of the phenol–acetylene dimer has been assigned by the investigation of the phenolic OH stretch vibration.[16] In this paper we assign the structure of $\mathrm{PhA_{1-3}}$ and $\mathrm{Ph_2A}$ on the basis of IR-UV double resonance spectroscopy of the phenolic OH stretch and the acetylene CH stretch vibrations and by comparison with quantum chemical calculations at different levels of theory. We also investigate the far-infrared fingerprint region of those clusters with dispersed fluorescence spectroscopy.

6.3 Experiment and Theory

6.3.1 R2PI and IR-UV double resonance spectroscopy

The apparatus and the basic principles of our experiment are described in detail elsewhere.[127–129] Phenol at room temperature (295 K) was seeded in a carrier gas of 1.0% acetylene (Air Liquide, 2.6) and 99.0% helium (Air Liquide, 5.0) at a pressure of 3 bar. This gas mixture was expanded through the 300 µm orifice of a pulsed valve (Series 9, General Valve) into a high vacuum of 10^{-6} mbar. By adiabatic expansion, the molecules are cooled to a few Kelvin and form clusters.

The molecular beam is shaped by a skimmer of 1 mm diameter before it crosses the UV excitation laser beam (frequency doubled LAS dye laser, ~ 15 µJ/pulse) and the ionization laser beam (frequency doubled LAS dye laser, > 1 mJ/pulse) at a right angle inside the ion extraction region of a linear time-of-flight (TOF) mass spectrometer in Wiley-McLaren configuration.[171] Both UV laser beams overlap spatially and temporarily.

Resonant two-photon ionization (R2PI) spectra are recorded by scanning the frequency of the excitation laser between 35800 and 36600 cm^{-1}, while the ionization laser is kept at a constant wavelength (312.5, 318.0, 325.0, or 330.0 nm). The two-colour scheme minimizes excess energy in the ions and reduces fragmentation after ionization. By change of the ionization laser wavelength, the extent of fragmentation can be estimated.

For the IR-UV double resonance experiments, a pulsed IR laser beam (burn laser) is aligned collinear to the UV excitation beam (probe laser). The burn pulse crosses the molecular beam 100 ns before the probe pulse. The UV excitation laser is kept at a frequency resonant with a $S_1 \leftarrow S_0$ vibronic transition of a single cluster isomer. The IR laser frequency is scanned over the whole spectral range in which the vibrational transitions of interest are located. If the IR frequency is resonant, the vibrational ground state population is removed, leading to a decrease in resonant UV absorption. By monitoring the ion mass signal as a function of IR frequency, we obtain cluster mass and isomer selective infrared spectra, detected as ion dips. IR laser light is generated by a two-stage setup[130] with an optical parametric oscillator (OPO) and an optical parametric amplifier (OPA), producing infrared radiation between 2800 and 4000 cm^{-1} (10 Hz, > 5 mJ/pulse, line width < 0.1 cm^{-1}). The narrow line width of the IR light is mainly attained by an injection seeded Nd:YAG pump laser (Spectra Physics Pro 230, linewidth $< 3 \cdot 10^{-3}$ cm^{-1}) and the resonator configuration of the OPO stage. In the grazing-incidence grating OPO setup, light of zero-order diffraction is coupled out, whereas first-order diffraction is retroreflected to the rotatable KTP crystal by a mirror.[130] Hence, the multiple pass of light through the crystal enables a decrease of the spectral line width by the factor of ~ 40 compared to the former setup. For identification of the cluster specific UV absorption frequencies the IR-UV double resonance experiment was reversed. The IR laser was kept fixed at the specific vibrational transition while the UV excitation laser was scanned. The recorded spectrum was then subtracted from the R2PI spectrum without IR irradiation. The remaining bands of the difference spectrum indicate the cluster specific UV absorptions.

6.3.2 Dispersed Fluorescence

The experimental setup for dispersed fluorescence (DF) spectroscopy is described in detail elsewhere.[131, 132]

The output of a Nd:YAG-laser (Innolas, SpitLight 600) pumped dye laser (Lambda Physics, FL3002) is frequency doubled (532 nm, 120-140 mJ) and crosses the molecular beam perpendicularly.

For the molecular beam, a gas mixture of acetylene (2.5%) in helium was led over a sample of solid phenol at room temperature and then expanded through a pulsed nozzle with a 300 μm orifice into high vacuum.

The fluorescence light is imaged on the 30 μm entrance slit of a 1 m monochromator (JobinYvon, grating with 2400 grooves/mm blazed at 400 nm for first and second order). The dispersed fluorescence is recorded by an intensified CCD camera (Flamestar II, La Vision). Each dispersed fluorescence spectrum was obtained by summing the signal of 200 laser pulses and by subtracting the background that emerges from scattered light. The final DF spectra are averaged over 50-100 single spectra to obtain a better signal-to-noise ratio. This scheme allows imaging a DF spectrum with a spectral range of ~ 300 cm^{-1} in second grating order with a resolution of 2 cm^{-1}.

6.3.3 Quantum Chemical Calculations

Starting geometries for the different cluster isomers were generated randomly from their monomeric units by a custom-made random structure generator and preoptimized using the MOPAC 2009 program.[57] The RI-MP2 and DFT-D calculations on the most promising isomers were performed with the TURBOMOLEV5.10 program package.[55] Ten different starting structures were used for the PhA_2, PhA_3, and Ph_2A_1 clusters, but only a few of those are shown in this paper, as they either converged to the same optimized geometries or showed very high energies of more than 10 $kJ \cdot mol^{-1}$ above the minimum energy structures.

Calculated harmonic frequencies of PhA_1 were scaled with a factor that matches the frequency of the OH stretching vibration of the phenol monomer calculated at the same level of theory with its experimentally observed frequency (0.975 for b97-d/TZVPP and 0.95 for mp2/TZVPP).

The calculated frequencies of the larger clusters were scaled to match the experimental absorption frequencies of selected vibrations in PhA_1 . We used 0.9767 (b97-d/TZVPP) and 0.953 (mp2/TZVPP) for the antisymmetric CH stretching vibrations of the acetylene moieties at $3245 - 3276$ cm^{-1} and 0.9761 (b97-d/TZVPP) and 0.955 (mp2/TZVPP) for the O–H stretching vibration of the phenol moiety at $3536 - 3584$ cm^{-1}. The frequencies of the intermolecular vibrations are given unscaled due to absence of a marker band in this spectral region.

6.4 Results

6.4.1 R2PI Spectra

Figure 6.1 shows the two-colour resonance-enhanced R2PI spectra on different mass channels at an ionization wavelength of 318 nm. The assignment of the UV resonance frequencies to clusters of specific size is somewhat complicated by cluster fragmentation; however, at longer ionization wavelengths like 318 nm the cluster spectra are generally identifiable at their parent masses. The R2PI spectrum obtained at the Ph_2A mass channel (not shown here) is broad with no discernible structure; however, we were able to get an IR-UV spectrum in the range of the OH and acetylene CH stretch vibrations, Figure 6.8.

6.4.2 PhA_1

Figure 2 shows the IR-UV double resonance spectrum of PhA_1 obtained at the PhA_1 mass channel with the UV excitation laser tuned to $Ph(0^0_0) - 245.9$ cm^{-1}, Figure 6.1. Also shown are the scaled IR stick spectra of possible isomers at the DFT/b97-d/TZVPP (black lines) and mp2/TZVPP (black dashed lines) levels of theory. Relative cluster energies ΔE refer to the most stable structure.

Structure A shows the best agreement between calculated and experimental IR spectra in agreement with ref.[16] . Their assignment was based only on the phenolic OH stretch vibrational frequency and our additional measurement of the antisymmetric CH stretch vibration of acetylene endows further safety to the assignment. The OH stretching vibration at 3584 cm^{-1} is shifted by -68 cm^{-1} relative to the corresponding phenol vibration at 3652 cm^{-1} again in agreement with the results of Fujii et al.[16] Such a rather small red shift can be expected for a weak $OH \cdots \pi$ hydrogen bond. The acetylene CH stretch vibration in PhA_1 is shifted by -12 cm^{-1} relative to bare acetylene. This very small

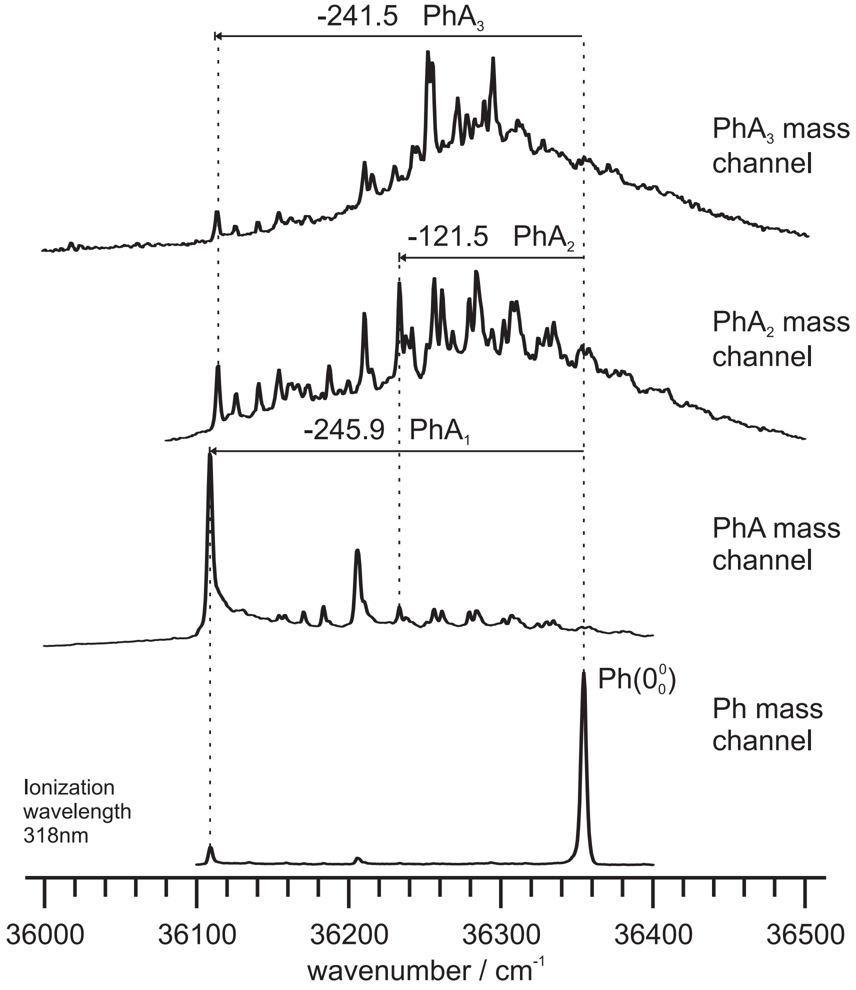

Figure 6.1: Mass resolved two-colour R2PI spectra of phenol (Ph)–acetylene (A) clusters PhA$_n$ and assignment to aggregates of specific size. Spectral shifts are related to the 0^0_0 band of phenol at 36348.7 cm^{-1}.[30, 168] Ionization of the electronically excited clusters was performed at 318 nm.

red shift results from withdrawal of electron density from the C≡C triple bond leading to a somewhat smaller force constant of the CH antisymmetric stretch vibration. Indeed structure A exhibits hydrogen bonding between the OH group and the C≡C bond with a perpendicular alignment of phenol and acetylene. The mp2/TZVPP frequencies do not agree as well with the experiment as the DFT/b97-d/TZVPP frequencies probably due to overestimation of the OH$\cdots\pi$ interaction strength leading to too low stretch frequencies.

Figure 6.3 reveals the DF spectrum of PhA$_1$(a) obtained upon excitation of the electronic origin of PhA$_1$ at Ph(0^0_0) − 245.9 cm^{-1} in the far-infrared spectral region below 200 cm^{-1}. In the cluster, new bands appear which are absent in the phenol monomer spectrum. They can be assigned to intermolecular vibrations and appear also as combination bands with the vibrations of the phenol moiety in the region above 400 cm^{-1}(not shown here).

Table 6.1 shows the measured intermolecular vibrational frequencies in comparison with the unscaled calculated vibrations.The agreement is not good probably due to strong anharmonicity of the intermolecular potential and the assignment can be made only very preliminary based merely on the calculated frequency order of the hindered translations

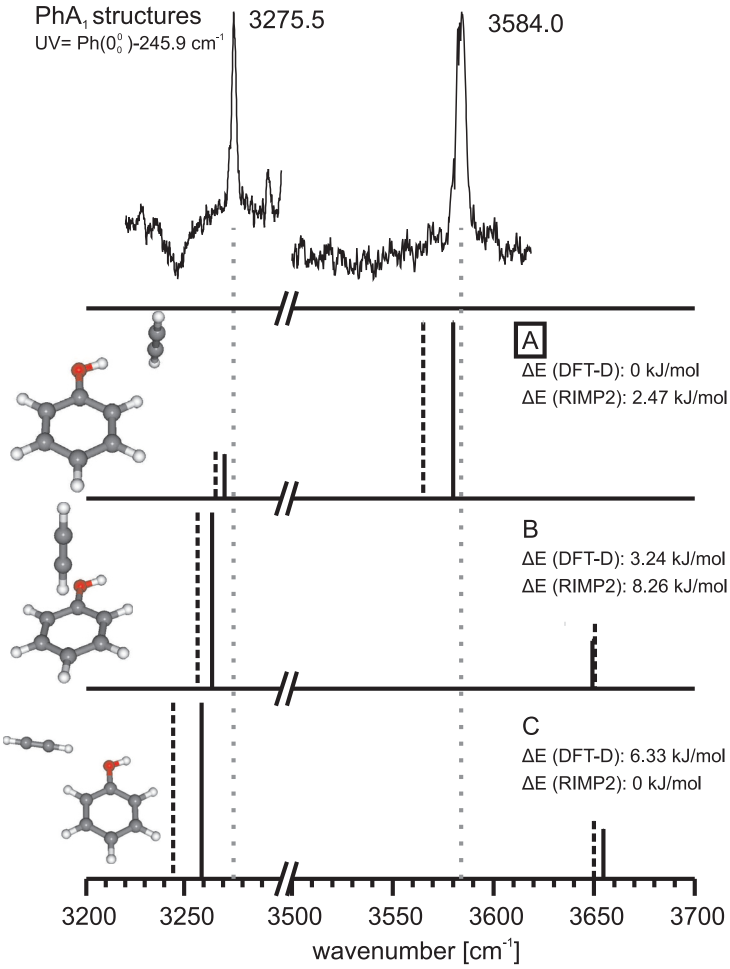

Figure 6.2: IR-UV double resonance spectrum of PhA$_1$ obtained on the PhA$_1$ mass channel with the UV excitation laser tuned to Ph(0_0^0) − 245.9 cm^{-1}. Also shown are the calculated and scaled stick spectra of possible isomers at the b97-d/TZVPP (black lines) and mp2/TZVPP (black dashed lines) levels of theory and the corresponding cluster structures. Relative cluster energies ΔE refer to the most stable structure. The assigned structure A is labelled with a square.

T_x, T_y, and T_z and hindered rotations R_y and R_z, Figure 6.4.

6.4.3 PhA$_2$

Figure 6.5 shows the IR-UV double resonance spectrum of PhA$_2$ obtained with the UV excitation laser tuned to Ph(0_0^0) − 121.5 cm^{-1} and recorded on the PhA$_2$ mass channel; see also Figure 6.1. Also shown are the calculated and scaled stick spectra of the most stable isomers at the b97-d/TZVPP (continuous lines) and mp2/TZVPP (dashed lines) levels of theory. Vibrational assignments to the antisymmetric CH stretching vibration of the acetylene moieties are colour coded: red and blue indicate the different acetylene stretch vibrations as marked in the cluster structures, green indicates coupled acetylene stretch vibrations. The black lines belong to the OH stretch vibration of the phenol moiety.

The comparison between experiment and theory exhibits that the calculated spectra of isomers A and B are candidates for the observed vibrational spectrum. Structures C and D have nearly free OH stretch vibrations, and their frequencies are therefore quite high

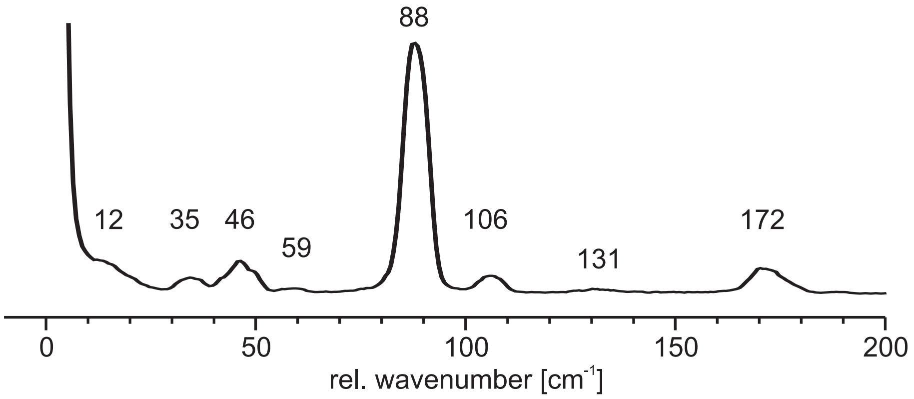

Figure 6.3: Dispersed fluorescence spectrum of phenol–acetylene obtained upon excitation at the PhA_1 electronic origin at $Ph(0^0_0) - 245.9$ cm^{-1}. The spectrum is measured in second grating order. The frequencies of the cluster bands are indicated.

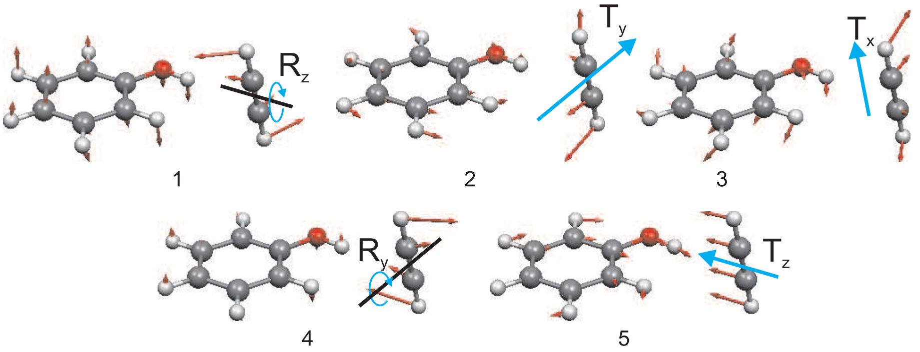

Figure 6.4: Intermolecular vibrations of PhA_1 calculated at the b97d/TZVPP level of theory. The vibrational displacement vectors are created with Molekel 4.3.[161] The intermolecular vibrations arise from hindered rotations and translations along the three spatial axis x, y, z. Cluster formation leads to omission of the corresponding monomer rotations and translations and emergence of these motions as hindered vibrations. At this level of calculation the hindered motions are mixed to some extent; e.g., T_x has some rotational contribution.

and not in agreement with the experiment. It is interesting that structure D is very low in energy on the RIMP2/TZVPP level of theory (even below structure A). This is most likely due to the two σ-hydrogen bonds CH$\cdots$O, which are preferred to π-H interactions on this level of theory. For structure A the OH stretch vibration matches nearly perfect with experiment whereas for structure B the CH stretch vibrations match best. However, as shown in ref [15] for the most stable benzene–(acetylene)$_2$ isomer, which is structurally very similar to isomer A, the calculations overestimate the spacing of the CH stretch vibrations in this compact ring like structure. Another indicator is the very small red shift (7 cm^{-1}) of the OH stretching vibration upon the addition of the second acetylene in both experiment and theory. If both acetylenes would bind to the OH-group, a larger red shift of the OH stretch vibration can be expected. Thus we prefer assignment of structure A.

Table 6.1: Assignment of the Low Frequency Bands of PhA_1 [a]

experiment	assignment	calculated	
		RIMP2	DFT-D
12	1	26.1	27.8
35	2	52.3	40.9
46	3	53.2	43.8
59	$3 + 1$	79.3	71.6
88	4	100.5	99.6
106	5	107.2	111.1
131	$4 + 3$	152.7	140.5
172	4^2	26.1	27.8

[a] Frequencies are given in cm^{-1}.
The calculated frequencies are unscaled.

Figure 6.6 shows the dispersed fluorescence spectrum of PhA_2 measured at the same electronic resonance as the IR-UV spectrum in Figure 6.5.

Our very preliminary assignment of the observed DF features in the low frequency range to the intermolecular vibrations of isomer A of PhA_2 is shown in Table 6.2.

Table 6.2: Assignment of the Low Frequency Vibrations of PhA_2 from the Spectrum Displayed in Figure 6.6[a]

experiment	assignment	calculated	
		RIMP2	DFT-D
44	1	35.37	39.90
73	2,3	60.85[b]	59.95[b]
87	4	77.46	78.20
105	5,6,7	90.41[b]	90.80[b]
116	8	106.51	114.40
142	9	136.33	134.20
160	10	164.32	164.00
174	4^3	154.92	156.40
188	$4 + (5, 6, 7)$	167.87	169.00
204	$4 + 8$	183.97	192.6

[a] Frequencies are given in cm^{-1} and unscaled.
[b] arithmetic average of calculated frequencies
that differ by 5 cm^{-1} or less.
They are marked by commas in the assignment

Because three translational and two rotational degrees of freedom from two acetylene monomers are transferred into vibrational modes of the cluster, ten new intermolecular vibrations are expected. However, some of these vibrations have similar frequencies at our levels of theory, so only seven vibrational modes are expected to be distinguishable

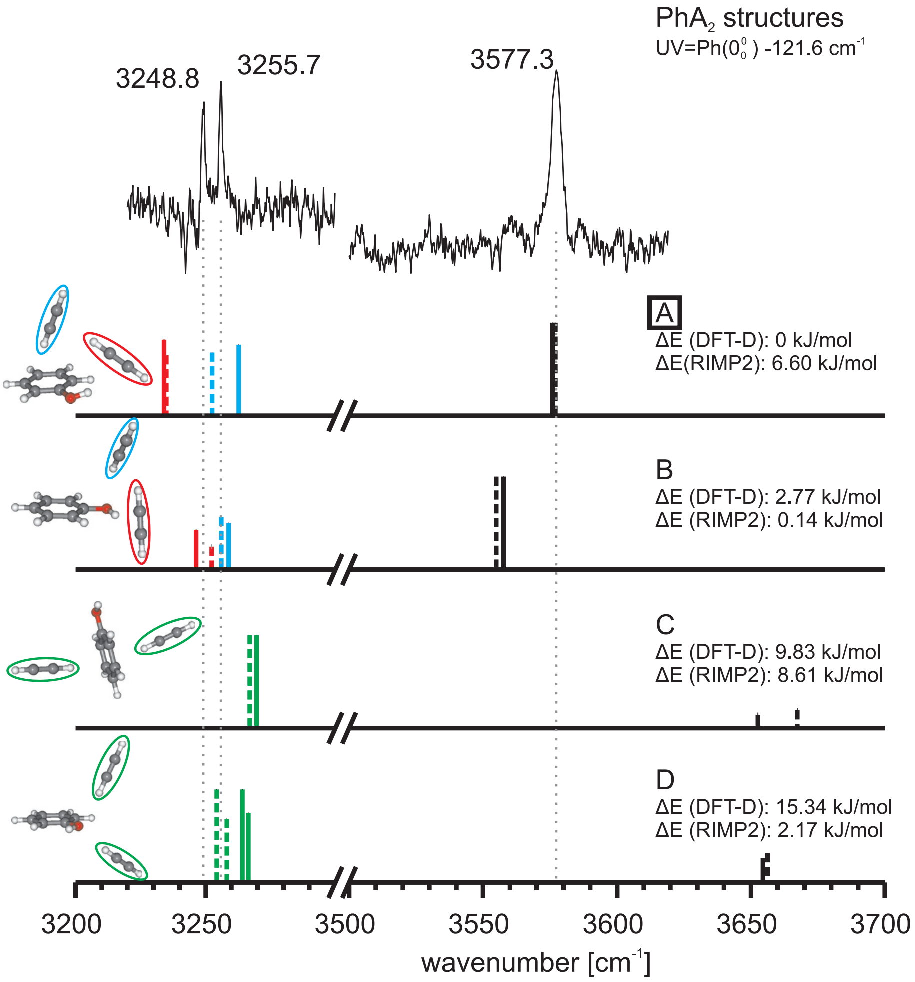

Figure 6.5: IR-UV double resonance spectrum of PhA_2 obtained with the UV excitation laser tuned to $Ph(0^0_0) - 121.6$ cm^{-1} on the PhA_2 mass channel. Also shown are the calculated and scaled stick spectra of possible isomers at the b97-d/TZVPP (black lines) and mp2/TZVPP (black dashed lines) levels of theory and the most stable cluster structures. Relative cluster energies ΔE refer to the most stable structure at the different levels of theory. Vibrational assignments are colour coded; see text.

in the experimental spectrum, Table 6.2. The agreement between DF experiment and theory is again not very good; however, structure A shows a somewhat better match than structure B. The calculated frequencies of both structures and a graphical depiction of their intermolecular vibrations are given as Supporting Information.

6.4.4 PhA_3

Figure 6.7 shows the IR-UV double resonance spectrum of PhA_3 recorded on the PhA_2 mass channel with the UV excitation laser tuned to $Ph(0^0_0) - 241.5$ cm^{-1} and the calculated structures and vibrational spectra of the most stable isomers.

The OH stretch vibration at 3561.8 cm^{-1} shows a further red shift compared to PhA_2

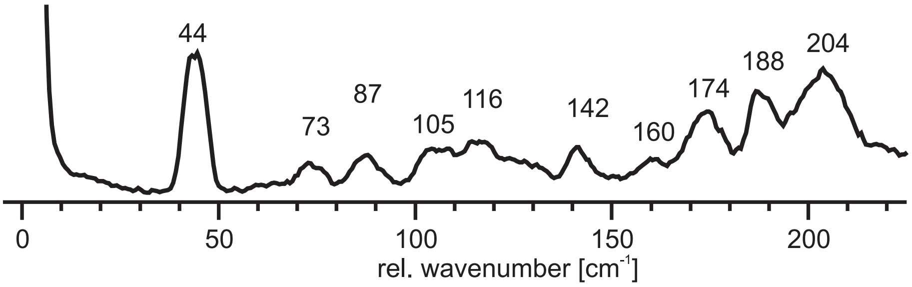

Figure 6.6: Dispersed fluorescence spectrum of PhA_2, measured at $Ph(0_0^0)$ − 121.6 cm^{-1} in second grating order. The labelled bands are from intermolecular vibrations and not visible in the phenol monomer DF spectrum.

(3577.3 cm^{-1}) and PhA_1 (3584.0 cm^{-1}). The OH bond is obviously weakened as more acetylene molecules are attached to the phenol moiety and this leads to a lower force constant for this vibration and to a lower frequency. Because the reduced mass of this almost local OH stretch vibration remains nearly constant independent of cluster size. Three antisymmetric CH stretch vibrations are observed as expected for a cluster with three acetylene molecules with frequencies at 3250.5 and closely spaced at 3253.7 and 3255.9 cm^{-1}. Only one CH stretch vibration per acetylene molecule is IR allowed because only the dipole moment of the antisymmetric CH stretch vibration changes during the vibrational motion and not the dipole of the symmetric stretch vibration. The same vibrational spectrum was recorded on the PhA_3 mass channel at phenol $0_0^0 - 241.5$ cm^{-1}. Here the R2PI band is smaller than on the PhA_2 mass due to strong fragmentation of PhA_3 to PhA_2 even under soft two-colour ionization conditions, Figure 6.1. Correspondingly the IR induced ion dips are smaller on the parent mass of PhA_3.

The calculated structures of isomers A, B, and C are similar and possibly linked by dynamic rearrangement with only small energy barriers. We therefore group these probably floppy structures to one family of isomers to which the observed vibrational spectrum can be assigned. The assignment is, however, not as safe as for PhA_1 and PhA_2.

6.4.5 Ph_2A_1

Figure 6.8 shows the IR-UV double resonance spectrum of Ph_2A_1 obtained with the UV excitation laser tuned to $Ph(0_0^0) - 61$ cm^{-1} and recorded on the Ph_2 mass channel. Also shown are the scaled vibrational stick spectra of the most stable isomers at the b97-d/TZVPP (continuous lines) and mp2/TZVPP (dashed lines) levels of theory. The same IR bands were observed on the Ph_2A_1 mass channel; however, depending on excitation wavelength more than 2 OH stretch vibrations were discernible. This points to contributions of larger phenol–acetylene clusters to the broad R2PI spectrum on the Ph_2A_1 mass

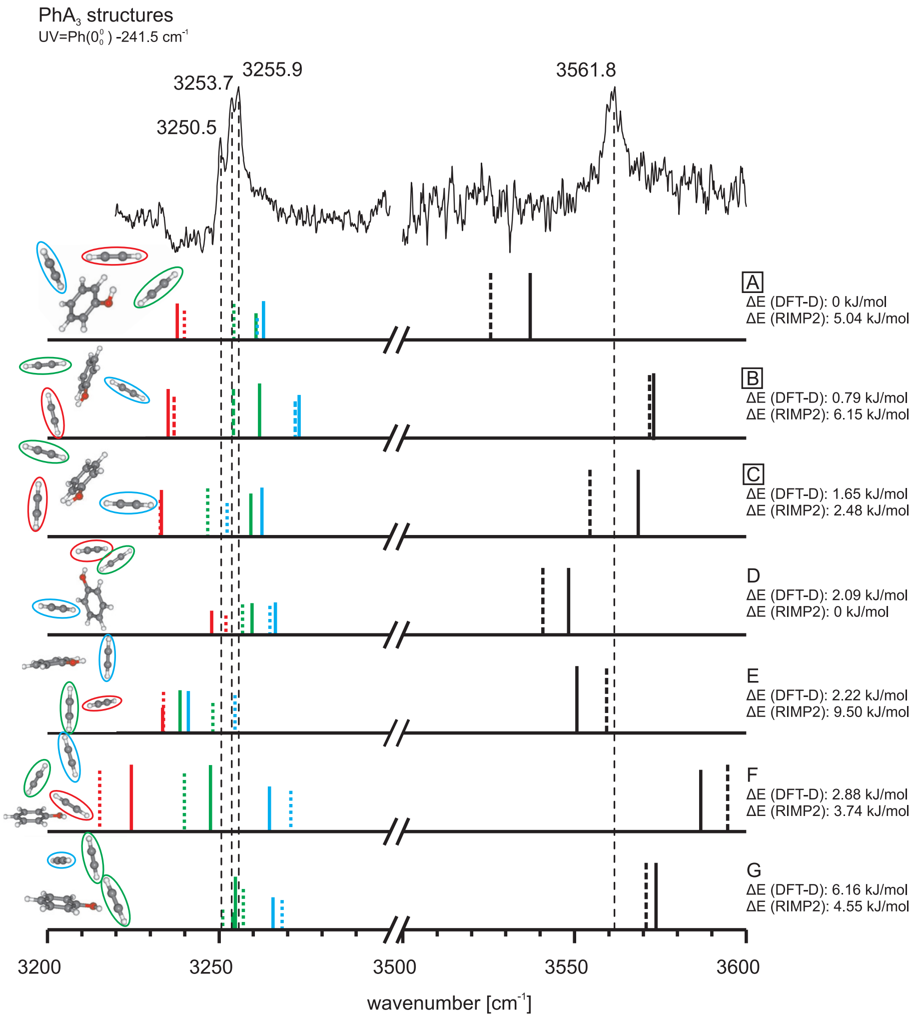

Figure 6.7: IR-UV double resonance spectrum of PhA$_3$ obtained with the UV excitation laser tuned to phenol $0^0_0 - 241.5$ cm^{-1} and recorded on the PhA$_2$ mass channel. Also shown are the scaled stick spectra of selected isomers ($\Delta E < 10$ kJ $\cdot$ mol^{-1} on either level of theory) calculated at the b97-d/TZVPP (continuous lines) and mp2/TZVPP (broken lines) levels of theory. Vibrational assignments to the asymmetric CH stretch vibration of the acetylene moieties are colour coded.

that arise from easy fragmentation of larger cluster ions. We therefore preferred to take the IR dip spectra on the Ph$_2$ mass where contributions of fragmentation are smaller. Superimposed on the sharp IR dip of the R2PI signal at 3244.3 cm^{-1} is a broad IR induced rise of the R2PI signal with a maximum at about 3250 cm^{-1}, which we ascribe to IR dissociation of larger clusters to Ph$_2$ leading to more ion signal at Ph$_2$ mass channel.

The calculated structures of isomers A and C are very similar and probably linked by dynamic rearrangement. The vibrational spectra of this cluster family with OH$\cdots$O σ-hydrogen bond and OH$\cdots$C≡C and CH$\cdots$phenyl π-hydrogen bonds show the best agreement with the experimental IR spectrum. This assignment is supported by the results of Hartland et al. for the phenol dimer, with the two OH stretch vibrations at ∼

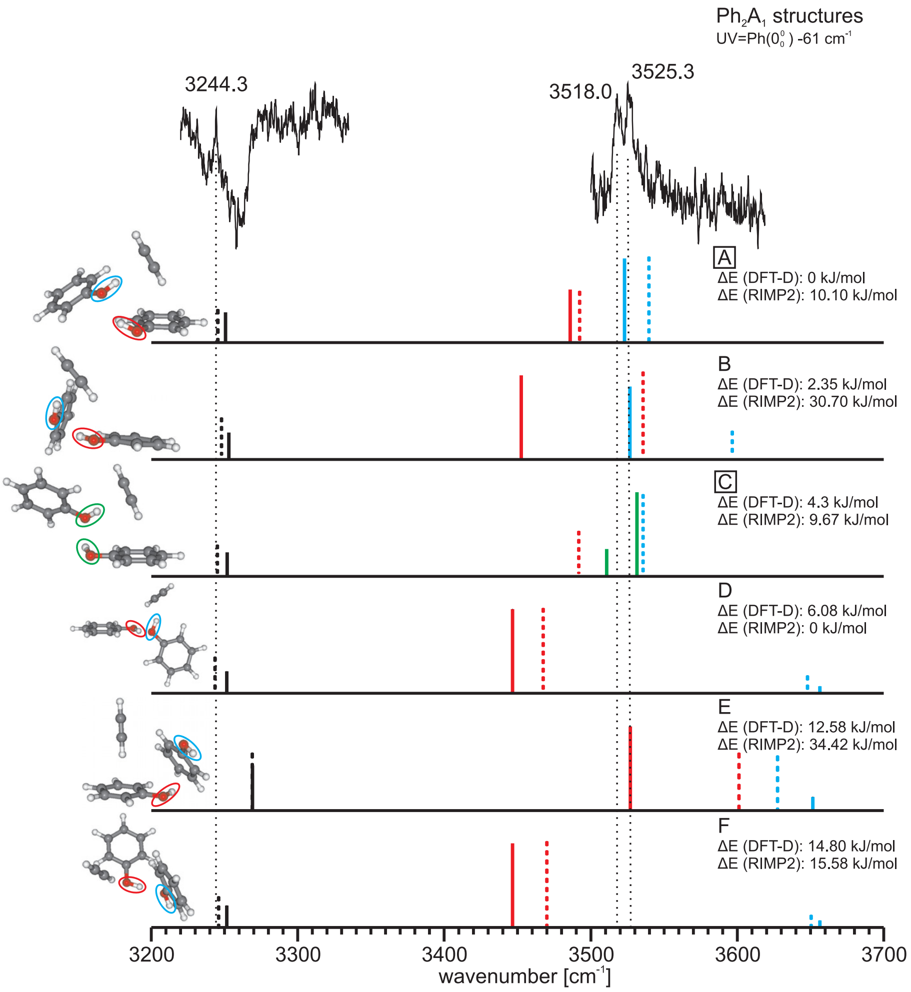

Figure 6.8: IR-UV double resonance spectrum of Ph_2A_1 obtained with the UV excitation laser tuned to $Ph(0-0^0)-61$ cm^{-1} and recorded on the Ph_2 mass channel. Also shown are the scaled stick spectra of the most stable isomers calculated at the b97-d/TZVPP (continuous lines) and mp2/TZVPP (broken lines) levels of theory.

3530 cm^{-1} (proton-donating phenol) and at ∼ 3653 cm^{-1} (proton-accepting phenol).[172] The observed strong red-shift (∼ 130 cm^{-1}) of the acceptor ν_{OH} in Ph_2A points to a $OH\cdots C{\equiv}C$ hydrogen bond, whereas $CH\cdots\pi$ and $CH\cdots O$ interactions like in structure E and F lead only to a minor shift of the free ν_{OH}. Structures B and D are very similar and their OH stretch frequencies are not in agreement with experiment.

6.5 Discussion

The discovered cluster structures support a stepwise aggregation kinetics as already observed for benzene–acetylene clusters.[15, 167] PhA_n clusters are formed kinetically by successive attachment of acetylene molecules to an already existing PhA_{n-1} cluster, rather than by first forming an acetylene homo cluster (A_n) and attaching it to a phenol molecule.

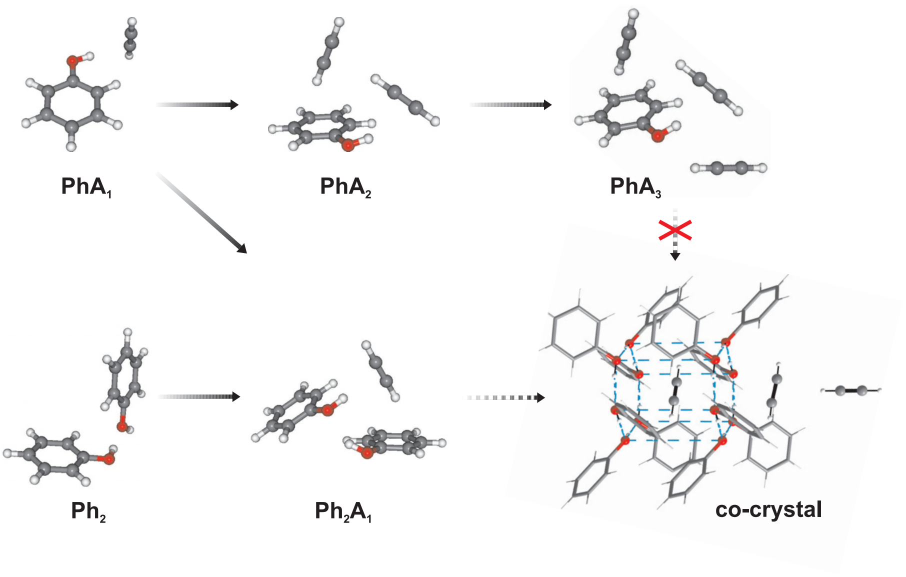

Figure 6.9: Postulated aggregation pathway of the phenol–acetylene clusters based on the assigned structures that were observed in supersonic jets.

Figure 6.9 depicts a possible aggregation pathway.

It is interesting to compare the structures of the nanoclusters with the structure of the macroscopic cocrystal of phenol with acetylene obtained by freeze desalination of the corresponding gases.[162] According to the X-ray structure analysis of the cocrystal by Kirchner, Boese, et al.[162] six phenol molecules are connected by OH$\cdots$O hydrogen bridges into a hexagonal ring system. Two of the ring systems are linked by phenolic CH-π interaction into a ”‘hexagonal prism”’. These prisms of 12 phenol molecules are hexagonal closed packed in the cocrystal.[162] Within the prism one disordered molecule of acetylene is enclathered whereas an acetylene dimer with perpendicular A–A orientation connects the prisms. The free distances between the phenol oxygen atoms in the prism and between the prisms are too short for a hydrogen bridge with A respectively A$_2$. Hence the strong phenol–phenol hydrogen bonds and edge-to-face phenyl interactions dominate the crystal structure and prevent phenol–acetylene hydrogen bonds.[162] In contrast, the nanocluster structures are dominated by phenol–acetylene hydrogen bonds leading to compact (often ring-like) arrangements. A slight hint of a development toward the cocrystal structure is observed in Ph$_2$A whose structure is composed of the phenol dimer with OH$\cdots$O hydrogen bond and edge-to-face phenyl interaction and an attached acetylene. From this structure it can be expected that the larger phenol clusters form rings similarly to water clusters[173, 174] because these are the most compact arrangements with maximum number of OH$\cdots$O hydrogen bonds. Acetylene then attaches to single rings and condensed rings via CH$\cdots\pi$ or CH$\cdots$O interaction if there is enough free space in the nanocluster or simply form clathrates if not.

Associated Content

Ⓢ Supporting Information

Graphical depiction of the intermolecular vibrations of the assigned PhA_2 structure A and calculated frequencies of the not assigned structure PhA_2 B in addition to Table 6.2. This information is available free of charge via the Internet at http://pubs.acs.org

6.6 Acknowledgements

The authors thank the Deutsche Forschungsgemeinschaft for financial support (FOR 618-TPE Kl 531/28-2), Prof. Dr. Roland Boese and Dr. Michael Kirchner for providing structural data of the cocrystal, and Dr. Thomas Häber for creation of the random structure generator.

6.7 Supplementary Information

Table 6.3: calculated frequencies of structures A and B of PhA_2 in the region of the intermolecular vibrations.

Mode	Isomer A		Isomer B	
	RIMP2	DFT-D	RIMP2	DFT-D
1	35.37	39.87	19.94	16.15
2	58.48	57.13	24.32	31.49
3	63.22	62.75	56.60	43.82
4	77.46	78.16	64.68	66.01
5	81.44	88.51	70.80	70.43
6	92.40	90.40	76.76	77.33
7	97.95	93.54	101.39	93.98
8	106.51	114.44	108.41	107.86
9	136.33	134.22	121.03	111.50
10	164.32	164.00	147.67	156.85

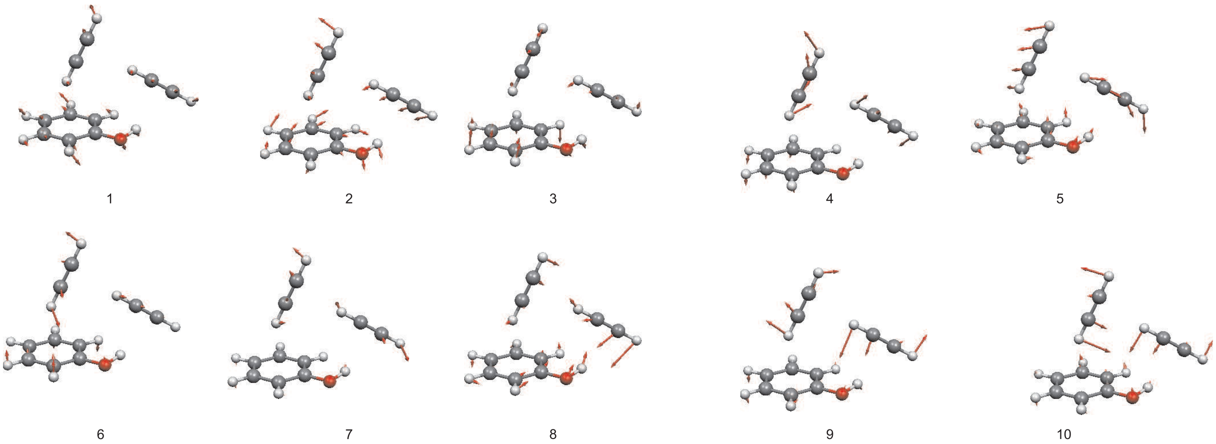

Figure 6.10: Intermolecular vibrations of the assigned structure A of PhA_2 calculated at the b97-d/TZVPP level of theory. The vibrational displacement vectors are created with Molekel 4.3[161]. The hindered rotations and translations are coupled to a large degree at this level of theory.

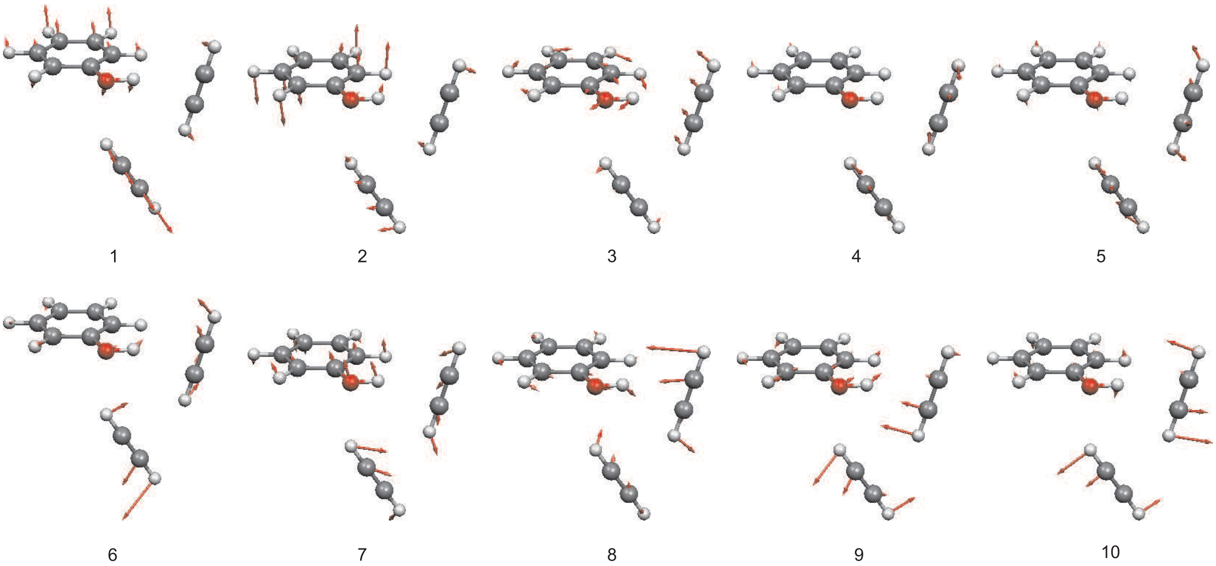

Figure 6.11: Intermolecular vibrations of structure B of PhA_2 calculated at the b97-d/TZVPP level of theory. The vibrational displacement vectors are created with Molekel 4.3[161]. The hindered rotations and translations couple to a large degree at this level of theory.

6.8 Contributions

Title: Isomer-Selective Vibrational Spectroscopy of Jet-Cooled Phenol-Acetylene Aggregates.

Authors: Markus Böning, Benjamin Stuhlmann, Gernot Engler, and Karl Kleinermanns.

submitted to: The Journal of physical Chemistry A (Impact Factor: 2.946)

The R2PI and IR-UV double resonance spectra in this paper were measured by Markus Böning and Gernot Engler with the improved setup first described in Chapter 5.3.

I recorded the dispersed fluorescence spectra and carried out the quantum chemical calculations on the RI-MP2/TZVPP and b97-d/TZVPP levels of theory. Parts of this work are also covered in the bachelor thesis of Christoph Rumancev, which was carried out under my supervision.

The well-arranged picture of the Phenol–Acetylene cocrystal in Figure 6.9 was made by Vivian Verheyen.

7. Determination of the Geometry Change of 5-Cyanoindole upon Electronic Excitation from a Combined Franck-Condon/Rotational Constants Fit.†

Benjamin Stuhlmann, Anne Gräßle, and Michael Schmitt*[1]

PCCP **2014**, *16(3)*, 899-905, doi: 10.1039/C3CP51795K

7.1 Abstract

The geometry change of 5-Cyanoindole upon electronic excitation from the ground to the lowest excited singlet state has been determined from a combined fit of the rotational constant changes upon excitation and the vibronic intensities in various fluorescence emission spectra using the Franck-Condon principle. The so determined geometry change is compared to the results of *ab initio* calculations and points to an excited state geometry, which is L_a-like in the nomenclature of Platt. A mode selective coupling of vibronic bands to higher-lying excited states is discussed on the basis of Herzberg-Teller contributions to the Frank-Condon intensities.

---

[1] Heinrich-Heine Universität, Institut für Physikalische Chemie I, D-40225 Düsseldorf, Germany. E-mail: mschmitt@uni-duesseldorf.de; Fax: +49 211 8115195; Tel: +49 211 8112100

[1] † Electronic Supplementary Information (ESI) available. See DOI: 10.1039/c3cp51795k

7.2 Introduction

The electronic nature of electronically excited singlet states of substituted indoles has found considerable interest over the last decades. Most of the studies, which have been performed to unravel the electronic nature of the lowest excited state, rely on methods that determine directly or indirectly the orientation of the transition dipole moment, like two-photon-induced fluorescence anisotropy experiments,[175], two-photon excitation spectroscopy,[176] linear dichroism spectra of partially oriented indole in stretched polyethylene films,[177] and rotationally resolved spectroscopy.[178, 179] A different method, which we present here, utilizes the Franck-Condon (FC) factors, in order to determine the geometry changes upon electronic excitation to the state of interest. Comparison of the experimental findings to the results of *ab initio* structure optimizations of the various excited states facilitates the determination of the electronic nature of the excited state. According to the FC principle the probability of a vibronic transition and thus the relative intensity of a vibronic band depends on the overlap integral of the vibrational wave functions of both electronic states. This overlap integral is determined by the relative shift of the two potential energy curves connected by the vibronic transition along the normal coordinates Q of both states. Thus, via comparison of measured intensity patterns to the calculated FC factors, the structural change upon electronic excitation can be deduced. Even though the FC principle does not allow for an independent determination of the geometric structure in each of the states, it allows to enumerate geometry *changes* upon electronic excitation.

Most of the substituted indoles, like indole itself have the L_b state as lowest electronically excited state. In some substituted indoles, the $^1L_a/^1L_b$ gap is so small, that complex formation with polar molecules like water stabilizes the more polar L_a state so much, that it becomes the lowest electronically excited state. The same effect can be obtained by the introduction of strongly electron withdrawing substituents (like the cyano group) in the 5-position of the chromophore or by electron donating groups (like methyl groups) in 2 and/or 3-position. Up to now, two substituted indoles have been described in which the L_a state is shifted below the L_b state: 5-Cyanoindole[180] and the 2,3-bridged indole derivative tetrahydrocarbazole. [181]

Very few studies of isolated 5-cyanoindole (5CI) in the gas phase have been reported until now. The spectral position and lifetime of the electronic origin of 5CI were determined by Huang and Sulkes using time-correlated single photon counting in a supersonic free jet expansion.[182] Oeltermann *et al.* deduced the structure of 5-cyanoindole in the ground and the lowest electronically excited singlet states from rotationally resolved electronic spectroscopy.[180] Higher vibronic bands of 5CI have been studied by Brand *et* *al.*[183] While previous studies concentrated on the geometric structures in the different electronic states and the nature of the excited states, we seek to understand the coupling to other electronically excited states in the present contribution.

7.3 Experimental and Computational Details

7.3.1 Experiment

The experimental setup for the dispersed fluorescence (DF) spectroscopy has been described in detail elsewhere [131, 132]. In brief, 5-cyanoindole was evaporated at 393 K and co-expanded through a pulsed nozzle with a 500 μm orifice (General Valve) into the vacuum chamber using Helium as carrier gas. The output of a Nd:YAG (Innolas SpitLight 600) pumped dye laser (Lambda-Physik, FL3002) was frequency doubled and crossed at right angles with the molecular beam. The resulting fluorescence was imaged on the entrance slit of a f = 1 m monochromator (Jobin Yvon, grating 2400 lines/mm blazed at 400 nm in first order). The dispersed fluorescence spectrum was recorded using a gated image intensified UV sensitive CCD camera (Flamestar II, LaVision). One image on the CCD chip spectrally covers approximately 600 cm^{-1}. Since the whole spectrum is taken on a shot-to-shot basis, the relative intensities in the DF spectra do not vary with the laser power. The relative intensities are afterwards normalized to the strongest band in the spectrum different from the resonance fluorescence band, which also contains the stray light and is therefore excluded from the FC analysis.

7.3.2 *Ab initio* calculations

Structure optimizations were performed employing Dunning's correlation consistent polarized valence triple zeta basis set (cc-pVTZ) from the TURBOMOLE library. [55, 59] The equilibrium geometries of the electronic ground and the lowest excited singlet states were optimized using the approximate coupled cluster singles and doubles model (CC2) employing the resolution-of-the-identity approximation (RI).[71, 73, 74] Spin-component scaling (SCS) modifications to CC2 were taken into account.[72] The Hessians and harmonic vibrational frequencies for both electronic states, which are utilized in the FC fit have been obtained from numerical second derivatives using the NumForce script [184] implemented in the TURBOMOLE program suite. [29]

7.3.3 Franck-Condon fit of the structural change

The change of a molecular geometry upon electronic excitation can be determined from the intensities of absorption or emission bands using the FC principle. According to the FC principle the relative intensity of a vibronic band depends on the overlap integral of the vibrational wave functions of both electronic states. The transition dipole moment for a transition between an initial electronic state $|m, v\rangle$ and a final electronic state $|n, w\rangle$ is defined as:

$$M_{vw} = \langle v \,|\, \mu_{mn}(Q) \,|\, w\rangle \tag{7.1}$$

with the electronic transition dipole moment $\mu_{mn}(Q)$:

$$\mu_{mn}(Q) = \langle \Psi_m \,|\, \mu \,|\, \Psi_n\rangle \,; \;\; \mu = \sum_g e r_g \tag{7.2}$$

where r_g is the position vector of the gth electron. The dependence of the electronic transition dipole moment μ_{mn} from the nuclear coordinates can be approximated by expanding μ_{mn} in a Taylor series about the equilibrium position at Q_0. The series is truncated after the first term in the FC approximation.

The fit has been performed using the program FCFit, which has been developed in our group and described in detail before.[28, 185] The program computes the FC integrals of multidimensional, harmonic oscillators mainly based on the recursion formula given in the papers of Doktorov, Malkin, and Man'ko.[47, 83] and fits the geometry (in linear combinations of selected normal modes) to the experimentally determined intensities. This is simultaneously done for all emission spectra, which are obtained via pumping through different S_1 vibronic modes.

The vibrational modes of the electronically excited state can be expressed in terms of the ground state modes using the following linear orthogonal transformation, first given by Duschinsky[46]:

$$Q' = SQ'' + d \tag{7.3}$$

where Q' and Q'' are the N-dimensional vectors of the normal modes of excited and ground state, respectively, S is a N x N rotation matrix (the Duschinsky matrix) and d is an N-dimensional vector which displaces the normal coordinates.

The fit of the geometry to the intensities in the vibronic spectra can greatly be improved if independent information for the geometry changes upon electronic excitation is available. This additional information is the change of the rotational constants upon electronic excitation, which can be obtained from rotationally resolved electronic spectroscopy. While geometry fits to the rotational constants (mostly of several isotopologues) are routinely performed using non-linear fits in internal coordinates, the combination of rotational constant changes and vibronic intensities allows for determination of many more geometry parameters.

7.3.4 Herzberg-Teller corrections to the FC analysis

Truncation of the expansion of μ_{mn} after the second expansion term and inserting into Equation 7.1 yields the transition dipole moment in the Franck-Condon-Herzberg-Teller (FCHT) approximation:

$$M_{vw} = \mu_{mn}(Q_0) \langle v \,|\, w \rangle + \sum_i \left(\frac{\partial \mu_{mn}}{\partial Q_i} \right)_{Q_0} \langle v \,|\, Q_i \,|\, w \rangle \tag{7.4}$$

For the evaluation of the Herzberg-Teller (HT) terms $\sum_i \left(\frac{\partial \mu_{mn}}{\partial Q_i} \right)_{Q_0} \langle v \,|\, Q_i \,|\, w \rangle$ in Equation 7.4 the partial derivatives of the transition dipole moment with respect to the normal modes must be calculated. These derivatives of μ_{mn} were determined numerically from DFT/MRCI calculations of the respective state using symmetric finite differences:

$$\left(\frac{\partial \mu_{mn}}{\partial Q_i} \right)_{Q_0} = \frac{\mu_{mn}\left(Q_0 + \Delta Q_i\right) - \mu_{mn}\left(Q_0 - \Delta Q_i\right)}{2 \Delta Q_i} \tag{7.5}$$

The integrals $\langle v \,|\, Q_i \,|\, w \rangle$ from the HT terms in Equation 7.4 can be calculated from the FC integrals using the following relation:

$$\langle v \,|\, Q_i \,|\, w \rangle = \sqrt{\frac{\hbar}{2\omega_i}} \left[\sqrt{w_i} \langle v \,|\, w_1, \ldots, (w_i - 1), \ldots, w_N \rangle \right. \tag{7.6}$$

$$\left. + \sqrt{w_i + 1} \langle v \,|\, w_1, \ldots, (w_i + 1), \ldots, w_N \rangle \right] \tag{7.7}$$

The procedure has been described in detail in Ref. [86]

7.4 Results

7.4.1 *Ab initio* calculations

The structure of 5CI in its ground and lowest excited singlet states has been determined from an optimization at the spin-component scaled second order coupled cluster (SCS-CC2) level of theory using the cc-pVTZ basis set. The atomic numbering for 5CI, used throughout this publication is shown in Figure 7.1. As we have shown in a recent publication on excited states of 5CI, [183] the use of spin-component scaling is mandatory for obtaining the correct order of electronically excited states in this molecule. The Cartesian coordinates of the optimized structures of 5CI in the S_0 and S_1 states are given in the online supplementary material. 5CI is planar in both electronic states and belongs to the point group C_s.

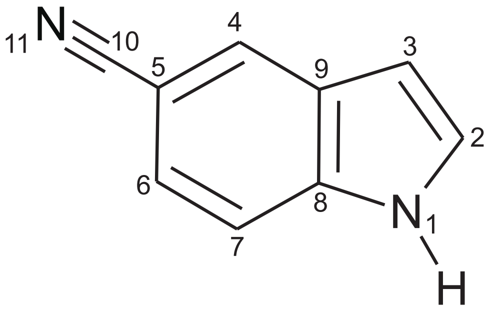

Figure 7.1: Atomic numbering of 5CI.

Based on the *ab initio* optimized structures, normal mode analyses of the ground and lowest excited singlet states have been performed at the level of optimization. 5CI has 17 atoms and 45 normal modes, of which 14 are of A″ symmetry and 31 of A′ symmetry. Table 7.1 summarizes the calculated vibrational frequencies of both electronic states and the largest coefficients (>0.3) of the Duschinsky matrix S. The excited state modes are expressed as linear combinations of the ground state modes with the coefficients given in Table 7.1. As in other substituted indoles, the Duschinsky matrix is mostly diagonal up to vibrations around 400 cm^{-1} and above 3200 cm^{-1}, for the CH stretching vibrations. Also the CN stretching vibration (Q_7, calculated at 2151.4 cm^{-1}) does not change its vibrational character upon electronic excitation.

No mixing of in-plane and out-of-plane modes occurs, as can be inferred from the last column of Table 7.1.The complete Duschinsky matrix is given in the online supplementary material. Additionally, the experimental vibrational frequencies in the S_0 state from the dispersed fluorescence spectra and in the S_1 state from the LIF spectra presented in Section 7.4.2, are given in Table 7.1. Since the ground and first electronically excited state of 5CI are of A″ symmetry and the transition dipole moment lies in the plane of the molecule only in-plane (A′) vibrations are allowed. Vibrational wavenumbers of the out-of-plane modes (A″) have been calculated from their first overtones, assuming harmonicity. They have been marked with an asterisk at the respective wavenumber in Table 7.1.

Compared to indole, 5CI has one more atom, and consequently three additional normal modes. These additional modes are quite local and can be described as in-plane and out-of-plane low frequency wagging modes of the cyano group and as a high frequency CN stretching mode. The lowest frequency mode Q_{45}, which was calculated at 105 cm^{-1} in the electronic ground state is an out-of-plane wagging motion mostly located in the cyano group. Its frequency strongly drops to 77 cm^{-1} upon electronic excitation. The following

Table 7.1: Calculated and experimental wavenumbers of the 45 normal modes of the ground and first electronically excited states of 5CI along with the respective symmetries and the coefficients of the Duschinsky matrix, which are larger than 0.3. The wavenumbers of the out-of-plane modes (A$''$) have been calculated from their first overtones, assuming harmonicity. They are marked with an asterisk

Mode	S$_0$			S$_1$			Duschinsky
	Sym.	Calc.	Obs.	Sym.	Calc.	Obs.	
Q_{45}	A$''$	105.2	100*	A$''$	77.2	73*	$Q_{45}(S_1) = +0.99Q_{45}(S_0)$
Q_{44}	A$'$	139.2	140	A$'$	134.7	138	$Q_{44}(S_1) = +0.99Q_{44}(S_0)$
Q_{43}	A$''$	225.7	220*	A$''$	172.1	165*	$Q_{43}(S_1) = +0.99Q_{43}(S_0)$
Q_{42}	A$''$	263.9		A$''$	224.3	222*	$Q_{42}(S_1) = +0.98Q_{42}(S_0)$
Q_{41}	A$'$	379.1	380	A$''$	308.7	306*	$Q_{41}(S_1) = -0.98Q_{38}(S_0)$
Q_{40}	A$''$	400.2	410*	A$''$	334.4	328*	$Q_{40}(S_1) = -0.98Q_{40}(S_0)$
Q_{39}	A$'$	417.1	416	A$'$	341.0	350	$Q_{39}(S_1) = -0.87Q_{41}(S_0) - 0.44Q_{39}(S_0)$
Q_{38}	A$''$	421.3	419*	A$''$	374.2	365*	$Q_{38}(S_1) = -0.87Q_{37}(S_0) + 0.28Q_{33}(S_0)$
Q_{37}	A$''$	481.7		A$'$	394.9	396	$Q_{37}(S_1) = -0.88Q_{39}(S_0) + 0.46Q_{41}(S_0)$
Q_{36}	A$'$	532.2	536	A$'$	474.3	484	$Q_{36}(S_1) = -0.88Q_{36}(S_0) - 0.36Q_{34}(S_0)$
Q_{35}	A$''$	606.1	600*	A$''$	508.0	508*	$Q_{35}(S_1) = +0.66Q_{33}(S_0) - 0.61Q_{35}(S_0)$
Q_{34}	A$'$	613.8	613	A$''$	551.4	545*	$Q_{34}(S_1) = +0.74Q_{35}(S_0) + 0.61Q_{33}(S_0)$
Q_{33}	A$''$	633.2		A$'$	582.2	573	$Q_{33}(S_1) = -0.88Q_{34}(S_0) + 0.41Q_{36}(S_0)$
Q_{32}	A$''$	722.0	710*	A$''$	599.5		$Q_{32}(S_1) = -0.77Q_{26}(S_0) + 0.42Q_{32}(S_0)$
Q_{31}	A$'$	729.2	720	A$''$	615.9		$Q_{31}(S_1) = -0.66Q_{28}(S_0) - 0.55Q_{32}(S_0)$
Q_{30}	A$''$	758.4		A$''$	639.1		$Q_{30}(S_1) = -0.71Q_{28}(S_0) + 0.50Q_{32}(S_0)$
Q_{29}	A$'$	788.2	784	A$'$	661.6	666	$Q_{29}(S_1) = -0.93Q_{31}(S_0)$
Q_{28}	A$''$	812.4	812*	A$''$	689.1		$Q_{28}(S_1) = -0.76Q_{30}(S_0) + 0.37Q_{32}(S_0)$
Q_{27}	A$''$	853.3		A$''$	730.8		$Q_{27}(S_1) = +0.97Q_{24}(S_0)$
Q_{26}	A$''$	896.8		A$'$	756.8	753	$Q_{26}(S_1) = -0.96Q_{29}(S_0)$
Q_{25}	A$'$	900.7	900	A$''$	818.7		$Q_{25}(S_1) = +0.84Q_{27}(S_0) - 0.43Q_{30}$
Q_{24}	A$''$	934.2		A$'$	866.9	876	$Q_{24}(S_1) = -0.92Q_{25}(S_0)$
Q_{23}	A$'$	946.4	944	A$'$	875.3	884	$Q_{23}(S_1) = +0.90Q_{23}(S_0)$
Q_{22}	A$'$	1087.9	1070	A$'$	961.8	951	$Q_{22}(S_1) = +0.41Q_{22}(S_0) + 0.41Q_{18}(S_0)$
Q_{21}	A$'$	1110.3	1104	A$'$	1062.8	1065	$Q_{21}(S_1) = -0.75Q_{22}(S_0) + 0.42Q_{21}(S_0)$
Q_{20}	A$'$	1148.0	1160	A$'$	1087.1	1095	$Q_{20}(S_1) = +0.73Q_{21}(S_0) - 0.46Q_{20}(S_0)$
Q_{19}	A$'$	1159.6	1167	A$'$	1107.3		$Q_{19}(S_1) = -0.84Q_{19}(S_0) - 0.30Q_{22}(S_0)$
Q_{18}	A$'$	1238.7	1224	A$'$	1170.5	1158	$Q_{18}(S_1) = -0.68Q_{20}(S_0) + 0.57Q_{18}(S_0)$
Q_{17}	A$'$	1269.9	1279	A$'$	1239.0		$Q_{17}(S_1) = +0.91Q_{17}(S_0)$
Q_{16}	A$'$	1303.8	1318	A$'$	1272.6		$Q_{16}(S_1) = -0.87Q_{16}(S_0)$
Q_{15}	A$'$	1353.2	1355	A$'$	1304.8		$Q_{15}(S_1) = -0.80Q_{15}(S_0) - 0.30Q_{16}(S_0)$
Q_{14}	A$'$	1390.2		A$'$	1354.0		$Q_{14}(S_1) = +0.50Q_{14}(S_0) + 0.48Q_{13}(S_0)$
Q_{13}	A$'$	1457.3	1453	A$'$	1385.2		$Q_{13}(S_1) = -0.75Q_{12}(S_0) - 0.48Q_{14}(S_0)$
Q_{12}	A$'$	1487.0		A$'$	1430.5		$Q_{12}(S_1) = -0.73Q_{11}(S_0) - 0.39Q_{13}(S_0)$
Q_{11}	A$'$	1499.8		A$'$	1444.0		$Q_{11}(S_1) = -0.75Q_{10}(S_0) - 0.48Q_{13}(S_0)$
Q_{10}	A$'$	1546.3	1524	A$'$	1526.0		$Q_{10}(S_1) = +0.89Q_{9}(S_0) - 0.33Q_{10}(S_0)$
Q_{9}	A$'$	1611.8	1604	A$'$	1617.7		$Q_{9}(S_1) = +0.59Q_{14}(S_0) - 0.51Q_{13}(S_0)$
Q_{8}	A$'$	1657.9	1658	A$'$	1630.2		$Q_{8}(S_1) = +0.93Q_{8}(S_0)$
Q_{7}	A$'$	2151.4	2145	A$'$	2085.1		$Q_{7}(S_1) = -1.00Q_{7}(S_0)$
Q_{6}	A$'$	3205.8		A$'$	3218.6		$Q_{6}(S_1) = +0.95Q_{6}(S_0)$
Q_{5}	A$'$	3214.3		A$'$	3233.1		$Q_{5}(S_1) = -0.69Q_{5}(S_0) + 0.66Q_{4}(S_0)$
Q_{4}	A$'$	3226.8		A$'$	3234.4		$Q_{4}(S_1) = +0.70Q_{5}(S_0) + 0.70Q_{4}(S_0)$
Q_{3}	A$'$	3267.6		A$'$	3265.6		$Q_{3}(S_1) = +0.95Q_{3}(S_0)$
Q_{2}	A$'$	3286.4		A$'$	3285.1		$Q_{2}(S_1) = -0.95Q_{2}(S_0)$
Q_{1}	A$'$	3680.4		A$'$	3672.3		$Q_{1}(S_1) = +1.00Q_{1}(S_0)$

vibration Q_{44}, calculated at 139 cm^{-1} (S$_0$) is the in-plane bending mode of the cyano group, with a slightly reduced frequency in the S$_1$ state (135 cm^{-1}). The CN stretching vibration is calculated to be 2151 cm^{-1} (S$_0$) and 2085 cm^{-1} (S$_1$).

The other normal modes are similar to those of the parent molecule indole. Q_{43}, calculated at 226 cm^{-1} represents the butterfly mode of the indole chromophore and is only slightly shifted to the value in indole itself (207 cm^{-1}).[186, 187] Q_{42} at 264 cm^{-1} is a ring puckering mode, which is mostly localized in the pyrrole ring. It is observed at 240 cm^{-1} in indole. The in-plane gearing mode of the two rings relative to each other (Q_{41}) is calculated at 379 cm^{-1}. Its S$_1$ state counterpart (predominately Q_{39}, cf. last column in Table 7.1) is calculated at 341 cm^{-1}. The strongly anharmonic NH out-of-plane mode Q_{40} considerably shifts from 400 cm^{-1} in the ground state to 334 cm^{-1} in the excited state.

7.4.2 Experimental results

Figure 7.2 shows the LIF spectrum of 5CI in the region between the electronic origin and $0,0+1200$cm^{-1}. Assignments of the vibronic (S$_1$) bands are given in Table 7.1. They are made on the basis of comparison to the frequencies of the *ab initio* calculations and using the propensity rule utilizing the intensities of the respective bands in the fluorescence emission spectra shown in Figure 7.3 and in the online supplementary material.

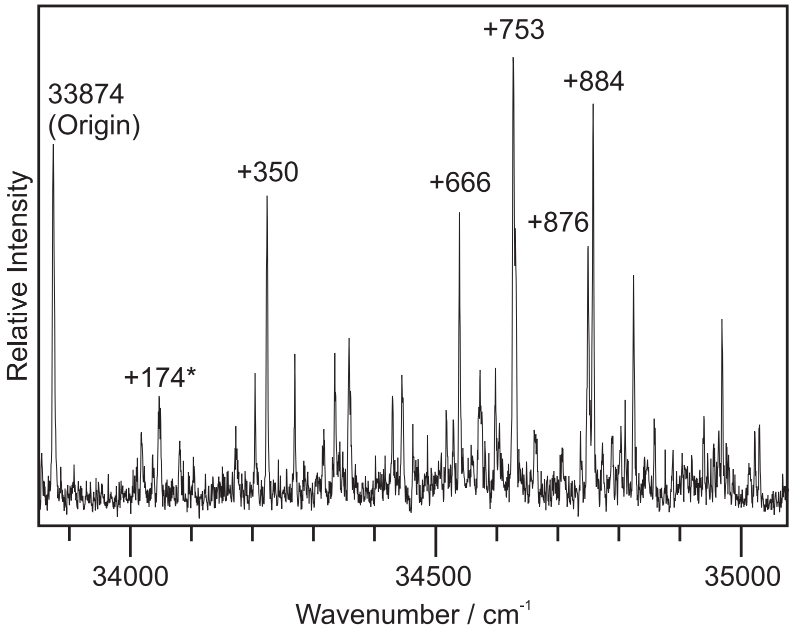

Figure 7.2: Laser induced fluorescence spectrum of 5CI. The marked bands at 34874 cm^{-1} (0,0), $0,0+350$ cm^{-1}, $0,0+666$ cm^{-1}, $0,0+753$ cm^{-1}, $0,0+876$ cm^{-1}, and $0,0+884$ cm^{-1} are used for pumping in order to get the DF spectra. The band at $0,0+174$ cm^{-1} presumably belongs to a 5CI-water cluster.

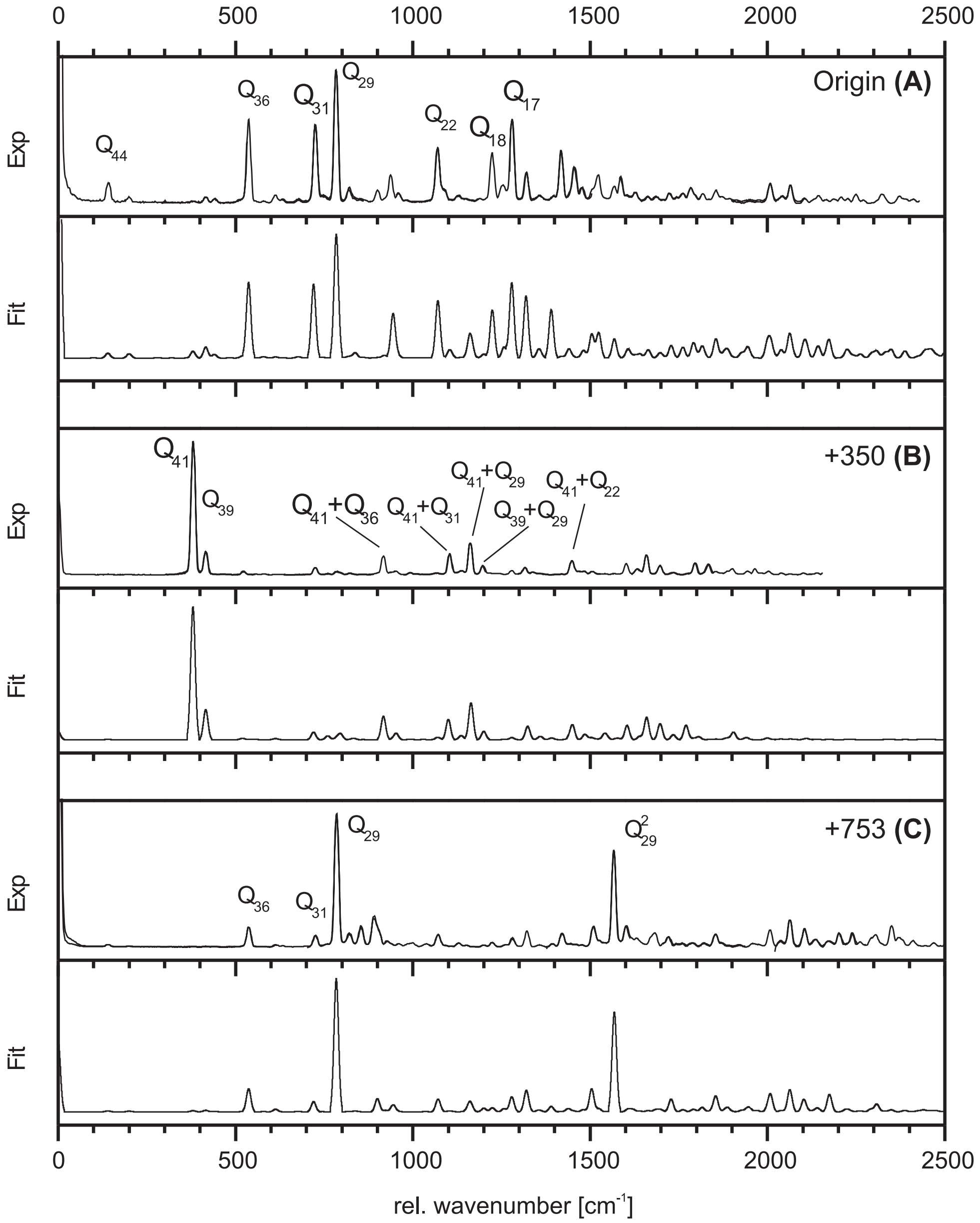

Figure 7.3: Dispersed fluorescence spectra of 5CI obtained via pumping the electronic origin at 33874 cm^{-1} (A), via the vibronic band at 0,0+350 cm^{-1} (B) and via the vibronic band at 0,0+753 cm^{-1} (C)). Within each block, the first trace gives the experimental spectrum, the second trace the FC fit. See text for details. The wavenumber of each band in the FC fit has been set to the experimental value for better comparison.

Exciting the S_1 band at 350 cm^{-1} leads to an emission spectrum with the strongest propensity to the S_0 band at 380 cm^{-1} (Figure 7.3 B) The vibronic band is assigned to the vibration Q_{39}, which represents the in-plane gearing mode of the two rings on the basis of its vibrational wavenumber. According to the Duschinsky matrix, this mode has the largest coefficient at mode Q_{41} in the ground state, leading to a safe assignment of the bands at 380 cm^{-1} (S_0) and 350 cm^{-1} (S_1) to the in plane gearing mode. The emission spectrum is dominated by combination bands of many in-plane vibrations with the diagonal mode Q_{41}, eg. $Q_{41} + Q_{36}$, $Q_{41} + Q_{31}$, and $Q_{41} + Q_{29}$.

The next band whose fluorescence has been dispersed is located at 666 cm^{-1}. It can be assigned to vibration Q_{29}, which has the largest coefficient in the Duschinsky matrix with vibration Q_{31} in the ground state. This is in good agreement with the strongest propensity to the emission band at 720 cm^{-1}. This mode represents a ring breathing mode, mainly localized in the six-ring and the C(5)–C(10) bond. The fluorescence emission spectrum through excitation of the 666 cm^{-1} band along with the simulation and the FC fit is given in the online supplementary material.

The vibronic band at 753 cm^{-1} leads to an emission spectrum with the strongest propensity to the 784 cm^{-1} mode in the ground state (Figure 7.3 C). For this vibration, mode Q_{26} in the excited state has the largest coefficient with mode Q_{29} in the ground state. This mode is an in-plane ring deformation mode with major elongations along C(4)–C(9) and N(1)–C(8). Apart from the $Q_{29}|^1_0$ and $Q_{29}|^1_1$ also $Q_{29}|^1_2$ has large intensity.

The vibronic band at 876 cm^{-1} is assigned to mode Q_{24} in the S_1 state, related to mode Q_{24} in the electronic ground state. The respective vibrational energy in the ground state is 935 cm^{-1}. The modes can be described as (in-plane) ring deformations, with main elongations in the pyrrole ring.The fluorescence emission spectrum through excitation of the 876 cm^{-1} band is given in the online supplementary material. When simulating the LIF spectrum using the best FC fit parameters from all emission spectra (cf. Section 7.4.3) it is obvious that the intensity of the 876 cm^{-1} band is too weak in the simulation (Figure 7.5). An alternative assignment of this band could also be based on a Fermi resonance between the combination of Q_{38} (A$''$) and Q_{35} (A$''$) with Q_{23} (A$'$) .

Excitation of the energetically close-lying 884 cm^{-1} band leads to an emission spectrum with largest intensity at 944 cm^{-1} (shown in the online supplementary material). Inspection of the Duschinsky matrix reveals, that the S_1 state mode Q_{23} is closely related to the respective Q_{23} band in the electronic ground state. It can be described as in-plane ring deformation, which has its largest elongations at bonds C(3)–C(9) and C(4)–C(5).

All wavenumbers of the experimentally observed bands both in absorption and in emission, along with the vibrational assignments and their intensities are given in the online supplementary material.

7.4.3 FC fit results

The fluorescence intensities in the emission spectra of the electronic origin 0,0 and the vibronic bands at $0,0+350$ cm^{-1}, $0,0+666$ cm^{-1}, $0,0+753$ cm^{-1}, and $0,0+884$ cm^{-1} have been utilized along with the rotational constants of 5CI in the ground and lowest excited states from Ref.[180] in the fit of the geometry changes upon electronic excitation. We employed a weighting factor of 5 for the fit of the rotational constants and of 1 for the fit of the fluorescence intensities. Inspection of the DF spectrum of the electronic origin (Figure 7.3 A) shows that all vibrational bands in the fit of the FC emission spectrum via pumping the electronic origin are well reproduced. Also the fluorescence emission spectra though $0,0+350$ cm^{-1} (7.3B), $0,0+753$ cm^{-1} (7.3C) and $0,0+666$ cm^{-1} (shown in the online supporting material) are nearly perfectly reproduced by the FC fit. Strong deviations are found for the two emission spectra through $0,0+876$ and $0,0+884$ cm^{-1} (shown in the online supporting material). The vibrational modes, which are used to model the geometry changes upon electronic excitation are compiled in Table 7.2 along with the magnitude and sign of their displacements.

Table 7.2: Fitted factors of the displacements along the normal modes from the FC fit

Mode	displacement	
Q_{36}	0.032325	±0.0071828
Q_{31}	0.0031924	±0.0031209
Q_{29}	0.0010253	±0.0022252
Q_{25}	−0.039721	±0.0072168
Q_{22}	−0.042237	±0.015752
Q_{18}	0.015171	±0.016185
Q_{17}	0.10041	±0.012041

Table 7.3 summarizes the results for the geometry changes from the combined fit to the rovibronic intensities and the rotational constant changes upon electronic excitation from Ref. [180]. While in the SCS-CC2 calculations, there are slight discrepancies in the description of the rotational constants, especially for the change of the A rotational constant upon electronic excitation, the combined fit perfectly reproduces all rotational constant changes upon electronic excitation. The intensities in the fluorescence emission spectra through the origin and the vibronic bands at $0,0{+}350$ $0,0{+}666$, and $0,0{+}753$ cm^{-1} are perfectly reproduced, while the emission spectra through the $0,0+876$ cm^{-1}, and $0,0+884$ cm^{-1} bands show strong deviations from the FC fit.

Figure 7.4 depicts the results of the structure fit to the rotational constants and the FC intensities graphically.

Table 7.3: Rotational constants, their changes upon electronic excitation, and bond lengths of 5CI in the electronic ground and lowest excited singlet state from SCS-CC2 calculations utilizing the cc-pVTZ basis set and from a FC fit. The reference state for the geometry changes is the electronic ground state. Therefore, the geometry parameters for the ground state in FC fit have been taken from the SCS-CC2 calculations. For atomic numbering cf. Figure 7.1.

state	S_0		S_1		$S_1 - S_0$		
method	SCS-CC2	FCFit	SCS-CC2	FCFit	SCS-CC2	FCFit	Exp.[180]
A	3364	3364	3281	3293	-83	-70.50	-70.47
B	734	734	725	726	-9	-7.83	-7.69
C	602	602	594	595	-6	-7.54	-7.37
N1C2	138.3	138.3	138.3	139.6	0	+1.3	-
C2C3	137.3	137.3	139.4	139.0	+2.1	+1.7	-
C3C9	143.5	143.5	141.4	141.6	-2.1	-1.9	-
C9C4	140.3	140.3	141.9	142.9	+1.6	+2.6	-
C4C5	139.4	139.4	144.2	144.3	+4.8	+4.9	-
C5C6	141.8	141.8	144.8	145.0	+3.0	+3.2	-
C6C7	138.6	138.6	142.0	141.2	+3.4	+2.6	-
C7C8	140.1	140.1	140.7	139.3	+0.6	-0.8	-
C8C9	142.2	142.2	146.2	145.2	+4.0	+3.0	-
C8N1	137.5	137.5	138.1	138.6	+0.6	+1.1	-
N1H12	100.5	100.5	100.5	100.6	0	+0.1	-
C5C10	143.7	143.7	141.6	140.9	-2.1	-2.8	-
C10N11	117.6	117.6	118.2	118.0	+0.6	+0.4	-

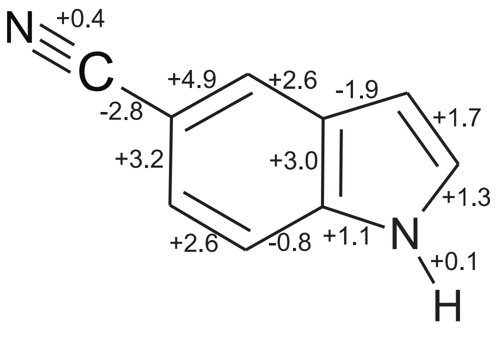

Figure 7.4: Geometry changes of 5CI upon electronic excitation from a combined FC/rotational constants fit. The numbers gives the bond length changes in pm upon excitation from the ground state to the lowest electronically excited state.

On the basis of the structural changes fit in this way, we calculated the LIF spectrum of 5CI using the FC approximation. Figure 7.5 shows the LIF spectrum of 5CI along with a FC simulation of the absorption spectrum using the geometry changes from the FC fit of the emission spectra, described above. Most intensities of the vibronic spectrum are quite well reproduced, with the exception of the intensity of the bands at 350, 876, and 884 cm^{-1}, which are considerably too weak. Using the geometry changes from the FC fit we implemented additional corrections from the Herzberg-Teller terms, calculated using the numerical derivatives of the DFT/MRCI transition dipole moments along the normal modes as described in Section 7.3.4. Most of the intensities, which are missing or weak in the FC simulation of the absorption spectrum are considerably improved in the FCHT simulation. An exception are the bands at 876 and 884 cm^{-1}, which also show large deviations in the FC fit of the emission spectra.

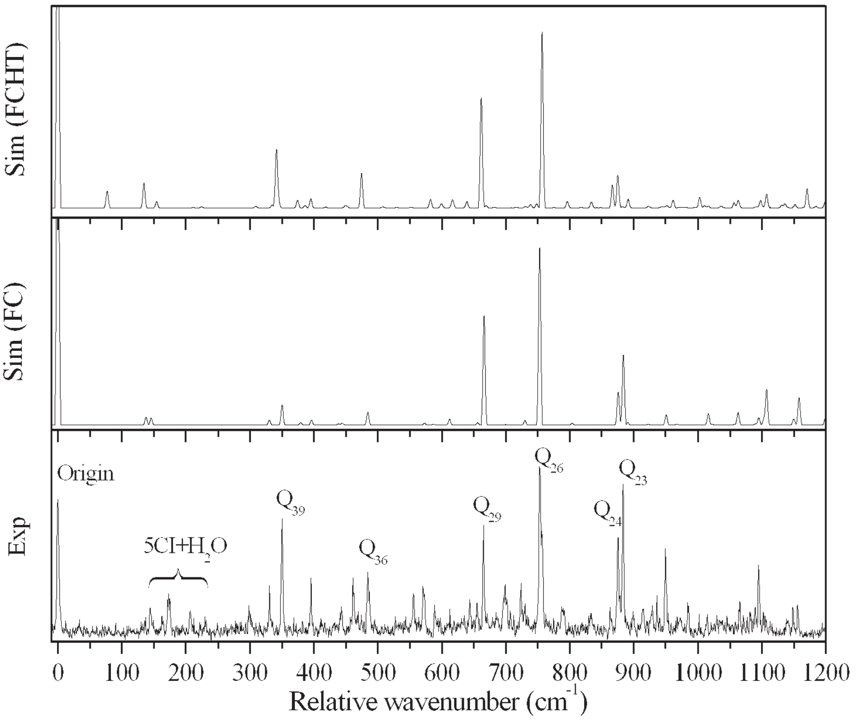

Figure 7.5: Laser induced fluorescence spectrum of 5CI along with a simulation using the structural changes from the FC fit and a simulation with additional Herzberg-Teller corrections.

7.5 Conclusions

The geometry changes, which have been determined from the FC analysis point to a structure of the excited state, which is L_a like in the nomenclature of Platt. Especially the strong elongations along the CC bonds C(2)–C(3), C(5)–C(6) and C(8)–C(9) are typical for the structure in this electronic state. Thus, the structure in the excited state, determined via the FC analysis fully confirms the findings from the analysis of the direction of the transition dipole moment.[180] Like in tetrahydrocarbazole (THC) [181], the lowest, optically bright state is of L_a character. While in the latter case the reason for the low-lying L_a state can be found in the positive inductive (+I) effect of the ethyl bridge, between positions 2 and 3 of the pyrrole ring, in 5 CI it is the strong negative mesomeric effect of the cyano group in the 5-position of the benzene moiety.

The assignment of S_1 state (L_a) transitions to the respective ground state modes is straightforward in this molecule. Like in THC, the Duschinsky matrix is predominately diagonal (cf. Figure 7.6), in contrast to the case of indole, in which the Duschinsky matrix

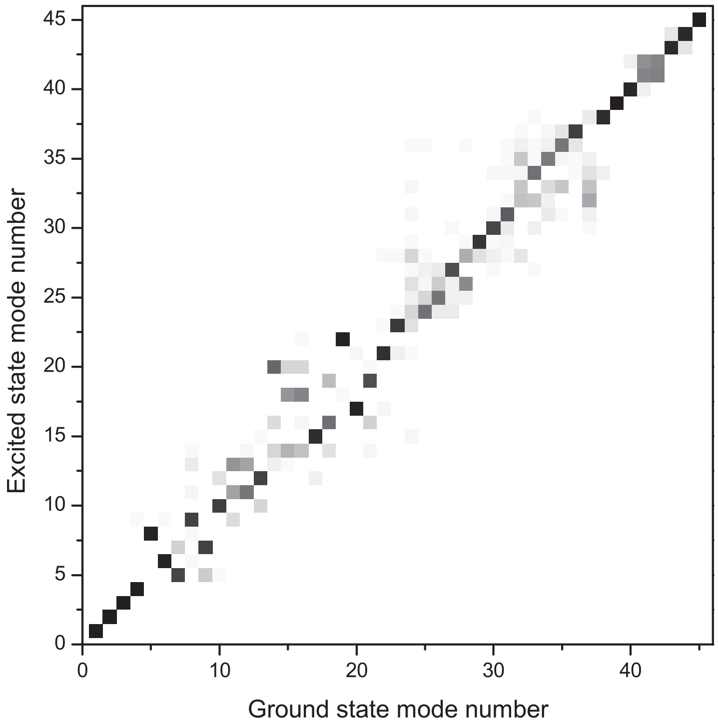

Figure 7.6: Graphical representation of the 45 x 45 Duschinsky matrix of 5CI, calculated using the numerically determined Hessian at the SCS-CC2/cc-pVTZ optimized structures.

is severely perturbed, and projection of the excited state modes onto specific ground state vibrations is difficult. Strong deviations from diagonal behaviour in indole is found for vibrational quantum number ranges, which strongly couple to the higher lying L_a state that induces strong Herzberg-Teller perturbations in the vibronic spectrum of the L_b state. In both 5CI and THC the lower state with higher oscillator strength is the L_a state, with the L_b being more than 1200 cm^{-1} higher in energy.

Mode selective perturbations are found for vibronic bands Q_{39} at 350 cm^{-1} Q_{24} at 876 cm^{-1}, and Q_{23} 884 cm^{-1}. While the FC intensities of the emission through all other vibronic bands is perfectly matched, the modes Q_{24} and Q_{23} show strong deviations, both in absorption and in emission, while deviations of the 350 cm^{-1} band are limited to the absorption spectrum. Based on the direction of the transition dipole moments it was previously concluded, that these bands strongly couple to the higher-lying L_b state via Herzberg-Teller coupling.[183] The Duschinsky matrix is nearly diagonal for these modes, excluding strong mode mixing to be responsible for the observed deviations. While our Herzberg-Teller analysis shows, that the intensity of the 350 cm^{-1} band can be explained by the additional contributions from the HT terms in Equation 7.4, the deviations of the bands at 875 and 884 cm^{-1} can't be explained on the basis of Herzberg-Teller contributions to the FC spectrum. Our FC analysis, presented here of the 5CI spectra showed, that excitation to the L_a state leads to an increased NH bond length. The energy of the repulsive $\pi\sigma^*$ state decreases with increasing NH bond length as deduced from CASPT2 potential energy profiles along the NH coordinate by Sobolewski *et al.* .[188] It seems therefore plausible to postulate an intersection with the $\pi\sigma^*$ state approximately 900 cm^{-1} above the adiabatic L_a origin to be responsible for the non-FC and non-HT behaviour in the absorption and emission spectra of 5CI. The longer NH bond length in the S_1 state is in agreement with a decrease of the pK_a value upon excitation to the lowest excited singlet state as known for the indoles. Using the absorption maxima of 5CI and of its anion from Ref. [189] and the relation from the Förster cycle [190]:

$$\Delta pK_a = \frac{hc(\tilde{\nu}_{HA} - \tilde{\nu}_{A^-})}{2.303 k_B T} \tag{7.8}$$

where $hc\tilde{\nu}_{HA}$ and $hc\tilde{\nu}_{A^-}$ are the wavenumber of the 5CI absorption maximum and of its anion, respectively we calculated the change of the pK_a of 5CI to be -6.0 in agreement with the increased NH bond length upon excitation.

7.6 Acknowledgements

The authors like to thank the Universitätsrechenzentrum Köln for the granted computing time on Cheops. The financial support of the Deutsche Forschungsgemeinschaft (SCHM 1043/12) is gratefully acknowledged.

7.7 Supplementary Information

Table 7.7: Complete Duschinsky matrix for the S_0 and S_1 modes of 5CI, calculated from the CC2/cc-pVTZ structures and Hessians.

Nr.	S_0/S_1	77.2	134.7	172.1	224.3	308.7	334.4
Q_{45}	105.2	-0.99266	-0.00150	-0.02392	0.00706	0.09688	0.01757
Q_{44}	139.2	0.00148	-0.99950	0.00087	0.00034	-0.00001	-0.00026
Q_{43}	225.7	-0.02643	0.00080	0.99049	-0.09676	0.00395	-0.07872
Q_{42}	263.9	0.01518	0.00044	0.10437	0.98138	0.01701	0.03902
Q_{41}	379.1	-0.00030	0.01045	-0.00057	0.00047	0.00169	-0.02373
Q_{40}	400.2	0.00066	-0.00018	-0.06837	0.01797	0.06434	-0.97164
Q_{39}	417.1	0.00154	0.00263	-0.00022	-0.00039	0.00532	0.01346
Q_{38}	421.3	-0.08688	-0.00007	0.00434	-0.00462	-0.97853	-0.03145

Continued on next page

Q_{37}	481.7	-0.07074	-0.00006	-0.02420	0.15862	-0.13447	-0.15762
Q_{36}	532.2	-0.00005	0.02166	-0.00037	0.00020	0.00083	-0.0034
Q_{35}	606.1	0.00490	0.00008	0.03538	-0.03401	0.04596	0.10667
Q_{34}	613.8	-0.00009	0.00841	-0.00047	0.00049	0.00042	-0.0028
Q_{33}	633.2	-0.01883	-0.00001	-0.00179	-0.00982	-0.05274	-0.0894
Q_{32}	722.0	-0.02359	-0.00002	0.01999	-0.01597	-0.01152	0.0268
Q_{31}	729.2	-0.00018	-0.00614	0.00015	0.00046	-0.00015	0.0026
Q_{30}	758.4	-0.00592	-0.00003	0.00458	-0.01007	0.03019	0.0152
Q_{29}	788.2	-0.00030	0.00104	0.00019	-0.00031	0.00021	-0.00101
Q_{28}	812.4	-0.00041	0.00001	0.01241	0.00374	0.06255	-0.02543
Q_{27}	853.3	0.00371	0.00000	-0.00917	0.00909	-0.00159	-0.01360
Q_{26}	896.8	-0.00323	-0.00000	0.01519	0.01464	-0.02465	-0.01002
Q_{25}	900.7	-0.00018	0.00325	-0.00031	-0.00002	0.00006	-0.00102
Q_{24}	934.2	-0.00473	-0.00001	-0.00067	-0.00034	-0.00712	-0.00276
Q_{23}	946.4	0.00021	0.00018	0.00002	-0.00006	0.00010	-0.00038
Q_{22}	1087.9	0.00018	0.00185	0.00007	0.00020	0.00005	-0.00084
Q_{21}	1110.3	0.00001	0.00386	0.00002	-0.00002	0.00002	-0.00131
Q_{20}	1148.0	-0.00022	0.00317	-0.00020	0.00016	0.00033	-0.00073
Q_{19}	1159.6	-0.00004	-0.00070	0.00008	0.00012	-0.00018	0.00085
Q_{18}	1238.7	0.00011	0.01057	-0.00005	-0.00023	0.00026	-0.00204
Q_{17}	1269.9	0.00008	-0.00223	0.00014	0.00005	-0.00010	0.00043
Q_{16}	1303.8	-0.00020	0.00115	0.00008	-0.00018	0.00047	-0.00024
Q_{15}	1353.2	0.00014	-0.00548	-0.00002	0.00013	-0.00021	0.00056
Q_{14}	1390.2	0.00000	0.00391	0.00004	0.00017	-0.00020	-0.00034
Q_{13}	1457.3	-0.00004	0.00421	-0.00020	-0.00005	0.00027	-0.00090
Q_{12}	1487.0	-0.00006	-0.00562	0.00009	-0.00001	0.00017	0.00004
Q_{11}	1499.8	-0.00014	-0.00152	0.00004	0.00010	-0.00010	-0.00004
Q_{10}	1546.3	0.00006	-0.00623	-0.00003	0.00022	-0.00043	0.00172
Q_{9}	1611.8	-0.00004	0.00044	-0.00002	0.00010	-0.00010	0.00017
Q_{8}	1657.9	-0.00003	-0.00229	-0.00001	0.00012	-0.00002	0.00033
Q_{7}	2151.4	0.00028	0.00149	0.00006	-0.00042	-0.00036	0.00005
Q_{6}	3205.8	-0.00001	-0.00017	0.00001	0.00001	0.00000	0.00006
Q_{5}	3214.3	-0.00000	0.00032	-0.00000	0.00001	0.00001	0.00005
Q_{4}	3226.8	0.00000	0.00004	-0.00003	-0.00001	-0.00001	-0.00000
Q_{3}	3267.6	-0.00003	0.00039	0.00005	-0.00004	0.00002	0.00003
Q_{2}	3286.4	0.00003	-0.00010	-0.00003	0.00004	-0.00003	0.00006
Q_{1}	3680.4	-0.00005	0.00007	0.00010	-0.00000	-0.00004	-0.00075
Nr.	S_0/S_1	341.0	374.2	394.9	474.3	508.0	551.4
Q_{45}	105.2	-0.00026	-0.06128	0.00081	-0.00007	0.01113	-0.01020
Q_{44}	139.2	0.01398	0.00010	0.00551	-0.02472	-0.00000	0.00000
Q_{43}	225.7	-0.00172	0.02642	0.00044	-0.00038	0.00370	-0.03497
Q_{42}	263.9	0.00083	-0.13653	0.00038	-0.00008	0.05311	0.04246
Q_{41}	379.1	0.86942	0.00264	0.46274	0.14228	0.00057	-0.00028
Q_{40}	400.2	-0.02677	-0.18969	0.00146	-0.00005	-0.05872	0.04510

Continued on next page

Q_{39}	417.1	-0.43611	0.00177	0.88117	-0.10823	-0.00049	0.00002
Q_{38}	421.3	-0.00129	-0.16321	0.00594	-0.00152	-0.01027	0.02081
Q_{37}	481.7	-0.00593	0.87417	-0.00146	0.00089	-0.38955	-0.05844
Q_{36}	532.2	0.11645	0.00110	-0.00468	-0.88806	-0.00042	-0.00047
Q_{35}	606.1	0.00453	-0.19979	-0.00008	-0.00171	-0.61296	0.73633
Q_{34}	613.8	0.09311	0.00116	-0.02934	-0.35951	0.00227	-0.00348
Q_{33}	633.2	-0.00303	0.28664	-0.00044	-0.00065	0.66018	0.60591
Q_{32}	722.0	0.00002	0.14201	0.00019	0.00043	0.11123	0.22240
Q_{31}	729.2	-0.11977	-0.00075	0.06491	0.10972	-0.00054	0.00015
Q_{30}	758.4	-0.00009	0.05668	0.00006	0.00050	0.02384	0.13443
Q_{29}	788.2	0.00532	-0.00004	0.00847	-0.08215	-0.00027	0.00120
Q_{28}	812.4	-0.00112	0.03511	-0.00003	0.00055	0.01080	0.09656
Q_{27}	853.3	-0.00040	0.00546	-0.00010	0.00004	0.02277	-0.06657
Q_{26}	896.8	0.00018	-0.02528	-0.00020	0.00043	-0.11112	-0.01906
Q_{25}	900.7	0.01594	-0.00012	-0.01639	-0.02502	-0.00076	0.00107
Q_{24}	934.2	-0.00027	0.05214	0.00005	0.00005	0.06510	-0.00258
Q_{23}	946.4	0.00135	0.00026	0.01394	0.00009	0.00004	0.00013
Q_{22}	1087.9	0.03865	0.00023	-0.01131	-0.03067	0.00003	0.00015
Q_{21}	1110.3	0.03716	-0.00007	-0.02299	-0.04736	-0.00010	0.00003
Q_{20}	1148.0	0.02837	-0.00007	-0.00791	-0.05236	-0.00011	-0.00009
Q_{19}	1159.6	-0.02971	-0.00022	0.00548	0.00536	0.00000	-0.00007
Q_{18}	1238.7	0.07339	0.00019	-0.03544	-0.08862	-0.00012	0.00012
Q_{17}	1269.9	-0.01936	-0.00007	0.00554	0.02931	-0.00017	0.00025
Q_{16}	1303.8	0.00365	-0.00007	0.00243	-0.02524	-0.00011	0.00032
Q_{15}	1353.2	-0.03307	0.00003	0.00164	0.05856	0.00008	0.00032
Q_{14}	1390.2	0.02161	-0.00016	0.00225	-0.06290	-0.00023	0.00003
Q_{13}	1457.3	0.03797	0.00023	-0.01550	-0.04145	0.00002	0.00025
Q_{12}	1487.0	-0.00622	0.00005	0.01499	0.04772	-0.00001	0.00020
Q_{11}	1499.8	-0.01421	-0.00031	0.01592	0.00327	-0.00009	-0.00021
Q_{10}	1546.3	-0.04837	-0.00002	0.02948	0.05419	0.00009	0.00011
Q_{9}	1611.8	-0.00820	0.00001	0.00451	-0.00799	0.00011	-0.00020
Q_{8}	1657.9	-0.00308	-0.00000	0.00014	0.01647	-0.00005	0.00001
Q_{7}	2151.4	-0.00889	0.00068	0.00726	0.01151	-0.00077	-0.00015
Q_{6}	3205.8	-0.00050	0.00002	-0.00051	0.00144	0.00000	-0.00003
Q_{5}	3214.3	0.00000	0.00003	-0.00014	-0.00147	-0.00003	-0.00005
Q_{4}	3226.8	-0.00129	0.00001	0.00143	0.00230	0.00004	0.00002
Q_{3}	3267.6	0.00023	0.00002	-0.00068	-0.00094	0.00009	-0.00020
Q_{2}	3286.4	-0.00071	0.00003	0.00033	0.00075	-0.00003	0.00012
Q_{1}	3680.4	-0.00087	-0.00027	-0.00010	0.00062	-0.00012	0.00026
Nr.	S_0/S_1	582.2	599.5	615.9	639.1	661.6	689.1
Q_{45}	105.2	-0.00006	-0.00759	0.01009	-0.00646	0.00033	-0.00281
Q_{44}	139.2	-0.00102	-0.00001	-0.00002	-0.00001	0.00492	0.00002
Q_{43}	225.7	-0.00024	0.00173	0.02305	-0.00691	0.00008	-0.00651
Q_{42}	263.9	0.00012	0.02219	-0.00289	0.01097	0.00062	0.00306

Continued on next page

Q_{41}	379.1	0.04451	0.00025	0.00001	-0.00010	-0.06782	-0.00011
Q_{40}	400.2	-0.00028	0.04838	-0.00871	0.04488	0.00078	0.01010
Q_{39}	417.1	-0.07045	-0.00095	0.00023	0.00016	0.10861	0.00012
Q_{38}	421.3	-0.00045	0.04394	-0.04221	-0.04484	0.00067	-0.02183
Q_{37}	481.7	-0.00030	-0.01863	0.06511	-0.04285	0.00007	0.00210
Q_{36}	532.2	0.41610	-0.00044	0.00009	0.00004	-0.07598	-0.00020
Q_{35}	606.1	-0.00393	-0.02858	0.11579	-0.03160	-0.00072	-0.00086
Q_{34}	613.8	-0.88058	0.00186	-0.00258	0.00026	-0.24831	-0.00049
Q_{33}	633.2	-0.00102	-0.24578	0.17728	-0.07919	-0.00018	-0.02587
Q_{32}	722.0	0.00183	0.42177	-0.54770	0.50165	-0.00085	0.36695
Q_{31}	729.2	0.16002	-0.00047	0.00128	-0.00029	-0.92820	-0.00058
Q_{30}	758.4	0.00113	0.38109	-0.13103	0.20510	0.00049	-0.76047
Q_{29}	788.2	-0.02024	0.00098	0.00033	-0.00003	-0.04349	-0.00019
Q_{28}	812.4	0.00134	0.00031	-0.65745	-0.70640	-0.00060	0.00054
Q_{27}	853.3	0.00018	-0.07361	-0.12981	-0.06090	0.00049	-0.51314
Q_{26}	896.8	-0.00036	-0.77766	-0.41613	0.40237	-0.00042	-0.11544
Q_{25}	900.7	-0.01414	-0.00379	-0.00166	0.00226	0.03325	-0.00034
Q_{24}	934.2	-0.00007	-0.01630	0.09498	0.16826	-0.00111	-0.09529
Q_{23}	946.4	0.03025	-0.00104	0.00028	0.00099	-0.01962	-0.00045
Q_{22}	1087.9	-0.04270	0.00013	0.00019	-0.00027	0.06536	0.00010
Q_{21}	1110.3	-0.04155	-0.00038	-0.00005	0.00026	0.04893	0.00001
Q_{20}	1148.0	-0.02765	0.00000	-0.00009	-0.00012	0.10306	0.00027
Q_{19}	1159.6	0.03466	-0.00020	-0.00001	0.00009	-0.02568	-0.00008
Q_{18}	1238.7	-0.06617	-0.00001	-0.00021	-0.00003	0.10776	0.00027
Q_{17}	1269.9	0.02302	-0.00006	-0.00008	0.00029	-0.04693	0.00012
Q_{16}	1303.8	-0.01505	-0.00014	-0.00006	0.00002	0.04457	0.00000
Q_{15}	1353.2	0.03322	-0.00025	0.00005	0.00016	-0.07233	0.00016
Q_{14}	1390.2	-0.02164	-0.00001	-0.00029	0.00007	0.03444	0.00007
Q_{13}	1457.3	-0.04139	-0.00010	0.00004	-0.00011	0.06887	0.00019
Q_{12}	1487.0	-0.00951	0.00017	0.00018	-0.00029	-0.01276	0.00017
Q_{11}	1499.8	0.01827	-0.00003	0.00020	-0.00014	-0.00519	0.00010
Q_{10}	1546.3	0.05329	0.00011	0.00027	-0.00020	-0.07603	-0.00017
Q_9	1611.8	0.00967	0.00024	-0.00017	0.00011	-0.01001	-0.00006
Q_8	1657.9	0.00376	0.00018	-0.00026	0.00001	-0.00908	-0.00009
Q_7	2151.4	0.00345	0.00013	0.00002	-0.00012	-0.01111	0.00002
Q_6	3205.8	-0.00011	0.00003	0.00011	0.00011	0.00006	-0.00003
Q_5	3214.3	0.00032	-0.00017	-0.00010	0.00007	-0.00178	-0.00003
Q_4	3226.8	0.00162	-0.00008	-0.00012	-0.00010	-0.00318	-0.00001
Q_3	3267.6	-0.00072	0.00004	0.00006	-0.00008	0.00030	-0.00059
Q_2	3286.4	0.00027	0.00001	-0.00002	0.00004	-0.00046	0.00049
Q_1	3680.4	0.00011	0.00008	0.00003	0.00001	-0.00089	-0.00007
Nr.	S_0/S_1	730.8	756.8	818.7	866.9	875.3	961.8
Q_{45}	105.2	-0.00188	0.00031	0.00243	0.00011	0.00012	0.00009

Continued on next page

Q_{44}	139.2	0.00001	-0.00046	0.00001	-0.00490	-0.00187	0.00672
Q_{43}	225.7	-0.00319	0.00019	0.00675	-0.00039	0.00011	-0.00008
Q_{42}	263.9	0.00368	-0.00028	-0.00172	-0.00003	0.00003	0.00003
Q_{41}	379.1	-0.00012	0.00225	-0.00002	0.00934	0.00692	-0.04315
Q_{40}	400.2	0.00674	0.00110	0.00249	0.00036	-0.00038	0.00000
Q_{39}	417.1	-0.00009	0.00332	0.00014	-0.03055	-0.02328	0.03808
Q_{38}	421.3	0.01253	0.00003	-0.01756	-0.00027	-0.00005	0.00054
Q_{37}	481.7	-0.02175	-0.00011	0.00130	-0.00002	-0.00010	0.00003
Q_{36}	532.2	-0.00050	0.07922	-0.00015	0.02365	0.00845	-0.07501
Q_{35}	606.1	0.04667	0.00170	0.09385	0.00103	0.00015	-0.00065
Q_{34}	613.8	-0.00060	0.07116	-0.00053	0.04060	0.06488	-0.10332
Q_{33}	633.2	-0.06906	0.00031	0.00777	0.00034	-0.00019	-0.00004
Q_{32}	722.0	-0.00796	0.00014	0.22737	-0.00003	0.00017	0.00047
Q_{31}	729.2	-0.00115	-0.00877	0.00031	-0.11821	-0.09212	0.23107
Q_{30}	758.4	-0.08897	0.00029	-0.43144	-0.00039	-0.00033	0.00051
Q_{29}	788.2	0.00421	-0.96601	-0.00055	0.22391	-0.03395	-0.04762
Q_{28}	812.4	0.18636	0.00078	-0.13645	0.00002	0.00007	0.00022
Q_{27}	853.3	-0.04174	-0.00088	0.83882	-0.00033	0.00065	-0.00016
Q_{26}	896.8	-0.04242	0.00005	-0.17467	0.00442	-0.00221	0.00056
Q_{25}	900.7	0.00265	-0.20919	-0.00127	-0.91938	0.24734	-0.19174
Q_{24}	934.2	0.97266	0.00466	0.01325	0.00119	-0.00328	-0.00056
Q_{23}	946.4	0.00285	-0.00067	-0.00069	0.17234	0.89459	0.36155
Q_{22}	1087.9	0.00003	-0.01671	-0.00006	-0.06978	-0.16791	0.41568
Q_{21}	1110.3	0.00030	-0.00934	0.00014	-0.08927	-0.13967	0.26997
Q_{20}	1148.0	0.00051	-0.07131	0.00031	-0.07363	0.03033	0.37078
Q_{19}	1159.6	0.00016	-0.00569	-0.00008	0.01601	0.09083	-0.19212
Q_{18}	1238.7	0.00013	-0.04775	0.00044	-0.15163	-0.16489	0.41320
Q_{17}	1269.9	-0.00003	0.02908	0.00011	0.04789	0.05181	-0.15400
Q_{16}	1303.8	0.00017	-0.01054	0.00005	-0.00407	-0.02476	0.09337
Q_{15}	1353.2	-0.00012	0.01453	0.00018	0.05846	0.05280	-0.20979
Q_{14}	1390.2	0.00043	0.02342	0.00018	-0.05615	-0.03456	0.10159
Q_{13}	1457.3	0.00001	-0.03932	0.00014	-0.04637	-0.07581	0.20059
Q_{12}	1487.0	-0.00045	0.01587	0.00013	0.03483	-0.04564	-0.00270
Q_{11}	1499.8	0.00005	-0.01205	-0.00022	0.00884	0.09930	-0.02438
Q_{10}	1546.3	-0.00021	0.01118	0.00024	0.05579	0.11504	-0.19379
Q_9	1611.8	-0.00010	0.00406	-0.00018	0.01260	0.02278	-0.02509
Q_8	1657.9	-0.00012	0.00329	-0.00005	0.02255	0.03192	-0.01397
Q_7	2151.4	0.00015	-0.00308	0.00001	0.00584	0.01379	-0.01954
Q_6	3205.8	0.00012	0.00138	0.00000	-0.00013	-0.00203	-0.00024
Q_5	3214.3	-0.00003	0.00026	0.00001	-0.00012	-0.00031	-0.00109
Q_4	3226.8	0.00007	0.00039	-0.00000	0.00085	-0.00011	-0.00276
Q_3	3267.6	-0.00008	-0.00051	0.00011	-0.00092	-0.00011	0.00303
Q_2	3286.4	0.00008	0.00030	-0.00027	0.00001	0.00103	-0.00186

Continued on next page

Q_1	3680.4	-0.00003	0.00093	-0.00006	0.00210	0.00029	-0.00180

Nr.	S_0/S_1	1062.8	1087.1	1107.3	1170.5	1239.0	1272.6
Q_{45}	105.2	-0.00023	0.00025	0.00008	0.00019	0.00016	0.00024
Q_{44}	139.2	0.00365	-0.00050	-0.00070	0.00436	0.00167	0.00013
Q_{43}	225.7	0.00002	-0.00016	-0.00000	-0.00013	-0.00006	0.00013
Q_{42}	263.9	0.00019	-0.00003	0.00021	0.00034	0.00003	-0.00010
Q_{41}	379.1	0.00600	0.00147	-0.01327	-0.01041	-0.00303	-0.00562
Q_{40}	400.2	-0.00032	-0.00018	-0.00018	0.00004	-0.00007	0.00018
Q_{39}	417.1	0.00881	0.01189	0.00898	0.01756	0.01243	0.01319
Q_{38}	421.3	0.00015	-0.00015	0.00005	0.00016	0.00008	-0.00021
Q_{37}	481.7	0.00022	-0.00006	-0.00010	-0.00002	-0.00006	-0.00013
Q_{36}	532.2	-0.03509	0.00385	0.01572	-0.02071	-0.00556	0.00983
Q_{35}	606.1	0.00000	-0.00013	-0.00007	-0.00017	-0.00037	0.00025
Q_{34}	613.8	-0.01679	-0.00501	-0.01581	-0.02814	-0.00671	0.00219
Q_{33}	633.2	0.00022	-0.00022	-0.00007	-0.00013	-0.00002	0.00003
Q_{32}	722.0	-0.00001	0.00008	-0.00006	0.00000	-0.00042	-0.00009
Q_{31}	729.2	0.04749	-0.03981	-0.02097	0.01597	-0.00416	-0.02072
Q_{30}	758.4	0.00023	-0.00009	-0.00010	-0.00012	0.00021	0.00017
Q_{29}	788.2	-0.02173	0.02997	0.02652	0.01193	0.01001	-0.00134
Q_{28}	812.4	0.00011	0.00020	0.00006	0.00001	0.00008	0.00004
Q_{27}	853.3	-0.00025	0.00013	0.00005	0.00005	-0.00014	-0.00012
Q_{26}	896.8	-0.00014	-0.00057	-0.00020	-0.00008	-0.00018	0.00024
Q_{25}	900.7	-0.06764	0.01992	0.03363	-0.01525	-0.00512	-0.02374
Q_{24}	934.2	-0.00001	-0.00060	-0.00017	-0.00011	-0.00011	0.00018
Q_{23}	946.4	-0.02730	0.10573	0.06274	0.11101	0.00881	0.01263
Q_{22}	1087.9	-0.75958	0.29464	-0.29531	-0.11415	-0.06585	-0.05048
Q_{21}	1110.3	0.42355	0.73694	0.27126	-0.27686	-0.02630	-0.00538
Q_{20}	1148.0	0.23433	-0.45878	-0.25699	-0.68371	0.06375	0.11594
Q_{19}	1159.6	0.27037	0.28646	-0.84615	0.11246	-0.08518	0.15253
Q_{18}	1238.7	0.16177	-0.12919	-0.05494	0.57263	0.34631	0.27575
Q_{17}	1269.9	-0.08571	0.12515	-0.04797	-0.17412	0.91278	-0.15260
Q_{16}	1303.8	0.11883	-0.06150	-0.14821	0.11460	-0.03046	-0.86170
Q_{15}	1353.2	-0.08261	0.13814	-0.01968	-0.09300	0.09134	0.22733
Q_{14}	1390.2	-0.06802	-0.03467	0.04433	0.01586	0.03435	0.03822
Q_{13}	1457.3	0.07430	-0.04178	-0.03188	0.10489	0.01977	0.00992
Q_{12}	1487.0	-0.11771	-0.03050	0.12360	-0.03791	-0.06740	0.22258
Q_{11}	1499.8	0.02456	-0.05418	0.01745	-0.04026	-0.11963	-0.09744
Q_{10}	1546.3	-0.15078	0.01754	0.00056	-0.14558	0.00572	0.05720
Q_9	1611.8	-0.01993	-0.02890	0.02678	-0.00277	-0.00667	0.03857
Q_8	1657.9	-0.06067	0.01113	0.05698	0.00829	0.01584	0.01844
Q_7	2151.4	-0.00559	-0.00090	-0.00067	0.00124	-0.00498	0.00222
Q_6	3205.8	-0.00136	-0.00081	0.00248	-0.00059	0.00232	-0.00382
Q_5	3214.3	0.00100	0.00206	-0.00120	0.00306	0.00073	-0.00045
Q_4	3226.8	-0.00496	-0.00200	0.00421	-0.00267	-0.00365	0.00281

Continued on next page

Q_3	3267.6	-0.00001	0.00184	0.00107	-0.00066	-0.00258	-0.00040
Q_2	3286.4	-0.00104	-0.00099	-0.00154	0.00112	-0.00189	-0.00090
Q_1	3680.4	-0.00107	-0.00016	0.00078	0.00061	-0.00179	0.00050

Nr.	S_0/S_1	1304.8	1354.0	1385.2	1430.5	1444.0	1526.0
Q_{45}	105.2	-0.00011	0.00004	0.00013	0.00010	0.00002	-0.00008
Q_{44}	139.2	0.00018	0.00231	0.00285	0.00083	0.00015	0.00030
Q_{43}	225.7	-0.00008	0.00010	0.00010	0.00003	-0.00016	-0.00007
Q_{42}	263.9	0.00005	-0.00005	0.00009	0.00010	0.00015	-0.00002
Q_{41}	379.1	-0.00712	-0.00263	0.00408	0.00312	-0.00273	0.00240
Q_{40}	400.2	0.00010	0.00030	-0.00003	0.00042	-0.00036	-0.00036
Q_{39}	417.1	-0.00406	0.00747	0.01738	0.00374	0.01419	-0.00255
Q_{38}	421.3	0.00002	-0.00001	0.00007	0.00006	0.00030	0.00000
Q_{37}	481.7	0.00006	0.00004	-0.00007	-0.00005	0.00002	0.00001
Q_{36}	532.2	0.00360	-0.03050	-0.00920	0.00218	0.00989	-0.00468
Q_{35}	606.1	0.00014	-0.00018	0.00037	0.00019	-0.00008	0.00027
Q_{34}	613.8	-0.00384	-0.02730	0.00321	0.00522	-0.01060	-0.00129
Q_{33}	633.2	0.00022	-0.00001	-0.00000	-0.00000	0.00003	0.00012
Q_{32}	722.0	0.00025	-0.00015	0.00013	-0.00012	-0.00004	-0.00009
Q_{31}	729.2	0.01343	0.02703	0.00287	-0.01413	0.00707	0.00180
Q_{30}	758.4	-0.00021	-0.00008	-0.00008	-0.00031	-0.00000	-0.00017
Q_{29}	788.2	0.00184	0.01326	-0.02271	0.00441	0.01527	-0.00036
Q_{28}	812.4	0.00000	-0.00002	0.00014	-0.00001	-0.00002	-0.00001
Q_{27}	853.3	0.00021	0.00003	0.00013	-0.00016	0.00019	0.00025
Q_{26}	896.8	0.00015	-0.00025	-0.00005	0.00001	-0.00038	-0.00005
Q_{25}	900.7	0.00849	-0.00040	-0.02093	0.00915	0.01999	0.01097
Q_{24}	934.2	0.00015	-0.00042	0.00007	-0.00010	-0.00034	0.00010
Q_{23}	946.4	-0.00019	0.04540	-0.02094	0.03089	0.05405	-0.00555
Q_{22}	1087.9	0.00338	-0.07131	0.08651	0.00308	0.00983	0.03931
Q_{21}	1110.3	-0.03067	-0.08121	-0.05557	0.02553	-0.07290	0.01107
Q_{20}	1148.0	-0.09902	-0.06971	-0.01913	0.04360	0.02634	-0.00259
Q_{19}	1159.6	0.10652	0.03081	-0.14531	-0.02677	-0.00863	0.02887
Q_{18}	1238.7	-0.19717	-0.34393	-0.03553	0.07184	-0.08873	-0.00978
Q_{17}	1269.9	0.20249	0.02477	-0.02858	-0.08719	0.01016	0.06142
Q_{16}	1303.8	-0.29221	-0.10954	-0.26357	0.01935	0.00273	0.02439
Q_{15}	1353.2	-0.80495	-0.03122	0.08359	-0.30333	0.16715	0.02970
Q_{14}	1390.2	-0.19630	0.49705	-0.48005	-0.27250	-0.01941	-0.11161
Q_{13}	1457.3	0.10962	0.47750	0.11224	-0.38808	-0.48200	-0.09114
Q_{12}	1487.0	0.21476	-0.22327	-0.74945	-0.12823	0.13604	0.15840
Q_{11}	1499.8	0.15014	-0.47700	0.14085	-0.72938	-0.20019	0.19549
Q_{10}	1546.3	-0.16690	-0.25566	-0.18770	0.26030	-0.74742	-0.32925
Q_9	1611.8	-0.13108	0.15715	-0.02568	0.22053	-0.31942	0.88903
Q_8	1657.9	0.00286	-0.05386	-0.16452	-0.02062	-0.03942	-0.09516
Q_7	2151.4	-0.00516	-0.02241	0.00310	0.01061	-0.01732	0.00006
Q_6	3205.8	0.00059	-0.00140	0.00416	-0.00076	0.00425	-0.00505

Continued on next page

Q_5	3214.3	-0.00437	0.00222	0.00258	0.00253	-0.00219	0.00125
Q_4	3226.8	-0.00419	-0.00159	-0.00450	0.00144	0.00501	-0.00212
Q_3	3267.6	0.00150	0.00175	0.00072	0.00430	-0.00103	0.00033
Q_2	3286.4	0.00334	-0.00177	0.00353	-0.00414	0.00422	0.00379
Q_1	3680.4	0.00105	0.00211	-0.00099	-0.00123	-0.00063	-0.00229

Nr.	S_0/S_1	1617.7	1630.2	2085.1	3218.6	3233.1	3234.4
Q_{45}	105.2	0.00004	-0.00005	-0.00036	-0.00001	0.00001	-0.00000
Q_{44}	139.2	0.00244	-0.00005	-0.00215	-0.00009	-0.00000	0.00034
Q_{43}	225.7	-0.00013	0.00004	0.00012	0.00000	0.00002	0.00003
Q_{42}	263.9	-0.00016	-0.00017	-0.00055	-0.00001	0.00002	0.00002
Q_{41}	379.1	0.00296	0.00149	-0.00072	0.00045	-0.00030	-0.00017
Q_{40}	400.2	0.00004	0.00023	0.00006	0.00003	-0.00007	0.00002
Q_{39}	417.1	-0.01196	0.00348	0.00581	-0.00009	-0.00078	-0.00058
Q_{38}	421.3	-0.00057	-0.00011	0.00025	0.00000	-0.00004	0.00000
Q_{37}	481.7	0.00022	0.00012	0.00090	-0.00001	0.00003	-0.00001
Q_{36}	532.2	-0.04971	-0.01070	-0.00660	0.00117	0.00074	-0.00067
Q_{35}	606.1	0.00008	0.00011	0.00020	0.00001	0.00000	0.00003
Q_{34}	613.8	-0.01042	-0.00165	-0.00150	0.00082	0.00105	0.00027
Q_{33}	633.2	0.00045	0.00031	-0.00042	0.00001	-0.00005	-0.00001
Q_{32}	722.0	0.00005	-0.00019	-0.00000	0.00000	0.00001	0.00001
Q_{31}	729.2	0.00290	0.00594	0.00586	-0.00070	-0.00068	-0.00270
Q_{30}	758.4	-0.00003	-0.00025	-0.00002	-0.00002	0.00001	0.00003
Q_{29}	788.2	0.02807	0.00215	0.00369	0.00141	-0.00031	-0.00023
Q_{28}	812.4	-0.00003	-0.00016	0.00010	0.00008	-0.00014	-0.00014
Q_{27}	853.3	-0.00004	-0.00001	-0.00001	0.00001	0.00001	-0.00006
Q_{26}	896.8	0.00018	-0.00002	-0.00009	0.00003	0.00010	-0.00019
Q_{25}	900.7	-0.04896	-0.01009	0.00161	0.00016	-0.00043	0.00006
Q_{24}	934.2	-0.00034	0.00009	0.00010	-0.00017	-0.00001	-0.00001
Q_{23}	946.4	-0.02899	-0.04542	0.00664	0.00154	-0.00044	0.00039
Q_{22}	1087.9	0.00512	0.00043	-0.00649	-0.00076	-0.00047	0.00016
Q_{21}	1110.3	0.02951	0.01082	-0.00982	0.00175	0.00211	0.00135
Q_{20}	1148.0	-0.02879	0.03341	-0.01007	0.00045	-0.00210	0.00211
Q_{19}	1159.6	0.02458	0.04190	0.00240	0.00585	0.00284	0.00149
Q_{18}	1238.7	0.06876	0.01016	-0.00481	0.00250	0.00377	0.00112
Q_{17}	1269.9	0.00147	-0.02065	-0.00172	-0.00160	0.00273	0.00302
Q_{16}	1303.8	-0.14249	-0.05545	-0.00037	-0.00171	0.00147	0.00063
Q_{15}	1353.2	-0.24695	-0.07652	0.00818	-0.00266	-0.00282	-0.00510
Q_{14}	1390.2	0.59427	0.10617	-0.01987	0.00480	0.00137	-0.00218
Q_{13}	1457.3	-0.50864	-0.13396	-0.01097	0.00029	0.00148	0.00431
Q_{12}	1487.0	-0.35438	-0.25415	0.00734	-0.00189	-0.00954	-0.00046
Q_{11}	1499.8	0.27019	0.07704	0.00687	0.00186	0.00123	0.00338
Q_{10}	1546.3	0.10033	-0.09534	0.03408	0.00194	-0.00025	-0.00244
Q_9	1611.8	0.04404	0.09617	0.00308	0.00786	0.00212	-0.00132
Q_8	1657.9	-0.28690	0.93054	-0.03065	0.00243	-0.00268	0.00038

Continued on next page

Q_7	2151.4	0.00322	-0.03466	-0.99837	0.00157	-0.00196	-0.00069
Q_6	3205.8	-0.00326	-0.00404	0.00219	0.95568	-0.27809	-0.09549
Q_5	3214.3	0.00556	0.00057	0.00071	-0.13093	-0.69356	0.70825
Q_4	3226.8	-0.00390	-0.00182	-0.00116	0.26318	0.66437	0.69936
Q_3	3267.6	0.00462	0.00294	0.00046	-0.00675	0.00280	0.00629
Q_2	3286.4	0.00045	0.00089	-0.00124	0.00750	0.00877	-0.00423
Q_1	3680.4	-0.00369	-0.00083	-0.00011	0.00033	0.00034	0.00014

Nr.	S_0/S_1	3265.6	3285.1	3672.3
Q_{45}	105.2	-0.00003	-0.00004	-0.00004
Q_{44}	139.2	0.00029	0.00017	0.00014
Q_{43}	225.7	-0.00005	-0.00007	-0.00014
Q_{42}	263.9	0.00003	0.00005	-0.00002
Q_{41}	379.1	0.00047	-0.00009	0.00059
Q_{40}	400.2	0.00007	-0.00001	-0.00082
Q_{39}	417.1	0.00027	0.00047	0.00001
Q_{38}	421.3	0.00001	0.00002	-0.00012
Q_{37}	481.7	-0.00000	0.00003	0.00008
Q_{36}	532.2	0.00015	-0.00038	0.00008
Q_{35}	606.1	0.00014	0.00013	-0.00023
Q_{34}	613.8	-0.00041	-0.00032	-0.00017
Q_{33}	633.2	0.00002	0.00004	-0.00006
Q_{32}	722.0	0.00020	0.00026	0.00002
Q_{31}	729.2	-0.00027	0.00023	-0.00031
Q_{30}	758.4	-0.00028	-0.00034	-0.00011
Q_{29}	788.2	-0.00027	-0.00048	0.00041
Q_{28}	812.4	0.00002	0.00005	-0.00001
Q_{27}	853.3	-0.00023	-0.00059	0.00004
Q_{26}	896.8	0.00004	0.00002	0.00002
Q_{25}	900.7	-0.00042	0.00039	0.00151
Q_{24}	934.2	0.00001	0.00004	0.00003
Q_{23}	946.4	-0.00080	-0.00020	-0.00031
Q_{22}	1087.9	-0.00201	-0.00008	0.00087
Q_{21}	1110.3	-0.00192	-0.00388	0.00158
Q_{20}	1148.0	0.00020	-0.00155	0.00209
Q_{19}	1159.6	0.00021	0.00162	0.00007
Q_{18}	1238.7	0.00090	-0.00198	0.00286
Q_{17}	1269.9	0.00257	0.00068	0.00102
Q_{16}	1303.8	0.00135	-0.00052	0.00057
Q_{15}	1353.2	0.00478	0.00117	-0.00079
Q_{14}	1390.2	-0.00144	-0.00313	0.00065
Q_{13}	1457.3	0.00271	-0.00086	-0.00330
Q_{12}	1487.0	0.00352	0.00070	-0.00228
Q_{11}	1499.8	-0.00010	0.00566	0.00124
Q_{10}	1546.3	0.00145	-0.00560	-0.00083

Continued on next page

Q_9	1611.8	-0.00201	-0.00010	0.00196
Q_8	1657.9	-0.00092	-0.00050	-0.00081
Q_7	2151.4	0.00021	0.00135	-0.00016
Q_6	3205.8	0.00581	0.00739	-0.00022
Q_5	3214.3	-0.00004	-0.01065	0.00019
Q_4	3226.8	-0.00575	0.00317	-0.00044
Q_3	3267.6	0.94773	0.31879	-0.00018
Q_2	3286.4	0.31885	-0.94767	-0.00195
Q_1	3680.4	0.00081	-0.00178	0.99998

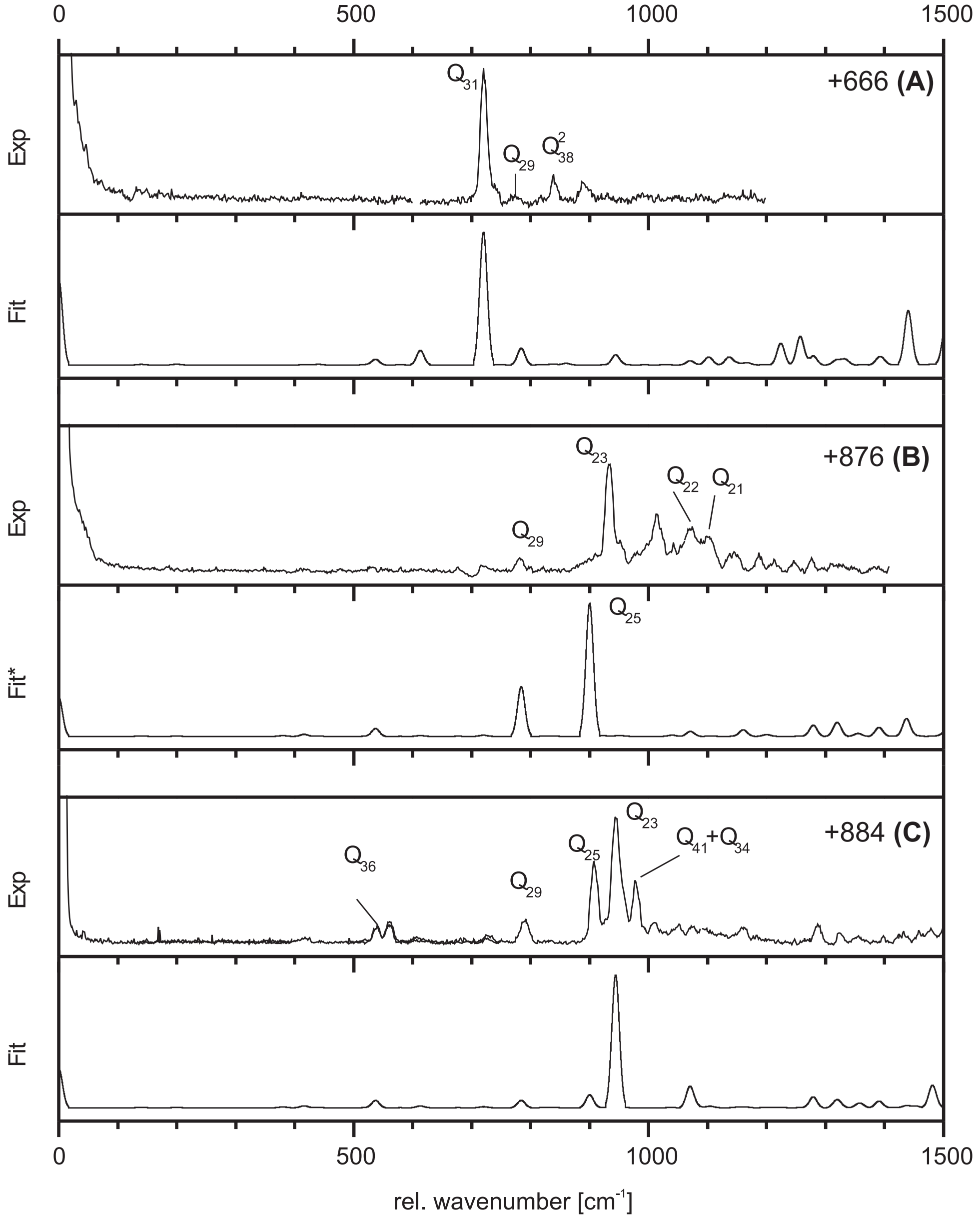

Figure 7.7: Dispersed fluorescence spectra of 5CI obtained via pumping the vibronic bands at 666 cm^{-1}, 876 cm^{-1}, and 884 cm^{-1}. Within each block, the first trace gives the experimental spectrum, the second trace the FC fit. See text for details.

Table 7.4: SCS-CC2/cc-pVTZ calculated optimized S_0 Cartesian coordinates of 5CI (in Bohr).

c	2.35019781	-3.46398276	-0.06583061
c	1.28135652	-0.97281537	-0.00578832
c	-1.38961411	-1.25884087	-0.06860637
n	-1.89043978	-3.80593228	-0.16184733
c	0.36301331	-5.13025296	-0.16013315
c	2.31302511	1.46736094	0.09439528
c	0.67241128	3.52912870	0.12867474
c	-1.98699674	3.20244899	0.06483292
c	-3.04346320	0.80888173	-0.03428126
c	1.68504998	6.04595455	0.23055902
n	2.50559442	8.11020028	0.31366763
h	4.32368942	-3.96057592	-0.04256695
h	0.36148410	-7.16517968	-0.22675658
h	-3.61968003	-4.58790024	-0.22239344
h	4.33593391	1.76399170	0.14448228
h	-5.07329575	0.56211543	-0.08298895
h	-3.18826627	4.85539776	0.09458110

Table 7.5: SCS-CC2/cc-pVTZ calculated optimized S_1 Cartesian coordinates of 5CI (in Bohr).

c	2.34807092	-3.45121350	-0.06567041
c	1.31745932	-0.98607006	-0.00698208
c	-1.42925839	-1.27098536	-0.07067684
n	-1.90275426	-3.83626947	-0.16247871
c	0.34811237	-5.16343948	-0.16031102
c	2.41402094	1.45822464	0.09393837
c	0.70538740	3.58187038	0.12996315
c	-2.00778801	3.23347115	0.06409216
c	-3.10968351	0.78973714	-0.03755976
c	1.67494416	6.07294292	0.23293712
n	2.48621201	8.15247905	0.31986988
h	4.32112387	-3.95620480	-0.04261124
h	0.36191796	-7.19766887	-0.22525079
h	-3.62911603	-4.62778158	-0.22186540
h	4.43380807	1.74901566	0.14363946
h	-5.13799148	0.55595816	-0.08572679
h	-3.19446532	4.89593403	0.09469290

Table 7.6: Experimental intensities of the assigned bands in the DF and LIF spectra relative to the strongest band in each spectrum. Keep in mind, that the mode numbering is different in the S_0 and the S_1 state as can be inferred from Table 1 of the main text. No 0,0 intensities for the fluorescence emission spectra is given since they might be contaminated by laser stray light and have not been used in the FC fit.

	Emission					Abs.
Mode	Origin	+350	+666	+753	+884	
$0, 0$						0.80
Q_{45}^2	0.05	0.001		0.01		
Q_{44}	0.15	0.004	0.06	0.02		
Q_{43}^2	0.03					
Q_{41}	0.02	1.000				
Q_{41}^2			0.07			
$Q_{41} + Q_{36}$		0.14				
$Q_{41} + Q_{34}$					0.49	
$Q_{41} + Q_{31}$		0.15				
$Q_{41} + Q_{29}$		0.24				
$Q_{41} + Q_{23}$		0.06				
$Q_{41} + Q_{22}$		0.10				
$Q_{41} + Q_{18}$		0.08				
$Q_{41} + Q_{17}$		0.15				
Q_{40}^2	0.12	0.010		0.10		
Q_{39}	0.05	0.001		0.05	0.04	0.68
$Q_{39} + Q_{31}$		0.03				
$Q_{39} + Q_{18}$		0.04				
Q_{38}^2			0.20			
Q_{37}^2	0.08			0.02		0.32
Q_{36}	0.63			0.15	0.12	0.36
Q_{32}^2	0.40			0.10		
Q_{31}	0.59	0.050	1.0	0.08	0.06	
Q_{30}^2		0.020		0.15	0.17	
Q_{29}	1.00	0.030		1.00	0.18	0.64
Q_{28}^2	0.08	0.040				
Q_{26}						1.00
Q_{25}	0.10					
Q_{23}					1.00	0.89
Q_{22}	0.42	0.010	0.05	0.09	0.02	0.50
Q_{20}					0.11	
Q_{18}	0.38			0.03	0.14	
Q_{17}	0.62	0.030	0.07			
Q_{16}	0.23			0.12	0.79	
Q_{15}	0.06				0.06	
Q_{13}	0.27					
Q_{11}		0.020		0.15	0.17	
Q_{10}	0.21					
Q_{8}	0.05	0.150				
Q_{7}	0.06			0.06		

7.8 Contributions

Title: Determination of the Geometry Change of 5-Cyanoindole upon Electronic Excitation from a Combined Franck-Condon/Rotational Constants Fit.

Authors: Benjamin Stuhlmann, Anne Gräßle, and Michael Schmitt.

submitted to: Physical Chemistry Chemical Physics (Impact Factor: 3.57)

The dispersed fluorescence spectra in this paper were either measured or remeasured by Anne Gräßle during her bachelor thesis under my supervision.

I carried out the Franck-Condon fit and created the figures for this publication.

The *ab initio* calculations were made by Michael Schmitt, who also gave helpful advice on all aspects of this work.

8. Determination of the Geometry Change of Benzimidazole upon Electronic Excitation from a Combined Franck-Condon/Rotational Constants Fit.

Benjamin Stuhlmann, Felix Gmerek, Daniel Krügler[1] and Michael Schmitt*[2]

J. Mol. Struc. **2014**, *XXX(XX)*, XXXX-XXXX, doi: XX.XXXX/XXXXXXXXXXX

8.1 Abstract

Single vibronic level fluorescence spectra of the electronic origin and of seven vibronic bands between $0,0$ and $0,0 + 1265$ cm^{-1} have been measured and analysed by means of a combined Franck-Condon/rotational constants fit. The rotational constants in ground and lowest electronically excited singlet state of four different isotopologues have been taken from previous rotationally resolved measurements of Schmitt *et al. Phys. Chem. Chem. Phys.*, 2006, **8**, 228. The intensities of 182 vibronic emission bands and of 8 rotational constants have been used for a fit of the complete heavy atom geometry changes upon electronic excitation. Vibronic modes, about 1000 cm^{-1} above the electronic origin, show strong deviations from Franck-Condon behaviour in emission. Herzberg-Teller coupling contributes to this effect. 1300 cm^{-1} above the origin, we observe the onset of intramolecular vibrational redistribution in the emission spectra.

---

[1] present address: Bremen

[2] Heinrich-Heine Universität, Institut für Physikalische Chemie I, D-40225 Düsseldorf, Germany. E-mail: mschmitt@uni-duesseldorf.de; Fax: +49 211 8115195; Tel: +49 211 8112100

8.2 Introduction

The combination of the information contained in the moments of inertia (or rotational constants), which are obtained from electronic rotationally resolved spectroscopy and of Franck-Condon factors from single vibronic level fluorescence (SVLF) spectroscopy, obtained by pumping various vibronic bands in the electronically excited states, provides reliable access to the structures of electronically excited states. A full substitution structure determination (referred to as r_s-structure) yielding Cartesian coordinates of each atom via Kraitchman analysis[191] of the moments of inertia of various isotopologues is in many cases unfeasible, since each atom in the molecule has to be replaced by one of its (stable) isotopologues. Information from multiple isotopic substitution can not be integrated, except for some symmetric cases. A nonlinear fit of the structure in internal coordinates to the rotational constants on the other hand, has many advantages. Also multiply substituted isotopologues can be used in the analysis and relations between the parameters can easily be implemented, since the fit is performed in internal coordinates. Symmetry constraints like planarity in the case of benzimidazole or relations between the parameters can easily be introduced via the internal coordinates.

Electronically excited states can be distinguished via different molecular parameters. In practice, a combination of several of them is used for an unequivocal assignment of the excited states. By comparison to the results of *ab initio* calculations, the adiabatic excitation energy and the oscillator strength can give a preliminary answer. Other useful and often used state dependent molecular properties are the direction of the transition dipole moment and the absolute size and components of the permanent dipole moments of the excited states. The information, which is contained in the nuclear structure of the electronically excited state is much less used. In previous studies, we have shown, how the rotational constants of the excited state of indole,[179] of 7-azaindole,[192] its water clusters,[193] and of 5-cyanoindole[180] can be used as guidance for distinction of energetically close-lying excited states like the ^1L_a- and ^1L_b-states in indoles and related compounds.

Raman and polarized infrared spectra of partially oriented benzimidazole crystals were recorded by Suwaiyan *et al.*[194] Tomkinson gave a reassignment of the vibrational spectrum of benzimidazole up to 1300cm^{-1} using inelastic neutron scattering spectroscopy.[195] Jalviste and Treshchalov [196] presented single vibronic level fluorescence (SVLF) spectroscopy and LIF spectroscopy of benzimidazole. Resonance enhanced multiphoton spectra of the monomer and several water clusters were studied by Jacoby *et al.*[197] The microwave spectrum of benzimidazole in the vibrational ground state and two low-lying vibrational satellites have been measured by Velino *et al.*[198]. Rotational constants of benzimidazole in the excited states were obtained from a band contour analysis in the vapour phase by Cané *et al.*[199] and Berden *et al.*[200] Rotationally resolved electronic spectroscopy of four isotopologues of benzimidazole yielded the absolute orientation of the transition dipole moment and part of the changes of the structure upon electronic excitation.[201] Adiabatic ionization energies and the vibrational spectrum of the cationic ground state of benzimidazole was investigated with mass analysed threshold ionization (MATI) by Lin *et al.*[202] The HD exchange in benzimidazole was studied by Yang and Tzeng using MATI.[203] The lowest triplet state of benzimidazole (electronic origin at 26536 cm^{-1}) was studied by Noda *et al.*[204] using electron paramagnetic resonance and optical detection of magnetic resonance in benzoic acid host crystals. Recently, an analysis of vibrational hot bands of benzimidazole has been given in our group.[205]

Borin and Serrano-Andrés calculated the absorption spectrum of benzimidazole using the complete active space (CAS) SCF method and multiconfigurational second-order perturbation theory (CASPT2).[21] The emission spectrum was calculated with the same theoretical methods by Serrano-Andrés and Borin.[22]

In the present publication we present a Franck-Condon analysis of the fluorescence emission spectra through eight different vibronic bands of benzimidazole. Along with the data from rotationally resolved spectroscopy of four different benzimidazole isotopologues[201] a full determination of the geometry changes upon electronic excitation could be obtained.

8.3 Experimental and Computational Details

8.3.1 Experiment

The experimental setup for the dispersed fluorescence (DF) spectroscopy has been described in detail elsewhere.[131, 132] In brief, benzimidazole was evaporated at 393 K and co-expanded through a pulsed nozzle with a 500 μm orifice (General Valve) into the vacuum chamber using Helium as carrier gas. The output of a Nd:YAG (SpectraPhysics INDI) pumped dye laser (Lambda-Physik, FL3002) was frequency doubled and crossed at right angles with the molecular beam. The resulting fluorescence was imaged on the entrance slit of a f = 1 m monochromator (Jobin Yvon, grating 2400 lines/mm blazed at 400 nm in first order). The dispersed fluorescence spectrum was recorded using a gated image intensified UV sensitive CCD camera (Flamestar II, LaVision). One image on the CCD chip spectrally covers approximately 600 cm^{-1}. Since the whole spectrum is taken on a shot-to-shot basis, the relative intensities in the DF spectra do not vary with the laser power. The relative intensities are afterwards normalized to the strongest band in the spectrum different from the resonance fluorescence band, which also contains the stray light and is therefore excluded from the FC analysis.

8.3.2 *Ab initio*calculations

Structure optimizations were performed employing Dunning's correlation consistent polarized valence triple zeta basis set (cc-pVTZ) from the TURBOMOLE library.[55, 59] The equilibrium geometries of the electronic ground and the lowest excited singlet states were optimized using the approximate coupled cluster singles and doubles model (CC2) employing the resolution-of-the-identity approximation (RI).[71, 73, 74] Spin-component scaling (SCS) modifications to CC2 were taken into account.[72] The Hessians and harmonic vibrational frequencies for both electronic states, which are utilized in the FC fit have been obtained from numerical second derivatives using the NumForce script[184] implemented in the TURBOMOLEprogram suite.[29]

8.3.3 Franck-Condon fit of the structural change

The change of a molecular geometry upon electronic excitation can be determined from the intensities of absorption or emission bands using the FC principle. According to the FC principle the relative intensity of a vibronic band depends on the overlap integral of the vibrational wave functions of both electronic states. The transition dipole moment for a transition between an initial electronic state $|m, v\rangle$ and a final electronic state $|n, w\rangle$ is defined as:

$$M_{vw} = \langle v \,|\, \mu_{mn}(Q) \,|\, w \rangle \tag{8.1}$$

with the electronic transition dipole moment $\mu_{mn}(Q)$:

$$\mu_{mn}(Q) = \langle \Psi_m \,|\, \mu \,|\, \Psi_n \rangle \,; \quad \mu = \sum_g e r_g \tag{8.2}$$

where r_g is the position vector of the gth electron. The dependence of the electronic transition dipole moment μ_{mn} from the nuclear coordinates can be approximated by expanding μ_{mn} in a Taylor series about the equilibrium position at Q_0. The series is truncated after the first term in the FC approximation.

The fit has been performed using the program FCFIT, which has been developed in our group and described in detail before.[28, 185] The program computes the FC integrals of multidimensional, harmonic oscillators mainly based on the recursion formula given in the papers of Doktorov, Malkin, and Man'ko.[47, 83] and fits the geometry (in linear combinations of selected normal modes) to the experimentally determined intensities.

This is simultaneously done for all emission spectra, which are obtained via pumping through different S_1 vibronic modes.

The vibrational modes of the electronically excited state can be expressed in terms of the ground state modes using the following linear orthogonal transformation, first given by Duschinsky[46]:

$$Q' = SQ'' + d \tag{8.3}$$

where Q' and Q'' are the N-dimensional vectors of the normal modes of excited and ground state, respectively, S is a $N \times N$ rotation matrix (the Duschinsky matrix) and d is an N-dimensional vector which displaces the normal coordinates.

The fit of the geometry to the intensities in the vibronic spectra can greatly be improved if independent information for the geometry changes upon electronic excitation is available. This additional information is the change of the rotational constants upon electronic excitation, which can be obtained from rotationally resolved electronic spectroscopy. While geometry fits to the rotational constants (mostly of several isotopologues) are routinely performed using non-linear fits in internal coordinates, the combination of rotational constant changes and vibronic intensities allows for determination of many more geometry parameters.

8.4 Results

8.4.1 *Ab initio* calculations

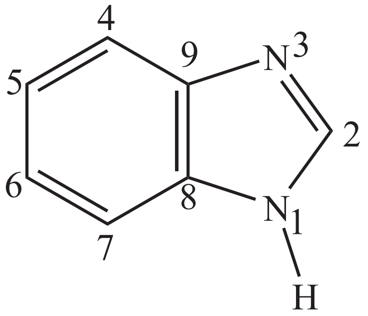

Figure 8.1: Structure and atomic numbering of benzimidazole.

The structure of benzimidazole in its ground and lowest excited singlet states has been determined from an optimization at the second order coupled cluster (CC2) level of theory using the cc-pVTZ basis set. The atomic numbering, used throughout this publication is shown in Figure 8.1. The Cartesian coordinates of the optimized structures of benzimidazole in the S_0, S_1, and S_2 states are given in the online supplementary material. Benzimidazole is planar in both electronic states, as proven by the inertial defects in the electronic ground state[198] and in the lowest excited state[201] and belongs to the point group C_s. Of the 39 normal modes 12 are out-of-plane vibrations (A$''$) and 27

Table 8.1: CC2/cc-pVTZ calculated and experimental wavenumbers of the 39 normal modes of the ground and first electronically excited states of benzimidazole along with the respective symmetry labels and the coefficients of the Duschinsky matrix, which are larger than 0.4.

Mode	S_0				S_1			Duschinsky
	Sym.	Calc.	Obs.[a]	Obs.[b]	Sym.	Calc.	Obs.	
$Q_1(S_0)$	A′	3657			A′	3637		$Q_1(S_1) = -1.00Q_1(S_0)$
$Q_2(S_0)$	A′	3267		3115	A′	3287		$Q_2(S_1) = -0.99Q_2(S_0)$
$Q_3(S_0)$	A′	3230		3079	A′	3249		$Q_3(S_1) = -0.88Q_3(S_0)$
$Q_4(S_0)$	A′	3221		3065	A′	3239		$Q_4(S_1) = -0.90Q_4(S_0)$
$Q_5(S_0)$	A′	3210		3040	A′	3224		$Q_5(S_1) = -0.77Q_5(S_0)$
$Q_6(S_0)$	A′	3200		3005	A′	3207		$Q_6(S_1) = -0.79Q_6(S_0)$
$Q_7(S_0)$	A′	1656			A′	1589	1565	$Q_8(S_1) = -0.90Q_7(S_0)$
$Q_8(S_0)$	A′	1615	1610	1620	A′	1515	1535	$Q_9(S_1) = -0.78Q_8(S_0)$
$Q_9(S_0)$	A′	1512			A′	1408	1425	$Q_{11}(S_1) = -0.55Q_9(S_0) + 0.53Q_{12}(S_0)$
$Q_{10}(S_0)$	A′	1500			A′	1432	1438	$Q_{10}(S_1) = -0.60Q_{10}(S_0) - 0.70Q_9(S_0)$
$Q_{11}(S_0)$	A′	1481		1478	A′	1382	1383	$Q_{12}(S_1) = +0.70Q_{11}(S_0) - 0.56Q_{12}(S_0)$
$Q_{12}(S_0)$	A′	1449		1412	A′	1603	1614	$Q_7(S_1) = +0.45Q_{12}(S_0) + 0.55Q_{11}(S_0)$
$Q_{13}(S_0)$	A′	1391	1363	1362	A′	1325	1323	$Q_{13}(S_1) = -0.80Q_{13}(S_0)$
$Q_{14}(S_0)$	A′	1323	1355	1353	A′	1256	1259	$Q_{15}(S_1) = +0.80Q_{14}(S_0)$
$Q_{15}(S_0)$	A′	1290		1280	A′	1286	1297	$Q_{14}(S_1) = +0.89Q_{15}(S_0)$
$Q_{16}(S_0)$	A′	1269	1270	1251	A′	1219	1226	$Q_{16}(S_1) = -0.91Q_{16}(S_0)$
$Q_{17}(S_0)$	A′	1195	1188	1191	A′	1158		$Q_{17}(S_1) = -0.72Q_{17}(S_0) - 0.65Q_{18}(S_0)$
$Q_{18}(S_0)$	A′	1163	1157	1162	A′	1140	1136	$Q_{18}(S_1) = +0.73Q_{18}(S_0) + 0.17Q_{20}(S_0)$
$Q_{19}(S_0)$	A′	1122		1115	A′	1054	1043	$Q_{19}(S_1) = +0.89Q_{19}(S_0)$
$Q_{20}(S_0)$	A′	1093	1079		A′	893	887	$Q_{21}(S_1) = -0.60Q_{20}(S_0) + 0.64Q_{21}(S_0)$
$Q_{21}(S_0)$	A′	1021	1008	1007	A′	966	961	$Q_{20}(S_1) = -0.70Q_{21}(S_0) - 0.60Q_{20}(S_0)$
$Q_{22}(S_0)$	A′	928	928	935	A′	875	883	$Q_{22}(S_1) = -0.90Q_{22}(S_0)$
$Q_{23}(S_0)$	A′	881	891	890	A′	853	828	$Q_{23}(S_1) = +0.95Q_{23}(S_0)$
$Q_{24}(S_0)$	A′	780	777	770	A′	725	731	$Q_{24}(S_1) = +0.96Q_{24}(S_0)$
$Q_{25}(S_0)$	A′	617	622	619	A′	566	567	$Q_{25}(S_1) = +0.98Q_{25}(S_0)$
$Q_{26}(S_0)$	A′	542	545	544	A′	474	478	$Q_{26}(S_1) = -0.96Q_{26}(S_0)$
$Q_{27}(S_0)$	A′	407	409	422	A′	395	397	$Q_{27}(S_1) = -0.99Q_{27}(S_0)$
$Q_{28}(S_0)$	A″	953	959[c]		A″	760	766	$Q_{28}(S_1) = -0.92Q_{28}(S_0)$
$Q_{29}(S_0)$	A″	925		936	A″	656		$Q_{30}(S_1) = -0.61Q_{29}(S_0) - 0.49Q_{30}(S_0)$
$Q_{30}(S_0)$	A″	855	860[c]	851	A″	588		$Q_{32}(S_1) = +0.70Q_{30}(S_0) + 0.40Q_{34}(S_0)$
$Q_{31}(S_0)$	A″	847	841[c]	848	A″	626		$Q_{31}(S_1) = +0.52Q_{31}(S_0) - 0.61Q_{33}(S_0)$
$Q_{32}(S_0)$	A″	767	778[c]	752	A″	537	541	$Q_{33}(S_1) = -0.62Q_{32}(S_0) - 0.51Q_{34}(S_0)$
$Q_{33}(S_0)$	A″	750		748	A″	677	675	$Q_{29}(S_1) = -0.62Q_{33}(S_0) - 0.49Q_{29}(S_0)$
$Q_{34}(S_0)$	A″	648	653[c]	637	A″	521	532[c]	$Q_{34}(S_1) = -0.72Q_{34}(S_0) + 0.28Q_{33}(S_0)$
$Q_{35}(S_0)$	A″	582	593[c]	581	A″	360	358[c]	$Q_{36}(S_1) = -0.91Q_{35}(S_0)$
$Q_{36}(S_0)$	A″	458			A″	441		$Q_{35}(S_1) = -0.92Q_{36}(S_0)$
$Q_{37}(S_0)$	A″	431	428[c]	425	A″	296	295[c]	$Q_{37}(S_1) = -0.92Q_{37}(S_0)$
$Q_{38}(S_0)$	A″	255	249[c]	246	A″	183	186[c]	$Q_{38}(S_1) = -0.88Q_{38}(S_0)$
$Q_{39}(S_0)$	A″	229	216[c]		A″	155	152[c]	$Q_{39}(S_1) = -0.87Q_{39}(S_0)$

[a] Ground state vibrational wavenumbers from fluorescence emission spectra of this work.

[b] Out-of-plane (A″) vibrations from Raman crystal data,[194]
in plane (A′) vibrations from IR (KBr mull) data.[206]

[c] Out-of-plane vibrations from their overtones assuming perfectly harmonic behaviour.

are in-plane (A′).

The numbering of the 39 normal modes, their symmetries and their wavenumbers in the electronic ground and excited states are compiled in Table 8.1. The last column of this Table shows the largest elements of the Duschinsky matrix, which was calculated from the respective Hessians at the equilibrium positions and facilitates the assignments of ground states modes to excited state vibrations.

From the excitations, the character of the lowest electronically excited state has been determined to be $^1\mathrm{L}_b$ like in the nomenclature of Platt, while the second excited singlet state is $^1\mathrm{L}_a$ like.

8.4.2 Experimental results

The fluorescence excitation spectrum is similar to that, already shown in a variety of publications. It can be found in the online supplementary material (Figure 8.10) with the bands marked with an asterisk, that were used as excitation bands for obtaining the SVLF spectra. All observed intensities and the respective assignments of the transitions are compiled in Table 8.6 of the online supporting material. We use the following convention for designation of vibrational levels and transitions: $(Q_{Mode\#})^n_m$ designates the vibronic transition with m quanta of $Q_{Mode\#}$ excited in the electronic ground state to n quanta of $Q_{Mode\#}$ excited in the electronically excited state. $(Q_{Mode\#})_m$ is the mth vibrational level of $Q_{Mode\#}$ in the ground state and $(Q_{Mode\#})^n$ the nth vibrational level of $Q_{Mode\#}$ in the electronically excited state.

The assignments of the vibronic bands in absorption and of the emission bands have been made on the basis of the results of the *ab initio* normal mode analysis presented in Table 8.1. In cases, where the assignments were not unequivocal, a FC simulation has been performed and the assignments checked, by the predicted intensities. In case of deviations, the assignments were iterated, until agreement with the wavenumbers from the *ab initio* calculations and the intensities from the FC simulations was obtained. All observed wavenumbers both in absorption and in emission, the transition intensities and the assignments are given in Tables 8.6 and 8.7 of the online supplementary material. Tentative assignments of vibrational hot bands have been given on the basis of combination differences using observed wavenumbers and their (harmonic) overtones.

Figure 8.2 shows the SVLF spectrum of the electronic origin of benzimidazole at 36021.4 cm^{-1}, along with a FC simulation using the unaltered *ab initio* parameters (second trace) and a FC fit with the best fit parameters reported in Table 8.8 (third trace). In the FC simulation, the *ab initio* geometry of the ground and the excited state and the *ab initio* Hessians of both states are used without changes, while in the FC fit the geometry

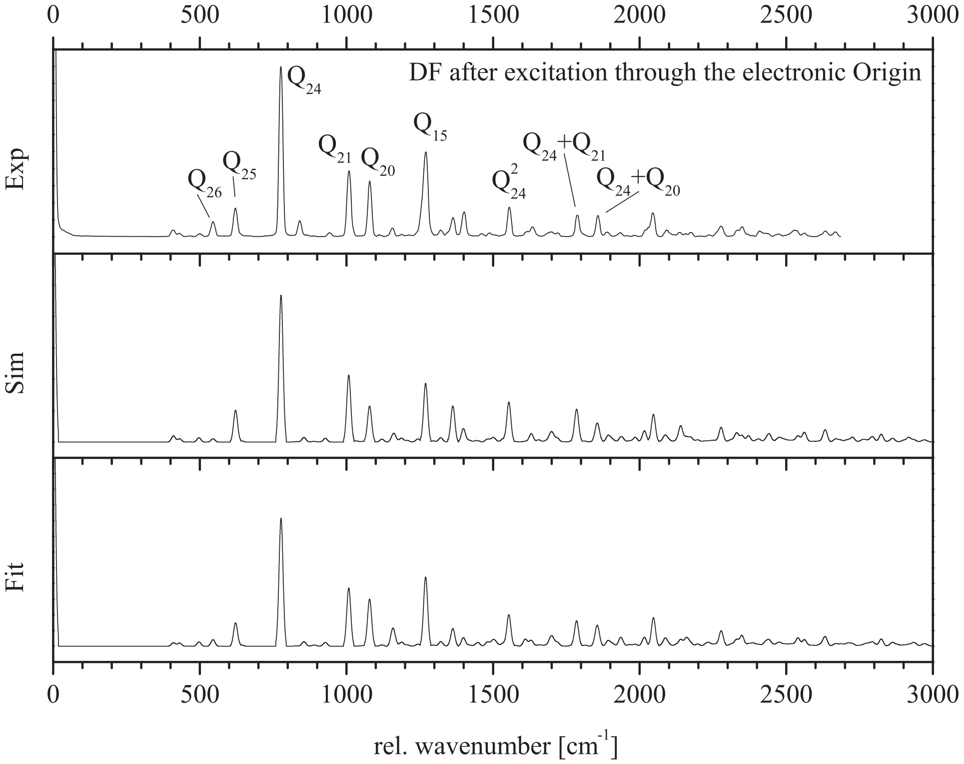

Figure 8.2: SVLF spectrum of the electronic origin of benzimidazole along with a simulation using the *ab initio* parameters and a FC fit.

of the excited state is altered in order to minimize the squared deviations of the vibronic intensities and the changes of the rotational constants upon excitation. The general agreement between the experimental and the simulated and the fit spectrum is good. It's noteworthy, that already the simulation with the *ab initio* parameters reproduces the experimental spectrum closely. Deviations, like the too small intensities of Q_{20} and Q_{15} in the simulation are corrected in the fit.

This means, that the geometry change upon electronic excitation is reasonably well described at the SCS-CC2/cc-pVTZ level of theory. The spectrum is dominated by in-plane modes, vibration Q_{24} being by far the most intense one. In the spectral region above 1500 cm^{-1} overtones and combination bands involving Q_{24} are found.

Figure 8.11 of the online supporting material shows the SVLF spectrum of the vibronic band at $0,0+303$ cm^{-1}, along with a FC simulation using the using the *ab initio* parameters and a FC fit with the best fit parameters from Table 8.8. Two different assignments of $0,0+303$ cm^{-1} seem possible. If the band is assigned to the fundamental of the Q_{37} out-of-plane motion (calculated at 296 cm^{-1}) the most intense emission band should be around 431 cm^{-1}, which is the respective mode according to the *ab initio* calculations for the electronic ground state. The strongest emission band is indeed found at 431 cm^{-1}, seemingly supporting this assignment. However, there should be no strong fundamental of an out-of-plane mode in a planar molecule with transition dipole moment in the plane of symmetry. Also, the emission spectrum is dominated by combination bands of in-plane vibrations with the excited, diagonal mode. This observation motivates a different assignment of the $0, 0 + 303$ cm^{-1} vibronic band. The first overtone of the lowest out-of-plane vibration Q_{39} can be deduced from the *ab initio* calculations assuming harmonicity for this mode to be 310 cm^{-1} (2×155 cm^{-1}, cf. Table 8.1). The respective vibration in the ground state would consequently be at 458 cm^{-1} (2×229 cm^{-1}), close enough to the experimental value to make this assignment the most probable one. Nevertheless, the agreement between the Franck-Condon simulation/fit with the experimental spectrum, shown in Figure 8.11 of the online supporting material is considerably less than for all the in-plane modes. The reason for this obvious discrepancy can be found inspecting the elongation vectors of this mode. The out-of-plane vibration Q_{39} can best be described as a butterfly motion of the two rings. This motion is represented by a symmetric double minimum potential, and the harmonic approximation, which is the basis for the FC fit, completely fails.

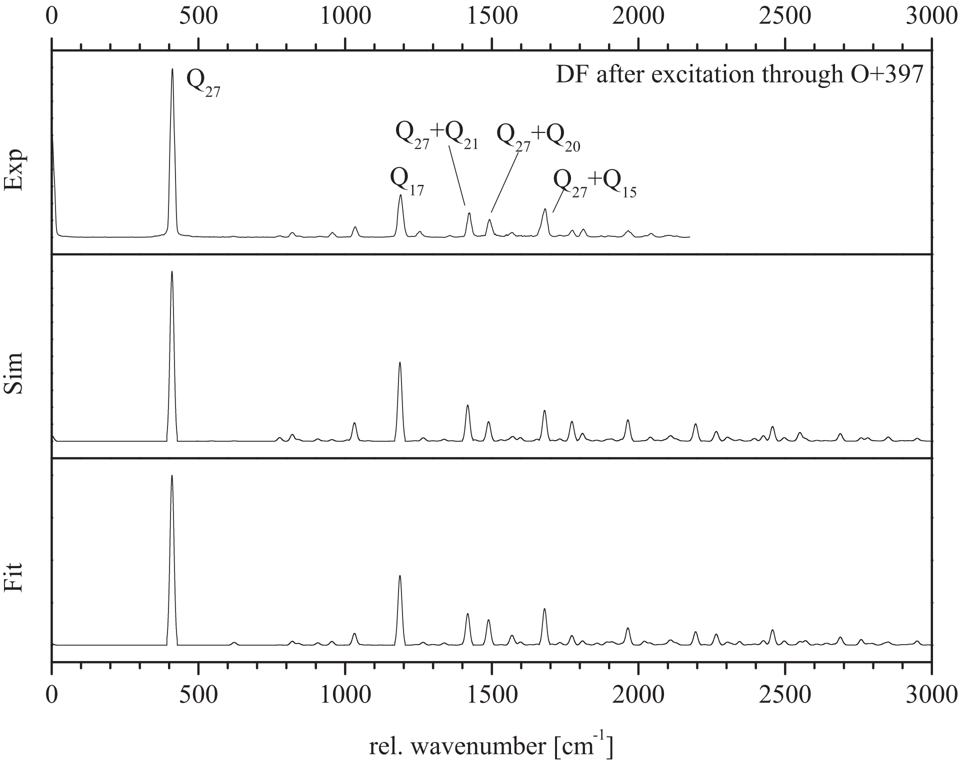

Figure 8.3: a) SVLF spectrum of the vibronic band at 397 cm^{-1}.
b) Simulation using the Geometries and Hessians from the CC2/cc-pVTZ *ab initio* calculations.
c) Best fit using the parameters for the geometry displacements given in Table 8.8.

Figure 8.12 of the online supporting material shows the SVLF spectrum of the vibronic band at $0,0 + 371$ cm^{-1}, along with a FC simulation using the best fit parameters from Table 8.8. While the assignment of the excited state vibronic band to the fundamental of the Q_{35} out-of-plane mode (calculated at 360 cm^{-1}) seems possible, the mode with the largest Duschinsky coefficient in the ground state would be at 582 cm^{-1} in clear disagreement with an experimental value of 497 cm^{-1}. As in the case of the 303 cm^{-1} vibronic band, the assignment to an overtone of an out-of-plane vibration gives an unequivocal assignment: The overtone of Q_{35} in the excited state is calculated to be 366 cm^{-1}, close to the observed vibronic band. The diagonal transition leads to the ground state vibrational level of 510 cm^{-1} (2×255 cm^{-1}), in good agreement with the experimental value of 497 cm^{-1}.

Since both vibronic bands at 303 and 371 cm^{-1} are due to motions, that cannot be described properly in the harmonic approximation, their emission intensities are excluded from the FC fit, and the respective spectra are only shown in the online supporting material.

The SVLF spectrum of the vibronic band at $0,0 + 397$ cm^{-1} is shown in Figure 8.3 along with a FC simulation using the geometries and Hessians from the CC2/cc-pVTZ *ab initio* calculations and with a FC fit, using the parameters for the geometry displacements given in Table 8.8. The excitation band has been assigned to the fundamental of the in-plane vibration Q_{27}. The dominating transition in emission is the diagonal $(Q_{27})_1^1$ band (apart from the resonance fluorescence $(Q_{27})_0^1$, which comes along with the stray light) All other bands, which have been assigned in the emission spectrum are combination bands of Q_{27} with other in-plane modes. In contrast to the SVLF spectra of the $0,0+303$ cm^{-1} and the $0,0 + 371$ cm^{-1} bands, the agreement between the experimental spectrum and the FC fit is nearly perfect.

The SVLF spectrum after excitation of the vibronic band at $0,0 + 566$ cm^{-1} is given in Figure 8.4, along with a FC simulation using the best fit parameters from Table 8.8. The excitation band in the absorption spectrum is assigned to the in-plane mode Q_{25}. The SVLF spectrum is dominated by the diagonal transition in Q_{25} and in overtones and combination bands containing this mode. Again a very close agreement between the experimental and the fit spectrum is found, as expected for an in-plane vibration.

The vibronic band at $0,0 + 731$ cm^{-1} is assigned to the in-plane vibration Q_{24}. This mode already dominates the emission spectrum through the vibrationless origin. After excitation of this mode, the emission spectrum shows a long progression in Q_{24}, while no combination bands of Q_{24} with other in-plane vibrations show up. Good agreement between the fit and the experimental spectrum is found.

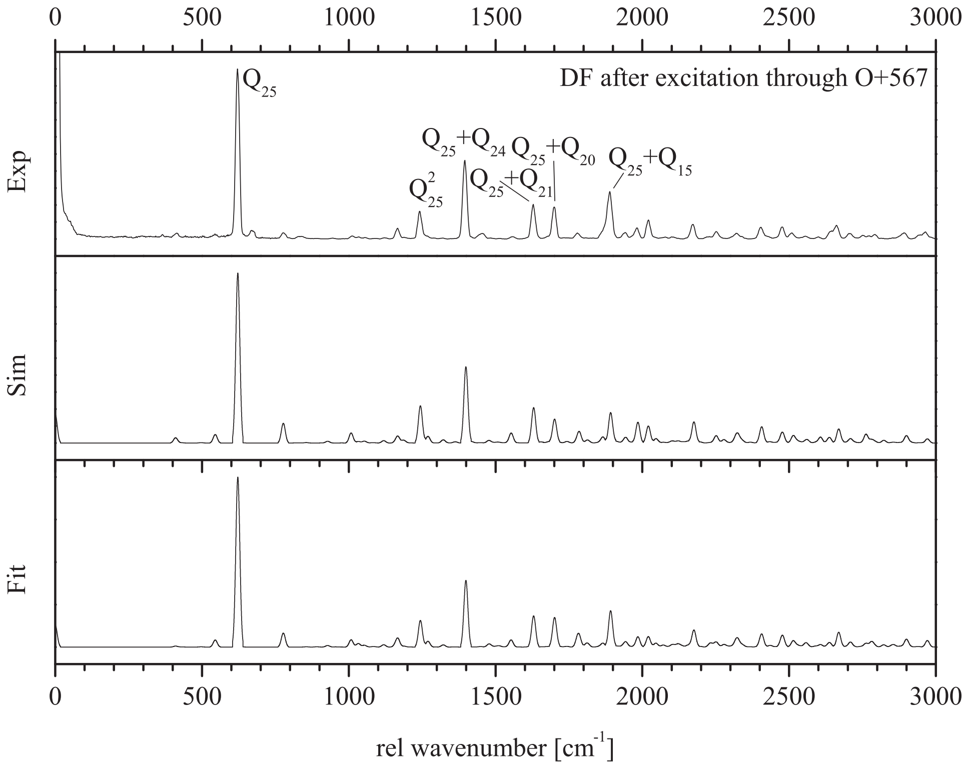

Figure 8.4: a) SVLF spectrum of the vibronic band at 566 cm^{-1}.
b) Simulation using the Geometries and Hessians from the CC2/cc-pVTZ *ab initio* calculations.
c) Best fit using the parameters for the geometry displacements given in Table 8.8.

The vibronic band at 961 cm^{-1} in absorption is assigned to the in-plane mode Q_{20}. The emission spectrum through this band is shown in Figure 8.6. Compared to the previous spectra the higher line density, the larger number of bands in the experimental spectrum which have no counterpart in the theoretical spectrum and the appearance of a non-resonant background is noticeable. Especially, the range $1200 - 1400$ cm^{-1} around Q_{15} shows strong intensity deviations. The last trace (Fit*) gives the fit results from a FC fit of all other modes, with the modes Q_{20} and Q_{31} (see below) excluded from the fit.

Even larger deviations are observed for the emission spectrum through the vibronic band at 1265 cm^{-1}, shown in Figure 8.7. This vibronic band is assigned to the overtone of the out-of-plane vibration Q_{31}. No satisfactory FC fit could be obtained for this emission spectrum, either. Although most bands are present in the fit, their intensities are much larger than in the experimental spectrum and there is a considerable background, which is much larger than in the spectrum of $0,0+961$ cm^{-1}. The last trace (Fit*) gives the fit results from a FC fit of all other modes, with the modes Q_{31} and Q_{20} (see above) excluded from the fit.

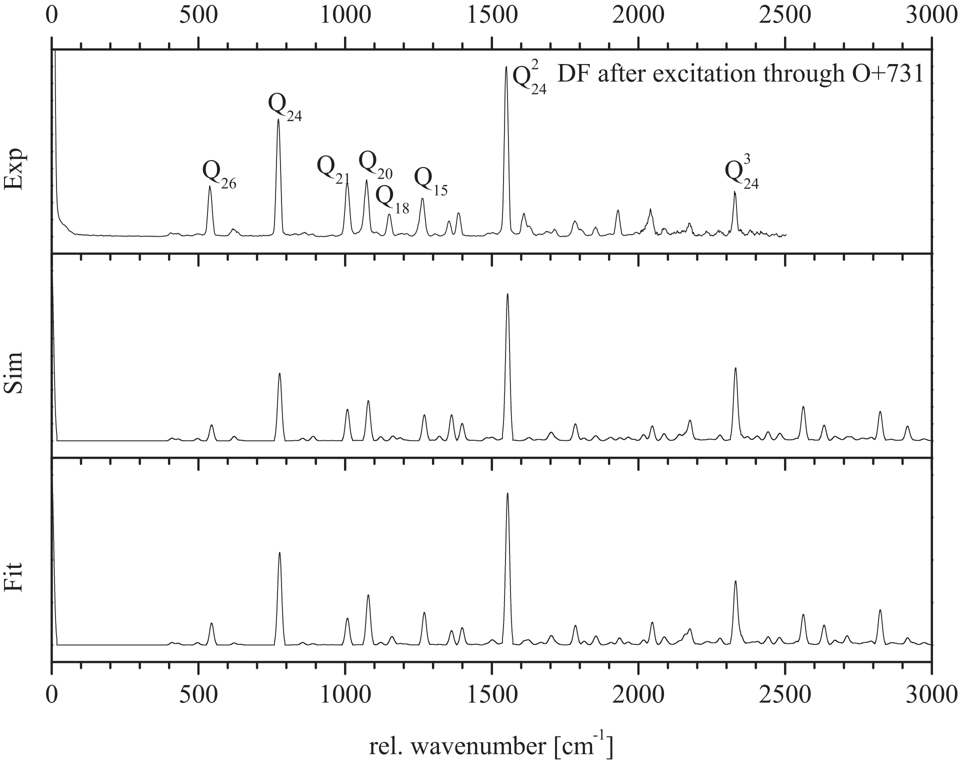

Figure 8.5: a) SVLF spectrum of the vibronic band at 731 cm^{-1}.
b) Simulation using the Geometries and Hessians from the CC2/cc-pVTZ *ab initio* calculations.
c) Best fit using the parameters for the geometry displacements given in Table 8.8.

8.5 Discussion

The intensities of the fluorescence emission bands after excitation of different vibronic bands have been fit using the program FCFIT, which was developed in our group.[28, 86, 185] Only emission band intensities, from excitation through in-plane vibrations have been taken into account, since the anharmonic nature of the out-of-plane vibrations, that describe the relative motions of the six- and the five-ring (butterfly and twist motion), prohibits the use of the FCFit model, which is based on the harmonic approximation. While in principle the use of out-of-plane vibrations is possible, as long as they are sufficiently harmonic, our model completely fails in the case of the energetically low lying butterfly and twist motions, which both are described by double minimum potentials in which tunnelling through the barrier demands for linear combinations of the harmonic wave functions within each potential well.

Additionally, the changes of the rotational constants upon electronic excitation of four benzimidazole isotopologues, which have been taken from Ref.[201] have been used in the fit of the geometry changes. The ground state *ab initio* geometry was displaced along

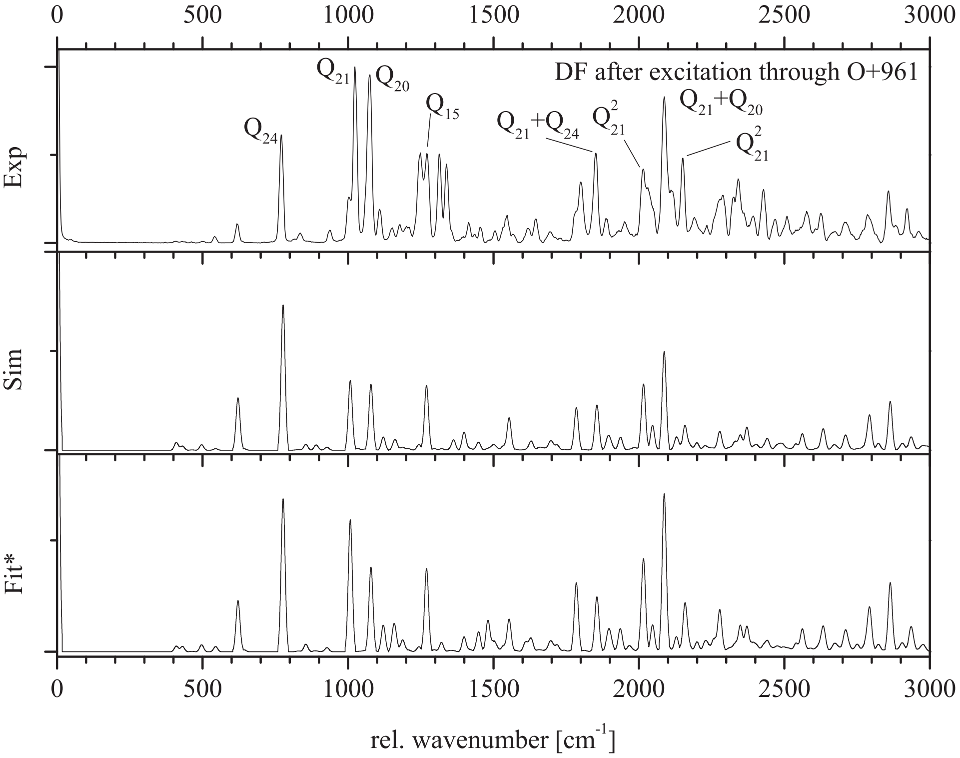

Figure 8.6: a) SVLF spectrum of the vibronic band at 961 cm^{-1}.
b) Simulation using the Geometries and Hessians from the CC2/cc-pVTZ *ab initio* calculations.
c) Best fit using the parameters for the geometry displacements given in Table 8.8.

the 21 modes given in Table 8.8 of the online supporting material and the displacement varied until the combined χ^2 of the rotational constants and vibronic intensities were minimized. A total of 182 emission line intensities and of 12 rotational constants has been used to fit 21 displacement modes. Only 8 of the 12 rotational constants could be used in the fit independently, since the molecule is planar and in each isotopologue one of the three rotational constants can be expressed by the other two using the planarity relation $I_a - I_b - I_c = 0$. In principal $3N - 6$ geometry parameters are necessary to define the structure of a molecule in internal coordinates. However, in a planar molecule, the $3N - 3$ coordinates that define the dihedral angles are fixed and the complete geometry is determined by $2N - 3$ internal coordinates. Thus 27 independent geometry parameters are needed for a full description of the geometry or the geometry changes upon electronic excitation. The geometry changes of the four hydrogen atoms at the six-ring and of the hydrogen at C2 in the five-ring have been omitted from the fit, by excluding CH stretching vibrations from the basis for the molecular distortion. Since no save assignments for the CH stretching region in the emission spectra could be given, their intensity fit would be too doubtful. Since we are mainly interested in the changes of the heavy atom structure,

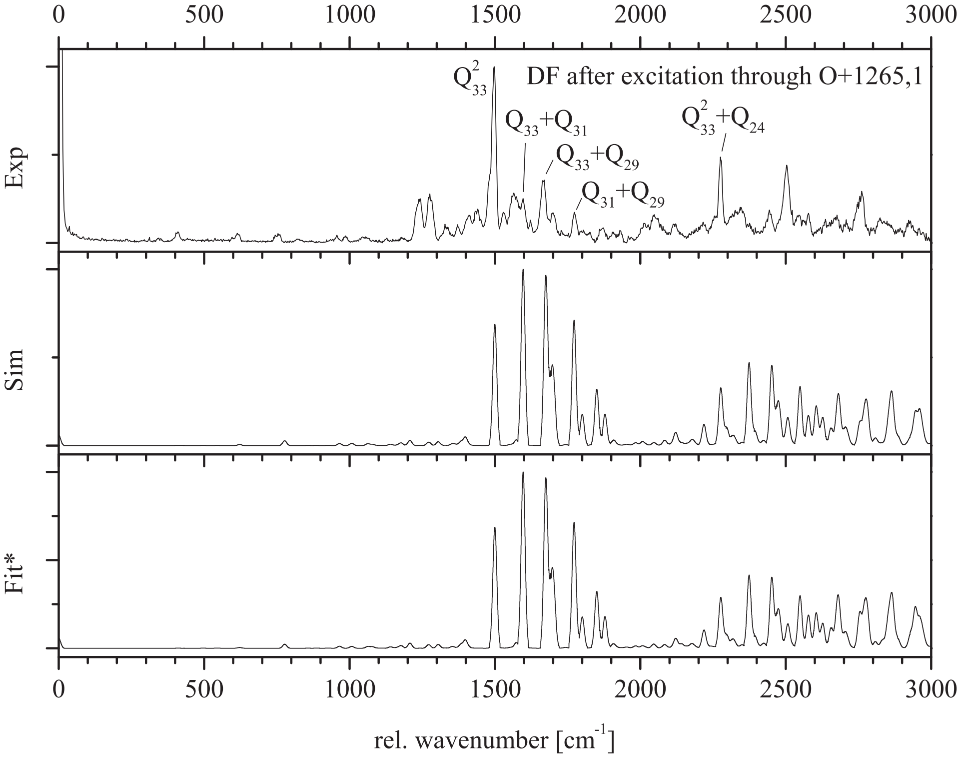

Figure 8.7: a) SVLF spectrum of the vibronic band at 1265 cm^{-1}.
b) Simulation using the Geometries and Hessians from the CC2/cc-pVTZ *ab initio* calculations.
c) Best fit using the parameters for the geometry displacements given in Table 8.8.

this is not a serious restriction.

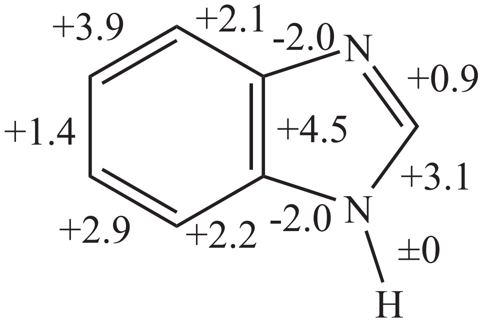

Figure 8.8: Geometry changes of benzimidazole upon electronic $S_1 \leftarrow S_0$ excitation from the FC fit.

Table 8.3 shows the good agreement between the experimental and fit values for the changes of the rotational constants of 1H2H, 1D2H, 1H2D, and 1D2D-benzimidazole (for numbering of the substitution position of the isotopologues refer to Figure 8.1).

The geometry changes which have been calculated in the basis of the 21 normal mode displacements are expressed as bond length changes in Figure 8.8 and in Table 8.2 and are compared to the results of SCS-CC2 calculations. Good agreement is found between the FC and the *ab initio* calculated displacements. A more or less uniform expansion of the six-ring is accompanied by alternating expansions and contractions of

Table 8.2: Bond lengths of benzimidazole in picometer in the electronic ground and lowest excited singlet state from SCS-CC2 calculations utilizing the cc-pVTZ basis set and from the FC fit. The reference state for the geometry changes is the electronic ground state. Therefore, the geometry parameters for the ground state in FC fit have been taken from the SCS-CC2 calculations. For atomic numbering cf. Figure 8.1.

state	S_0		S_1		S_1-S_0	
method	CC2	FCFit	CC2	FCFit	CC2	FCFit
N1C2	137.4	137.4	141.6	140.5	+4.2	+3.1
C2N3	131.8	131.8	132.4	132.7	+0.6	+0.9
N3C9	138.8	138.8	137.6	136.8	−1.2	−2.0
C9C4	139.9	139.9	141.0	142.0	+1.1	+2.1
C4C5	139.0	139.0	143.4	142.9	+4.4	+3.9
C5C6	140.9	140.9	143.0	142.3	+2.1	+1.4
C6C7	139.1	139.1	142.3	142.0	+3.2	+2.9
C7C8	139.6	139.6	141.6	141.8	+2.0	+2.2
C8C9	141.6	141.6	146.2	146.1	+4.6	+4.5
C8N1	138.0	138.0	136.0	136.0	−2.0	−2.0
N1H	100.7	100.7	100.8	100.7	+0.1	±0

the bond lengths in the five-ring (cf. Figure 8.8).

The emission intensities after pumping the two energetically highest vibronic bands at 961 and 1265 cm^{-1} have not been used in the FC fit of the geometry changes, due to large intensity deviations. They will be discussed in the following.

In the spectrum of the vibronic band at $0,0 + 961$ cm^{-1} (the fundamental of mode Q_{20}), considerable deviations in the FC intensities between the experiment and the fit occur for some bands. While most of the intensities are well described, there are regions in the SVLF spectrum (mostly around Q_{15}) with quite a large number of additional bands in the experimental spectrum, displaying unexpectedly high intensities. They cannot be described properly within the Condon approximation made in the FC description of the spectra.

Perturbations due to Herzberg-Teller (HT) interaction to a higher lying electronic state are probably responsible for the appearance of the additional bands. Borin and Serrano-Andrés[22] calculated an adiabatic energy difference of 4000 cm^{-1} between the lower-lying ^1L_b and the higher-lying ^1L_a state at CASPT2 level and a difference in oscillator strength of a factor of two. Such a large energy difference to the perturbing state, along with a relatively small difference in oscillator strength would make HT interactions pretty small. Nevertheless, both states strongly mix, what has been shown by the orientations of the transition dipole moments,[201] that are in disagreement with the predictions from the CASPT2 calculations. The three modes, that show the largest emission intensity differences between FC theory and experiment are Q_{16} at 1270 cm^{-1}, Q_{20} at 1079 cm^{-1}

Table 8.3: Experimentally determined changes of the rotational constants (in MHz) of the electronic origin band of four benzimidazole isotopologues from Ref. [201] along with the results of the FC fit. The numbering of the substitution positions refers to Figure 8.1.

	1H2H		1D2H	
	exp.	fit	exp.	fit
ΔA/MHz	−155.72	−155.86	−149.98	−149.99
ΔB/MHz	−15.28	−15.12	−13.77	−13.78
ΔC/MHz	−21.40	−21.57	−20.47	−20.79
	1H2D		1D2D	
	exp.	fit	exp.	fit
ΔA/MHz	−156.27	−156.00	−150.26	−150.20
ΔB/MHz	−14.67	−14.56	−13.53	−13.33
ΔC/MHz	−20.65	−20.86	−19.85	−20.036

and Q_{21} at 1008 cm^{-1}. The left part of Figure 8.9 gives the main contributions of the displacement vectors to the respective modes. On the right hand side, the main bond length differences between the optimized S_1 and S_2 structures from CASSCF calculations of Serrano-Andrés and Borin[22] are displayed. Comparison shows, that these three modes contribute strongly to the geometry differences between S_1 and S_2 state. Therefore, we expect them to be strong coupling modes for Herzberg-Teller perturbations, and their vibronic intensities will deviate from the pure FC intensities.

The experimental SVLF spectrum of the $0,0 + 1265$ cm^{-1} band, assigned to the first overtone of the out-of-plane vibration Q_{31} finally shows very poor agreement with the FC fit. Many lines in the experimental spectrum are broadened, or even completely missing. We attribute this behaviour to the onset of IVR in the excited state, coupling the bright zero-order state, which shows resonance fluorescence to the ground state to the bath of background states, from which sequence transitions to a multitude of ground state levels is possible, leading to an effective broadening of the emission spectrum. The onset of IVR at about 1300 cm^{-1} is in agreement with the finding for similar molecules like indole.[207]

8.6 Conclusions

Using the combined information from SVLF spectra and rotational constants we were able to fit the complete structural changes of benzimidazole upon electronic excitation to the lowest excited singlet state. Since the basis for the geometry changes is of equal size as the $2N - 3$ coordinates, that are needed for a full description of the geometry of a planar molecule, and thus no further model approximations have to be made, the agreement between *ab initio* calculated and FC fit bond length displacement is good.

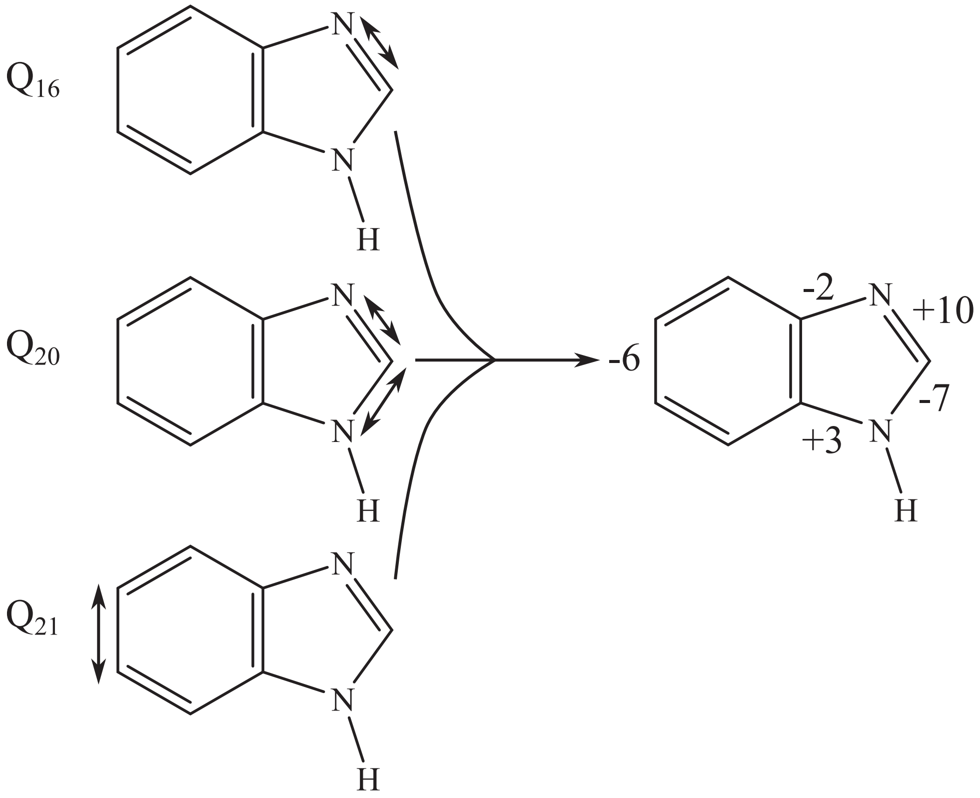

Figure 8.9: Left: Main distortions of the three vibrational modes Q_{16}, Q_{20} and Q_{21}, whose experimentally determined intensities are considerably larger, than expected from a pure FC fit.
Right: Main geometry differences in picometer between the optimized S_1 and S_2 structures from CASSCF calculations in Ref. [22]

Even, if only a relatively small number of inertial data from different isotopologues is at hand, the addition of a sufficient number of intensity data from various SVLF spectra can add sufficient information for a reliable determination of the structural changes upon electronic excitation.

8.7 Acknowledgements

The authors like to thank the Universitätsrechenzentrum Köln for the granted computing time on Cheops. The financial support of the Deutsche Forschungsgemeinschaft (SCHM 1043/12) is gratefully acknowledged.

8.8 Supplementary Material

The supplementary material contains:

(I) A table with the ground state Cartesian coordinates of benzimidazole. (Table 8.4)

(II) A table with the lowest excited singlet state Cartesian coordinates of benzimidazole. (Table 8.5)

(III) A figure with the fluorescence excitation spectrum of benzimidazole. (Figure 8.10)

(IV) A figure with the SVLF spectrum of the vibronic band at 303 cm^{-1} (Figure 8.11)

(V) A figure with the SVLF spectrum of the vibronic band at 371 cm^{-1} (Figure 8.12)

(VI) A table with the experimental wavenumbers of the fluorescence absorption spectrum, the observed intensities of the lines, and the assignments. (Table 8.6)

(VII) A table with the experimental wavenumbers of the fluorescence emission spectra through seven vibronic bands, the observed intensities of the lines, and the assignments. (Table 8.7)

(VIII) A table with the displacements along the normal modes of benzimidazole from the FC fit. (Table 8.8)

Table 8.4: CC2/cc-pVTZ Cartesian geometry of benzimidazole in the S_0 state.

n	-.14872100752120E-02	0.43061654212683E-04	0.75773522320356E-03
c	0.14058637136661E-02	0.46696735999478E-04	0.13805019106195E+01
c	0.13728297865564E+01	0.32918151152164E-05	0.17319096644828E+01
n	0.21724208271817E+01	-.27469220324677E-04	0.59691041106500E+00
c	0.13123003271677E+01	-.31261634963923E-04	-.40158306730824E+00
c	0.17442841293053E+01	0.25728268810343E-04	0.30808404468343E+01
c	0.73191829396489E+00	-.31002604018071E-05	0.40330206269268E+01
c	-.62807397532737E+00	-.24140864133956E-04	0.36639774807448E+01
c	-.10216132125019E+01	0.23418507464858E-04	0.23296446285417E+01
h	-.20675630607618E+01	0.18114464865495E-04	0.20521762795296E+01
h	-.13850059300310E+01	-.85868199021605E-04	0.44369224301608E+01
h	0.27892319781003E+01	0.86925392394073E-04	0.33597392072331E+01
h	0.98884401551363E+00	-.28080647054006E-04	0.50838202084697E+01
h	0.15765602626383E+01	-.10766999605868E-03	-.14471467365296E+01
h	-.80841057108976E+00	0.70353983886455E-04	-.60116295916244E+00

Table 8.5: CC2/cc-pVTZ Cartesian geometry of benzimidazole in the S_1 state.

n -.15088051365492E+01	0.11249283618714E+01	-.56165335445247E-05
c -.20637492603043E+00	0.73352891716317E+00	0.79885690783133E-04
c -.28917222497153E+00	-.72656077015467E+00	0.78486455615082E-04
n -.16009989959339E+01	-.11423517809766E+01	0.39514098808589E-04
c -.23240570413911E+01	-.33360688647961E-01	-.32428402598133E-04
c 0.89477028465158E+00	-.14918750110500E+01	0.48816265209545E-04
c 0.21252746988899E+01	-.75590357968428E+00	-.26923725640952E-04
c 0.21891600667896E+01	0.67282393156004E+00	-.64522810816076E-05
c 0.10063447211165E+01	0.14643050068673E+01	0.59680976307026E-04
h 0.10349086889021E+01	0.25440428247890E+01	0.48929414767412E-04
h 0.31581488874343E+01	0.11506258311790E+01	-.37321370298253E-04
h 0.87270590259656E+00	-.25708648279845E+01	0.18187707801719E-04
h 0.30568819931175E+01	-.13065926038902E+01	-.11469290764281E-03
h -.33983878118795E+01	0.33824666774757E-01	-.72321356073828E-04
h -.18394377086700E+01	0.20773246475748E+01	-.77733448893872E-04

Table 8.6: Wavenumbers (relative to 0,0 at 36021.4 cm^{-1}, intensities and assignments of the experimentally observed absorption bands. H designates hot bands.

S_1	Intensity	Assignment	S_1	Intensity	Assignment
-24	0.06	H $(Q_{27})_2^2$	1100	0.17	
-12	0.08	H $(Q_{27})_1^1$	1103	0.09	
0	1	0_0^0	1125	0.20	$(Q_{24})_0^1(Q_{27})_0^1$
100	0.11	0_0^0 (Cluster)	1136	0.12	$(Q_{18})_0^1$
148	0.06	0_0^0 (Cluster)	1142	0.07	
303	0.20	$(Q_{39})_0^2$	1185	0.07	
371	0.18	$(Q_{38})_0^2$	1192	0.10	
397	0.20	$(Q_{27})_0^1$	1196	0.11	$(Q_{24})_0^1(Q_{26})_0^1$
432	0.08	H	1208	0.08	
460	0.08	$(Q_{37})_1^3$	1217	0.08	
478	0.16	$(Q_{26})_0^1$	1226	0.13	$(Q_{16})_0^1$
518	0.09	$(Q_{25})_1^2$	1250	0.08	
541	0.04	$(Q_{33})_0^1$	1259	0.14	$(Q_{15})_0^1$
554	0.08	H	1265	0.30	$(Q_{31})_0^2$
567	0.27	$(Q_{25})_0^1$	1279	0.06	
590	0.05	$(Q_{37})_0^2$	1297	0.25	$(Q_{14})_0^1$
647	0.06	H	1303	0.06	
668	0.08	H	1303	0.26	

Continued on next page

S_1	Intensity	Assignment	S_1	Intensity	Assignment
675	0.05	$(Q_{29})^1_0$	1323	0.30	$(Q_{13})^1_0$
683	0.04	$(Q_{34})^1_0(Q_{39})^1_0$	1340	0.10	
690	0.04	H	1345	0.1	$(Q_{29})^2_0$
704	0.07	H	1359	0.05	$(Q_{20})^1_0(Q_{27})^1_0$
715	0.21	$(Q_{35})^2_0$	1363	0.11	$(Q_{21})^1_0(Q_{26})^1_0$
731	1.00	$(Q_{24})^1_0$	1383	0.07	$(Q_{12})^1_0$
766	0.02	$(Q_{28})^1_0$	1396	0.05	
821	0.08		1401	0.06	
828	0.03	$(Q_{23})^1_0$	1414	0.07	
833	0.13	$(Q_{33})^1_0(Q_{37})^1_0$	1425	0.12	$(Q_{11})^1_0$
855	0.04		1438	0.09	$(Q_{10})^1_0$
864	0.08	$(Q_{26})^1_0(Q_{27})^1_0$	1446	0.05	$(Q_{20})^1_0(Q_{26})^1_0$
883	0.29	$(Q_{22})^1_0$	1451	0.17	$(Q_{24})^2_0$
887	0.21	$(Q_{21})^1_0$	1463	0.36	
901	0.13	H	1472	0.05	
910	0.11		1486	0.24	
938	0.30		1503	0.04	
947	0.29	H	1527	0.06	$(Q_{28})^2_0$
957	0.32		1535	0.18	$(Q_9)^1_0$
961	0.8	$(Q_{20})^1_0$	1557	0.06	
965	0.35		1565	0.07	$(Q_8)^1_0$
967	0.52		1614	0.05	$(Q_7)^1_0$
1031	0.09	$(Q_{25})^1_0(Q_{26})^1_0$	1669	0.04	
1043	0.12	$(Q_{19})^1_0$	1676	0.03	
1064	0.09	$(Q_{34})^2_0$	1691	0.06	

Table 8.7: Intensities of the observed emission bands. The first line gives the wavenumber of the excited bands, the first column the wavenumbers of the emission bands. The entries of the table represent the intensities, with the most intense band (apart form the excited band whose intensity is biased by stray light.) in each of the emission spectra normalized to 1.

S_0/S_1	0	302	371	397	566	731	961	1265	Assignment
	0^0_0	$(Q_{39})^2_0$	$(Q_{38})^2_0$	$(Q_{27})^1_0$	$(Q_{25})^1_0$	$(Q_{24})^1_0$	$(Q_{20})^1_0$	$(Q_{31})^2_0$	
409	0.039			1.000					$(Q_{27})_1$
431	0.020	1.000							$(Q_{39})_2$
465	0.004	0.097	0.109						$(Q_{39})_1(Q_{38})_1$
497	0.018		1.000						$(Q_{38})_2$

Continued on next page

S_0/S_1	0	302	371	397	566	731	961	1265	Assignment
	0_0^0	$(Q_{39})_0^2$	$(Q_{38})_0^2$	$(Q_{27})_0^1$	$(Q_{25})_0^1$	$(Q_{24})_0^1$	$(Q_{20})_0^1$	$(Q_{31})_0^2$	
545	0.088					0.300			$(Q_{26})_1$
622		0.077		0.006	1.000	0.046			$(Q_{25})_1$
671			0.021		0.049				$(Q_{37})_1(Q_{39})_1$
777	1.000	0.011		0.009	0.036	0.691	0.610		$(Q_{24})_1$
820				0.028		0.018			$(Q_{27})_2$
841	0.093			0.007	0.015				$(Q_{35})_1(Q_{38})_1$
855		0.036				0.025			$(Q_{37})_2$
891		0.013		0.007		0.014			$(Q_{23})_1$
928		0.014							$(Q_{36})_2$
945	0.022			0.03		0.008			$(Q_{22})_1$
993		0.022	0.045						$(Q_{39})_1(Q_{32})_1$
1008	0.387				0.017	0.311	1.000		$(Q_{21})_1$
1035			0.029	0.062	0.011				$(Q_{38})_1(Q_{32})_1$
1052		0.049			0.009				$(Q_{39})_1(Q_{31})_1$
1079	0.327					0.333	0.950		$(Q_{20})_1$
1113			0.067						$(Q_{35})_2$
1157	0.050				0.064	0.132			$(Q_{18})_1$
1188	0.014			0.251					$(Q_{17})_1$
1207		0.235							$(Q_{28})_1(Q_{38})_1$
1236		0.022	0.040	0.035	0.163				$(Q_{25})_2$
1270	0.499	0.046	0.376			0.226	0.510		$(Q_{16})_1$
1305						0.016			$(Q_{15})_1$
1321	0.039				0.005				
1337			0.031						
1353						0.092			$(Q_{14})_1$
1363	0.113			0.011					$(Q_{13})_1$
1386		0.01				0.14			$(Q_{26})_1(Q_{31})_1$
1401	0.146	0.019			0.462				$(Q_{24})_1(Q_{25})_1$
1424				0.145					$(Q_{21})_1(Q_{27})_1$
1440		0.093	0.017						
1454					0.032				$(Q_{28})_1(Q_{35})_1$
1462	0.018								$(Q_{25})_1(Q_{31})_1$
1489	0.022	0.016	0.143	0.105		0.02		1.000	$(Q_{33})_2$
1512		0.067				0.023			
1556	0.173	0.01			0.013	1.000			$(Q_{24})_2$
1571			0.14	0.03					
1585		0.014						0.25	$(Q_{33})_1(Q_{31})_1$
1610						0.137			$(Q_8)_1$
1634	0.058	0.019			0.204	0.063			$(Q_{21})_1(Q25)_1$
1649			0.026						
1682				0.169		0.031		0.36	$(Q_{33})_1(Q_{29})_1$
1701	0.028	0.135			0.188				$(Q_{25})_1(Q_{20})_1$

Continued on next page

S_0/S_1	0	302	371	397	566	731	961	1265	Assignment
	0_0^0	$(Q_{39})_0^2$	$(Q_{38})_0^2$	$(Q_{27})_0^1$	$(Q_{25})_0^1$	$(Q_{24})_0^1$	$(Q_{20})_0^1$	$(Q_{31})_0^2$	
1719	0.023			0.013		0.045			$(Q_{30})_2$
1759			0.236						
1787	0.125	0.032		0.042	0.035	0.093			$(Q_{21})_1(Q_{24})_1$
1809			0.022	0.049		0.045			
1829		0.043							
1858	0.124	0.1	0.055			0.057			$(Q_{20})_1(Q_{24})_1$
1888	0.027	0.021	0.069		0.279				$(Q_{15})_1(Q_{25})_1$
1933	0.024				0.038	0.157			
1966				0.040					
1984		0.043			0.065				
2021					0.112				$(Q_{13})_1(Q_{25})_1$
2044	0.140	0.140	0.074	0.023		0.164	0.830		$(Q_{21})_2$
2091	0.039				0.012	0.05			
2117			0.027	0.114					
2135	0.025	0.015							
2174	0.025	0.028	0.020		0.086	0.079			
2235	0.0100					0.034			
2251					0.044				
2277	0.062	0.025	0.052			0.037		0.49	$(Q_{33})_2(Q_{24})_1$
2322					0.033	0.267			$(Q_{24})_3$
2350	0.058		0.061						
2409	0.032				0.069				
2473	0.015	0.338			0.071				
2509					0.036				
2528	0.039	0.138	0.068						
2562	0.020				0.016				
2601					0.012				
2634	0.033								
2665	0.027				0.080				
2709					0.031				
2762			0.033		0.022				
2837			0.037						
2890					0.036				
2963					0.041				

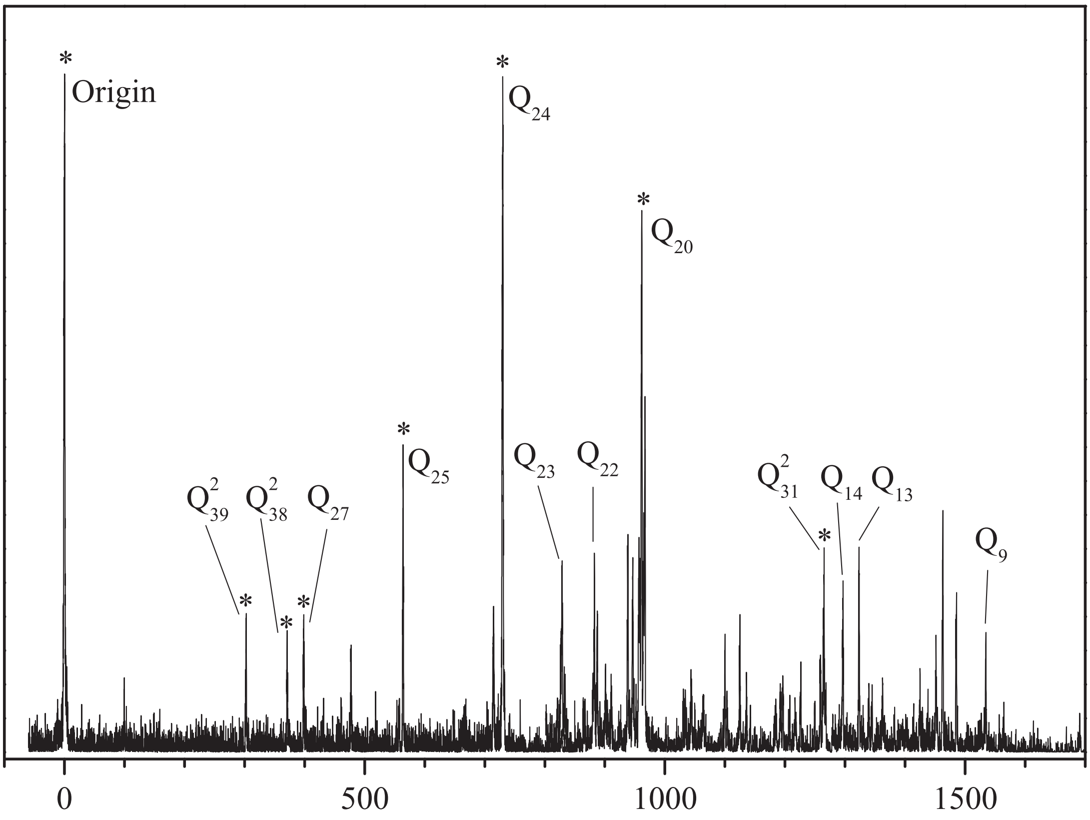

Figure 8.10: Fluorescence excitation spectrum of benzimidazole. The bands which have been excited for recording the SVLF spectra are marked with an $*$.

Table 8.8: Fitted factors of the displacements along the normal modes from the FC fit

Mode	displacement	Mode	displacement
Q_7	-0.0030386	Q_{18}	-0.021068
Q_8	-0.0086941	Q_{19}	0.00019715
Q_9	0.0089972	Q_{20}	-0.035343
Q_{10}	0.026003	Q_{21}	-0.013001
Q_{11}	0.0068613	Q_{22}	0.010402
Q_{12}	-0.018033	Q_{23}	-0.011491
Q_{13}	-0.0011287	Q_{24}	0.0026586
Q_{14}	0.037623	Q_{25}	-0.021579
Q_{15}	-0.0011802	Q_{26}	-0.0079566
Q_{16}	0.06977	Q_{27}	0.013988
Q_{17}	-0.013387		

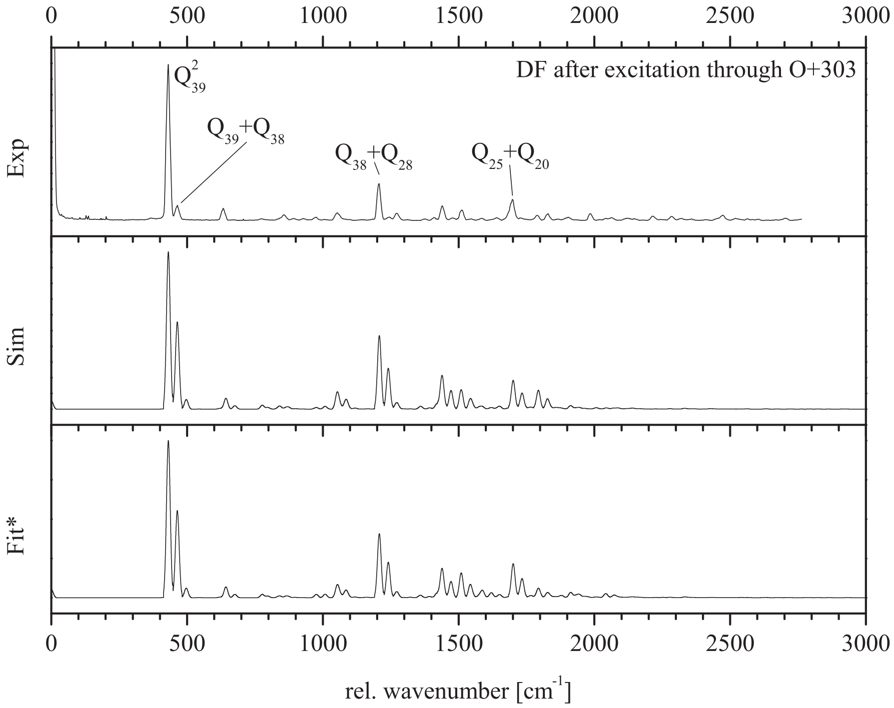

Figure 8.11: a) SVLF spectrum of the vibronic band at 302 cm^{-1}.
b) Simulation using the Geometries and Hessians from the CC2/cc-pVTZ *ab initio* calculations.
c) Best fit using the parameters for the geometry displacements given in Table 8.8

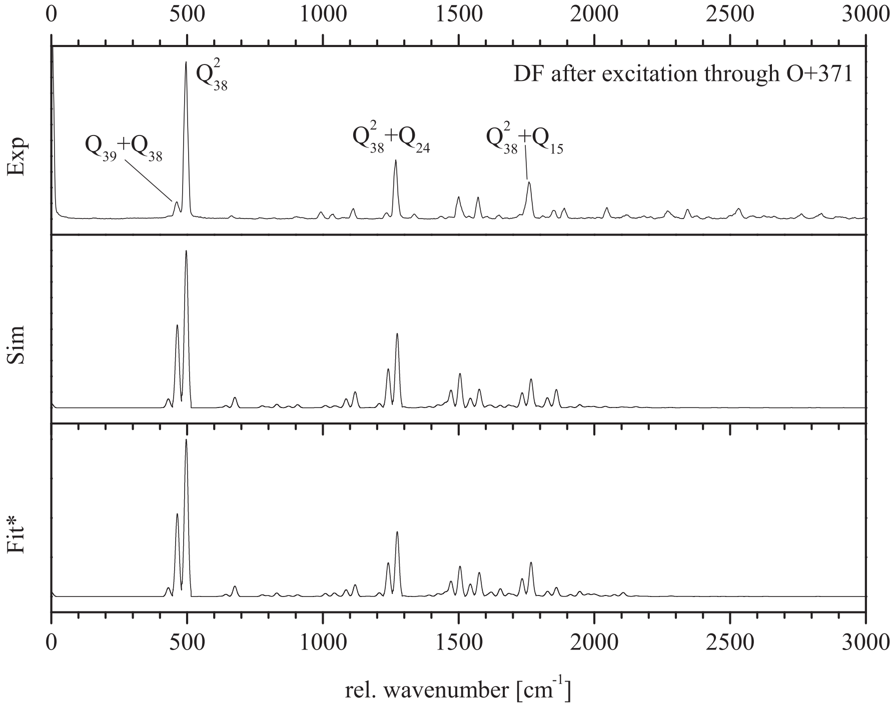

Figure 8.12: a) SVLF spectrum of the vibronic band at 371 cm^{-1}
b) Simulation using the Geometries and Hessians from the CC2/cc-pVTZ *ab initio* calculations.
c) Best fit using the parameters for the geometry displacements given in Table 8.8.

8.9 Contributions

Title: Determination of the Geometry Change of Benzimidazole upon Electronic Excitation from a Combined Franck-Condon/Rotational Constants Fit.

Authors: Benjamin Stuhlmann, Felix Gmerek, Daniel Krügler and Michael Schmitt.

submitted to: Journal of Molecular Structure (Impact Factor: 1.404)

The spectra presented in this paper were either measured either by myself or by Felix Gmerek during his master thesis under my supervision.

I proposed the initial assignment of the emission bands and carried out the intermediate Franck-Condon fits until the last refinement.

The final fit with all intensity points and the measurement of the spectra in Figures 8.6 and 8.7 were made by Felix Gmerek.

Daniel Krügler provided support with all aspects of the FCFIT program and its use in this project.

The *ab initio* calculations were made by Michael Schmitt, who also contributed his know-how to many aspects of this publication.

9. Summary

In this work, aromatic systems (both as isolated molecules and aggregates) have been studied with laser spectroscopy to gain information about their structure by the analysis of these vibronic spectra. The focus of interest shifted from the binding motives in different aromatic-acetylene clusters to the geometry change upon electronic excitation of monomers with different substituents.

The basic idea behind the cluster-projects was the elucidation of the formation pathways from monomers to the crystal seed. A stepwise formation was proposed and tested by comparing the binding motifs found in small clusters to those in the unit cell. Since the clusters are generated in a non-equilibrium process (co-expansion in a supersonic free jet), kinetically formed isomers are found alongside thermodynamically formed ones. The first project was concerned with clusters of benzene and acetylene. Electronic ground state energies and vibrations of these clusters were calculated by Jansen *et al.* with a combination of symmetry-adapted perturbation theory and density functional theory (DFT-SAPT) and confirmed with spin-component scaled Møller-Plesset perturbation theory (SCS-MP2). The infrared frequencies of these vibrations were compared to vibronic spectra (IR-UV hole-burning by Gernot Engler and Markus Böning for the valence vibrations around 3200 cm^{-1} and dispersed fluorescence for the fingerprint region below 1500 cm^{-1}) for a structural assignment.

For this, the 6_0^1-transition - also called the “false origin” - of benzene was excited with the UV laser. The UV resonances depend on the energy difference between electronic ground and excited state and therefore on the cluster size and binding motif. Electron density is drawn from the π-system of benzene in the cluster and this destabilises the excited $\pi\pi^*$ state, leading to a blue shift of the false origin that is different for each cluster isomer. This allows for isomer-specific spectroscopy even though all stable clusters are present in the jet.

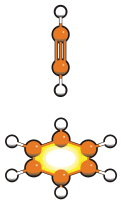

(a) BA$_1$

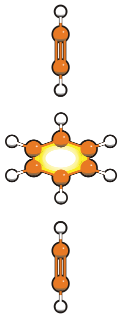

(b) BA$_2$

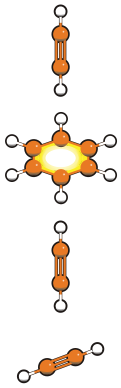

(c) BA$_3$

Figure 9.1: T-shaped benzene-acetylene clusters

In x-ray diffraction analyses of the benzene-acetylene co-crystal, B-A-B-A-…-ribbons are found where each two benzene molecules are bridged by one acetylene molecule that binds to one π-system with each of its hydrogen atoms.

As expected from the structure of the benzene-acetylene co-crystal, T-shaped structures such as these shown in Figure 9.1 are found predominantly. In addition to these T-shaped structures, ring-like structures - where some acetylene moieties bind with the π-electrons of their C≡C-triple-bond to hydrogen atoms of the benzene moiety - are observed. These ring-like structures are thermodynamic products while the T-shaped structures are less stable and formed kinetically.

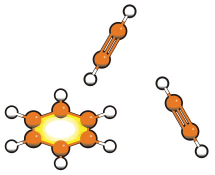
Figure 9.2: The ring-shaped BA_2 isomer

Each benzene-acetylene cluster BA_n up to the tetramer shows the structure of the underlying cluster BA_{n-1} with the additional acetylene moiety bonded either to the benzene or one acetylene. This becomes apparent from Figure 9.1 for the T-shaped isomers, but is also true for the ring-like isomers. The structure of the B_2A_2 tetramer results from adding one benzene moiety to the ring-like isomer of BA_2. This proves, that the aggregation proceeds stepwise starting from the T-shaped benzene-acetylene dimer.

The inter-molecular vibrations of the benzene-acetylene dimer - that originate from hindered rotations and translations of acetylene - have been detected with dispersed fluorescence both with their fundamental frequencies between 50 and 150 cm^{-1} and as combination bands with benzene skeleton vibrations. The hindered rotations and hindered translations perpendicular to the C_6 symmetry axis of benzene are doubly degenerate, which also confirms a T-shaped structure where the acetylene is oriented along the C_6 symmetry axis of benzene.

The dispersed fluorescence spectra of higher clusters are broadened by intramolecular vibrational redistribution.

The second composite that was investigated was the mixture of phenol and acetylene. The calculations were this time done by myself, with dispersion corrected density functional theory (DFT-D with the functional B97D) and Møller-Plesset perturbation theory (RI-MP2) and both results for each cluster isomer were compared to isomer-selective infrared spectra as described above. Spectral holeburning spectra were again measured by Gernot Engler and Markus Böning.

The energetic order of different isomers depends on the theory used, as DFT-D tends to favour structures where acetylene acts as donor and MP2 favours structures where acetylene acts as acceptor. However, the fundamental frequencies - that are used for the structure assignment - for each isomer are comparable between both theories.

The excited UV transition was the electronic origin of phenol this time around. It shows a strong red shift in the PhA_1 cluster as the excited state (in which electron density is drawn from the O–H bond to the phenyl-ring) is stabilised by the donor-acetylene. This shift varies between isomers of larger clusters depending on the binding site of the additional acetylene moieties.

Contrary to the benzene-acetylene clusters, ring-like structures dominate. The essential difference lies in the hydroxyl-group of phenol that becomes the favourite binding partner compared to the π-system of the benzene ring. Acetylene acts mainly as a π-electron density donor in the these clusters, while it acts as a π-electron density acceptor in the favoured benzene-acetylene clusters. The dimer is found exclusively as the isomer shown in Figure 9.3(a), where acetylene acts as a π-electron density donor to the hydrogen of the hydroxyl-group.

Even those isomers, where one acetylene-moiety binds as acceptor to the phenol as shown in Figure 9.3(b) show a "floppy" behaviour, making it impossible on the time scale of our measurements to distinguish between isomers where the moving acetylene binds to either the π-system of the ring or to the free electron pair of the oxygen atom.

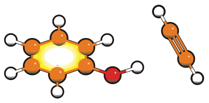

(a) PhA_1

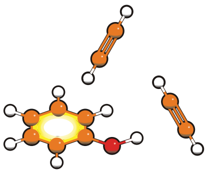

(b) PhA_2

Figure 9.3: Ring-shaped phenol-acetylene clusters

The intermolecular vibrations of the dimer and trimer have been investigated with dispersed fluorescence. Surprisingly, more than the expected bands are found in the region below 200 cm^{-1} for the dimer and trimer and none of them shows a rotational contour. A degeneracy as for the benzene–acetylene vibrations is not observed and the additional bands are assigned to combination bands between intermolecular vibrations. The hindered rotations and translations of acetylene mix to some extent on the level of theory used.

Even though the results indicate once again a stepwise aggregation, the motif of the co-crystal is not recognisable in these small clusters as opposed to that of benzene-acetylene. The survey was also complicated by the apparent fast rearrangement of the acetylene moieties in clusters above PhA_2.

The second half of this work concentrates on the Franck-Condon and Herzberg-Teller analyses of indole derivatives. The geometries of 5-cyanoindole and benzimidazole are presented and the fit of their emission intensities has in both cases been enhanced by the changes of their rotational constants from high resolution laser induced fluorescence measurements by Brand *et al.*. Their initial geometries were calculated with spin-component scaled coupled cluster singles and doubles (SCS-CC2) theory by Michael Schmitt.

Seven normal modes are used to describe the geometry change of 5-cyanoindole. The

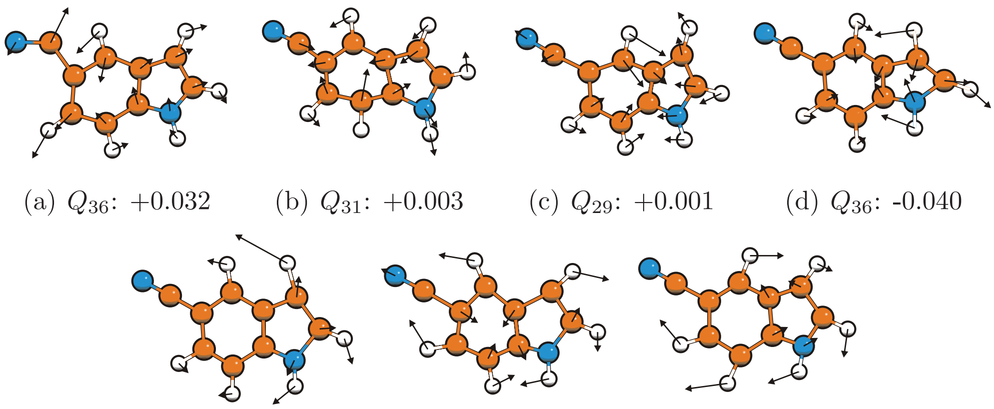

(a) Q_{36}: +0.032 (b) Q_{31}: +0.003 (c) Q_{29}: +0.001 (d) Q_{36}: -0.040

(e) Q_{22}: -0.042 (f) Q_{18}: +0.015 (g) Q_{17}: +0.100

Figure 9.4: Normal modes defining geometry change of 5-cyanoindole and their coefficients from the Franck-Condon Herzberg-Teller fit. See also Table 7.2.

displacement vectors of these normal modes are shown in Figure 9.4 with their coefficients from the Franck-Condon Herzberg-Teller fit for illustration purposes. These modes are mostly described as ring deformation modes.

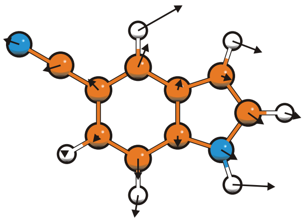

Figure 9.5: Geometry change of 5-cyanoindole upon electronic excitation to the ^1L_a, see also Figure 7.4 and Table 7.3 on page 128 for the exact values.

The resulting geometry change upon electronic excitation to the ^1L_a state is illustrated by arrows in Figure 9.5. The changed bond lengths are on the magnitude of some picometres (some percent of a bond length). It is mainly dictated by an unsymmetric enlargement of the six-membered ring. The five-membered ring is deformed accordingly. The N≡C bond and the N–H bond are stretched as electron density is drawn to the indole skeleton. This leads to a higher acidity in the excited state that is further increased by the electron withdrawing substituent compared to that of indole.

The last investigated system that is presented in this work is benzimidazole. The fluorescence from eight absorption bands was dispersed while the changes of the rotational constants of four different isotopomers were determined by Brand *et al.*.

Even though three dispersed fluorescence spectra were discarded for the analysis[1], 187 intensity points and 8 changes of rotational constants were available for the fit, allowing a complete description of the geometry along 21 normal coordinates (18 would have been sufficient for a complete fit). This fit was even possible without the use of Herzberg-Teller

---

[1] Emission intensities from a state in which an inversion vibration was excited cannot be used in the Franck-Condon fit, because the double minimum potential of such a vibration cannot be described by the harmonic approximation used in our program. They were however, compared to spectra simulated with the fitted geometry change, allowing a coherent assignment of all spectral lines.

correction regardless of the very close second excited singlet state.

The electronic structure of benzimidazole is very interesting. It was investigated extensively before with high level *ab initio* methods and the character of its first excited singlet state seems to be almost impossible to describe as either ^1L_a or ^1L_b due to a strong mixing with the second excited singlet state. The position of this state was located to be at around 1000 cm^{-1} above the emitting state by observing the energy threshold after that Herzberg-Teller effects are visible in the vibronic spectra. A high IVR rate was also observed in spectra obtained after an excitation energy 1200 cm^{-1} above the electronic origin.

The geometry change of benzimidazole is once again dominated by an enlargement of the six- membered ring, which is more symmetric than that found in 5-cyanoindole. Three of the bonds (the bond that is shared by both rings and those between each nitrogen atom and the CH-group bridging them) in the five membered ring are stretched accordingly while the other two bonds (between the six-membered ring and each of the nitrogen atoms) are contracted.

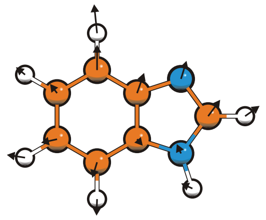

Figure 9.6: Geometry change of benzimidazole upon electronic excitation, see also Figure 8.8 and Table 8.2 on page 159 for the exact values.

All those projects show, that the combination of dispersed fluorescence and Franck-Condon analyses is a powerful tool for the investigation of molecular geometries. A huge amount of cooperation is always needed in this research: Changes of rotational constants greatly enhance the fit as the simulated intensities are insensitive to the sign of the geometry change, isomer-selective measurements necessitate data from REMPI or similar methods and high-level *ab initio* calculations are important for a good description of the reference state (as only geometry changes are determined in the FC-fit) and the vibrational frequencies.

10. Zusammenfassung

In dieser Arbeit wurden aromatische Systeme (sowohl isoliert als auch im Aggregat) mittels Laserspektroskopie untersucht, um durch die Analyse der erhaltenen vibronischen Spektren Rückschlüsse über ihre Struktur zu ziehen. Der Fokus verlagerte sich dabei von den Bindungsmotiven in unterschiedlichen Aromat-Acetylen Clustern zur Geometrieänderung nach elektronischer Anregung von Monomeren mit unterschiedlichen Substituenten.

Die grundsätzliche Idee hinter den Cluster-Projekten bestand in der Aufklärung der Aggregationspfade vom Monomer zum Kristallkeim. Eine schrittweise Bildung wurde vorgeschlagen und durch den Vergleich zwischen den Bindungsmotiven in kleinen Clustern und der Elementarzelle überprüft. Da die Cluster in einem Ungleichgewichts-Prozess (Ko-Expansion im Überschall-Düsenstrahl) gebildet werden, liegen sowohl kinetisch gebildete als auch thermodynamisch gebildete Isomere vor.

Das erste Projekt behandelte Cluster von Benzol mit Acetylen. Die Bindungsenergien und Schwingungen im elektronischen Grundzustand dieser Cluster wurden von Jansen *et al.* mit einer Kombination aus Symmetrieangepasster Störungstheorie mit Dichtefunktionaltheorie (DFT-SAPT) berechnet und mit Spin-Komponenten skalierter Møller-Plesset Störungstheorie (SCS-MP2) bestätigt. Die Infrarot-Frequenzen dieser Schwingungen wurden mit vibronischen Spektren (IR-UV Lochbrennen von Gernot Engler und Markus Böning für die Valenzschwingungen um 3200 cm^{-1} und dispergierte Fluoreszenz für den Fingerabdruck-Bereich unterhalb 1500 cm^{-1}) verglichen, um eine Strukturzuordnung zu treffen.

Dafür wurde mit dem UV-Laser der 6_0^1-Übergang - auch der „falsche Ursprung“ genannt - von Benzol angeregt. Die UV-Resonanz hängt von der Energiedifferenz zwischen elektronischem Grund- und angeregtem Zustand ab und daher von der Clustergröße und dem Bindungsmotiv. Elektronendichte wird im Cluster vom π-System des Benzols abgezogen und somit wird der angeregte $\pi\pi^*$-Zustand destabilisiert, was zu einer Blauverschiebung des

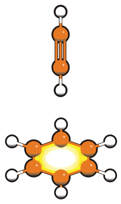
(a) BA_1

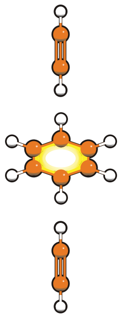
(b) BA_2

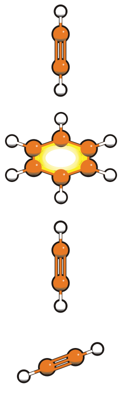
(c) BA_3

Figure 10.1: T-förmige Benzeol-Acetylen cluster

falschen Ursprungs führt, die sich je nach Clusterisomer unterscheidet. Dies ermöglicht Isomer-spezifische Spektroskopie, obwohl alle stabilen Cluster im Düsenstrahl vorliegen.

In Röntgenstrukturanalysen des Benzol-Acetylen Kokristalls werden B-A-B-A-Bänder gefunden, in denen je zwei Benzol-Moleküle durch ein Acetylen-Molekül verbunden werden, welches mit je einem Wasserstoffatom an die π-Systeme bindet.

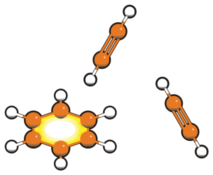

Figure 10.2: Das Ringförmige BA_2 Isomer

Wie von der Struktur des Benzol-Acetylen-Kokristalls erwartet, werden überwiegend T-förmige Strukturen wie in Abbildung 10.1 dargestellt gefunden. Zusätzlich zu diesen T-förmigen Strukturen werden auch Ringförmige Strukturen - in denen einige Acetylen-Einheiten mit den π-Elektronen ihrer C≡C Dreifachbindungen an Wasserstoffatome des Benzols binden -gefunden. Diese ringförmigen Strukturen sind thermodynamische Produkte während die T-förmigen Strukturen weniger stabil sind und kinetisch gebildet werden.

Jeder Benzol-Acetylen Cluster BA_n bis hin zum Tetramer enthält die Struktur des niedrigeren Clusters BA_{n-1} und eine zusätzliche Acetylen-Einheit, die entweder an das Benzol oder ein Acetylen bindet. Dies wird in Abbildung 10.1 für die T-förmigen Isomere deutlich, trifft aber auch auf die ringförmigen Isomere zu. Die Struktur des B_2A_2 Tetramers folgt aus dem ringförmigen BA_2 Isomer mit einer zusätzlichen Benzol-Einheit. Dies beweist, dass die Aggregation tatsächlich schrittweise abläuft und beim T-förmigen Benzol-Acetylen Dimer beginnt.

Die intermolekularen Schwingungen das Benzol-Acetylen Dimers -die aus gehemmten Rotationen und Translationen des Acetylens entstehen - wurden durch dispergierte Fluoreszenz sowohl mit ihren Grundfrequenzen zwischen 50 und 150 cm^{-1} als auch in Kombinationsbanden mit Benzol-Gerüstschwingungen detektiert. Die gehemmten Rotationen und die gehemmten Translationen senkrecht zur C_6 Symmetrieachse des Benzols sind zweifach entartet, was ebenfalls eine T-förmige Struktur bestätigt, in der Acetylen entlang der C_6 Symmetrieachse des Benzols orientiert ist.

Die dispergierten Fluoreszenzspektren der höheren Cluster werden durch intramolekulare Schwingungsumverteilung verbreitert.

Die zweite Zusammensetzung die untersucht wurde war die Mischung von Phenol und Acetylen. Die Rechnungen wurden diesmal von mir durchgeführt, undzwar mit Dispersions-korrigierter Dichtefunktionaltheorie (DFT-D mit dem Funktional B97D) und Møller-Plesset Störungstheorie (RI-MP2) und beide Resultate für jedes Isomer wurden mit den Isomer-Selektiven Infrarotspektren wie oben beschrieben verglichen. Die Lochbrenn-Spektren wurden wieder von Gernot Engler und Markus Böning aufgenommen.

Die energetische Reihenfolge der verschiedenen Isomere hängt von der benutzten Theorie ab, da DFT-D Strukturen bevorzugt, in denen Acetylen als Donor bindet und MP2 Strukturen bevorzugt, in denen Acetylen als Akzeptor bindet. Die Grundfrequenzen jedoch - die zur Strukturzuordnung herangezogen werden- sind für jedes Isomer zwischen beiden Methoden vergleichbar.

Der angeregte UV-Übergang war diesmal der elektronische Ursprung von Phenol. Er weist eine deutliche Rotverschiebung im PhA$_1$ Cluster auf, da der angeregte Zustand (in dem Elektronendichte aus der O–H-Bindung zum Phenylring abgezogen wird) durch das Donor-Acetylen stabilisiert wird. Diese Verschiebung variiert zwischen Isomeren der größeren Cluster abhängig von der Bindungsstelle der zusätzlichen Acetylen-Einheit.

Im Gegensatz zu den Benzol-Acetylen Clustern dominieren hier Ringförmige Strukturen. Der entscheidende Unterschied liegt in der Hydroxyl-Gruppe der Phenols, die zum bevorzugten Bindungspartner im Vergleich zum π-System des Benzolrings wird. Acetylen wirkt in diesen Clustern hauptsächlich als π-Elektronendichte Donor, während es als π-Elektronendichte Akzeptor in den bevorzugten Benzol-Acetylen Clustern wirkt. Das Dimer tritt nur als das in Abbildung 10.3(a) gezeigte Isomer auf, in dem Acetylen als π-Elektronendichte Donor an den Wasserstoff der Hydroxylgruppe bindet.

Selbst die Isomere, in denen eine Acetylen-Einheit als Akzeptor an das Phenol bindet wie in Abbildung 10.3(b) gezeigt weisen ein „flexibles“ Verhalten auf, das es unmöglich macht auf der Zeitskala unserer Messungen zwischen Isomeren zu unterscheiden, in denen das bewegliche Acetylen an entweder das π-System des Rings oder das freie Elektronenpaar des Sauerstoffs gebunden ist.

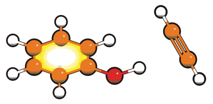

(a) PhA$_1$

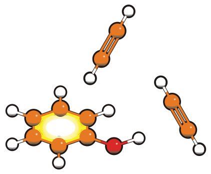

(b) PhA$_2$

Figure 10.3: Ringförmige Phenol-Acetylen Cluster

Die intermolekularen Schwingungen des Dimers und Trimers wurden mit dispergierter Fluoreszenz untersucht. Überraschenderweise wurden in der Region unterhalb 200 cm^{-1} mehr Banden gefunden als erwartet und diese zeigen keine Rotationskontur. Eine Entartung wie bei den Benzol-Acetylen-Schwingungen wird nicht beobachtet und die zusätzlichen Banden werden Kombinationsbanden zwischen intermolekularen Schwingungen zugeordnet. Die gehemmten Rotationen und Translationen von Acetylen mischen teilweise auf dem benutzten Theorieniveau.

Auch wenn die Ergebnisse erneut auf eine schrittweise Aggregation hinweisen ist das Motiv des Kokristalls in diesen kleinen Clustern im Gegensatz zum Benzol-Acetylen noch nicht erkennbar.

Die zweite Hälfte dieser Arbeit ist auf die Franck-Condon und Herzberg-Teller Analysen von Indolderivaten konzentriert. Die Geometrien von 5-Cyanoindol und Benzimidazol werden vorgestellt und der Fit ihrer Emissionsintensitäten wurde in beiden Fällen verbessert durch die Änderung ihrer Rotationskonstanten, die von Brand *et al.* mit hochauflösender Laserinduzierter Fluoreszenspektroskopie bestimmt wurden. Ihre Startgeometrien wurden mit Spin-Komponenten skalierter Coupled-Cluster (SCS-CC2) Theorie von Michael Schmitt berechnet.

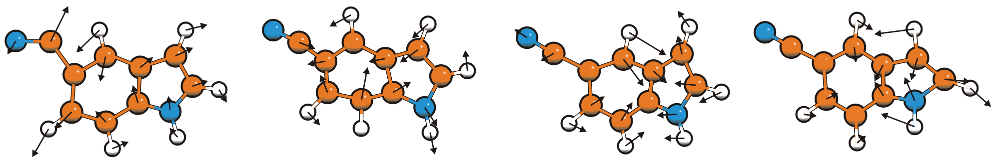

(a) Q_{36}: +0.032 (b) Q_{31}: +0.003 (c) Q_{29}: +0.001 (d) Q_{36}: -0.040

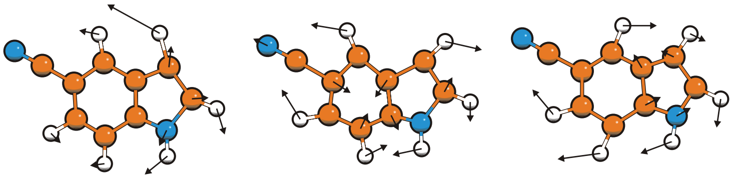

(e) Q_{22}: -0.042 (f) Q_{18}: +0.015 (g) Q_{17}: +0.100

Figure 10.4: Normalmoden die die Geometriänderung von 5-Cyanoindol beschreiben, mit ihren Koeffizienten aus dem Franck-Condon Herzberg-Teller Fit. Siehe auch 7.2.

Sieben Normalmoden werden benutzt, um die Geometrieänderung von 5-Cyanoindol zu beschreiben. Die Auslenkungsvektoren dieser Normalmoden sind zur Veranschaulichung in Abbildung 10.4 mit ihren Koeffizienten aus dem Franck-Condon Herzberg-Teller Fit gezeigt. Die meisten dieser Moden sind Ringdeformationsmoden.

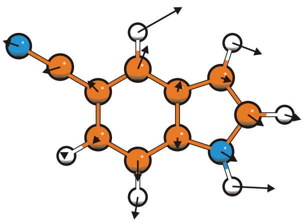

Figure 10.5: Geometrieänderung von 5-Cyanoindol bei elektronischer Anregung in den ^1L_a, siehe auch Abbildung 7.4 und Tabelle 7.3 auf Seite 128 für die genauen Werte.

Die resultierende Geometrieänderung bei elektronischer Anregung in den ^1L_a Zustand ist durch Pfeile in Abbildung 10.5 dargestellt. Die Änderungen der Bindungslängen bewegen sich in der Größenordnung von einigen Picometern (einige Prozent einer Bindungslänge). Die Geometrieänderung besteht hauptsächlich aus einer unsymmetrischen Aufweitung des Sechsrings. Der Fünfring wird entsprechend deformiert. Die N≡C-Bindung und die N–H-Bindung werden länger, da Elektronendichte zum Indolgerüst abgezogen wird. Dies führt zu einer höheren Azidität im angeregten Zustand, die im Vergleich zum Indol durch den elektronenziehenden Substituenten verstärkt wird.

Das letzte untersuchte System, das in dieser Arbeit vorgestellt wird, ist Benzimidazol. Die Fluoreszenz aus acht Absorptionsbanden wurde dispergiert, während die Änderungen der Rotationskonstanten von vier verschiedenen Isotopomeren von Brand *et al.* bestimmt wurden.

Obwohl drei dispergierte Fluoreszenzspektren für die Analyse verworfen wurden[1], standen 187 Intensitäten und 8 Änderungen der Rotationskonstanten für den Fit zur Verfügung und ermöglichten die vollständige Beschreibung der Geometrie entlang 21 Normalkoordinaten (18 hätten für einen vollständigen Fit bereits ausgereicht). Dieser Fit war sogar ohne die Einbeziehung der Herzberg-Teller Korrektur möglich, obwohl der zweite angeregte Zustand energetisch sehr nahe liegt.

Die elektronische Struktur von Benzimidazol ist sehr interessant. Sie wurde zuvor bereits ausführlich mit *ab initio* Methoden auf hohem Niveau untersucht und der Charakter des ersten angeregten Singlet Zustands scheint umnöglich eindeutig als ^1L_a oder ^1L_b beschreibbar zu sein, da er sehr stark mit dem zweiten angeregten Singlet Zustand mischt. Die energetische Lage dieses Zustands wurde bei ca. 1000 cm^{-1} oberhalb des emittierenden Zustands lokalisiert, indem die Energieschwelle beobachtet wurde ab der Herzberg-Teller Effekte in vibronischen Spektren auftreten. Außerdem wird eine hohe IVR Rate in Spektren nach einer Anregungsenergie von 1200 cm^{-1} über dem eletronischen Urpsrung beobachtet.

Die Geometrieänderung von Benzimidazol wird erneut dominiert durch die Aufweitung des Sechsrings, die symmetrischer als beim 5-Cyanoindol erfolgt. Drei der Bindungen (die Bindung, die von beiden Ringen geteilt wird und die beiden Bindungen zwischen den Stickstoffatomen und der verbrückenden CH-Gruppe) in dem Fünfring werden entsprechend länger, während die anderen beiden Bindungen (zwischen dem Sechsring und je einem Sticktoffatom) kürzer werden.

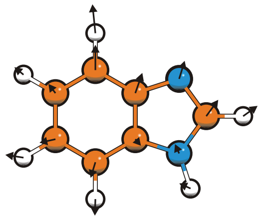

Figure 10.6: Geometrieänderung von Benzimidazol bei elektronischer Anregung, siehe auch Abbildung 8.8 und Tabelle 8.2 auf Seite 159 für die genauen Werte.

Alle diese Projekte zeigen, dass die Kombination aus dispergierter Fluoreszenzspektroskopie und Franck-Condon Analysen ein starkes Werkzeug zur Untersuchung molekularer Geometrien ist. Ein großes Maß an Kooperation ist in dieser Forschung stets gefragt: Änderungen der Rotationskonstanten verbessern den Fit, da simulierte Intensitäten allein unempfindlich gegenüber dem Vorzeichen der Geometrieänderung sind, Isomer-selektive Messungen erfordern Daten aus REMPI oder ähnlichen Methoden und *ab initio* Rechnungen auf hohem Niveau sind wichtig für eine gute Beschreibung des Referenzzustands (da nur Geometriänderungen im FC-Fit bestimmt werden) und der Schwingungsfrequenzen.

---

[1] Emissionsintensitäten aus Zuständen, in denen eine Inversionsschwingung angeregt wurde können in dem Franck-Condon Fit nicht benutzt werden, da das Doppelminimumspotenzial einer solchen Schwingung nicht in der harmonischen Nähering beschrieben werden kann, auf der unser Programm basiert. Sie wurden jedoch mit Spektren verglichen, die mit der angepassten Geometrie ermittelt wurden, um eine durchgehende Zuordnung der spektralen Linien zu ermöglichen

Danksagung

Mit diesem Kapitel endet eine „strange journey" meines Lebens und ich danke allen die dabei waren!

Wie sich das gehört gilt mein Dank in erster Linie meinem Doktorvater Karl Kleinermanns und Zweitgutachter Michael Schmitt für die Möglichkeit in diesem Arbeitskreis zu promovieren, die durchaus abwechslungsreiche Aufgabenstellung und die Betreuung während dieser - zum Teil düsteren - Zeit. Ohne euch müsste ich vielleicht nicht dumm - aber doch sehr viel weniger gebildet - sterben!

Daniel Ogermann und Thorsten Wilke muss ich an dieser Stelle dafür danken, mich mit ihren Farbstoff-sensibilisierten TiO_2-Solarzellen erst in die Physikalische Chemie gelockt zu haben, auch wenn ich dann an der Laser-Spektroskopie nicht vorbei kam.

Der restlichen Physikalischen Chemie I (AKKK&AKMS&Friends) möchte ich für die angenehme und unterhaltsame Zeit im Institut danken. Namentlich Christian Brand, Matthias Busker und Kai Seefeld für die Betreuung während meiner Diplomarbeit und Aufmunterung bei der Laser-Justage, Gernot Engler und Markus Böning für viele kleine Hilfen bei Hard- und Software und die erfolgreiche Zusammenarbeit bei den Cluster-Projekten und Laura Buschhaus, Lars Biemann, Thomas Häber, Michalina Braun, Josy Rolf und Martin Wilke für diverse Korrekturen und andere Hilfen bei Berichten, Anträgen, LaTeX und allgemeinem Uni-Wahnsinn. Insbesondere Katharina Hunger als eine der wenigen Personen die diese Arbeit gründlich gelesen haben. Wo ihr seid ist vorne!

Des weiteren danke ich meinen Bachelor- und Master-Studenten Alex Wohlert, Felix Gmerek, Anne Gräßle und Christoph Rumancev für eine produktive Zusammenarbeit die mir keine grauen Haare verursacht hat. Im Speziellen möchte ich Alex für sein Dolmetschen Mathe–Deutsch/Deutsch–Mathe und Anne für jede Menge Kuchen danken!

Ohne das technische know-how und die Engelsgeduld von Klaus „magic hands" Kelbert und das Feinmechanik-Team um Gerd Büttgenbach wäre der Experimentalteil dieser Arbeit allerdings das eine oder andere Mal (pro Woche) zum Scheitern verurteilt gewesen!

Natürlich muss ich auch meiner Chemielehrerin Sandra Spitzbart danken, die mich für Chemie begeistert hat und vor allem davon abgehalten hat, Biochemie zu studieren. Wenn man meinen Werdegang bedenkt wäre ich dort wohl nicht glücklich geworden. Unser Rollenspiel „Stellt euch vor, ihr seid Mitarbeiter vom Professor Nernst. Der Chef ist im Urlaub und erwartet bis zu seiner Rückkehr Ergebnisse. Hier ist eine Seite aus dem chaotisch geführten Laborjournal eures Vorgängers." (das Ziel war natürlich die Nernstsche Gleichung aus Messreihen der Spannung zwischen verschiedenen Halbzellen herzuleiten) hat sich ebenfalls als erschreckend realistisch herausgestellt.

Der Magic- und Rollenspiel-Clique (Katharina, Christian, Laura, Ingo, Moritz) gilt mein Dank dafür, den in der Uni angestauten Wahnsinn nach Feierabend in kreative Bahnen gelenkt zu haben und meinen Wuppertaler Freunden dafür dass sie mein Geplärre in mancher dunklen Stunde (insbesondere vor gewissen Deadlines und nach gewissen Dates) ertragen und mit Alkohol, Videospielen und anderen Abenteuern (Bernd, Melissa, Benny, Tristan und Jonas wissen wovon ich rede) kompensiert haben. Einige von euch (Benny, Ingo, John und Dominik) begleiten mich schon seit meiner Schulzeit und Wuppertal wird für immer meine Heimat bleiben, es sei denn die Schwebebahn wird zur Schuldentilgung nach China verkauft.

Außerhalb Wuppertals gibt es außerdem noch Freunde aus der Uni, ohne die ich manches Mal die Flinte in's Korn geworfen und mein Diplom nie im Leben bekommen hätte: Namentlich Andi, Claudia, Julia und Steffie.

Auch soll die Cosplay-Gruppe nicht unerwähnt bleiben, die ich mehr als ein Jahr vertrösten musste. Bald bin ich wieder dabei, versprochen!

Und an jeden der sich hier nicht wiedererkannt hat: Du darfst dich angesprochen fühlen und ich darf mich glücklich schätzen dass hier viel zu viele Namen stehen würden um auf zwei Seiten Platz zu finden ^_~

Zu guter Letzt danke ich natürlich meiner Familie für den Rückhalt während Studium und Promotion, insbesondere meinen Eltern für manches warme Mahl und meiner Schwester für sprachliche Korrekturen auch wenn sie kaum ein Wort von dem versteht was sie korrigiert hat.

Bleibt nur noch Oskar, der flauschigste Kater den ich je hatte und ohne den mein Leben ein ganzes Stück einsamer sein wird. Ich werde dich mehr vermissen als so manchen Menschen!

Bibliography

[1] National Institute of Standards and Technology. CODATA Recommended Values: Physical Constants, Retrieved 2013-12-23, 2010.

[2] B. M. J. S. Dewar, E. G. Zoebisch, E. F. Heady, and J. J. P. Steward. AM1: A New General Purpose Quantum Mechanical Model. *J. Am. Chem. Soc.*, 107:3902–3909, 1985.

[3] Stefan Grimme. Semiempirical GGA-type Density Functional Constructed with a Long-Range Dispersion Correction. *Journal of Computational Chemistry*, 27(15):1787–1799, 2006.

[4] S. Grimme and M. Waletzke. A Combination of Kohn-Sham Density Functional Theory and Multi-Reference Configuration Interaction Methods. *J. Chem. Phys.*, 111(13):5645–5655, 1999.

[5] O. Christiansen, H. Koch, and P. Jørgensen. The Second-Order Approximate Coupled Cluster Singles and Doubles Model CC2. *Chem. Phys. Lett.*, 243:409–418, 1995.

[6] S. Grimme. Improved Second-Order Møller-Plesset Perturbation Theory by Separate Scaling of Parallel- and Antiparallel-Spin Pair Correlation Energies. *J. Chem. Phys.*, 118(20):9095–9102, May 2003.

[7] A. Schäfer, C. Huber, and R. Ahlrichs. Fully Optimized Contracted Gaussian Basis Sets of Triple Zeta Valence Quality for Atoms Li to Kr. *J. Chem. Phys.*, 100:5829, 1994.

[8] J. R. Platt. Classification of Spectra of Cata-Condensed Hydrocarbons., journal = J. Chem. Phys. 17(5):484–495, 1949.

[9] M. Hesse, H. Meier, and B. Zeeh. *Spektroskopische Methoden in der Organischen Chemie.* Thieme, 2005.

[10] W. Demtröder. *Laserspektroskopie.* Springer, 5 edition, 2007.

[11] T. E. Creighton. *Proteins: Structures and Molecular Properties.* W. H. Freeman, New York, 2nd edition, 1997.

[12] H. Lodish, A. Berk, and Zipursky S. *Molecular and Cellular Biology.* W. H. Freeman, New York, 4th edition, 2000.

[13] Lehninger. *Principles of Biochemistry.* W. H. Freeman, New York, 4th edition, 2005.

[14] M. Nishio. CH/π Hydrogen Bonds in Crystals. *Crystengcomm*, 6:130–158, May 2004.

[15] Matthias Busker, Thomas Häber, Michael Nispel, and Karl Kleinermanns. Isomer-Selective Vibrational Spectroscopy of Benzene-Acetylene Aggregates: Comparison with the Structure of the Benzene-Acetylene Cocrystal. *Angew. Chem. Int. Edit.*, 47(52):10094–10097, 2008.

[16] A. Fujii, T. Ebata, and N.. Mikami. An Infrared Study of π-Hydrogen Bond in Micro-Solvated Phenol: OH Stretching Vibrations of Phenol–X (X = C_6H_6, C_2H_4 and C_2H_2) Clusters in the Neutral and Cationic Ground State. *J. Phys. Chem. A*, 106:8554–8560, 2002.

[17] Bradley Ferguson and Xi-Cheng Zhang. Materials for Terahertz Science and Technology. *Nat Mater*, 1(1):26–33, September 2002.

[18] P. H. Siegel. Terahertz Technology. *MTT*, pages 910–928, 2002.

[19] B. S. Williams. Terahertz Quantum-Cascade Lasers. *Nature Photonics*, 1:517–525, 2007.

[20] P.W. van Amersfoort, R.J. Bakker, J.B. Bekkers, R.W.B. Best, R. van Buuren, P.F.M. Delmee, B. Faatz, C.A.J. van der Geer, D.A. Jaroszynski, P. Manintveld, W.J. Mastop, B.J.H. Meddens, A.F.G. van der Meer, J.P. Nijman, D. Oepts, J. Pluygers, M.J. van der Wiel, W.A. Gillespie, P.F. Martin, M.F. Kimmitt, C.R. Pidgeon, M.W. Poole, and G. Saxon. First Lasing with FELIX. *NUCL INSTRUM METH A*, 318:42–46, 1992.

[21] A. C. Borin and L. Serrano-Andrés. A Theoretical Study of the Absorption Spectra of Indole and its Analogs: Indene, Benzimidazole, and 7-Azaindole. *Chem. Phys.*, 262:253–265, 2000.

[22] L. Serrano-Andrés and A. C. Borin. A Theoretical Study of the Emission Spectra of Indole and Its Analogs: Indene, Benzimidazole, and 7-Azaindole. *Chem. Phys.*, 262:267–283, 2000.

[23] M. Schmitt, K. Feng, M. Böhm, and K. Kleinermanns. Low Frequency Backbone Vibrations of Individual Conformational Isomers: Tryptamine. *The Journal of chemical physics*, 125:144303, 2006.

[24] Edward Condon. A Theory of Intensity Distribution in Band Systems. *Phys. Rev.*, 28:1182–1201, Dec 1926.

[25] Edward U. Condon. Nuclear Motions Associated with Electron Transitions in Diatomic Molecules. *Phys. Rev.*, 32:858–872, Dec 1928.

[26] J. Franck and E. G. Dymond. Elementary Processes of Photochemical Reactions. *Trans. Faraday Soc.*, 21:536–542, 1926.

[27] S. Schumm, M. Gerhards, and K. Kleinermanns. Franck-Condon Simulation of the $S_1 \rightarrow S_0$ Spectrum of Phenol. *The Journal of Physical Chemistry A*, 104(46):10648–10655, 2000.

[28] D. Spangenberg, P. Imhof, and K. Kleinermanns. The S_1 State Geometry of Phenol Determined by Simultaneous Franck-Condon and Rotational Constants Fits. *Phys. Chem. Chem. Phys.*, 5:2505–2514, 2003.

[29] TURBOMOLE V6.3 2011, a development of University of Karlsruhe and Forschungszentrum Karlsruhe GmbH, 1989-2007, TURBOMOLE GmbH, since 2007; available from
`http://www.turbomole.com`.

[30] G. Berden, W. L. Meerts, M. Schmitt, and K. Kleinermanns. High Resolution UV Spectroscopy of Phenol and the Hydrogen Bonded Phenol-Water Cluster. *J. Chem. Phys.*, 104(3):972–982, 1996.

[31] G. Herzberg and E. Teller. Schwingungsstruktur der Elektronenübergänge bei Mehratomigen Molekülen. *Z. Phys. Chem.*, 21:410, 1933.

[32] P. Klan and J. Wirz. *Photochemistry of Organic Compounds.* Postgraduate Chemistry Series. Wiley-VCH, 2009.

[33] W. Demtröder. *Experimentalphysik.*, volume 3 Atome, Moleküle und Festkörper. Springer, 3 edition, 2005.

[34] D.M. Bishop. *Group Theory and Chemistry.* Dover, 1973.

[35] F. Engelke. *Aufbau der Moleküle.* Teubner Studienbücher, 1985.

[36] C. Janiak, H.J. Meyer, D. Gudat, and R. Alsfasser. *Riedel: Moderne Anorganische Chemie.* De Gruyter, 4. edition, 2012.

[37] A. Jablonski. Efficiency of Anti-Stokes Fluorescence in Dyes. *Nature*, 131:839–840, 1933.

[38] F. Hund. The Interpretation of Complicated Spectra. *Z. Phys.*, 33:345–371, 1925.

[39] J. M. L. Pecourt, J. Peon, and B. Kohler. DNA Excited-State Dynamics: Ultrafast Internal Conversion and Vibrational Cooling in a Series of Nucleosides. *J. Am. Chem. Soc.*, 123:10370–10378, 2001.

[40] M. Kasha. Characterization of Electronic Transitions in Complex Molecules. *Discuss. Faraday Soc.*, 9:14–19, 1950.

[41] J. A. Nicholson, W. D Lawrance, and G. Fischer. Single Vibronic Level Fluorescence Spectra from A($^1B_{2u}$) Benzene: Fermi Resonances and S_0 IVR Lifetimes. *Chem. Phys.*, 196:327–351, 1995.

[42] G. G. Stokes. On the Change of Refrangibility of Light. *Phil. Trans. R. Soc.*, 142:463–562, 1852.

[43] M. Born and R. Oppenheimer. Zur Quantentheorie der Molekeln. *Annalen der Physik*, 389(20):457–484, 1927.

[44] P. W. Atkins and R. Friedman. *Molecular Quantum Mechanics.* Oxford University Press, fifth edition edition, 2011.

[45] Shin Takahashi. *The Manga Guide to Linear Algebra.* No Starch Press, Inc. and Ohmsha Ltd., 2012.

[46] F. Duschinsky. On the Interpretation of Electronic Spectra of Polyatomic Molecules. *Acta Physicochimica*, 7:551–566, 1937.

[47] E. V. Doktorov, I. A. Malkin, and Man'ko. V. I. Dynamical Symmetry of Vibronic Transitions in Polyatomic Molecules and the Franck-Condon Principle II. *J. Mol. Spec.*, 64:302–326, 1977.

[48] G. Orlandi, P. Palmieri, R. Tarroni, F. Zerbetto, and M. Z. Zgierski. The $S_0\,(1A_g)$-$S_1\,(1B_{2u})$ Vibronic Transition in Benzene: An *Ab Initio* Study. *J. Chem. Phys.*, 100(4):2458–2464, 1994.

[49] W. F. Radle and C. A. Beck. An Experimental Study of the Near Ultraviolet Absorption Spectrum of Benzene. *J. Chem. Phys.*, 8(7):507–513, 1940.

[50] G. Weber. Fluorescence-Polarization Spectrum and Electronic-Energy Transfer in Tyrosine, Tryptophan and Related Compounds. *Biochem. J.*, pages 335–345, 1960.

[51] Patrik R. Callis. Transition Density Topology of the L_a and L_b States in Indoles and Purines. *Int. J. Quantum Chem.*, 26(S18):579–588, 1984.

[52] Michel Herman, Robert Georges, Martin Hepp, and Daniel Hurtmans. High Resolution Fourier Transform Spectroscopy of Jet-Cooled Molecules. *International Reviews in Physical Chemistry*, 19(2):277 – 325, April 2000.

[53] H. Ashkenas and F.S. Sherman. Rarefied Gas Dynamics, 4th Symposium. *Appl. Phys.*, 1966.

[54] J.B. Anderson and J.B. Fenn. Velocity Distributions in Molecular Beams from Nozzle Sources. *Physics of Fluids*, 8(5):780–787, 1965.

[55] R. Ahlrichs, M. Bar, M. Haser, H. Horn, and C. Kolmel. Electronic-Structure Calculations on Workstation Computers - The Program System Turbomole. *Chem. Phys. Lett.*, 162(3):165–169, October 1989.

[56] Thomas Häber. Random Structure Generator.

[57] J. J. P. Steward. *MOPAC 2009 Version 11.366*. Stewart Computational Chemistry, Colorado Springs, CO, USA.

[58] J. C. Slater. The Theory of Complex Spectra. *Phys. Rev.*, 34:1293–1322, Nov 1929.

[59] T. H. Dunning. Gaussian-Basis Sets for Use in Correlated Molecular Calculations. I. The Atoms Boron through Neon and Hydrogen. *J. Chem. Phys.*, 90(2):1007–1023, January 1989.

[60] E. R. Davidson and D. Feller. Basis Set Selection for Molecular Calculations. *Chemical Reviews*, 86(4):681–696, 1986.

[61] M. J. S. Dewar and W. Thiel. Ground States of Molecules. 38. The MNDO Method. Approximations and Parameters. *Journal of the American Chemical Society*, 99(15):4899–4907, 1977.

[62] P. Hohenberg and W. Kohn. Inhomogeneous Electron Gas. *Phys. Rev.*, 136:B864–B871, 1964.

[63] P. Hobza, J. Sponer, and T. J. Reschel. Density-Functional Theory and Molecular Clusters. *Comput Chem*, 11:1315, 1995.

[64] M. Allen and D. J. Tozer. Helium Dimer Dispersion Forces and Correlation Potentials in Density Functional Theory. *J. Chem. Phys.*, 117:11113, 2002.

[65] S. Kristyan and P. Pulay. Can (Semi)local Density-Functional Theory Account for the London Dispersion Forces? *Chem. Phys. Lett.*, 229:175, 1994.

[66] C. Møller and M. S. Plesset. Note on an Approximation Treatment for Many-Electron Systems. *Phys. Rev.*, 46:618–622, Oct 1934.

[67] F. Weigend, A. Kohn, and C. Hattig. Efficient Use of the Correlation Consistent Basis Sets in Resolution of the Identity MP2 Calculations. *J. Chem. Phys.*, 116(8):3175–3183, February 2002.

[68] F. Weigend and M. Häser. RI-MP2: First Derivatives and Global Consistency. *Theor. Chem. Acc.*, 97:331, 1997.

[69] F. Coester. Bound States of a Many-Particle System. *Nucl. Phys*, 7:421, 1958.

[70] F. Coester and H. Kümmel. Short-Range Correlations in Nuclear Wave Functions. *Nucl. Phys*, 17:477, 1960.

[71] C. Hättig and F. Weigend. CC2 Excitation Energy Calculations on Large Molecules Using the Resolution of the Identity Approximation. *J. Chem. Phys.*, 113:5154–5161, 2000.

[72] A. Hellweg, S. Grün, and C. Hättig. Benchmarking the Performance of Spin-Component Scaled CC2 in Ground and Electronically Excited States. *Phys. Chem. Chem. Phys.*, 10:1159–1169, 2008.

[73] C. Hättig. Geometry Optimizations with the Coupled-Cluster Model CC2 Using the Resolution-Of-The-Identity Approximation. *J. Chem. Phys.*, 118(17):7751–7761, May 2003.

[74] C. Hättig and A. Köhn. Transition Moments and Excited State First-Order Properties in the Second-Order Coupled Cluster Model CC2 Using the Resolution of the Identity Approximation. *J. Chem. Phys.*, 117:6939–6951, 2002.

[75] J. W. Ochterski, editor. *Vibrational Analysis in Gaussian.*, www.gaussian.com, 1999. Gaussian.

[76] F. Ansbacher. Über die Berechnung von Franck-Condon-Integralen. *Z. Naturforsch.*, 14a:889, 1959.

[77] S. Koide. A Note on the Overlap Integral of Two Harmonic Oscillator Wave Functions. *Z. Naturforsch.*, 15a:123, 1960.

[78] T. E. Sharp and H. M. Rosenstock. Franck-Condon Factors for Polyatomic Molecules. *The Journal of Chemical Physics*, 41(11):3453–3463, 1964.

[79] Carl Eckart. Some Studies Concerning Rotating Axes and Polyatomic Molecules. *Phys. Rev.*, 47:552–558, Apr 1935.

[80] J. D. Louck and H. W. Galbraith. Eckart Vectors, Eckart Frames, and Polyatomic Molecules. *Rev. Mod. Phys.*, 48:69–106, Jan 1976.

[81] J. T. Hougen and J. K. G. Watson. Anomalous Rotational Line Intensities in Electronic Transitions of Polyatomic Molecules: Axis-Switching. *Can. J. Phys.*, 43:298, 1965.

[82] G. M. Sando and K. G. J. Spears. *Ab Initio* Computation of the Duschinsky Mixing of Vibrations and Nonlinear Effects. *J. Phys. Chem. A*, 105:5326, 2001.

[83] E. V. Doktorov, I. A. Malkin, and Man'ko. V. I. Dynamical Symmetry of Vibronic Transitions in Polyatomic Molecules and the Franck-Condon Principle I. *J. Mol. Spec.*, 56:1–20, 1975.

[84] Roy J. Glauber. Photon Correlations. *Phys. Rev. Lett.*, 10:84–86, Feb 1963.

[85] M. A. Khan, N. Ahmad, and A. H. Khan. A Note on a New Two Variable Analogue of Hermite Polynomials. *World Applied Programming*, 2(12):515–522, 2012.

[86] M. Böhm, J. Tatchen, D. Krügler, K. Kleinermanns, M. G. D. Nix, T. A. LeGreve, T. S. Zwier, and M. Schmitt. High-Resolution and Dispersed Fluorescence Examination of Vibronic Bands of Tryptamine: Spectroscopic Signatures for L_a/L_b Mixing near a Conical Intersection. *J. Phys. Chem. A*, 113(11):2456–2466, 2009. PMID: 19231889.

[87] ©2000-2013 Daniel Krügler, ©2000-2004 Petra Imhof, ©1997-1998 Stephan Schumm. FCFIT, A Program for Franck Condon Simulation and Fits version 2.8.20. Published under the GNU General Public License.

[88] S. Schumm. Ab Initio *Rechnungen und spektroskopische Untersuchungen an Hydroxyaromaten im S_0- und S_1-Zustand sowie im Grundzustand des Kations.* PhD thesis, Heinrich Heine-Universität Düsseldorf, 1998.

[89] D. Gruner and P. Brumer. Efficient Evaluation of Harmonic Polyatomic Franck-Condon Factors. *Chem. Phys. Lett.*, 138(4):310 – 314, 1987.

[90] R. Berger, C. Fischer, and M. Klessinger. Calculation of the Vibronic Fine Structure in Electronic Spectra at Higher Temperatures. 1. Benzene and Pyrazine. *J. Phys. Chem. A*, 102:7157–7167, 1998.

[91] R. J. Le Roy. Where Is the Intensity Maximum in a Pure Rotational Spectrum? *Journal of Molecular Spectroscopy*, 192(1):237 – 238, 1998.

[92] J.E. Dennis, D. M. Gay, and R. E. Welsch. An Adaptive Nonlinear Least-Squares Algorithm. *ACM Transactions on mathematical Software*, 7(3):348–368, September 1981.

[93] J. Dennis, D. M. Gay, and R. E. Welsch. Algorithm 573: NL2SOL - An Adaptive Nonlinear Least-Squares Algorithm [E4]. *ACM Transactions on mathematical Software*, 7(3):369–383, September 1981.

[94] K. Levenberg. A Method for the Solution of Certain Problems in Least Squares. *Quart. Appl. Math.*, 2:164–168, 1944.

[95] D. Marquardt. An Algorithm for Least-Squares Estimation of Nonlinear Parameters. *SIAM J. Appl. Math.*, 11:431–441, 1963.

[96] K. R. Gegenfurter. PRAXIS: Brent's Algorithm for Function Minimization. *Behav. Res. Meth Intr. & Comp.*, 24:560, 1992.

[97] R. P. Brent. *Algorithms for Minimisation without Derivatives.* Prentice hall, Englewood cliffs, 1973.

[98] D. Levine. PGAPack V1.0, PgaPack Can Be Obtained via Anonymous ftp from: ftp://ftp.mcs.anl.gov/pub/pgapack/pgapack.tar.z, 1996.

[99] W. L. Goffe, G. D. Ferrier, and J. Rogers. Global Optimization of Statistical Functions with Simulated Annealing. *Econometr.*, 60:65, 1994.

[100] Lambda Physik GmbH. Dye Laser FL 3001/2 Instruction Manual, 1984.

[101] Gerrit Borstel. Dyelaser Database 2003. Sirah Laser- und Plasmatechnik, Ludwig-Erhard Str. 10, 41564 Kaarst, 2010.

[102] Stanford Computer Optics. ICCD High Speed Camera Technology.

[103] R. Boese, T. Clark, and A. Gavezzotti. Cocrystallization with Acetylene. The 1:1 Complex with Benzene: Crystal Growth, X-Ray Diffraction and Molecular Simulations. *Helv. Chim. Acta*, 86(4):1085–1100, 2003.

[104] Y. Kodama, K. Nishihata, M. Nishio, and Y. Iitaka. X-Ray Study of (alphas,ss-alphar,sr)-1-(p-Bromophenyl)ethyl T-Butyl Sulfoxide and Conformational-Analysis of Diastereoisomeric Pairs of 1-Phenylethyl T-Butyl Sulfoxides. *J. Chem. Soc. Perk. T.*, 2(13):1490–1495, 1976.

[105] M. Nishio, M. Hirota, and Y. Umezawa. *The CH/uppi Interaction: Evidence, Nature and Consequences.* Wiley-VCH, New York, 1998.

[106] M. Brandl, M. S. Weiss, A. Jabs, J. Suhnel, and R. Hilgenfeld. C-H$\cdots\pi$-Interactions in Proteins. *J. Mol. Biol.*, 307(1):357–377, March 2001.

[107] J. C. D. Brand, G. Eglinton, and J. Tyrell. Ethynyl-Hydrogen Bond . II. Association of Benzoylacetylene with Aromatic Hydrocarbons and with N-Butyl Ether Studied by Infrared and Proton Resonance Spectroscopy and by Calorimetry. *J. Chem. Soc.*, -(NOV):5914–5919, 1965.

[108] K. Sundararajan, K. S. Viswanathan, A. D. Kulkarni, and S. R. Gadre. H-π Complexes of Acetylene-Benzene: A Matrix Isolation and Computational Study. *J. Mol. Struct.*, 613(1-3):209–222, August 2002.

[109] A. Fujii, S. Morita, M. Miyazaki, T. Ebata, and N. Mikami. A Molecular Cluster Study on Activated CH/π Interactions: Infrared Spectroscopy of Aromatic Molecule-Acetylene Clusters. *J. Phys. Chem. A*, 108(14):2652–2658, April 2004.

[110] N. Nakagawa and S. Fujiwara. Association Shifts of NMR Spectra of Phenylacetylene. *Bull. Chem. Soc. Jpn.*, 33(11):1634–1634, 1960.

[111] R. K. Sampson, S. M. Bellm, J. R. Gascooke, and W. D. Lawrance. Velocity- and Mass-Resolved Rempi Spectroscopy of Van-der-Waals Molecules. A Technique for Determining the Cluster Size Responsible for Spectral Features. *Chem. Phys. Lett.*, 372(3-4):307–313, April 2003.

[112] E. Carrasquillo, T. S. Zwier, and D. H. Levy. The Multiphoton Ionization Spectrum of Complexes of Benzene and Acetylene. *J. Chem. Phys.*, 83(10):4990–4999, 1985.

[113] M. Y. Shelley, H. L. Dai, and T. Troxler. Electronic Relaxation and Vibrational Predissociation of Benzene-Acetylene Van-der-Waals Complexes. *J. Chem. Phys.*, 110(18):9081–9090, May 1999.

[114] M. Okruss, R. Muller, and A. Hese. High-Resolution UV Laser Spectroscopy of Jet-Cooled Benzene Molecules: Complete Rotational Analysis of the $S_1 \leftarrow S_o 6^1_o (i = \pm 1)$ Band. *J. Mol. Spectrosc.*, 193(2):293–305, February 1999.

[115] Kenta Shibasaki, Asuka Fujii, Naohiko Mikami, and Seiji Tsuzuki. Magnitude and Nature of Interactions in Benzene-x (x = Ethylene and Acetylene) in the Gas Phase: Significantly Different Ch/π Interaction of Acetylene as Compared with Those of Ethylene and Methane. *J. Phys. Chem. A*, 111(5):753–758, February 2007.

[116] S. Tsuzuki, K. Honda, T. Uchimaru, M. Mikami, and K. Tanabe. The Magnitude of the CH/π Interaction between Benzene and Some Model Hydrocarbons. *J. Am. Chem. Soc.*, 122(15):3746–3753, April 2000.

[117] J. J. Novoa and F. Mota. The C-H$\cdots\pi$ Bonds: Strength, Identification, and Hydrogen-Bonded Nature: A Theoretical Study. *Chem. Phys. Lett.*, 318(4-5):345–354, February 2000.

[118] G. R. Desiraju and T. Steiner. *The Weak Hydrogen Bond.* Oxford University Press, New York, 1999.

[119] S. Scheiner. *Hydrogen Bonding. A Theoretical Perspective.* Oxford University Press, Oxford, 1997.

[120] A. Tekin and G. Jansen. How Accurate Is the Density Functional Theory Combined with Symmetry-Adapted Perturbation Theory Approach for Ch-π and $\pi - uppi$ Interactions? A Comparison to Supermolecular Calculations for the Acetylene-Benzene Dimer. *Phys. Chem. Chem. Phys.*, 9(14):1680–1687, 2007.

[121] K. O. Börnsen, H. L. Selzle, and E. W. Schlag. Spectra of Isotopically Mixed Benzene Dimers - Details on the Interaction in the VdW Bond. *J. Chem. Phys.*, 85(4):1726–1732, August 1986.

[122] B. F. Henson, G. V. Hartland, V. A. Venturo, and P. M. Felker. Raman-Vibronic Double-Resonance Spectroscopy of Benzene Dimer Isotopomers. *J. Chem. Phys.*, 97(4):2189–2208, August 1992.

[123] K. S. Law, M. Schauer, and E. R. Bernstein. Dimers of Aromatic-Molecules - $(\mathrm{Benzene})_2$, $(\mathrm{Toluene})_2$, and Benzene Toluene. *J. Chem. Phys.*, 81(11):4871–4882, 1984.

[124] W. Scherzer, O. Kratzschmar, H. L. Selzle, and E. W. Schlag. Structural Isomers of the Benzene Dimer from Mass Selective Hole-Burning Spectroscopy. *Z. Naturforsch. A*, 47(12):1248–1252, December 1992.

[125] R. Schmied, P. Carcabal, A. M. Dokter, V. P. A. Lonij, K. K. Lehmann, and G. Scoles. UV Spectra of Benzene Isotopomers and Dimers in Helium Nanodroplets. *J. Chem. Phys.*, 121(6):2701–2710, August 2004.

[126] V. A. Venturo and P. M. Felker. Intermolecular Raman Bands in the Ground-State of Benzene Dimer. *J. Chem. Phys.*, 99(1):748–751, July 1993.

[127] Thomas Häber, Kai Seefeld, and Karl Kleinermanns. Mid- and Near-Infrared Spectra of Conformers of H-Pro-Trp-OH., journal = J. Phys. Chem. A. 111(16):3038–3046, April 2007.

[128] I. Hünig and K. Kleinermanns. Conformers of the Peptides Glycine-Tryptophan, Tryptophan-Glycine and Tryptophan-Glycine-Glycine as Revealed by Double Resonance Laser Spectroscopy. *Phys. Chem. Chem. Phys.*, 6(10):2650–2658, May 2004.

[129] C. Janzen, D. Spangenberg, W. Roth, and K. Kleinermanns. Structure and Vibrations of Phenol $(H_2O)(7,8)$ Studied by Infrared-Ultraviolet and Ultraviolet-Ultraviolet Double-Resonance Spectroscopy and Ab Initio Theory. *J. Chem. Phys.*, 110(20):9898–9907, May 1999.

[130] W. R. Bosenberg and D. R. Guyer. Broadly Tunable, Single-Frequency Optical Parametric Frequency-Conversion System. *JOSA B*, 10(9):1716–1722, September 1993.

[131] M. Schmitt, H. Henrichs, H. Muller, and K. Kleinermanns. Intermolecular Vibrations of the Phenol Dimer Revealed by Spectral Hole-Burning and Dispersed Fluorescence Spectroscopy. *J. Chem. Phys.*, 103(23):9918–9928, December 1995.

[132] W. Roth, C. Jacoby, A. Westphal, and M. Schmitt. A Study of 2H- and 2D-Benzotriazole in Their Lowest Electronic States by UV-Laser Double-Resonance Spectroscopy. *J. Phys. Chem. A*, 102(18):3048–3059, April 1998.

[133] G. Jansen and A. Heßelmann. Comment on “Using Kohn-Sham Orbitals in Symmetry-Adapted Perturbation Theory to Investigate Intermolecular Interactions”. *J. Phys. Chem. A*, 105(49):11156–11157, December 2001.

[134] A. Heßelmann and G. Jansen. Intermolecular Dispersion Energies from Time-Dependent Density Functional Theory. *Chem. Phys. Lett.*, 367(5-6):778–784, January 2003.

[135] A. Heßelmann and G. Jansen. The Helium Dimer Potential from a Combined Density Functional Theory and Symmetry-Adapted Perturbation Theory Approach Using an Exact Exchange-Correlation Potential. *Phys. Chem. Chem. Phys.*, 5(22):5010–5014, 2003.

[136] A. Heßelmann, G. Jansen, and M. Schutz. Density-Functional Theory-Symmetry-Adapted Intermolecular Perturbation Theory with Density Fitting: A New Efficient Method to Study Intermolecular Interaction Energies. *J. Chem. Phys.*, 122(1):14103, January 2005.

[137] B. Jeziorski, R. Moszynski, and K. Szalewicz. Perturbation-Theory Approach to Intermolecular Potential-Energy Surfaces of Van-der-Waals Complexes. *Chem. Rev.*, 94(7):1887–1930, November 1994.

[138] K. Szalewicz, K. Patkowski, and B. Jeziorski. Intermolecular Interactions via Perturbation Theory: From Diatoms to Biomolecules. *Intermolecular Forces and Clusters II*, 116:43–117, 2005.

[139] G. W. M. Vissers, A. Heßelmann, G. Jansen, P. E. S. Wormer, and A. van der Avoird. New CO-CO Interaction Potential Tested by Rovibrational Calculations. *J. Chem. Phys.*, 122(5):54306, February 2005.

[140] C. Leforestier, A. Tekin, G. Jansen, and M. Herman. First Principles Potential for the Acetylene Dimer and Refinement by Fitting to Experiments. *J. Chem. Phys.*, 135(23):234306, December 2011.

[141] A. J. Misquitta, R. Podeszwa, B. Jeziorski, and K. Szalewicz. Intermolecular Potentials Based on Symmetry-Adapted Perturbation Theory with Dispersion Energies from Time-Dependent Density-Functional Calculations. *J. Chem. Phys.*, 123(21):214103, December 2005.

[142] R. Bukowski, R. Podeszwa, and K. Szalewicz. Efficient Calculation of Coupled Kohn-Sham Dynamic Susceptibility Functions and Dispersion Energies with Density Fitting. *Chem. Phys. Lett.*, 414(1-3):111–116, October 2005.

[143] R. Podeszwa, R. Bukowski, and K. Szalewicz. Density-Fitting Method in Symmetry-Adapted Perturbation Theory Based on Kohn-Sham Description of Monomers. *J. Chem. Theory Comput.*, 2(2):400–412, March 2006.

[144] R. Podeszwa, R. Bukowski, and K. Szalewicz. Potential Energy Surface for the Benzene Dimer and Perturbational Analysis of $\pi - \pi$ Interactions. *J. Phys. Chem. A*, 110(34):10345–10354, August 2006.

[145] Ad van der Avoird, Rafal Podeszwa, Krzysztof Szalewicz, Claude Leforestier, Rob van Harrevelt, P. R. Bunker, Melanie Schnell, Gert von Helden, and Gerard Meijer. Vibration-Rotation-Tunneling States of the Benzene Dimer: An *Ab Initio* Study. *Phys. Chem. Chem. Phys.*, 12(29):8219–8240, 2010.

[146] Stone. *The Theory of Intermolecular Forces.* Claredon, Oxford, 1996.

[147] A. Tekin and G. Jansen. Unpublished Results. on Benzene-Acetylene clusters.

[148] C. A. Hunter and J. K. M. Sanders. The Nature of $\pi - uppi$ Interactions. *J. Am. Chem. Soc.*, 112(14):5525–5534, July 1990.

[149] A. Corana, M. Marchesi, C. Martini, and S. Ridella. Minimizing Multimodal Functions of Continuous-Variables with the Simulated Annealing Algorithm. *Acm T. Math. Software*, 13(3):262–280, September 1987.

[150] N. Metropolis, A. W. Rosenbluth, M. N. Rosenbluth, A. H. Teller, and E. Teller. Equation of State Calculations by Fast Computing Machines. *J. Chem. Phys.*, 21(6):1087–1092, 1953.

[151] J. G. Hill, J. A. Platts, and H. J. Werner. Calculation of Intermolecular Interactions in the Benzene Dimer Using Coupled-Cluster and Local Electron Correlation Methods. *Phys. Chem. Chem. Phys.*, 8(35):4072–4078, 2006.

[152] D. Kuchenbecker and G. Jansen. Intermolecular Interactions in Weak Donor-Acceptor Complexes from Symmetry-Adapted Perturbation and Coupled-Cluster Theory: Tetracyanoethylene-Benzene and Tetracyanoethylene-p-Xylene. *Chemphyschem*, 13(11):2769–2776, August 2012.

[153] R. A. Kendall, T. H. Dunning, and R. J. Harrison. Electron-Affinities of the 1st-Row Atoms Revisited - Systematic Basis-Sets and Wave-Functions. *J. Chem. Phys.*, 96(9):6796–6806, May 1992.

[154] D. E. Woon and T. H. Dunning. Gaussian-Basis Sets for Use in Correlated Molecular Calculations. III.The Atoms Aluminum through Argon. *J. Chem. Phys.*, 98(2):1358–1371, January 1993.

[155] M. Häser and R. Ahlrichs. Improvements on the Direct Scf Method. *J. Comput. Chem.*, 10(1):104–111, January 1989.

[156] M. von Arnim and R. Ahlrichs. Performance of Parallel TURBOMOLE for Density Functional Calculations. *J. Comput. Chem.*, 19(15):1746–1757, 1998.

[157] S. F. Boys and F. Bernardi. Calculation of Small Molecular Interactions by Differences of Separate Total Energies - Some Procedures with Reduced Errors. *Mol. Phys.*, 19(4):553–566, 1970.

[158] A. J. Gotch and T. S. Zwier. Multiphoton Ionization Studies of Clusters of Immiscible Liquids. I. C_6H_6-$(H_2O)_n)_n$, $n = 1, 2$. *J. Chem. Phys.*, 96(5):3388–3401, March 1992.

[159] A. W. Garrett and T. S. Zwier. Multiphoton Ionization Studies of Clusters of Immiscible Liquids. II. C_6H_6-$(H_2O)_n$, $n = 3 - 8$ and $(C_6H_6)_2{-}(H_2O)_{1,2}$. *J. Chem. Phys.*, 96(5):3402–3410, March 1992.

[160] P. Flükiger, S. Luethi, H. P.and Portmann, and J. Weber. *MOLEKEL 4.3.* Swiss Center for Scientific Computing, Manno, Switzerland, 2000-2002.

[161] S. Portmann and H. P. Lüthi. MOLEKEL: An Interactive Molecular Graphics Tool. *Chimia*, 54(12):766–770, 2000.

[162] M. T. Kirchner, D. Bläser, and R. Boese. Co-Crystals with Acetylene: Small Is Not Simple! *Chem-Eur. J.*, 16:2131–2146, 2010.

[163] G. C. Pimentel and A. L. McClellan. Hydrogen Bonding. *Annu. Rev. Phys. Chem.*, 22:347, 1971.

[164] G. A. Jeffrey. *An Introduction to Hydrogen Bonding.* Oxford University Press, New York, 1997.

[165] A. Fujii, G. N. Patwari, T. Ebata, and N. Mikami. Vibrational Spectroscopic Evidence of Unconventional Hydrogen Bonds. *Int. J. Mass Spectrom.*, 220:289–312, 2002.

[166] V. R. Thalladi, A. Gehrke, and R Boese. C-H Group Acidity and the Nature of C-H$\cdots$N Interactions: Crystal Structural Analysis of Pyrazine and Methyl Substituted Pyrazines. *New J. Chem.*, 24:463–470, 2000.

[167] Markus Böning, Benjamin Stuhlmann, Gernot Engler, Matthias Busker, Thomas Häber, Adem Tekin, Georg Jansen, and Karl Kleinermanns. Towards a Spectroscopic and Theoretical Identification of the Isolated Building Blocks of the Benzene-Acetylene Cocrystal. *ChemPhysChem*, 14(4, SI):837–846, MAR 18 2013.

[168] O. Dopfer, G. Lembach, T. G. Wright, and K. Müllerdethlefs. The Phenol Dimer - Zero-Kinetic-Energy Photoelectron and 2-Color Resonance-Enhanced Multiphoton Ionization Spectroscopy. *J. Chem. Phys.*, 98:1933–1943, 1993.

[169] L. Pejov, M. Solimannejad, and V. Stefov. The π-Type Hydrogen Bond with Triple C-C Bond Acting as a Proton-Acceptor. A Gradient-Corrected Hybrid HF-DFT and MP2 Study of the Phenol-Acetylene Dimer in the Neutral S_0 Ground State. *Chem. Phys.*, 323:259–270, 2006.

[170] P. J. Stang and F. Diederich. *Modern Acetylene Chemistry.* VCH, Weinheim, 1995.

[171] W. C. Wiley and I. H. McLaren. Time-of-Flight Mass Spectrometer with Improved Resolution. *Rev. Sci. Instrum.*, 26:1150–1157, 1955.

[172] G. V. Hartland, B. F. Henson, V. A. Venturo, and P. M. Felker. Ionization-Loss Stimulated Raman-Spectroscopy of Jet-Cooled Hydrogen-Bonded Complexes Containing Phenols. *J. Phys. Chem.*, 96:1164–1173, 1992.

[173] U. Buck and F. Huisken. Infrared Spectroscopy of Size-Selected Water and Methanol Clusters. *Chem. Rev.*, 100:3863–3890, 2000.

[174] W. Roth, M. Schmitt, C. Jacoby, D. Spangenberg, C. Janzen, and K. Kleinermanns. Double Resonance Spectroscopy of Phenol(H_2O)(1-12): Evidence for Ice-Like Structures in Aromate-Water Clusters? *Chem. Phys.*, 239:1–9, 1998.

[175] P. R. Callis. *Topics in Fluorescence Spectroscopy.*, volume 5. Plenum Press, new York, 1977.

[176] D. M. Sammeth, S. Yan, L. H. Spangler, and P. R. Callis. Two-Photon Fluorescence Excitation Spectra of Indole in Vapor and Jet: ^1L_a States. *J. Phys. Chem.*, 94:7340–7342, 1990.

[177] B. Albinsson and B. Norden. Excited-State Properties of the Indole Chromophore: Electronic Transition Moment Directions from Linear Dichroism Measurements: Effect of Methyl and Methoxy Substituents. *J. Phys. Chem.*, 96:6204–6212, 1992.

[178] C. Brand, J. Küpper, D. W. Pratt, W. L. Meerts, D. Krügler, J. Tatchen, and M. Schmitt. Vibronic Coupling in Indole: I. Theoretical Description of the $^1L_a - ^1L_b$ Interaction and the Electronic Spectrum. *Phys. Chem. Chem. Phys.*, 12:4968–4979, 2010.

[179] J. Küpper, D. W. Pratt, W. L. Meerts, C. Brand, J. Tatchen, and M. Schmitt. Vibronic Coupling in Indole: Ii. Investigation of the ^1L_a-^1L_b Interaction Using Rotationally Resolved Electronic Spectroscopy. *Phys. Chem. Chem. Phys.*, 12:4980–4988, 2010.

[180] O. Oeltermann, C. Brand, B. Engels, J. Tatchen, and M. Schmitt. The Structure of 5-Cyanoindole in the Ground and the Lowest Electronically Excited Singlet States, Deduced from Rotationally Resolved Electronic Spectroscopy and *Ab Initio* Theory. *Phys. Chem. Chem. Phys.*, 14:10266–10270, 2012.

[181] O. Oeltermann, C. Brand, W. L. Meerts, J. Tatchen, and M. Schmitt. Rotationally Resolved Electronic Spectroscopy of 2,3-Bridged Indole Derivatives: Tetrahydrocarbazole. *J. Mol. Struc.*, 993:2–8, 2011.

[182] Y. Huang and M. Sulkes. Anomalously Short Fluorescence Lifetimes in Jet Cooled 4-Hydroxyindole. Evidence for Excited State Tautomerism and Proton Transfer in Clusters. *Chem. Phys. Lett.*, 254:242–248, 1996.

[183] C. Brand, B. Happe, O. Oeltermann, M. Wilke, and M. Schmitt. High Resolution Spectroscopy of several Rovibronically Excited Bands of 5-Cyanoindole - The Effect of Vibrational Averaging. *J. Mol. Struc.*, 2013.

[184] P. Deglmann, F. Furche, and R. Ahlrichs. An Efficient Implementation of Second Analytical Derivatives for Density Functional Methods. *Chem. Phys. Lett.*, 362:511–518, 2002.

[185] R. Brause, M. Schmitt, D. Spangenberg, and K. Kleinermanns. Determination of the Excited State Structure of 7-Azaindole Using a Franck-Condon Analysis. *Mol. Phys.*, 102:1615–1623, 2004.

[186] T. L. Smithson, R. A. Shaw, and H. Wieser. The Vapor Phase Far-Infrared Spectra of ^{1}H-Indene, Benzo[b]Furan, 1, 3, 2-Benzodioxaborole, and Indole: Evidence for Planar Skeletons and Kinetic Anharmonicity in the Out-of-Plane Ring Deformations. *J. Chem. Phys.*, 81:4281–4287, 1984.

[187] G. A. Bickel, D. R. Demmer, A. Outhouse, and S. C. Wallace. The S_1-S_0 Transition of Indole and N-Deuterated Indole: Spectroscopy and Picosecond Dynamics in the Excited State. *J. Chem. Phys.*, 91:6013–6019, 1989.

[188] A. L. Sobolewski, W. Domcke, C. Dedonder-Lardeux, and C. Jouvet. Excited-State Hydrogen Detachment and Hydrogen Transfer Driven by Repulsive $1^{\pi}\sigma^*$ States: A New Paradigm for Nonradiative Decay in Aromatic Biomolecules. *Phys. Chem. Chem. Phys.*, 4:1093–1100, 2002.

[189] G Yagil. Effect of Ionic Hydration in Equilibria and Rates in Concentrated Electrolyte Solutions. III. The H- Scale in Concentrated Hydroxide Solutions. *J. Phys. Chem.*, 71:1034–1044, 1967.

[190] A. Weller. Quantitative Untersuchungen der Fluoreszenzumwandlung bei Naptholen. *Z Elektrochem*, 56:662–668, 1952.

[191] J. Kraitchman. Determination of Molecular Structure from Microwave Spectroscopic Data. *AM J PHYS*, 21:17, 1953.

[192] M. Schmitt, Ch. Ratzer, K. Kleinermanns, and W. Leo Meerts. Determination of The Structure of 7-Azaindole in the Electronic Ground and Excited State Using High Resolution Ultraviolet Spectroscopy and an Automated Assignment Based on a Genetic Algorithm. *Mol. Phys.*, 102:1605–1614, 2004.

[193] Yuriy Svartsov and Michael Schmitt. Electronically Excited States of Water Clusters of 7-Azaindole: Structures, Relative Energies and Electronic Nature of the Excited States. *J. Chem. Phys.*, 128:214310(1–9), 2008.

[194] A. Suwaiyan, R. Zwarich, and N. Baik. Infrared and Raman Spectra of Benzimidazole. *J. Raman Spect.*, 21:243–249, 1990.

[195] J. Tomkinson. Reassignment of the Vibrational Spectrum of Benzimidazole. *The Journal of Physical Chemistry A*, 112(27):6115–6119, 2008. PMID: 18549198.

[196] E. Jalviste and A. Treshchalov. Spectroscopy of Jet-Cooled Benzimidazole and Benzotriazole. *Chem. Phys.*, 172:325, 1993.

[197] C. Jacoby, W. Roth, and M. Schmitt. A Comparison of Intermolecular Vibrations and Tautomerism in Benzimidazole, Benzotriazole and their Binary Water Clusters. *Appl. Phys. B*, 71:643, 2000.

[198] B. Velino, A. Trombetti, and E. Cané. Microwave Spectrum of Benzimidazole. *J. Mol. Spec.*, 152:434–440, 1992.

[199] E. Cané, A. Trombetti, B. Velino, and W. Caminati. Microwave Spectrum of Benzimidazole. *J. Mol. Spec.*, 150:222, 1991.

[200] G. Berden, W. Leo Meerts, and E. Jalviste. Rotationally Resolved Ultraviolet Spectroscopy of Indole, Indazole and Benzimidazole: Inertial Axis Reorientation in the $S_1(^1L_b) \leftarrow S_0$ Transition. *J. Chem. Phys.*, 103:9596–9606, 1995.

[201] M. Schmitt, D. Krügler, M. Böhm, C. Ratzer, V. Bednarska, I. Kalkman, and L. W. Meerts. A Genetic Algorithm Based Determination of the Ground and Excited (^1L_b) State Structure and the Orientation of the Transition Dipole Moment of Benzimidazole. *Phys. Chem. Chem. Phys.*, 8:228–235, 2006.

[202] Jung Lee Lin, Yi Chang Li, and Wen Bih Tzeng. Mass Analyzed Threshold Ionization Spectroscopy of Aza-Aromatic Bicyclic Molecules: Benzimidazole and Benzotriazole. *Cem. Phys.*, 334:189–195, 2004.

[203] Shih Chang Yang and Wen Bih Tzeng. Mass-Analyzed Threshold Ionization of Deuterium Substituted Indazole and Benzimidazole and Site-Specific H/D Exchange Reaction. *Chem. Phys. Lett.*, 501:6–10, 2010.

[204] M. Noda and S. Nagaoka andN. Hirota. Electron Paramagnetic Resonance and Optical Detection of Magnetic Resonance Studies of the Lowest Excited Triplet States of Purine, Benzimidazole, and Indazole in Benzoic Acid Host Crystals. *Bull. Chem. Soc. Jpn*, 57:2376–2386, 1984.

[205] Christian Brand, Josefin Rolf, Martin Wilke, and Michael Schmitt. High Resolution Electronic Spectroscopy of Vibrationally Hot Bands of Benzimidazole. *J. Phys. Chem. A*, 117:12812–12820, 2014.

[206] M. Cordes and J. L. Walter. Infared and Raman Studies of Heterocyclic Compounds–II Infrared Spectra and Normal Vibrations of Benzimidazole and Bis-Benzimidazole-Metal Complexes. *Spectrochim. Acta A*, 24:1421–1435, 1968.

[207] D. A. Dolson, K. W. Holtzclaw, S. H. Lee, S. Munchak, C. S. Parmenter, and B. M. Stone. Intramolecular Vibrational Redistribution at Low State Densities in S_1 Aromatics. Evidence for Rotational Contributions. *Laser Chem.*, 2:271–283, 1983.